University of Southampton

National Oceanography Centre

Mechanisms of Atlantic Variability and Sensitivity of the Atlantic to Surface Initial Conditions

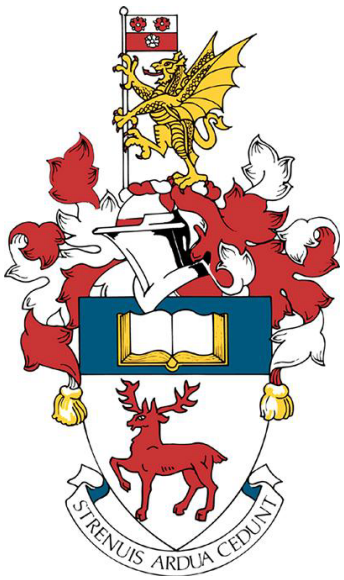

Thesis for the degree of Doctor of Philosophy

Author:

Victor Estella Perez

Supervisors:

Dr. Florian Sévellec

Dr. Bablu Sinha

2nd February 2019

UNIVERSITY OF SOUTHAMPTON

ABSTRACT

FACULTY OF NATURAL AND ENVIRONMENTAL SCIENCES

Doctor of Philosophy

Mechanisms of Atlantic Variability and Sensitivity of the Atlantic to Surface Initial Conditions

by Victor Estella Perez

The climate system is a complex system, in the sense that it has many components that interact with each other and in the difficulty of modelling all the interactions within the system. The nonlinear nature of these interactions raise questions on the ability of the system to be predicted. Climate predictability is concerned not only with skill of the prediction itself, but address questions that could lead to a better understanding of climate sensitivity or processes of variability in the climate. The goal of this thesis is contributing to this understanding focusing on the Atlantic and Weddell Sea, key regions of the climate system.

Decadal predictability is limited by errors in the initial conditions and boundary conditions (model parametrizations, forcing, etc.). Understanding the impact of initial errors in surface fields (Sea Surface Temperature, SST, or Sea Surface Salinity, SST) has not been developed fully in a non-linear framework, previous approaches have provided optimal perturbations in a linear framework. The impact of errors in the SSS field are explored with a set of experiments perturbing the SSS field with Gaussian perturbations centred in the Irminger Sea parametrized by its horizontal extension and intensity (magnitude of the maxima of the Gaussian distribution). Focusing on the impact of these errors on the Atlantic Meridional Overturning Circulation (AMOC), main driver of the Atlantic climate in various time-scales, we obtained a response to these initial errors ranging between 0.001 to 0.08 Sv psu^{-1} for lower and higher extensions respectively. Defining statistically a linear regime allowed us to compare this approach to previous linear approaches and, to understand the differences between the predicted linear responses and the model non-linear response. The different sign of the initial perturbation, positive or negative, have an enhancing or reducing response when compared to the linear prediction. The departure from the linear prediction is associated with different

parameters of the perturbation: magnitude and extension respectively.

In addition to initial condition errors, we focused on a mechanisms of North Atlantic variability obtained in Océan PArallélisé (OPA) under Mixed Boundary Conditions (MBC). The variability, characterized by oscillations with a time scale of 42-years, is driven by the westward propagation of Thermal Rossby waves changing the zonal density gradient promoting or reducing the meridional transport. We found a strong link between AMOC and Atlantic Multidecadal Oscillation (AMO) oscillations, which are on phase. The mechanism of propagation, through geostrophic self-advection, contributes to changes in other components of the subpolar region modifying convection and horizontal transport in the region.

Under the same model configuration, variability driven by the Weddell Sea causes a peak in the North Atlantic power spectrum on a centennial time scale was investigated. The multi-centennial time scale rises from a combination of convective and non-convective periods in the Weddell Sea. These two periods are associated with changes in the Atlantic Heat content and variations in the overturning rate. Changes between the two periods are driven by changes in the subsurface heat storage and ice cover in a region west of the Weddell Sea. A similar signature of ice variability is been observed coinciding with regions where previous polynyas have been observed.

Contents

List of Tables

List of Figures

Academic Thesis: Declaration Of Authorship

I, Victor Estella Perez, declare that this thesis and the work presented in it are my own and has been generated by me as the result of my own original research.

Mechanisms of Atlantic Variability and Sensitivity of the Atlantic to Surface Initial Conditions

I confirm that:

.

1. This work was done wholly or mainly while in candidature for a research degree at this University;

2. Where any part of this thesis has previously been submitted for a degree or any other qualification at this University or any other institution, this has been clearly stated;

3. Where I have consulted the published work of others, this is always clearly attributed;

4. Where I have quoted from the work of others, the source is always given. With the exception of such quotations, this thesis is entirely my own work;

5. I have acknowledged all main sources of help;

6. Where the thesis is based on work done by myself jointly with others, I have made clear exactly what was done by others and what I have contributed myself;

7. Either none of this work has been published before submission, or parts of this work have been published as:

Signed:_____

Date:_____

"The importance of being nolinear"

Steven H. Strogatz

Acknowledgements

I would like to thank to both my supervisors, Florian and Bablu. I really appreciate the effort, time and trust that you made over me by taking the chance of a student with no background in Oceanography. I am very grateful for having found a career that I could do for the rest of my life. Secondly to Sybren for the input during this thesis. Thanks to Florian for being a mentor for me on how to work, how to approach certain situations and always back me up. To Bablu, thank you for being very supportive and always be very positive about my work and illuminating me on almost every meeting we had. As well, I would like to thank in particular to Eleanor and Alberto for being together with my supervisors role models that I would like to become in the academic, teaching and personal side.

Me gustaría agradecerle a mi familia todo el apoyo que me han ofrecido todos estos años, emocional y económicamente. Sin la ayuda de mis padres y mi hermana no estaría donde estoy. También a mi tía Toya por haber sido un ejemplo para mí. Me gustara hacer especial mención a mis abuelos, que nos han ofrecido la educación y recursos a toda mi familia para asegurarnos un futuro y bienestar a todos. Gracias por todo.

I would like to thank my friends back in Spain in the several groups that have been putting up with me all these years. Alex and Ana, for accommodating every time I was stopping in Madrid and all the personal support they gave me. To my friends Ana, Pilar and Silvia for being a great example for me. To my friend Guillermo, for being a role model for me on how to take an academic career and being there on all steps of the way. My friends from school (Raquel, Irene, Paula, Isabel, Julia y Alberto) that despite me being abroad, made me feel always like

I didn't leave. As well friends from high school (Pilar, Belen, Sara and Marta), despite not seeing each other that much they made seem like time didn't pass at all every time we met along these years. To complete my acknowledges for people at home, I would like to thank my friends Elena and Vic, the three of us lived/worked/studied in the UK sharing the experience, so I would like to thank them for being there for me all the way. Thanks to Marta, despite seeing each other once a year her lessons in life and help lasted for the whole year. Finally, I would like to both Silvia and Silvia, for being always up for some visits to the beautiful Southampton, those surf trips and helping each other elevating the PhD-mood these years, we all will be doctors!

To the people at NOC that have been together with me along the PhD from the beginning and special thanks to the physical oceanography gang (Helen, Jesse, Zoe, Freya, Matt and Jon). We started together and they remained part of my life aside from work. To Maike, that despite leaving some time ago she has been always very inspiring and motivating on making me to pursue the cool topics that I am interested in. I am really looking forward to work together with you one day! As well thanks to Maria and Rafa for being a great support over the last months of PhD. I would like to thank as well to Delphine, for making me see the improvements and experience I gained these years and hopefully will help her to go through her PhD. Special mention to another important person that passed through my time at NOC, Simona, thanks for all the support and it's been a pleasure to share the PhD with you! To almost finish my round of acknowledgements to NOC people I would like to thank to the other two members of "La tríada" Elena and Cristian. Elena thank you for reminding me the unbiased view of the things and situations and all the support along the PhD journey. Cristian thanks to everything, from coffees, to scold me for working too much, for knock on my door for lunchs, etc. Thank you to the both of you. Last but not least I would like to thank to Giulia. Thank you for letting me be part of your journey, I am very grateful for meeting you and sharing these years by your side. The journey is been hard and long but we made it!

Glossary

u, v, w Velocity components.

AABW Antarctic Bottom Water.

AAIW Antarctic Intermediate Water.

ACC Antartic Circumpolar Current.

AMO Atlantic Multidecadal Oscillation.

AMOC Atlantic Meridional Overturning Circulation.

AMOCI Atlantic Meridional Overturning Circulation Index.

AMV Atlantic Multidecadal Variability.

CMIP5 Coupled Model Inter-Comparison Project 5.

DWBC Deep Western Boundary Current.

EOF Empirical Orthogonal Function.

EOFs Empirical Orthogonal Functions.

FBC fixed Flux Boundary Conditions.

GCMs General Circulation Models.

GSAs Great Salinity Anomalies.

IPCC Intergovernmental Panel on Climate Change.

kyrs kiloyears, 1kyr=10^3 years.

LNADW Lower North Atlantic Deep Water.

LOPs Linear Optimal Perturbations.

MBC Mixed Boundary Conditions.

MLD Mixed Layer Depth.

NADW North Atlantic Deep Water.

NAO North Atlantic Oscillation.

NASPG North Atlantic SubPolar Gyre.

NEMO Nucleus for European Modelling of the Ocean.

OHC Ocean Heat Content.

OPA Océan PArallélisé.

PCs Principal Components.

PDO Pacific Decadal Oscillation.

PV Potential Vorticity.

RAPID Rapid Climate Change program.

RBC Restoring Boundary Conditions.

S Salinity.

SLH Sea Level Height.

SLP Sea Level Pressure.

SPG Subpolar Gyre.

SSS Sea Surface Salinity.

SST Sea Surface Temperature.

STG Subtropical Gyre.

T Temperature.

THC ThermoHaline Circulation.

UNADW Upper North Atlantic Deep Water.

WBC Western Boundary Current.

Chapter 1

Introduction

1.1 Climate dynamics

The prospects of human-induced climate change have become more relevant in the scientific community and to the general public. Climate research has focused its efforts on quantifying and distinguishing the role of anthropogenic forcing and natural variability (Bindoff et al., 2013). The Intergovernmental Panel on Climate Change (IPCC) fifth assessment report (Stocker et al., 2013), presents the influence of human activities on the climate with scientific evidence. In order to detect and predict the influence of humans in the future climate state, we need first to understand the complexity of the climate on Earth.

The interaction of the different components in the Earth system display a large variety of interconnections and spatio-temporal fluctuations. The main components are the lithosphere (the world of solid earth), cryosphere (the world of the ice), hydrosphere (the world of water), biosphere (the world of living beings) and atmosphere. The climate system is a complex system in which these subsystems exchange matter, energy and information (Donner et al., 2009). A great number of climate processes are involved in this exchange, the most relevant for modelling the climate system are illustrated in Fig. 1.1. The main input of energy into the climate is through solar radiation. Half of the solar radiation incident at the top of the atmosphere is absorbed at the surface. About a third is reflected back by

the atmosphere and surface and, about 20% absorbed by the atmosphere (Kiehl and Trenberth, 1997). In the ocean, this heat is mixed by turbulent motions in the near-surface up to the mixed layer (which can vary between 20 m to 1000s of meters depending on location) and transported horizontally by oceanic currents. The upper ocean exchange heat to and from the atmosphere, contributing to the generation of wind stress that supplies energy back to the ocean currents.

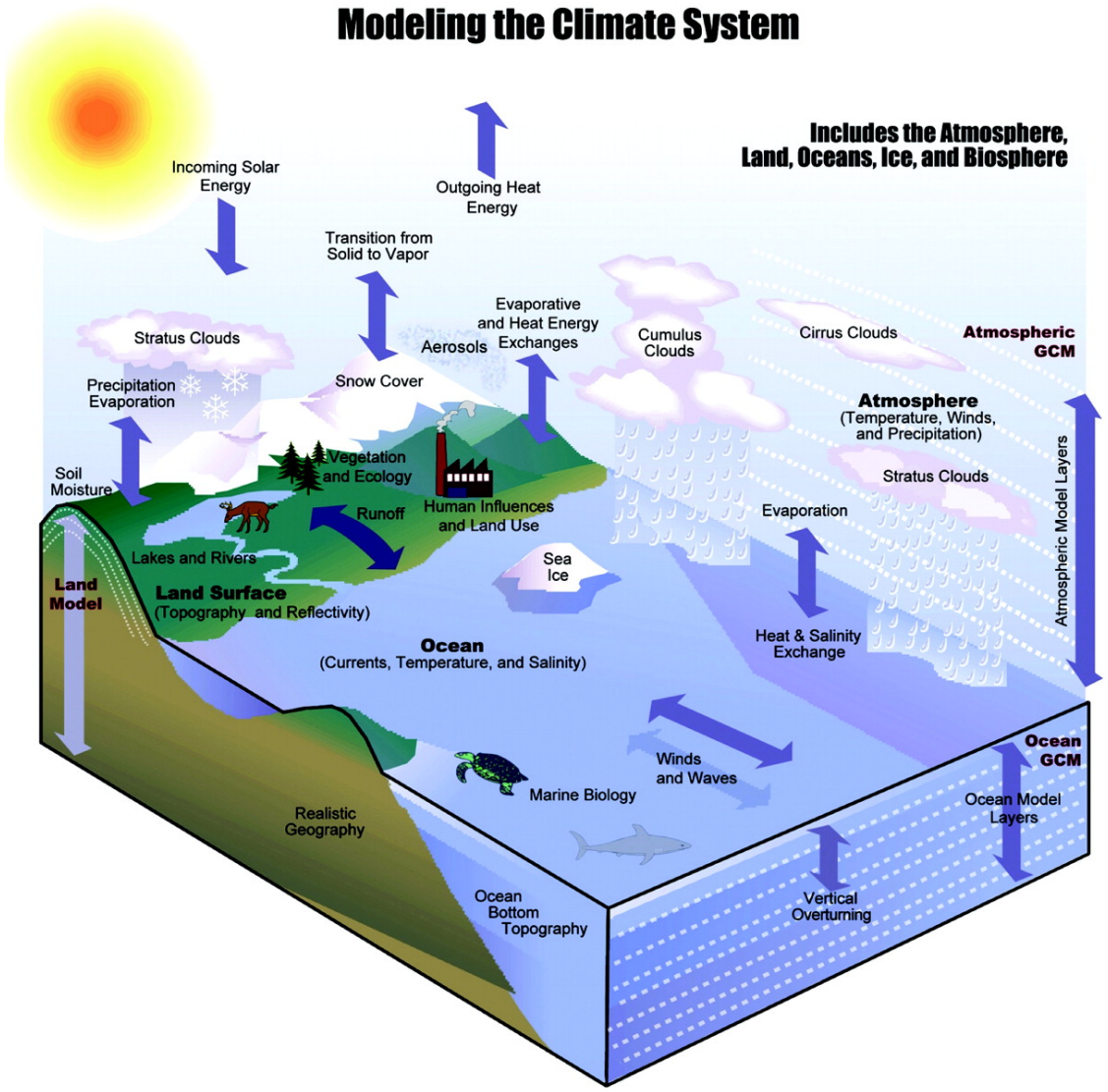

Figure 1.1: Figure from Karl and Trenberth (2003) showing some of the components of the climate system and their interactions. These are the main factors and interactions considered in climate models.

The different components of the climate respond to changes at different times-

cales. For example, atmospheric variability can be measured in minutes, whereas changes in the crust of the earth may take up to millions of years. Climate cycles are measured in periods (T, unit in seconds s) or frequencies ($\omega = T^{-1}$ unit s^{-1}). In general, the amount of variability in different frequencies is measured by the spectral power $S(\omega)$ of a time series, e.g. SST of the last 200 years in the North Atlantic. Unfortunately, there is no extant series of direct measurements that includes periods from hours to kiloyears, 1kyr=10^3 years (kyrs). Fig. 1.2 shows a "hypothetical" spectrum of the climate system computed from a set of spectra from different time series computed initially by Mitchell (1976). The left of Fig.1.2 corresponds to longer periods obtained from paleoclimatic records: marine-sediment, ice-cores, tree rings or coral records. As the period decreases, peaks of variability in the range of decadal to multidecadal variability appear. Some of this variability is related to the North Atlantic climate, in particular to the Atlantic Multidecadal Oscillation (AMO). It is characterized by changes in the SST of the North Atlantic on timescales of 20 and 50-70 years. Also other modes of variability contribute to these time scales: Pacific Decadal Oscillation (PDO) an ocean-atmosphere variability with a pattern of warm or cool surface waters in the Pacific Ocean north of 20° (Biondi et al., 2001) or North Atlantic Oscillation (NAO) fluctuations of the difference of atmospheric pressure at sea level (SLP) between the Icelandic low and the Azores high controlling the strength and direction of westerly winds and location of storm tracks across the North Atlantic (Hurrell et al., 2003).

Reducing further the period we have interannual timescales with El Niño/Southern Oscillation (ENSO) as one of the main drivers on these timescales. It is a combination between an oceanic component, El Niño, and the atmospheric Southern Oscillation. In its warm phase, El Niño, the Sea Surface Temperature (SST) of the eastern tropical Pacific warms by a few degrees for about a year. It is accompanied by high air pressure in the western Pacific and low air pressure in the eastern Pacific inducing a change of direction of the Trade Winds. These characteristics change to their opposite phase, La Niña, with a cold anomaly in the surface temperature and high-low pressure in the eastern-western pacific respectively. ENSO has an observed variability with a period between 2 to 7 years in which the two phases last up to several months together with a neutral phase.

If we reduce further the scales to years and days (both sharp peaks on the right of the figure). Smaller bumps on the right of the figure are associated with variability of weather systems in intraseasonal variability between 1 and 3 months and ranges of 3-7 days. The dominant component of the intraseasonal timescales is the Madden-Julian Oscillation, a coupling between large-scale patterns in atmospheric circulation and deep convection (Zhang, 2005). It is mainly observed in the Indian and Pacific Ocean, it consists of large regions of enhanced and suppressed tropical rainfall moving eastward.

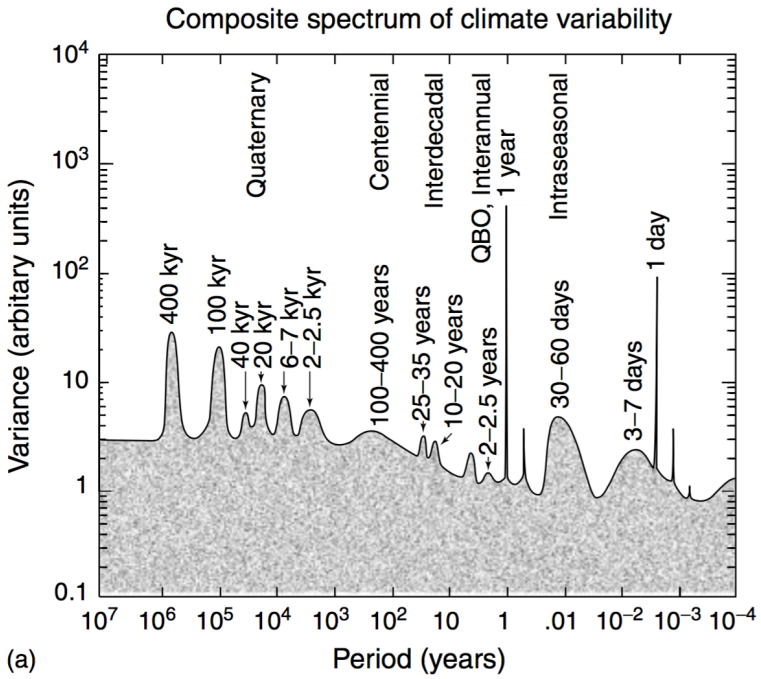

Figure 1.2: Composite of the planetary climate variance spectrum from Ghil (2002) over the last 10 Myr (1 Myr = 10^6 yr and 1 kyr = 10^3 yr). Figure adapted from Mitchell (1976).

The oceans cover about 71% of the planet, and are the main energy receptors of the climate system from the only external energy input, solar radiation. This solar input is larger at low latitudes than at high latitudes, requiring a global scale redistribution of energy by the atmosphere and the ocean. Water properties makes it a good material to store heat, three metres of ocean have the same heat capacity as the whole atmosphere (Siedler et al., 2011), and therefore a key element to record any anthropogenic change. The ocean can be viewed as a "mechanically driven fluid engine" (Wunsch, 2002) whose properties change as they react to the

applied boundary conditions. The ocean circulation is driven by heat, fresh water and momentum fluxes between the atmosphere and the ocean. The asymmetric land distribution on both hemispheres contributes to add more complexity to the range of spatial and timescales contributing to exchanges between the ocean and atmosphere.

Three types of circulation can be differentiated in the ocean, one upper ocean circulation (mainly forced by the wind), the thermohaline circulation and smaller scale eddy circulation. All are generated by different mechanisms but are actively linked to each other. The wind-driven circulation is produced by the wind stress curl of the large-scale wind distribution. The subtropical Trade Winds and mid-latitude westerlies contribute to the formation of subtropical and subpolar gyres. On one hand, the balance between the conservation of Potential Vorticity (PV) and wind stress curl govern the eastern region of the gyre, the wind stress curl balances the meridional flow (Sverdrup balance). On the western part, and due to the Earth's rotation, in order to conserve the PV an intensified narrow current in the west known as Western Boundary Current (WBC) closes the circulation.

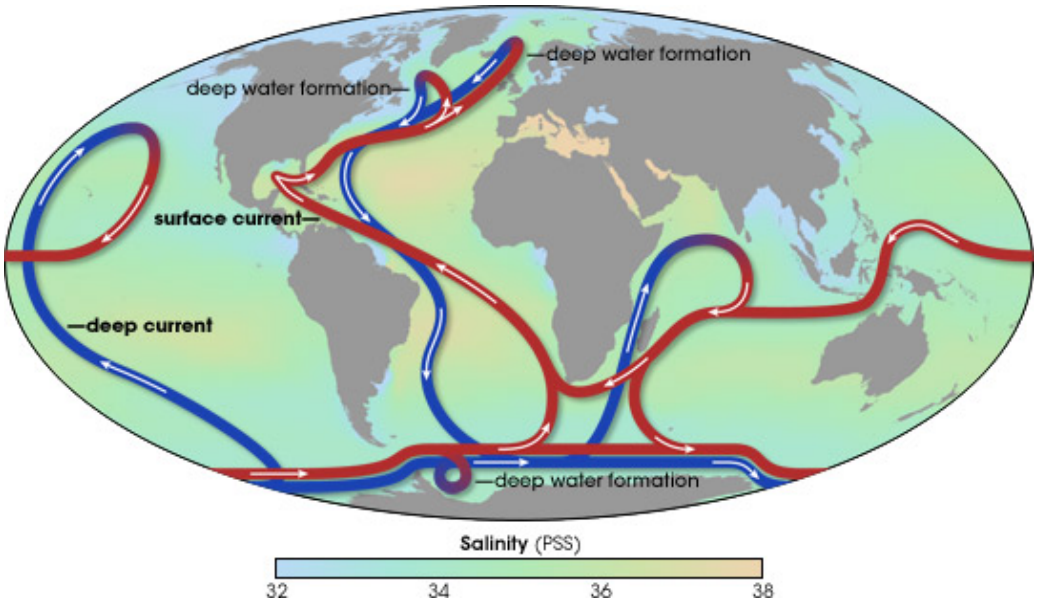

Figure 1.3: Figure of the Thermohaline Circulation. Map by Robert Simmon, adapted from the IPCC (2001) and Rahmstorf (2002).

The ThermoHaline Circulation (THC) (Stommel, 1961) contributes to heat re-distribution from low to high latitudes. It is driven by temperature and salinity

but owes its existence to the oceanic-atmosphere interaction (Wunsch, 2002). At high-latitudes, the cold atmosphere extracts large amounts of heat from the ocean. Combined with salt rejection from the formation of sea ice, both promote the formation of cold and dense water masses that sink and spread filling the bottom of the ocean. In order to conserve the volume of sinking water, warmer surface water flows polewards into the sinking regions closing the circulation. Deep water formation occurs, aside from open convection, over the Antarctic and Arctic continental shelves. Here, in coastal shallow waters, intense air-sea interaction aid to form very dense waters that flow along the sea bed reaching the ocean depths through the continental slopes. One of the main water masses formed through this mechanism is the Antarctic Bottom Water (AABW) formed along the coasts of Antartica.

1.1.1 The Atlantic, key driver of the global climate

The North Atlantic is one of the main drivers of the global climate. It contains regions of open deep water formation and it has multiple connections with other key components of the climate: atmospheric teleconnections with the Pacific Ocean (Msadek and Frankignoul, 2009; Swingedouw et al., 2013), direct influence on the Arctic Ocean and Southern Ocean through Atlantic waters (Swingedouw et al., 2009), contribution to continental climate (Jackson et al., 2015), etc.

The two phenomena influencing the Atlantic climate are the Atlantic Meridional Overturning Circulation (AMOC)/THC in the ocean component and the NAO the atmospheric variability (Hurrell et al., 2010). . Although these processes have a different nature, their interconnection and the implications for the rest of the global climate are numerous. The AMOC is defined as the zonally averaged meridional transport and consists of a surface northward flow of relatively warm and salty water and a southward return flow at depth (Kuhlbrodt et al., 2007). The NAO instead is primarily an atmospheric phenomenon, measured by sea level pressure difference between the Icelandic Low and the Azores high.

The AMOC contributes to poleward heat transport with a maximum of northward heat transport of about 1.33±0.40 PW (1PW=10^{15}W) (Johns et al., 2011),

over the initial estimations of 1 PW (Hall and Bryden, 1982; Ganachaud and Wunsch, 2000). Although it is generally represented in a zonally averaged view, it actually has a 3-dimensional distribution to which different components such as wind-driven circulation or atmospheric state contribute to its variability in different locations. A schematic of the North Atlantic circulation is in Fig.1.4. The warm surface, and slightly saltier, waters coming from the lower latitudes either continue their path following the wind driven circulation, the Subtropical Gyre (STG), or continue northwards as the North Atlantic Current. At the location marked with a black square in the figure, it divides in two branches: one directed north-west towards the east-coast of Greenland, closing the Subpolar Gyre (SPG), and a second branch carrying heat into the Nordic Seas (north of Iceland). The cold temperature of the atmosphere in the northern latitudes, especially in winter, promotes the release of heat from the ocean generating convective mixing in the Labrador/Irminger Seas. The generation of these intermediate deep waters known as Upper North Atlantic Deep Water (UNADW) feed together with the denser water coming from the Nordic Seas, Lower North Atlantic Deep Water (LNADW), the return flow of the AMOC.

Figure 1.4: Schematic of the North Atlantic circulation modified from Srokosz and Bryden (2015). The red thick plane arrows correspond to the STG circulation that is fed by surface water coming from the Southern Ocean and continuing northward after the STG. The temperature difference with the atmosphere provides an exchange of heat represented in the 3-dimensional arrows as they change colours (atmospheric circulation). The cooling in the ocean is represented in the transition to blue as the ocean circulation continues in the SPG.

The northward heat transport results in milder weather for western Europe when compared to similar latitudes, and hence has a potentially larger impact on the climate as global warming continues (Jackson et al., 2015). Its importance led to the installation of an observing system across the Atlantic at 26.5°N providing direct measurements of the transport since 2004 (Hirschi et al., 2003; Cunningham et al., 2007). The Rapid Climate Change program (RAPID) has provided unexpected information about the variability of the overturning: including a larger than expected range of variability (between 4 to 35 Sv, 1 Sv=10^6 m^3s^{-1}) (Srokosz and Bryden, 2015) , a large amplitude of the seasonal cycle (about 6.7 Sv) driven by the wind stress in the eastern Atlantic (Pérez-Hernández et al., 2015) and a large interannual variability with events such as the significant dip in 2009-2010 (Bryden et al., 2014). Events such as the former have not been reproduced before by climate models used in the IPCC assessments (Srokosz and Bryden, 2015). The

lack of long-term observations leaves models as important tools for understanding the decadal-to-centennial timescale variability. A long list of studies have focused on AMOC long term variability providing insights on possible mechanisms of variability (e.g. Msadek and Frankignoul (2009); Frankcombe et al. (2010); Tulloch and Marshall (2012); Ortega et al. (2015); Menary et al. (2015)). Further details are given in Subsection 1.1.3.

The NAO instead is primarily an atmospheric phenomenon, measured by Sea Level Pressure (SLP) difference between the Icelandic Low and the Azores High. It is very closely related to the 'Artic Oscillation', defined as the leading Empirical Orthogonal Function (EOF) of wintertime monthly mean Northern Hemisphere SLP. In a positive NAO phase (high pressure difference), the dominated westerly winds contribute to a higher number of storms with increasing strength crossing the North Atlantic. This phase provides wetter and stormier conditions in the North of Europe and East of the US. Conversely, the negative phase (low pressure difference) readjusts the jet stream position supplying colder air from the north-east and, weaker and less frequents storms. A negative NAO phase results in colder and dryer winters in Europe and Eastern US. With these characteristics, the NAO, in particular the positive phase contributes to modulate the deep ocean mass properties interacting in the convective regions in the North Atlantic, and also changing the overturning and the Atlantic gyre circulation (Curry et al., 1998; Eden and Willebrand, 2001).It is also one of the candidates to drive the AMO variability, although there is still discussion about it. For some is seen as driven by either NAO (Clement et al., 2015), a purely ocean driven mode (Marshall et al., 2001; McCarthy et al., 2015; Delworth et al., 2017) or a combination of both (Zhang et al., 2016a).

A deep knowledge of the different modes of variability and the relation between the key components of the climate system is a priority of the climate sciences. The North Atlantic, as one of the main drivers of the global climate, is a logical focus of research due to both the large complexity of its interactions and the impact of its variability.

1.1.2 Climate modelling

The complexity of climate mechanisms cannot be understood completely based on observations of the climate state. Large-scale observations, in both ocean and atmosphere, lack records with high spatial and long temporal resolution. In order to complement and understand those sparse observations, climate models are a useful tool to represent the climate on a global scale and a valuable source to provide realistic projections of the evolution of the climate. Depending on the spatial and temporal scales of interest a wide hierarchy of models can be used: from toy models that are able to explain the variability of the AMOC on a millennial time scale (Sévellec and Fedorov, 2014) to General Circulation Models (GCMs) that are able to couple the different components of the climate system (cryosphere, biosphere, hydrosphere, etc.). The main interactions and features of a GCM are shown in Fig. 1.1. Representing all these interactions accurately and completely is a difficult task and, simplifications and parametrizations have to be introduced to reduce the computational cost of a model. A model that could resolve completely all processes in the climate system would be impossible, since to resolve completely all the processes involved in the climate system is an impossible task.

A GCM can be set-up in many configurations: ocean only, ocean coupled with an ice model, ocean coupled with the atmosphere, atmosphere only, etc. All the other components of the climate system can be added according to the aim of the study. The oceanic component of a GCM is based on nonlinear differential equations described by Bryan (1969). The numerical resolution of these equations through finite differences require the spatial discretization of the ocean on a three-dimensional grid. The temporal discretization is then computed on each grid point ensuring the convergence under appropriate choices of parameters such as the timestep and diffusion coefficient. Models such as GCMs have to account for a large number of degrees of freedom (variables), both physical variables and model parameters, of orders larger than than 10^6 (Stammer et al., 1999). Currently global ocean models can reach up to a horizontal resolution of 1/12-1/10°, or even 1/50° but for short integrations, and regional models with even higher resolution.

In mathematical terms, a climate model can be considered as the numerical

solution to a set of differential equations. Once the accuracy required for the solution of the differential equations is accomplished in the development stage of the model, the next step is to understand the evolution of the solutions. In particular what is of interest is, not only an accurate representation of the evolution of the observables (variables that can be measured) but also the sensitivity of the model to changing parameters such as those used for the parametrizations of certain processes that reduce the computational costs. The implication of these changes is the main focus of a field of mathematics known as dynamical systems.

1.1.3 Mechanisms of decadal variability in the North Atlantic

The paucity of long term and high spatial resolution data, especially from the deep ocean, limit our understanding of AMOC large-scale changes in the long term (Cunningham et al., 2007). The use of climate models helps to complete records and help to detect modes of variability. This gain is traded by introducing individual model variability, which in the particular case of the AMOC variability translates into a diversity in the mechanisms and time scales (Review in Yoshimori et al. (2010)). Many models agree on a common period of variability associated with a 20-30-year oscillation period (Muir and Fedorov, 2017), although there is still uncertainty in the mechanisms driving these time scales. In particular, whether it is a mechanism driven purely by the ocean or need to be coupled to the atmosphere to be sustained. For example, Dong and Sutton (2005) did not invoke atmospheric coupling to explain the 25-year peak in the AMOC spectrum in HAdCM3. In this model, a decrease in the overturning stores cold water and leads to an acceleration of the subpolar gyre. This produces an increase in the salinity transport to the convection region, intensifying convection and the overturning. On the other hand, Ortega et al. (2016) described in the coupled model IPSL-CM5A a bi-decadal oscillation as a result of the interaction between two modes of variability: westward propagation of subsurface buoyancy anomalies and upper ocean-atmosphere-sea ice coupled mode driving convection activity south of Iceland. In general, on decadal timescales the main processes affecting the AMOC are: large-scale basin modes

(Cessi and Paparella, 2001; Ben Jelloul and Huck, 2003, 2005), effects of Great Salinity anomalies (Belkin et al., 1998; Zhang and Delworth, 2006), episodes of deepening mixed layer depths in the deep convection areas (Spall, 2008), baroclinic instabilities with large-scale Rossby Waves propagating on the thermocline (further description next), the intergyre-gyre effect (Marshall et al., 2001) or western boundary buoyancy forcing (Buckley et al., 2012).

There is a general consensus that the AMOC variability on decadal to multidecadal timescales is associated with changes in the Atlantic SST, denoted as AMO or Atlantic Multidecadal Variability (AMV) by Kerr (2000). The AMO, with its various definitions represents an averaged SST over the North Atlantic. Proxy climate records, suggest that the AMO is not limited to the observational period but a natural phenomenon intrinsic to the north Atlantic climate. Although the index is an average over the Atlantic, there is a spatial pattern associated when the evolution of the SST is regressed to the index (Fig. 1.5-b). The SST pattern consists of positive anomalies in the Subpolar and subtropical north Atlantic in a so-called horseshoe pattern. The exact details of the pattern can be sensitive to the detrending method used and the period of data used (Trenberth and Shea, 2006). In this thesis I used Trenberth and Shea (2006) for the AMO index.

The AMO is associated with periods between 50-70 years (Knight et al., 2005; Kushnir, 1994) and 20-30 years (Frankcombe et al., 2008; Chylek et al., 2012). In the observational record, since 1900 the index was negative 1905-1920 and 1965-1995 (i.e. cool phase) and positive in 1925-1960 and 1998-present (i.e. warm phase). The evolution of the index is shown in Fig. 1.5-a. Changes in the AMO have been shown to impact: precipitation over northern Europe (Sutton and Hodson, 2005a), Atlantic hurricane formation (Smith et al., 2010) or droughts in the Sahel region (Zhang and Delworth, 2006).

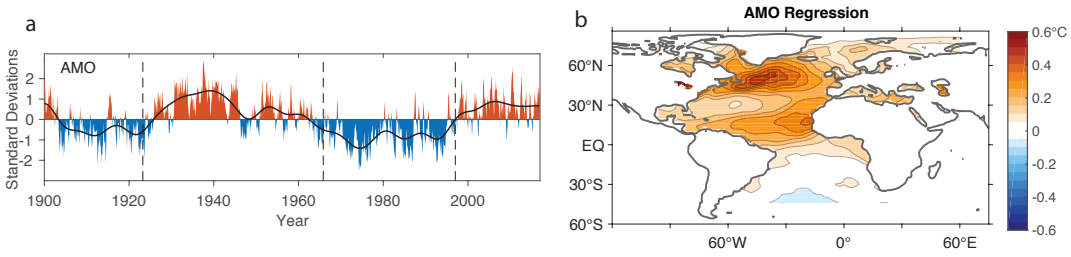

Figure 1.5: Figure from Wills et al. (2018) showing the time series of the AMO (**a**) and the pattern of the regression of Atlantic SST anomalies on the AMO index (**b**). Black lines show each index filtered with a 10-year lowpass filter. Vertical dashed lines show AMO transitions. The authors considered the NOAA Extended Reconstructed SST (ERSST) data set, version 3b (Smith et al., 2008)

The lack of deep-ocean observations makes it difficult to prove the hypothesis of oceanic changes driving the AMO. Several "proxies" of the ocean circulation such as Labrador Sea density (Robson et al., 2014) and sea level pressure (McCarthy2015) suggest that changes in the AMO are led by changes in the ocean circulation. In particular, model simulations associate changes in the AMO to variability in the Atlantic Ocean northward heat transport (e.g. Delworth and Mann 2000; Knight et al. 2005). This vision of the ocean driving the surface temperatures is been challeneged recently by Clement et al. 2015 proposing the atmosphere, mainly the NAO, as the driving mechanism for changes in the AMO. Although this is still an ongoing topic of research, a general consensus agrees on the lagged relationships between the NAO, Labrador Sea Water formation, thermohaline circulation/AMOC, and low frequency SST (with possible feedback to the atmosphere closing the loop) (Latif et al., 2006). Further understanding of the potential mechanisms driving AMO decadal variability, i.e. importance of large-scale ocean dynamics versus local atmospheric role, would help us to understand and improve potential observational systems that could give us an accurate state of the North Atlantic climate.

In this thesis I focus on the interaction between the ocean, in particular the AMOC, and the surface temperatures. The complexity of the AMO phenomenon relies on many interactions between the AMO and the AMOC. Some studies argue that this interaction is Arctic Ocean driven (Jungclaus et al., 2005), other authors assign a central role to the tropics (Vellinga and Wu, 2004; Knight et al., 2005), while other authors focus on an exclusive North Atlantic interaction (Del-

worth et al., 1993; Dong and Sutton, 2005). Finally, several theoretical studies (Frankcombe et al., 2009, 2010) and stability analysis (Sévellec and Fedorov, 2013b; Sévellec and Huck, 2015) have related the two metrics by a damped oscillating mode driven by density anomalies propagating westward across the North Atlantic.

Westward propagation of density anomalies is proposed as one of the mechanisms promoting decadal variability in the North Atlantic. Evidence of these modes have been observed in the SST (Feng and Dijkstra, 2014), in the subsurface (Frankcombe et al., 2008) and in sea level height (Tulloch et al., 2009; Vianna and Menezes, 2013). Due to the lack of high temporal and spatial ocean data, models are needed to describe mechanisms describing the propagation of these anomalies. Colin de Verdière and Huck (1999) introduced large-scale baroclinic instability as a contributor to the Atlantic interdecadal oscillations. This idea was supported also by other studies in both idealized and realistic basins (Huck et al., 1999; te Raa and Dijkstra, 2002; te Raa et al., 2004; Dijkstra et al., 2006) and backed up further with an analysis of density budgets (Arzel et al., 2006). Buckley et al. (2012) identified the role of the thermal wind relation as the intermediary for Rossby waves generated in the subpolar gyre contributing to AMOC variability. Opposed to previous studies, the authors excluded the possible impact of these waves modifying the SST and the upper-ocean heat content budget in the northern North Atlantic. This work has been further extended by Tulloch and Marshall (2012) remarking the role of upper-ocean density anomalies altering geostrophically the north-west region of the subpolar gyre after being advected around the gyre.

More recently, Sévellec and Fedorov (2013b) and later Sévellec and Huck (2015) demonstrated using linear stability analysis the existence of a natural weakly damped oscillatory mode of the AMOC controlled solely by ocean dynamics. This mode is controlled from the interaction of three factors: the geostrophic self-advection of the anomalies on the background of the mean meridional temperature gradient, the β-effect contributing to westward propagation and the mean eastward flow. This dependency is clear in Sévellec and Fedorov (2013b) where an idealized model is used to understand the oscillatory mechanism obtained in Océan PArallélisé (OPA), the model used in this thesis. Considering a two-level model with

certain key approximations (no seasonal cycle, restricting the dynamics to temperature variations, absent stratification in the lower level - deep ocean) the evolution of the linearized advective-diffusion equation with horizontal diffusivity κ is:

$$\partial_t T' = -\bar{u}\partial_x T' - v'\partial_x \bar{T} - w'\partial_z \bar{T} + \partial_x(\kappa \partial_x T'), \tag{1.1}$$

with T' temperature anomalies, v' meridional anomalous velocity and w' anomalous vertical velocity. The linearization is performed over a mean temperature gradient, $\bar{T}$, and imposing a mean zonal flow, $\bar{u}$. Then using the thermal wind balance, the baroclinicity condition, and continuity equation for the anomalous flow results in an expression for v' and w', Eq. 1.1 becomes

$$\partial_t T' = -c\partial_x T' - \kappa \partial_{xx} T', \tag{1.2}$$

with the full speed of the mode propagation represented by $c = \bar{u} + \hat{u} + c_{Ro}$. The different components of the propagation velocity are the factors controlling the propagation of the waves mentioned early. $\bar{u}$ is the mean eastward flow and c_{Ro} represents the role of the β-effect contributing to the propagation of long (non-dispersive) Rossby waves. $\hat{u}$ represents the speed of westward propagation due to the mechanisms of geostrophic self-advection depicted in Fig. 1.6. The temperature anomalies are propagated with velocity $\hat{u}$ on the background meridional temperature gradient.

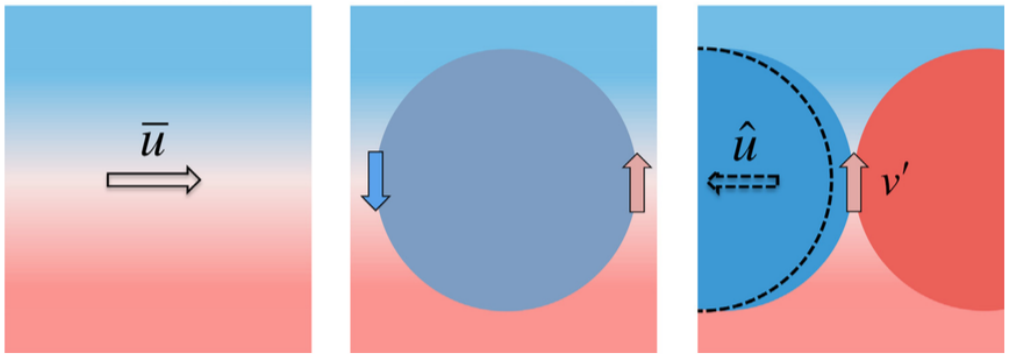

Figure 1.6: Schematic from Sévellec and Fedorov (2013b) showing the mechanisms of westward propagation through geostrophic self-advection. The background colours indicate the anomalous temperature gradient. Within the gradient and associated mean zonal flow $\bar{u}$, an imposed anomaly in blue generates geostrophic cyclonic flow extracting cold and warm temperature anomalies from the mean field on each side of the density anomaly (arrows in the middle figure). The anomalous flow propagates the density westward (denoted by $\hat{u}$) and generates an anomaly of the opposite sign through thermal wind balance.

The idealized model described previously,Sévellec and Fedorov (2013b), was extended in Sévellec and Huck (2015) to a three-layer idealized model obtaining a rich behaviour of the oscillatory mode by varying the vertical density gradient. The authors demonstrated that the instability mechanism has the same behaviour as classical baroclinic instability but acting on a basin scale. The mechanism relates closely to the evolution of the AMOC and SST in the North Atlantic, and hence to the AMO.

This mechanism of density anomalies propagating westward in the North Atlantic has been identified in numerous models contributing to the last Coupled Model Inter-Comparison Project 5 (CMIP5) (Muir and Fedorov, 2017). Although it has been obtained as part of a more complex multidecadal mechanism of variability in the North Atlantic,**it has not been obtained as self-sustained in a realistic ocean model**.

1.2 Dynamical systems - applications to climate dynamics

The climate system is both a complicated and a complex system: complicated due to the various subsystems interacting and complex due to the nonlinear interactions between the subsystems. In a simplistic manner, the evolution of the climatic variables $\boldsymbol{X}$ can be described by a nonlinear operator $\mathbf{F}$ representing their time evolution,

$$\dot{\boldsymbol{X}} = \mathbf{F}(\boldsymbol{X}). \tag{1.3}$$

The variables $\boldsymbol{X}$ (Temperature (T), Salinity (S), Velocity components (u, v, w), etc.) evolve according to a deterministic set of equations within a subspace of $\mathbb{R}^n$, with n the number of variables ($S \subset \mathbb{R}^n$). S is known as the *phase space*.

The theory of dynamical systems was introduced in the 19^{th} century by the mathematician Henri Poincaré. It aims to understand the geometry of the trajectory of the solutions in the phase space and, to investigate the robustness of this geometry when certain parameters of the system are changed (Lorenz, 1963).

Poincaré proved the non-existence of a closed form solution to the problem of three bodies interacting under the Newton laws (Poincaré and Magini, 1899). The three-body problem could only be solved by using numerical techniques. The obtained solution had two remarkable features: the trajectories of the solutions had very complex and tangled geometries impossible to draw and, the corresponding trajectories of solutions with small differences in the initial conditions traced very different paths. These features, glimpsed by Poincaré, are the key features of what was later known as a *deterministic chaotic system*. This topic was largely forgotten before its rediscovery in the field of meteorology by Edward Lorenz. Based on the work of Saltzman and Saltzman (1962), Lorenz (1963) defined a low order deterministic system describing the evolution of convection rolls in the atmosphere. The system, later known as the *Lorenz 63* model, consisted of a system of three differential equations with three unknowns.

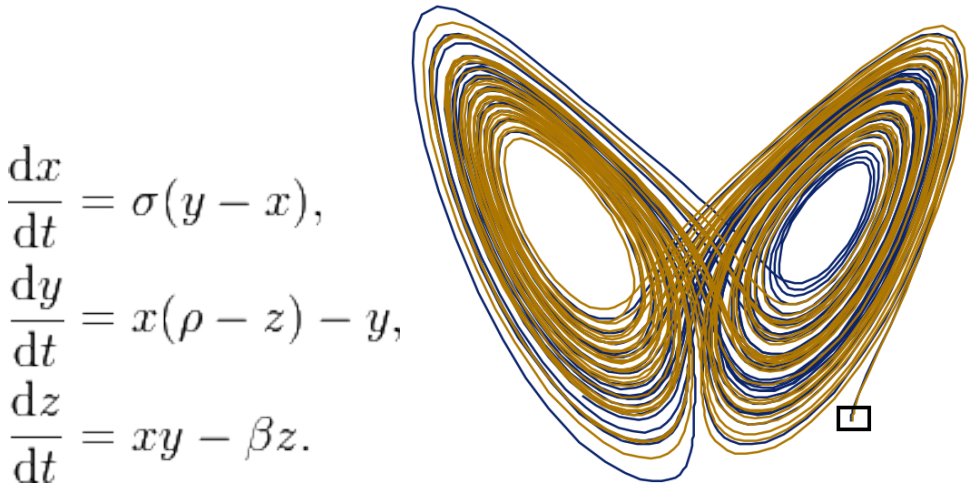

$$\frac{\mathrm{d}x}{\mathrm{d}t} = \sigma(y - x),$$
$$\frac{\mathrm{d}y}{\mathrm{d}t} = x(\rho - z) - y,$$
$$\frac{\mathrm{d}z}{\mathrm{d}t} = xy - \beta z.$$

Figure 1.7: Representation of the equations of *Lorenz 63* (left) and the resultant attractor from the model (right).The equations describe the rate of change of three quantities with respect to time: x is proportional to the rate of convection, y to the horizontal temperature variation, and z to the vertical temperature variation. The constants σ, ρ, and β are system parameters proportional to the Prandtl number, Rayleigh number, and certain physical dimensions of the layer itself. The figure on the right shows the evolution of two initial conditions (purple and yellow) located in the black square. Although with very similar initial conditions, the evolution of the trajectories is easily differentiated. Each of the trajectories fill the attractor in phase space. The equations relate the properties of a two-dimensional fluid layer uniformly warmed from below and cooled from above.

For a certain subset of constants in the equations, Lorenz observed features that resembled the characteristics remarked by Poincaré in the numerical solutions of the three-body problem. The trajectory of the system never reached a steady state or a periodic solution, but remained in a bounded space (Lorenz, 1963). The first feature was the characteristic geometry of the trajectories in the three-dimensional space. These trajectories, although confined in a 3-dimensional region, did not intersect at any time. Therefore they could pass the same region an infinite number of times without intersecting, this was described by Lorenz as "an infinite complex of surfaces" (Strogatz, 2001). These orbits traced a characteristic geometrical structure (right of Fig. 1.7), latter called the Lorenz attractor and classified as *strange attractor* by Ruelle and Takens (1971). The second important feature described by Lorenz was that two very closed initial conditions didn't maintain the same distance as the model progressed, resulting in very different behaviours of the system. This property is now known as sensitive dependence to initial conditions and it is a characteristic of deterministic chaotic systems.

In general, climate models are deterministic systems based on physical equations that describe their evolution in phase space. With the same chaotic nature as the Lorenz model, the climate system shows the special features of these geometrical structures as the Lorenz attractor. Even with an hypothetically perfect numerical model representing the climate, unavoidable uncertainties in the initial conditions would grow and "contaminate" the numerical solution of the system. This leads to fundamental implications to question the ability of the climate to be predicted,climate predictability. Not only is it important to study the climate system itself but also to assess its predictability. This thesis aims to look at the climate system from the point of view of dynamical systems. Together with predictions developed by the different models, predictability studies can provide some ideas on how to produce a more realistic reproduction of the observed variability in the climate.

1.3 Predictability of the climate system

The aim of studying predictability is to characterize the ability of a measure or quantity to be predicted (Meehl et al., 2014). To each metric of the climate system, there is an associated time limit that represents the time for which we cannot distinguish between a prediction and randomly generated variability (Branstator and Teng, 2012). Hence for each prediction, a predictability study should be considered first in order to evaluate the forecast skill. Although a predictability theory cannot provide a solution to the forecasting problem, it can instead provide useful information about the problem and help on its solution. In this sense, predictability plays a role equivalent to an existence proof of a theorem in mathematics, it is not the solution of the problem but rather a statement that there is such solution. Moreover, it can provide some information on how to find it.

In his work, Lorenz (1975) distinguished between two basic types of predictability. The first kind, known as the initial value problem, is related to the accuracy on the initialization of the system and how the initial errors introduced affect the predictability skill. The second kind is identified with longer timescales, the boundary

value problem. It relies on the importance of having a good representation of the "external" forcing in the system. For example, having a good representation of external changes in radiative forces, such as variations in atmospheric composition or solar forcing will determine the evolution of the climate on long timescales. This thesis will focus first on decadal time scales, for which both the impacts of initial conditions and forced problem is still not clear (Chapter 3). Secondly on longer time scales from multidecadal to centennial in the fourth and fifth chapter.

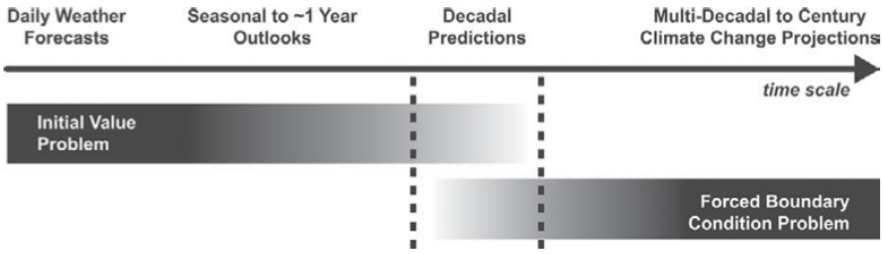

Figure 1.8: Schematic from Meehl et al. (2009) showing the predictability problem in different timescales. On the left, initial value problems associated with daily weather forecasts and forced boundary condition problem related to multidecadal to century projections on the right. In the middle, seasonal and decadal predictions, for which the relative influence of initial versus boundary conditions is not yet clear.

First Kind of Predictability

This predictability is concerned with the question about how uncertainties in the initial state evolve during the forecast and how they limit the forecast skill. The initial condition problem is associated for example with medium-range weather forecasts or seasonal forecasts in a coupled ocean-atmosphere model. A standard approach to understand the sensitivity of the system to initial conditions is to use linearization techniques to study the linear response of the system. Assuming an equation such as Eq. 1.3, the evolution of a small perturbation $\boldsymbol{x}$ can be represented in a short time step by a linearized approximation of this equation:

$$\dot{\boldsymbol{x}} = \mathbf{F}_l(\boldsymbol{x}), \tag{1.4}$$

with $\mathbf{F}_l$ the linearization of the operator $\mathbf{F}$ in Eq. 1.3. This linear operator can be re-written as a linear propagator, the *linear tangent propagator* $\mathbf{L}$,

$$\dot{\boldsymbol{x}}(t) = \mathbf{L}(t, t_0)\boldsymbol{x}(t_0). \tag{1.5}$$

t represents the time in which the state of the system we want to study and t_0 the initial integration time. The linear propagator can then be analyzed using linear algebra techniques to compute the initial vectors that create the largest growth in the system (eigenvectors), i.e. Zanna et al. 2010. These techniques have been widely adopted with the use of tangent and adjoint versions of regular GCMs (te Raa et al., 2004; Sévellec et al., 2009; Heimbach et al., 2011; Zanna et al., 2012; Muir and Fedorov, 2017). The tangent version is represented in Eq. 1.5 and the adjoint is based on the transpose matrix of the tangent operator that gives the sensitivity of the outputs to the inputs.

The previous tools allow to propose optimization problems to understand the SST or Sea Surface Salinity (SSS) pattern that can maximize/minimize certain metrics, e.g. meridional heat transport or meridional volume transport in the North Atlantic. The obtained solutions, defined as Linear Optimal Perturbations (LOPs) in the work of Sévellec and Fedorov (2015), would perturb the most the metric optimized in a linear framework. The climate system is a non-linear system and, **a thorough understanding of its response to these perturbations in a fully nonlinear model still has to be performed**, for example in which situations we can accept the linear assumption as appropriate or explore fully its limitations. This thesis will contribute to the understanding of the limits of these linear approaches as well as to the impact of these perturbations in a non-linear framework.

The ability to understand impacts of the initial errors allows us to quantify or, at least, to set boundaries on the prediction errors. When predictions are performed, the initialization of the oceanic and atmospheric components are key factors to provide an accurate prediction associated to a timescale. Sensitivity studies help to locate regions whose sensitivity to initial errors can limit the predictability. Less biased initial conditions in those regions can therefore improve the predictability of the climate system. As with initial conditions, the impact of data introduced along a model run, known as data assimilation, would be improved by these techniques. They introduce information such as SSS or SST to improve the performance of the model representing the climate system (Servonnat et al., 2014; Ortega et al.,

2017). The LOPs would bound the errors introduced in the these quantities, SSS or SST, in a linear framework. However, the impact of nonlinearities have not been understood completely and will be studied in this thesis. They allow to propagate initial errors to the metrics of interest; hence they are of key importance to understand the response of the model to these errors introduced.

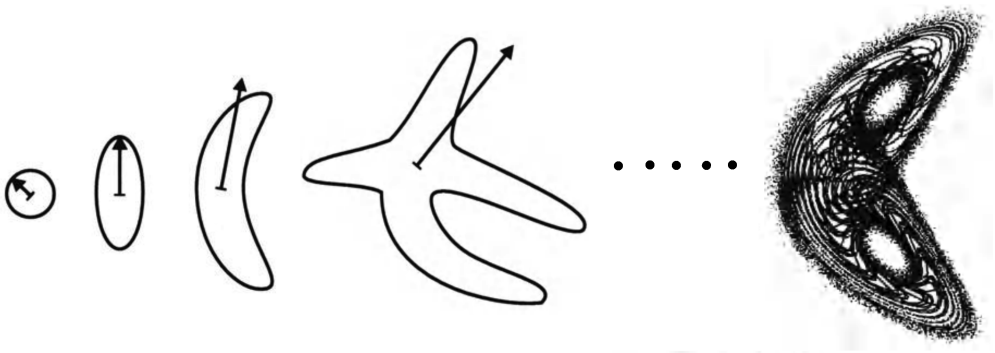

Figure 1.9: Schematic evolution of the probability density function (PDF) of an initial error in the forecast of the *Lorenz 63* from Davey (1998). The initial error is limited by a neighbourhood with a circle shape and radius as in the first figure on the left. On the next time step, with the linear approximations, the directions of maximum growth can be computed (indicated by an arrow). As the system evolves, the error increases in each time step. It grows towards the vectors of maximal growth computed through linear approximations. The ability to understand the impacts of initial errors stops when the extension of the error occupies the whole attractor, last figure on the right.

Second kind of predictability

The second kind of predictability differentiated by Lorenz (1975) estimates the impact of changes in prescribed parameters or variables of the system on the attractor of the system. Uncertainty comes on the one hand from the lack of means to completely represent the climate system and, on the other from the uncertainty in the information introduced in the evolution of a climate simulation.

Longer time scales are studied with climate models, which are developed independently. The choice on numerical methods to solve the equations, parametrizations, model grids, etc. provide independent approximations of the climate system. They are used, for example, to understand the impacts of increased greenhouse gases, currently the highest priority in the climate predictability problems. Experiments in the CMIP5 compare the evolution of models from about 20 climate modelling groups under different emission scenarios. They contribute to the under-

standing of our ability to predict and estimate the future climate. The experiments are focused on both near term simulations (10-30 years) initialized with observed ocean and sea-ice state, and long-term simulations (from 1850 up to 2100) initialized from long runs using estimates of historical future forcing (Taylor et al., 2012). The different components and metrics of the climate are then studied as the evolution of an ensemble of simulations, obtaining both a mean evolution and a spread. The spread provides a measure of the possible prediction confidence of the climate evolution delivered by the models, and the mean an estimate of the general trend. For example, models agree that the continued emissions of greenhouse gases will likely generate a reduction of the AMOC but do not agree on the extent and the exact quantity of its impact, as shown in Fig.1.10 with the spread of the model evolution.

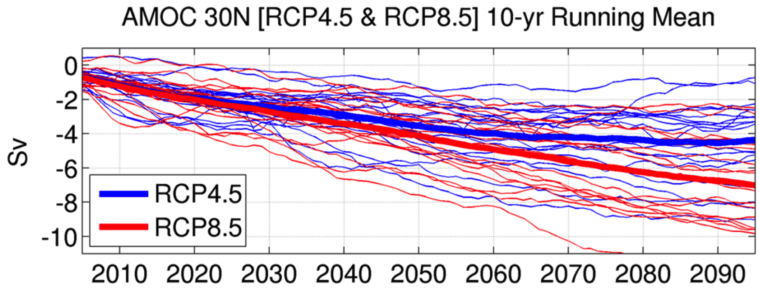

Figure 1.10: Figure taken from Reintges et al. (2016) showing the long-term changes in the AMOC index at 30°N in the individual models used in CMIP5. A 10-year running mean is presented with thick lines removing the reference period 1970-2000. Blue represents experiments associated with the emissions scenario RCP4.5 and red for RCP8.5. RCP4.5 considers a radiative forcing reaching about $\approx$4.5 W m^{-2} near 2100 (Taylor et al., 2012).

The uncertainties in model simulations can be reduced by introducing real data as the model is running. Besides the previously mentioned nudging methods, more complex mathematically based methods from control theory can be used. These formulate the data assimilation as minimization problems of the difference between the ocean state and the observations. Reanalyses such as ECCO (Stammer et al., 1999) or ORAS4 (Balmaseda et al., 2013) produce data sets on multidecadal timescales on horizontal scales of $0.5 - 1°$ of resolution of the state of the ocean. The inclusion of realistic data onto the model evolution approximates the evolution of

the model trajectory in phase space to the observations. These methods can potentially represent more accurately the evolution of the climate system in a historical context. Also, they help to understand the role of climatic events such as volcanic eruptions or the impact of North Atlantic events such as the Great Salinity Anomalies (GSAs). The latter were observed in the North Atlantic in the past decades (Belkin et al., 1998), but **no experiments understanding the possible impacts of GSAs on the AMOC or in the North Atlantic have been done previously**. This thesis will contribute to increase the knowledge of potential impact of the GSAs on the AMOC in Chapter 3.

At the core of the predictability problem, is the understanding of the conditional nature of the prediction skill; that is, on one hand to understand the possibility of locations whose initialization can lead to more accurate predictions than others (Collins et al., 2006; Branstator and Teng, 2010, 2012). On the other hand, to understand the variable impact of the different predictability problems induced by model errors, uncertainty in external forcing, etc. When considering decadal timescales, the impact of both initial conditions and forcing are both important, but the extent to which one dominates the other depends on the metric under consideration (Hawkins and Sutton, 2009b).

1.3.1 The role of oceans in decadal predictability

As depicted in Fig. 1.8, errors in the initial conditions and boundary conditions have an impact on the climate predictability. The impact of each of the predictability limiting factors depends on the metric chosen (Hawkins and Sutton, 2009b). The uncertainty in the future state of the climate have raised interest in predictions on decadal timescales. In particular from public administrations wishing to have an idea of the future state of the climate, and its impacts on regional climate, water resources, fisheries, etc.

The atmosphere has a short memory when compared to the ocean. Atmospheric prediction on longer than seasonal timescales requires some sort of memory, usually provided by the oceanic component (Davey, 1998). Hence the improvements on the

oceanic component is a pre-requisite for decadal predictability. When considering the concept of decadal predictability of the oceanic component, the choice of the metric is relevant to asses our ability to predict its evolution. In the case of the thermohaline circulation, studies suggest a predictability over 1-2 decades (Collins and Sinha, 2003). In the case of SSTs, Pohlmann et al. (2004) showed the potential for predictions in the North Atlantic even on multidecadal timescales. For other quantities such as Arctic sea ice the predictability is limited to just a few years (Holland et al., 2011; Toyoda et al., 2011).

In order to keep providing estimates of the ocean predictability of this kind, technical challenges need to be overcome: an appropriate initialization, model bias adjustments or methods to measure predictability skill (Meehl et al., 2014). These approaches try to reduce the uncertainty in predictions, increasing the predictability. To improve initialization of decadal predictions, methods such as perturbations of the initial state have used different methodologies: breeding methods for optimal perturbations, extensions from ensemble Kalman filter-type assimilation methods, etc. (Du et al., 2012; Karspeck et al., 2013; Yeager et al., 2012; Germe et al., 2017). Another approach, using full 3-dimensional initialization (Ham et al., 2014) has successfully improved decadal predictions. Biases in decadal predictions arise from the model drift from the observed state as the model may not realistically simulate natural modes of variability (interannual-to-multidecadal), from not enough observations or imperfect observations to guide the model or uncertainty in the forcing of the model (volcanic eruptions or aerosol concentrations). A way proposed to deal with these biases is to adjust biases removing the mean biases from the predictions. The idea is to compute for each forecast range the predicted climatological average and consider then the forecast anomalies obtained by subtracting the average (Smith et al., 2013; García-Serrano and Doblas-Reyes, 2012). This approach helps to quantify the observed transient climate response and equilibrium climate sensitivity to increasing CO_2 (Meehl et al., 2014).

Finally, the different methods to assess the predictability or forecast skill can be quantified in various ways including: correlations, mean square errors or more advanced statistical techniques such as relative entropy (DelSole, 2004; Branstator

and Teng, 2010), inverse modelling (Hawkins and Sutton, 2009a; Teng et al., 2011; Zanna et al., 2012), multivariate regression propagators (Branstator et al., 2012) or Analogues (Branstator et al., 2012; Ho et al., 2013). These methods also give time limits for decadal predictions using different GCMs that vary depending on model and location. For example, Branstator et al. (2012); Teng et al. (2011) focused on subsurface temperatures, whose time limits vary in the North Atlantic between 6 to 15 years.

The ocean is a slow component of the climate system that stores information on longer timescales when compared to the atmosphere. In addition, it is a crucial factor in the redistribution of heat and carbon in the climate system (Bigg et al., 2003). Understanding its ability to be predicted and deliver accurate forecasts on the state of the climate is of primary importance to the climate sciences.

1.4 Research objectives

The discussion presented in the previous sections exposed the importance of increasing knowledge on ocean predictability and variability with a focus on the Atlantic as one of the main drivers of the climate. In particular, some of the open questions to be investigated in this thesis are:

- To what extent can the ocean internally generate decadal/multidecadal and centennial variability - and under what forcing conditions?
- How does the ocean respond to realistic perturbations (e.g. GSAs) - is the response linear and, if not, to what extent is it non linear?
- On what timescales is the AMOC important?
- What are the relative roles/relationships between AMOC, deep convection, AMO and gyre circulations?

The aims of this thesis, framed to try to answer the previous questions, are:

1. To assess the impact of errors in the initialization of the surface salinity and predictability on decadal time scales and its impacts on the AMOC.
2. To investigate under what surface forcing conditions does the ocean spontaneously generate (Atlantic) variability on decadal and longer timescales and to elucidate the mechanisms of such variability

In Chapter 2, I describe the model and configurations used in this thesis. Chapter 3 presents a set of experiments perturbing the SSS in the initial conditions of the model exploring the impact of errors in the initial conditions on the North Atlantic. Chapter 4 describes a mechanism of multi-decadal variability of the North Atlantic obtained in a GCM. Chapter 5 explores the impact of the Southern Ocean into the North Atlantic. Finally, Chapter 6 has the conclusions of this thesis and discussion of the implications of the results.

Chapter 2

Model description and boundary conditions

Climate modelling is limited by computational power. Models with high resolution, coupled with a large number of components of the climate system and refined component interactions is one of the goals of climate modelling. In order to understand the long-term behaviour of the climate, large experiments are required, which are computationally expensive to run. The use of low-resolution coupled models or even ocean only models is a common practice to understand long time scales in the climate. In order to obtain different behaviours of ocean only models, the use of different boundary conditions helps to understand possible mechanisms that could be potentially detected in more computationally expensive coupled models.

In this chapter I introduce the model I use in this thesis, Océan PArallélisé (OPA). I include also different parametrizations and configurations used for the experiments and give a short discussion on the use of different types of boundary conditions in ocean only models.

2.1 Model Océan PArallélisé (OPA)

The model used in this thesis is the Ocean General Circulation Model (OGCM) OPA 8.2 in its 2° global configuration (Madec et al., 1998). This model has been the predecessor of the oceanic component of the model known as NEMO, Nucleus for European Modelling of the Ocean (Madec, 2008). Together with OPA for the ocean dynamics and thermodynamics, NEMO encloses as well LIM (Louvain-la-Neuve Sea Ice Model) as the component modelling the ice, and TOP-PISCES (Tracer in the Ocean Paradigm) for biogeochemistry.

The model is based on the Navier-Stokes equations along with a non-linear equation of state which couples the two active tracers (temperature and salinity) to the fluid velocity, plus certain assumptions (spherical earth approximation, thin-shell approximation, turbulent closure hypothesis, Boussinesq hypothesis, Hydrostatic hypothesis and Incompressibility hypothesis). The equations are described next:

$$\begin{aligned}\frac{\partial \mathbf{U}_h}{\partial t} =& -\left[(\nabla \times \mathbf{U}) \times \mathbf{U} + \frac{1}{2}\nabla^2(\mathbf{U}^2)\right] \\ & - f\boldsymbol{k} \times \mathbf{U}_h - \frac{1}{\rho_0}\nabla_h p + \mathbf{D}^{\mathbf{U}} + \mathbf{F}^{\mathbf{U}},\end{aligned} \tag{2.1a}$$

$$\frac{\partial p}{\partial z} = -\rho g, \tag{2.1b}$$

$$\nabla \cdot \mathbf{U} = 0, \tag{2.1c}$$

$$\frac{\partial T}{\partial t} = -\nabla \cdot (T\mathbf{U}) + \mathbf{D}^T + \mathbf{F}^T, \tag{2.1d}$$

$$\frac{\partial S}{\partial t} = -\nabla \cdot (S\mathbf{U}) + \mathbf{D}^S + \mathbf{F}^S, \tag{2.1e}$$

$$\rho = \rho(T, S, p). \tag{2.1f}$$

where $\boldsymbol{k}$ is the local upward vector, $\mathbf{U}$ the vector velocity, ∇ is the generalised derivative vector operator in (i, j, k) directions, t the time, z the vertical coordinate, ρ the in situ density given by the equation of state (2.1f), ρ_0 a reference density, p the pressure, f the Coriolis acceleration ($f = 2\Omega \cdot k$, where Ω is the Earth angular velocity vector), and g the gravitational acceleration. $\mathbf{D}^{\mathbf{U}}$, $\mathbf{D}^T$ and $\mathbf{D}^S$ are the parametrizations of small-scale physics for momentum, temperature and salinity,

including surface forcing terms and $\mathbf{F^U}$, $\mathbf{F}^T$ and $\mathbf{F}^S$ the surface forcing terms. For more information refer to Madec (2008).

The model is based on the ORCA2 grid with three poles, two in the northern hemisphere and a southern pole. This grid avoids a north pole singularity in the ocean by locating the two north mesh poles on land (Fig. 2.1). The primitive equations are then solved in the three-dimensional space of prognostic variables (velocity and thermohaline variables) defined in the grid. In particular, it is based on z-coordinates on an Arakawa C-grid with vertical resolution that varies between 10 m and 500 m at depth in 31 levels. It uses the rigid-lid approximation at the ocean surface (Madec et al., 1998).

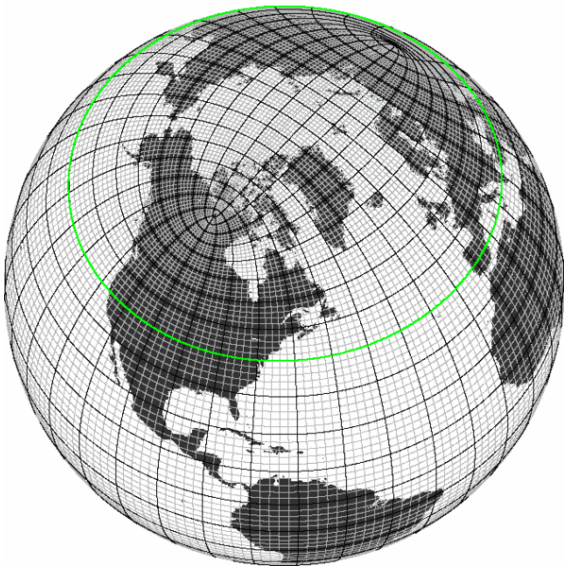

Figure 2.1: Tripolar grid used in the ORCA configurations. The green line limits the different north pole configuration with respect to a regular geographic grid with a unique north pole. Figure taken from the Geomar Laboratory web page.

In our experimental set-up we use the standard parametrization of the model. Convection is defined by an increase in vertical diffusion caused by an unstable stratification. The viscosity follows the turbulent closure scheme of Blanke and Delecluse (1993), which depends on latitude, longitude and depth. To represent double diffusion processes, two different terms for mixing temperature and salinity are taken into account. The diffusion coefficients of temperature and salinity vary in the horizontal dimensions following Redi (1982), isopycnal and diapycnal

diffusivities are set to 2×10^3 m^2 s^{-1} and 1.2×10^{-5} m^2 s^{-1} respectively. Finally, Eddy-induced velocities follow the approximation of Gent and McWilliams (1990) with a coefficient of 2x10^3 m^2 s^{-1} in our experiments.

Ocean models require surface boundary conditions to provide information on the atmosphere-ocean interaction. The evolution of the surface variables is shown in equations 2.1d and 2.1e. Considering only the flux term from the equations, its simplified form is as follows:

$$\begin{aligned} \frac{\partial T}{\partial t} &= \cdots - \gamma_T (T - T_0) + \mathcal{F}_T \\ \frac{\partial S}{\partial t} &= \cdots - \gamma_S (S - S_0) + \mathcal{F}_S. \end{aligned} \tag{2.2}$$

Where γ is a restoring coefficient with units W m^{-2} K^{-1} for γ_T and psu for γ_S, T_0 and S_0 are atmospheric or surface values, and $\mathcal{F}_S$, $\mathcal{F}_T$ are fixed fluxes considered such as freshwater fluxes from rivers or melting ice. I used a value of 40 for both restoring coefficients, which corresponds to a relaxation time-scale of about 60 days over a mixed layer depth of 50 m. This value is used in modelling studies with surface nudging and has been justified in previous studies (Swingedouw et al., 2013; Servonnat et al., 2014). In the case of γ_S a conversion to the equivalent salinity relaxation coefficient is done in the model.

For the climatological fluxes, or forcing, I used surfaces fluxes estimated by the European Centre for Medium-Range Weather Forecasts (ECMWF) averaged for the interval 1979-1993, wind stress measured by the European Remote Sensing satellite (ERS) and blended with the Tropical Atmosphere Ocean (TAO) data between 1993 and 1996, and an estimate of the climatological river runoff. The surface temperature is restored to the Reynolds and Smith (1994) climatological values averaged from 1982 to 1989 (T_0), together with surface salinity restoring to the Levitus (1989) climatology S_0. An additional mass restoring term to the Levitus climatological values of temperature and salinity is applied in the Red and Mediterranean Seas.

2.2 Model Spin-Up under Restored Boundary Conditions

The spin-up of the model is performed under Restoring Boundary Conditions (RBC) taking about 200 years to reach to equilibrium. The equilibrium state was defined in terms of the Atlantic Meridional Overturning Circulation (AMOC), measured at 30°N and 1000 m depth, as theindex reached a stable state. The use of RBC forces the model towards the imposed climatology. Or, with a terminology borrowed from dynamical systems theory, the climatology acts as a sink in phase space. This configuration provides a high stability to perturbations after the spin-up.

The mean state of the model after the spin-up, Fig. 2.4, is described and compared to the Levitus (1989) climatology. After the spin-up, the SST and SSS shows most biases are below one degree (thin contours in Fig. 2.2 c-d). Cold biases appear in the central-eastern pacific and Atlantic. The Southern Ocean shows warm biases in the northern boundary with the rest of the ocean basins with warm foci over 3-4 °C south of New Zealand and the Argentinian coast. Salinity biases are mainly located instead in the Arctic, reaching both positive and negative values over several psu. The limited ice parametrization in the model may contribute to these salinity biases.

The global circulation in the model shows a strong overturning in the Southern Ocean with a negative overturning in the deep ocean and positive in the upper 2000 m between 40°-60°S. In the northern hemisphere there is a northward transport in the upper ocean and a return flow below the 1500 m corresponding to the main influence of the Atlantic contribution to this overturning (Fig.2.4). The Pacific-Indian overturning instead has a very shallow overturning in the upper 500 metres in the northern hemisphere. In the southern hemisphere, a negative overturning is shown in the surface and below 500 m. A positive overturning is at 60°S related to the ACC.

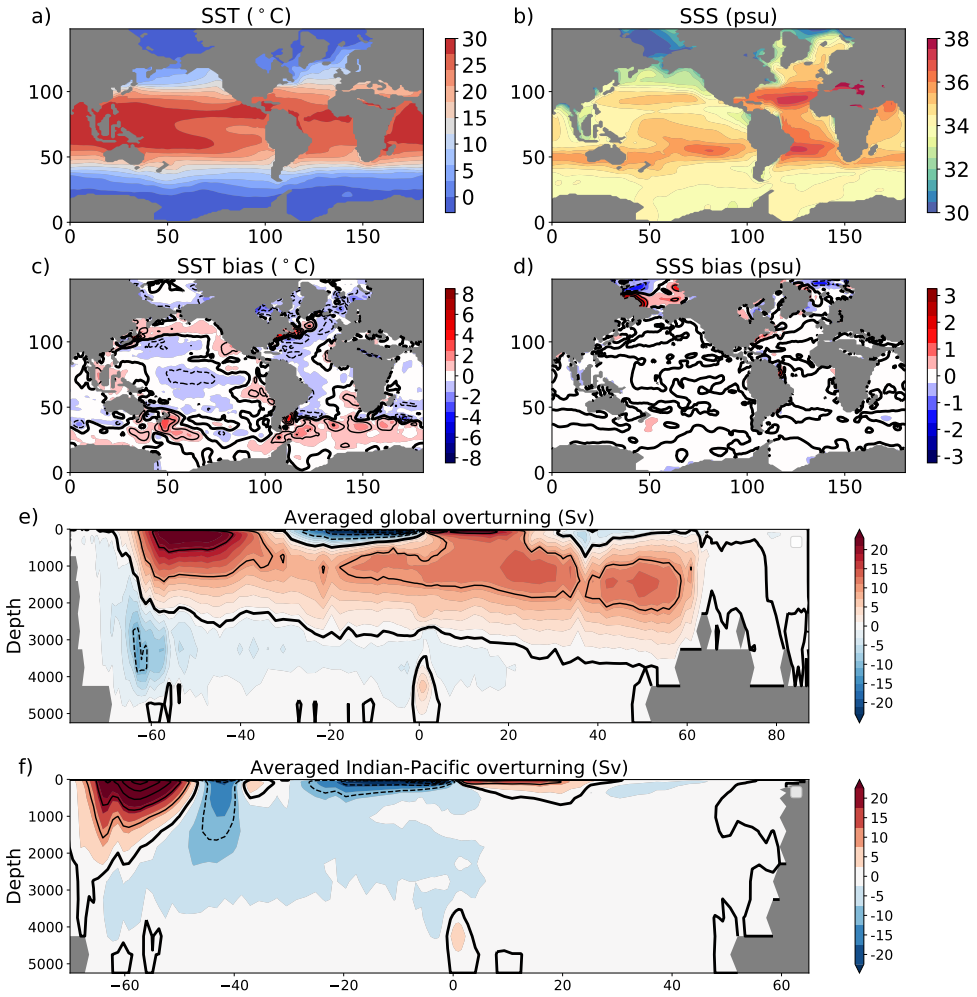

Figure 2.2: Global mean state of the model after the spin-up, average of the first 100 years under RBC. **a)** Global SST. **b)** Global SSS. **c)** Global SST biases compared to the Levitus (1989) climatology. Thick contour corresponds to 0°C bias and the rest of the contours indicate 1°C increase/decrease. **d)** Global SSS biases compared to the Levitus (1989) climatology. Thick contour corresponds to 0 psu bias and the rest of the contours indicate 1 psu increase/decrease. **e)** Global overturning circulation. **f)** Indian-Pacific overturning circulation.For both overturnings thick contours corresponds to 0 Sv and the rest of the contours indicate 5 Sv of increase/decrease (solid and dashed lines respectively).

If we focus on the Atlantic, surface salinity shows a maximum around 20°N and a strong meridional temperature gradient. The difference between model and climatology between 60°S and 60°N in Sea Surface Salinity (SSS) shows a mean of about 0.002 psu and 0.11 psu of averaged spatial standard deviation. This can be seen in Fig.2.3 in which anomalies only arise north of 70°N. The surface temperature shows a slight cooling at the surface of the North Atlantic of about -0.15°C on average between 60°S and 60°N. Strong positive biases (3-4°C) arise

north of the Gulf stream detachment region and slightly warm anomaly south of Greenland. As noted in the global biases, strong SST biases appear in the limit with the Southern Ocean.

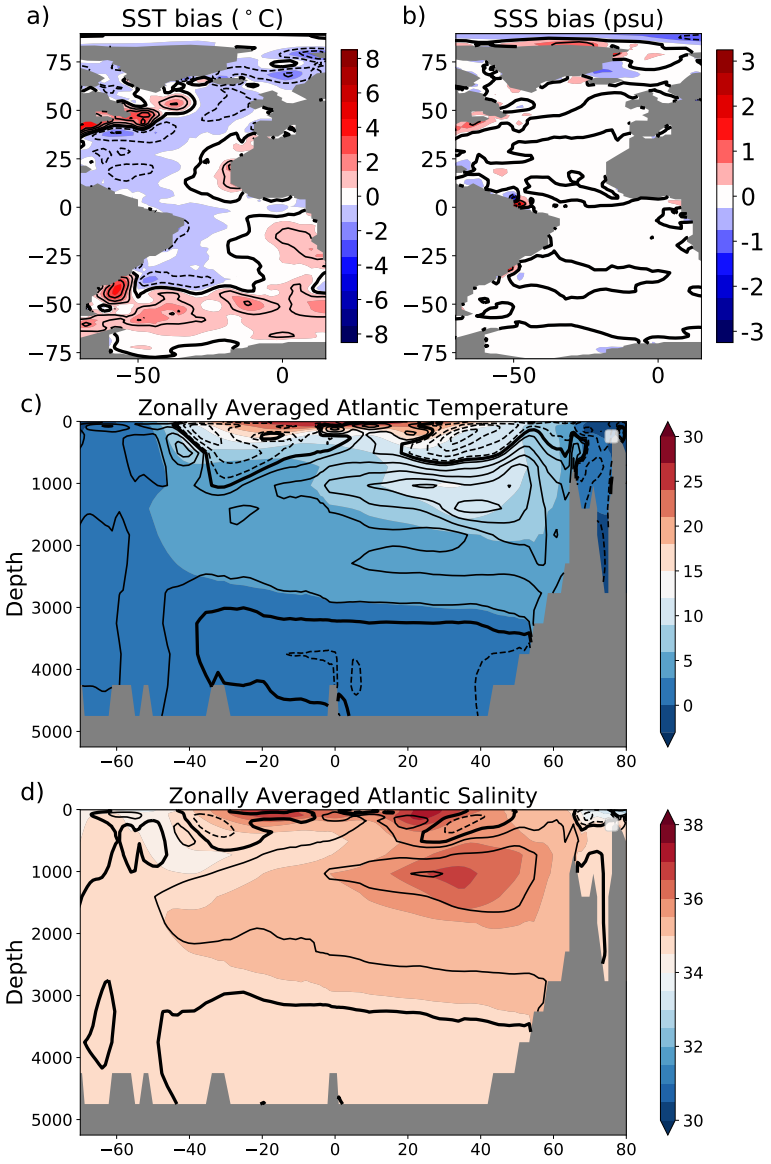

Figure 2.3: State of the Atlantic after the spin-up and biases. **a)** Atlantic SST biases after the spinup compared to the Levitus (1989) climatology. Thick contour corresponds to 0°C bias and the rest of the contours indicate 1°C positive (continuous line) and negative (dashed line). **b)** Global SSS biases after the spinup compared to the Levitus (1989) climatology. Thick contour corresponds to 0 psu bias and the rest of the contours indicate 1 psu positive (continuous line) and negative (dashed line). **c)** Zonally averaged Atlantic temperature in colours. Biases with respect to the Levitus (1989) climatology is shown by the contours: bold line the 0°C anomaly, continuous line positive anomalies each 1°C and dashed lines negative anomalies each 1°C. **d)** as in **c)** but for salinity. Instead of °C are psu.

When the whole 3-D field is considered in the Atlantic, the averaged values show instead a warming in the mean difference with respect to the climatology of about 0.18°C on average. The biases in the zonally averaged temperature shows a cooling in the upper 700 m in both subtropics -40°-0°S and in the northern hemisphere it extends until high latitudes reaching far north of 70°N. The salinity content difference has a larger mean but still very small values, 0.05 psu of mean in the North Atlantic. The zonally averaged salinity shows that the positive bias is associated with the salinity in the climatology, we are "making" the saltier parts more saltier reaching up to 3 psu close to the maxima of zonally averaged salinity.

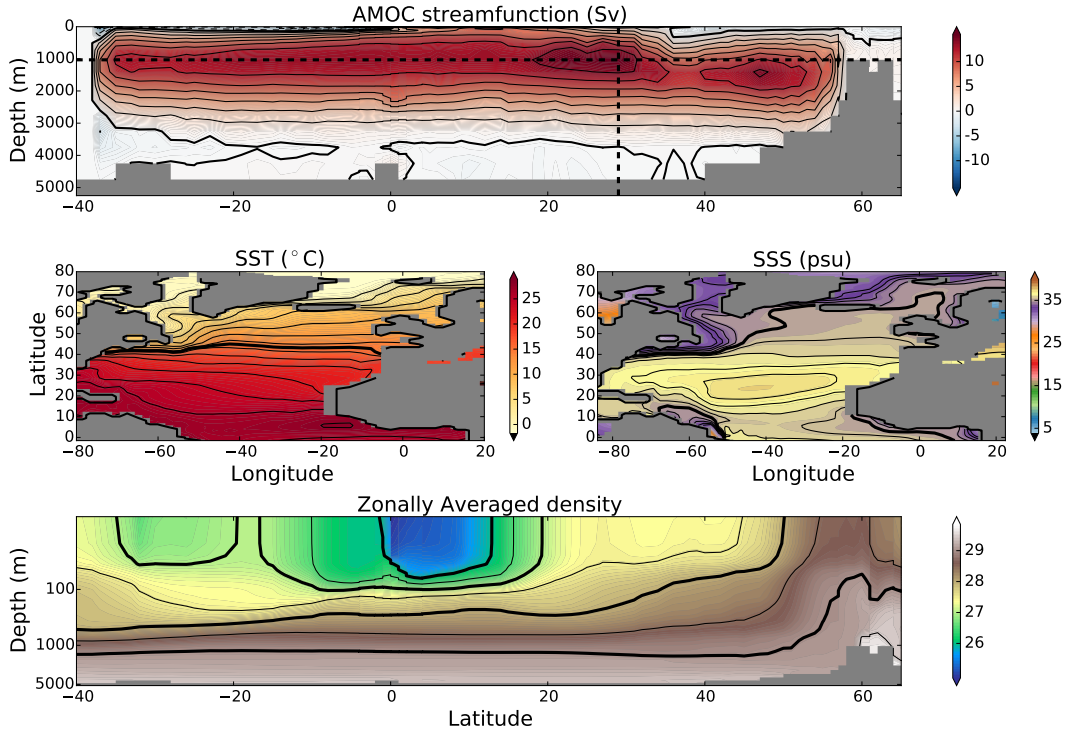

Figure 2.4: State of the Atlantic after the spin-up. Top: zonally-averaged meridionally stream function showing the Atlantic meridional stream function; contours denote 2 Sv. Thin lines, bold lines and dashed lines indicate respectively positive, zero and negative values of the stream function. Intersection of the dashed lines corresponds to the definition of the Atlantic Meridional Overturning Circulation Index (AMOCI). Middle left: Sea surface temperature on left with contours 2°C and bold line corresponding to 15°C. Middle right: Sea surface salinity; contours every 0.5 psu and bold line at 35 psu. The bottom panel shows zonally-averaged density on a logarithmic depth scale; contours every 0.5 kg m^{-3} and bold lines at integers between 26 and 30 kg m^{-3}.

The northward volume transport in the Atlantic is characterized by the AMOC stream function above the thermocline and a return flow below 1500 m depth, top

of Fig. 2.4. The state shows a very weak AABW cell of around zero below 3000 m. The index of the AMOC was taken for this study as the maximum of the stream function at around 30°N and 1000 m depth with a value of around 15.49 Sv, referred to as the AMOCI (Atlantic Meridional Overturning Index). The index considered has lower magnitude when compared to observations at 26.5°N but still within its variability (16.9 ± 4.4 Sv, see McCarthy et al., 2015) .

The model has an overturning within realistic values. Although some key regions to are misrepresented, in the surface, Southern Ocean and possibly the Arctic, the Atlantic shows a warmer and saltier ocean interior. Also, when compare to observation of mixed layer depth (climatological annual mean from the IFREMER/LOS Mixed Layer Depth Climatology website (www.ifremer.fr/cerweb/deboyer/mld)), Fig. 2.9, the model under restoring conditions has a more steady and strong convective regions. In the Labrador Sea both mean and location seems more in line with the observations, with less similarities in the other convective regions.

2.3 Evolution under other Boundary Conditions

After the spin-up, I restarted the evolution of the model under other boundary conditions. For each variable in Equation 2.2, the evolution can be defined by either restoring to the climatological value or by imposing extra fluxes computed from averaged restoring values. For the first option, RBC, I fixed the parameter $\gamma_{T/S}$=40 and the $\mathcal{F}_S$ is taken as the standard fluxes from ECMWF. For the second option, I considered $\gamma_{T/S}$=0 and then modified the ECMWF fluxes including averaged restoring values from RBC. The parameters $\gamma_T(T-T_0)$ and $\gamma_S(S-S_0)$ are averaged over 10 years of the RBC run and included in the $\mathcal{F}_{S/T}$ parameter. I used a combination of these options for temperature and salinity to compute the different boundary conditions: fixed Flux Boundary Conditions (FBC) and Mixed Boundary Conditions (MBC) (Table 2.1 shows the coefficients and fluxes considered). In the case of MBC only the temperature is restored with standard heat fluxes and the salinity is forced under fixed fluxes. For the FBC neither salinity nor temperature are restored and modified fluxes are imposed as boundary conditions.

Types of Boundary Conditions

Restoring Boundary Conditions (**RBC**)	*Mixed Boundary Conditions* (**MBC**)	*Flux Boundary Conditions* (**FBC**)
Restore S ($\gamma_S = 40$)	Prescribe freshwater fluxes ($\gamma_S = 0$)	Prescribe freshwater fluxes ($\gamma_S = 0$)
Restore T ($\gamma_T = 40$)	Restore T ($\gamma_T = 40$)	Prescribe heat fluxes ($\gamma_T = 0$)

Table 2.1: Table showing the values of the different terms involved in the evolution of temperature and salinity under the different boundary conditions.

The use of different boundary conditions started in the 90s with simplified models looking at possible equilibrium states of the thermohaline circulation. Manabe and Stouffer (1988) combined MBCs and FBCs in the Geophysical Fluid Dynamics Laboratory model of NOAA using the coupled model to compute the restoring and flux terms obtaining two different equilibrium states: one with a strong thermohaline circulation and relative saline and warm surface water and another one with reduced/non-existent thermohaline circulation with an intense halocline in the surface layers at higher latitudes. These two modes are known as ON and OFF AMOC equilibrium states. Marotzke and Willebrand (1991) obtained several equilibrium states in an idealized geometry of the Pacific and Atlantic with a combination of on and off states in the overturning on both basins. In their work the authors attributed a principal role to the freshwater forcing.

The different setups explained previously provide with various flavours of model behaviour. Under FBC the model experiences an imposed flux of heat and fresh water forcing with no continuous feedback from the climatology. This gives the model the "freedom" to move in the phase space with no explicit restriction from the surface boundary conditions, and the response to any perturbation or external force is not damped at the surface continuously. Compared to reality, the atmosphere doesn't provide with steady forcings such as the ones presented in this

configuration. The variability in the atmosphere can be a key driver of the ocean, in particular referring to the AMOC (Bryden et al., 2014).

The MBC configuration is used more commonly as an intermediate state between an ocean only model and a coupled model (Weaver and Sarachik, 1991). It resembles the oceanic evolution of a coupled model due to the absence of feedback between SSS and freshwater fluxes: the surface salinity values have no effect on evaporation or heat fluxes, and the SSS evolution is independent from the atmospheric coupling. Instead, the strong temperature coupling to the atmosphere is the only active agent that can modify heat fluxes and evaporation, damping possible temperature anomalies by restoring to the climatology. As with the previous case with FBC, under MBC we are assuming that the surface heat forcing experienced in the model is almost constant, considering the atmosphere with an infinite capacity for heat storing or rather assuming that the atmosphere can easily lose excess heat to space.

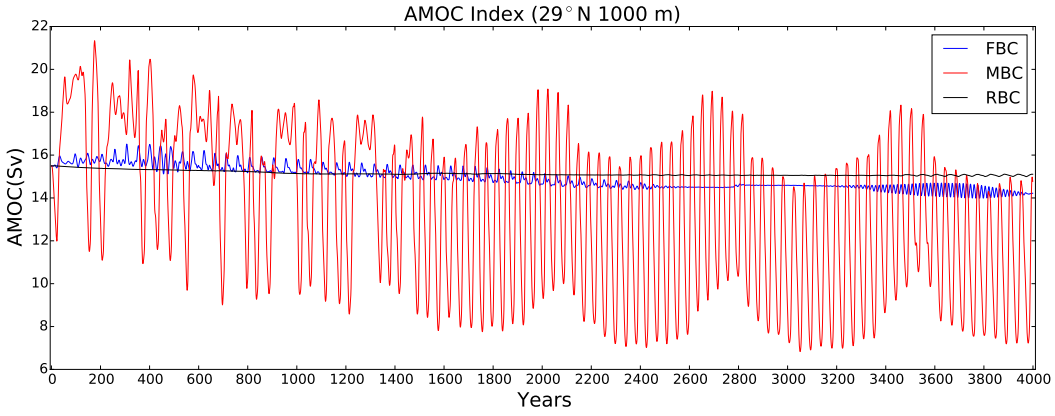

Figure 2.5: Evolution of the AMOCI computed at 30°N and 1000 m depth. The evolution of RBC (black) shows the steady evolution of this mode. FBC (blue) shows a weak steady evolution with a mild cycle in the evolution (1-2 Sv) and MBC (red) with a multidecadal oscillation stable after year 1600.

In previous studies, when transitioning from RBC to both FBC and MBC, simplified models have shown changes in the steady states of the model. Weaver and Sarachik 1991 obtained oscillations on decadal timescales with time scales associated with the advection of surface salinity anomalies from the boundary between the two gyres to the convective regions. In this stability, a key role is given by the

restoring coefficient and the corresponding restoring time. A short restoring SST time can contribute to the stability of the forced configuration (Sirkes and Tziperman, 2001). Also, these forced configurations, in particular MBC, have shown to be very sensitive to freshwater perturbations transitioning to multiple equilibria (Maier-Reimer et al., 1993). The work of Mikolajewicz and Maier-Reimer 1994 improved the traditional approach of using a combination of heat fluxes and near-surface air temperature with a weaker feedback increasing the stability of the model.

Arzel et al. (2006) performed a density variance budget using a coarse-resolution ocean model in an idealized flat-bottom single-hemisphere basin for both FBC and MBC. They were able to identify the different energy sources of variability for each of the boundary condition type. For FBC the energy comes from the downgradient meridional eddy heat flux in the region of the western boundary current, whilst for MBC the energy source is the convective adjustment and restoring of heat fluxes.

Some authors argued that the lack of feedback between SSS and freshwater fluxes in a coupled ocean-atmosphere system was very similar to MBCs in an ocean-only model (Weaver and Sarachik, 1991). Others considered instead that the ocean sees almost a constant surface heat flux (Colin de Verdière and Huck, 1999). Therefore forced models may be seen as a complement to the use of more realistic atmospheric representation. They allow also to analyse the relevant physical mechanisms. But knowing their limitations and the body of work that they have been used is relevant to understand certain limitations of the work here presented. Limitations such as the sensitivity of previous works to changing the boundary conditions, high sensitivity to freshwater perturbations or lack of accurate atmospheric interaction.

The evolution of the model after switching the boundary conditions is shown in Fig. 2.5. The evolution of RBC is steady in terms of the AMOCI. As the fluxes are fixed for FBC, the system shows a weak cycle whose variability is less than 2 Sv. When this cycle occurs, the evolution has a similar range of values as RBC over the 4000 years of integration, with a small departure of about ± 1.5 Sv and a larger negative trend. As obtained by previous authors, the change to MBC has produced a change to an oscillatory state with a period of about 40 years. This

oscillation will be described further in the next sections.

2.3.1 Further description of the equilibrium state under MBC

The evolution of the model under MBC reaches an oscillatory state which stabilizes to a statistical equilibrium after 2000 years of integration. The stability of the mode is measured in terms of the AMOC (AMOCI) in Fig. 2.5. On the one hand we observe a multidecadal cycle with a period of 42 years, on the other there is a longer cycle of about 600 years. The 42-year cycle will be discussed further in Chapter 4, and the 600-year cycle in Chapter 5. The AMOC between year 2000 and 4000 has a mean value of 12.5 Sv reaching maximal values of 21.2 Sv and minimal of 6.4 Sv. The AMOCI index has a lower mean when compared to the RAPID project observations at 26.5°N 16.9$\pm$4.4 Sv (McCarthy et al., 2015) and a larger variability than observed.

I took the year 2000 as the beginning of a "stable" period of the evolution under MBCs. Further analysis of the mean state of this period is described next. Surface temperature and salinity shows realistic gradients and maxima in the different basins. I compared the mean state to the Levitus (1989) climatology (Fig.2.6 c-d), climatology used as reference for the computation of the boundary conditions and which temperature the model restores to. The surface temperature shows cold biases in the central-eastern Pacific and Atlantic. The Southern Ocean shows warm biases in the northern boundary with the rest of the ocean basins with warm foci over 3-4 °C south of New Zealand and the Argentinian coast. These biases are similar to the ones obtained under fixed boundary conditions in Fig. 2.2-c. The salinity instead shows a generalized positive bias in the model of between 0.25-0.75 psu. Some coastal regions and the Arctic have larger biases reaching up to 2 psu. The fact that, despite not restoring the salinity, the biases are within reasonable values reinforces the adequacy of this mean state.

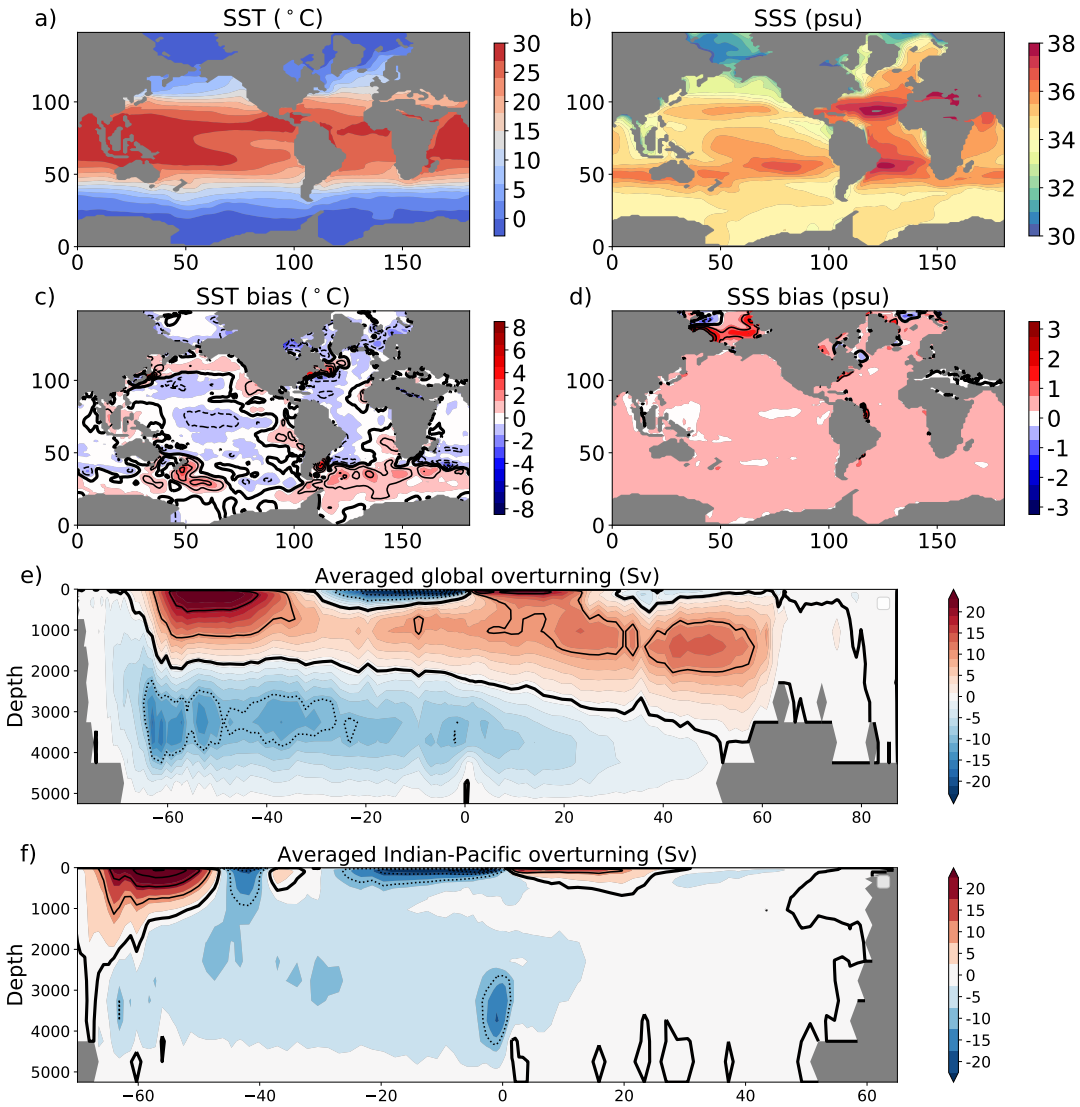

Figure 2.6: Mean state of the model under MBCs between year 2000-4000 of the simulation.**a)** Global mean SST. **b)** Global mean SSS. **c)** SST biases of the mean state compared to the Levitus (1989) climatology. Thick contour corresponds to 0°C bias and the rest of the contours indicate 1°C positive (continuous line) and negative (dashed line). **d)** Global SSS biases after the spinup compared to the Levitus (1989) climatology. Thick contour corresponds to 0 psu bias and the rest of the contours indicate 1 psu positive (continuous line) and negative (dashed line).**e)** Global overturning circulation. Thick contour corresponds to 0 Sv circulation and the rest of the contours indicate 10 Sv positive (continuous line) and negative (dashed line).**f)** Indian-Pacific overturning circulation. Contours as in e)

The global circulation in the model shows a strong overturning in the Southern Ocean with a negative overturning in the deep ocean and a positive in the upper 2000 m between 40°-60°S. In the northern hemisphere there is a northward

transport in the upper ocean and a return flow below the 1500 m corresponding to the main influence of the Atlantic contribution to this overturning (Fig. 2.7). The Pacific-Indian overturning instead has a very shallow overturning in the upper 500 metres in the northern hemisphere. In the southern hemisphere, a negative overturning is shown in the surface and below 500 m. A positive overturning is at 60°S associated to the Southern Ocean. Compared to the circulations shown under RBC in Fig. 2.2 the circulation in the upper ocean northern hemisphere seem to have similar values, whereas the circulation in the deep ocean and indian Southern Ocean the circulation seems so have intensified reaching values around -10 Sv between 60°S-30°S around 3000 m depth.

Considering only the Atlantic, surface salinity shows a maximum around 25°N and a realistic meridional temperature gradient. The difference between model and climatology is shown in Fig. 2.8 a and b. The surface temperature shows a slight cooling at the surface of the North Atlantic of about -0.15°C on average between 60°S and 60°N. Strong positive biases (3-4°C) arise north of the Gulf stream region detachment and slightly warm anomaly south of Greenland. As noted in the global biases in the limit with the Southern Ocean shows strong temperature biases, similar biases as with RBC. The main difference with RBC is a generalized positive bias between 0.25-0.75 psu (Fig.2.6 b).

The structure of the AMOC stream function is characterized by a northward mass transport above the thermocline and a southward return flow between 1500 and 3000 m (top panel of Fig. 2.7). Also, Antarctic Bottom Water (AABW) produces a recirculation cell with negative values below 3000 m (bottom right panel of Fig. 2.7). The gyre circulation has a mean of -12.6 Sv in the subpolar gyre and 31.1 in the subtropics, with a variability of 2.7 Sv and 3.6 Sv respectively (temporal standard deviation).

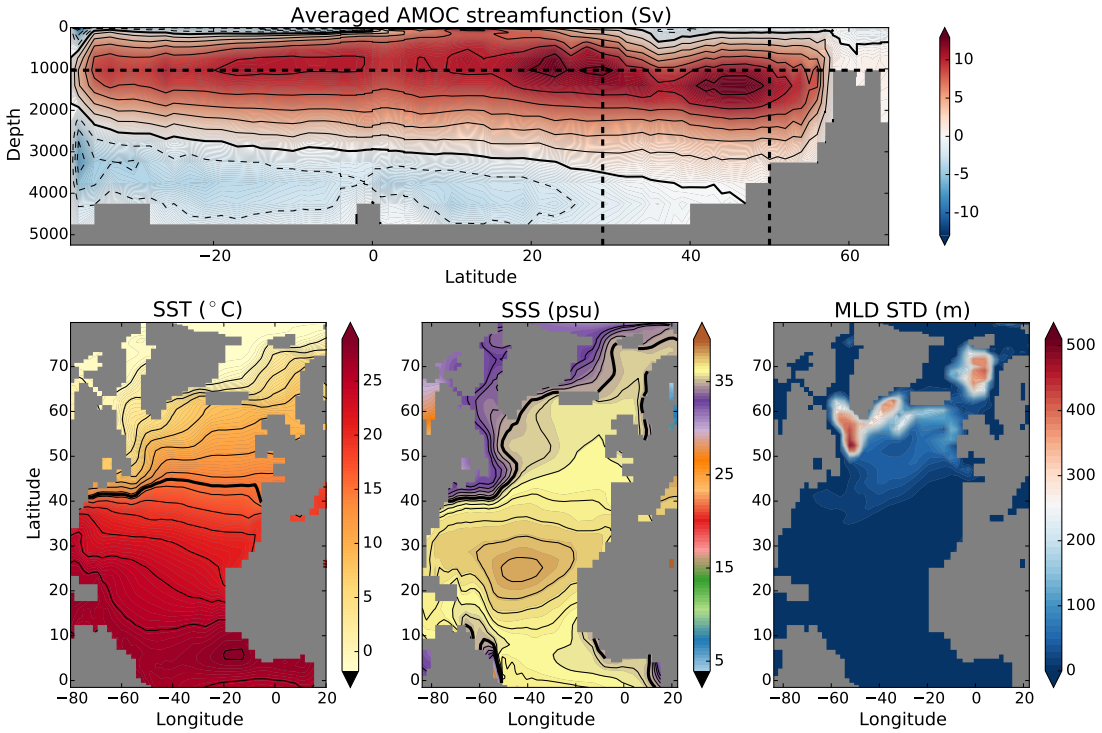

Figure 2.7: Mean fields obtained from the 2000 years integration and associated variability of the mixed layer depth under MBC. Top: zonally averaged stream function showing the Atlantic meridional stream function; contours each 2 Sv. Thin, bold and dashed lines indicate respectively positive, zero and negative values of the stream function. The intersection of dashed lines shows the points chosen to measure the evolution at 1000m and 30°N (AMOCI), and 50°N. Bottom left, Sea Surface Temperature (SST) on left with contours each 2° C and a bold line corresponding to 15° C. Centre: SSS with contours every 0.5 psu and a bold line at 35 psu. Bottom right: the standard deviation (SD) of the mixed layer depth during the time integration.

When biases are observed with depth, zonal averages in the Atlantic (Fig. 2.8), positive biases are obtained in the salinity. A generalized positive bias covers the whole Atlantic basin reaching up to 2-3 psu around 1000 m between 0-20°N and 40-50°N. When compared to the biases of the FBC spinup, the positive bias is reaching below 3000 m and slightly stronger in the upper 3000 m, about 1 psu of mean. The temperature instead maintained the structure of biases in the deep ocean compared to the FBC except for a slightly warmer deep ocean 1-2°C and cooler mid ocean.

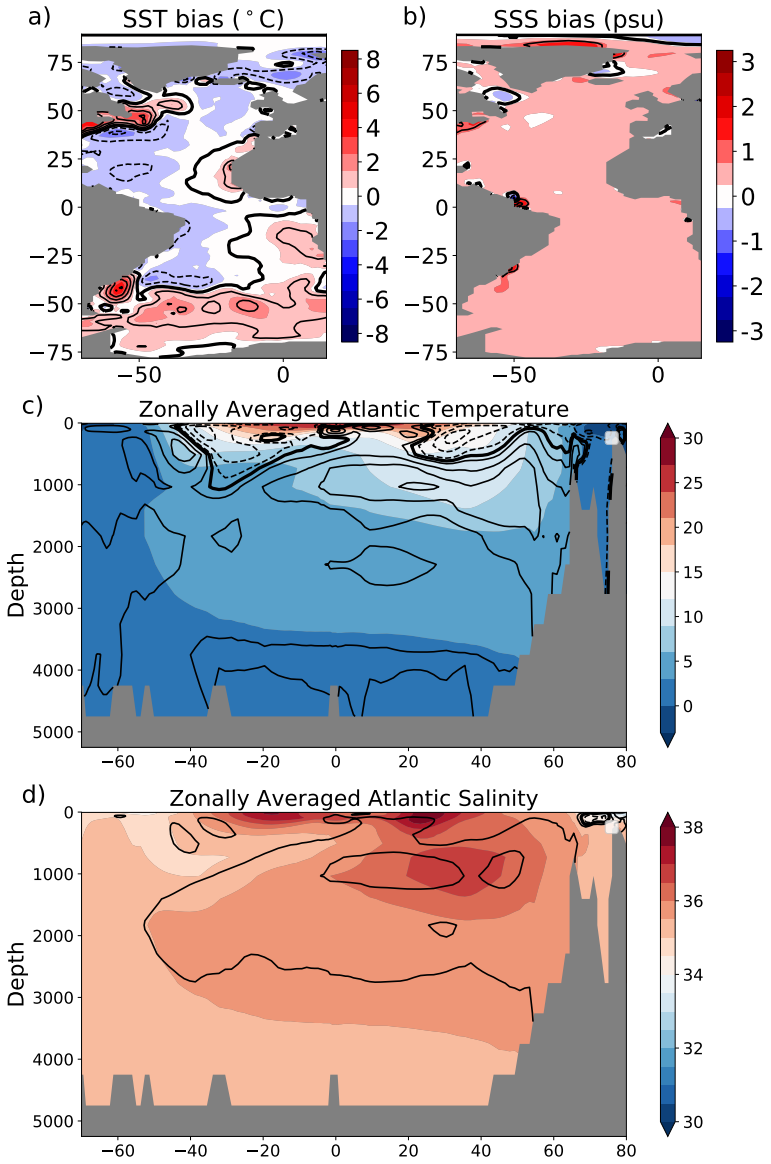

Figure 2.8: State of the Atlantic under MBC and biases. **a)** Atlantic mean SST biases under MBC compared to the Levitus (1989) climatology. Thick contour corresponds to 0°C bias and the rest of the contours indicate 1°C positive (continuous line) and negative (dashed line). **b)** Atlantic SSS mean biases under MBC compared to the Levitus (1989) climatology. Thick contour corresponds to 0 psu bias and the rest of the contours indicate 1 psu positive (continuous line) and negative (dashed line). **c)** Zonally averaged Atlantic temperature in colours. Biases with respect to the Levitus (1989) climatology is shown by the contours: bold line the 0°C anomaly, continuous line positive anomalies each 1°C and dashed lines negative anomalies each 1°C. **d)** as in **c)** but for salinity. Instead of °C are psu.

The main convection sites in the North Atlantic are represented by the standard deviation of the mixed layer depth in the North Atlantic in Fig. 2.7. They are located in the Labrador Sea, Irminger Sea and Greenland Sea. In order to compare

the convection in the model with observations, I compare the annual means of the models to the climatology of the *IFREMER/LOS Mixed Layer Depth Climatology website (www.ifremer.fr/cerweb/deboyer/mld)*. I considered annual means, since is the only output we have from the model. In comparison with the observations, our model has a lower mean state in the Labrador Sea but when considering the variability in the site, it is the site with the largest variability in the model (Fig. 2.7 bottom-right panel). The other convection sites have similar values compared with the observations.

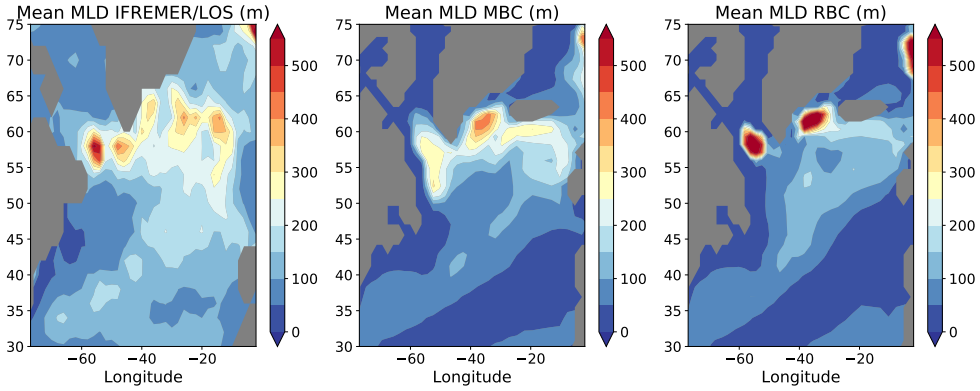

Figure 2.9: left: climatological annual mean from the IFREMER/LOS Mixed Layer Depth Climatology website (www.ifremer.fr/cerweb/deboyer/mld). Middle: Mean MLD under MBC. Right: Mean MLD under RBC. All are averages of annual means.

The time scales involving the observed variability were detected obtaining the power spectral density, $S(\omega)$, of several metrics of the Atlantic on the 2000 years considered (top of Fig. 2.10). The method of Welch (1967) provides a distribution of the variability in terms of the different frequencies, ω, associated to the considered time series. The spectrum, bottom of Fig. 2.10, shows significant peaks on the AMOC indices above a 99% red noise null hypothesis (dashed lines) with periods of 42, 21, 14 and 10.5 years. We ignored higher frequency variabilities as they were not significant. The same significant peaks appear in the Atlantic Ocean heat content (black line in Fig. 4.1), supporting the strong entanglement of these metrics. An extra source of variability appears in the Atlantic Ocean heat content spectral density at a centennial time scale. The peak is also significant for the Weddell Sea MLD which would suggest that there is another mechanism different from the AMOC that can modify the Atlantic heat content.

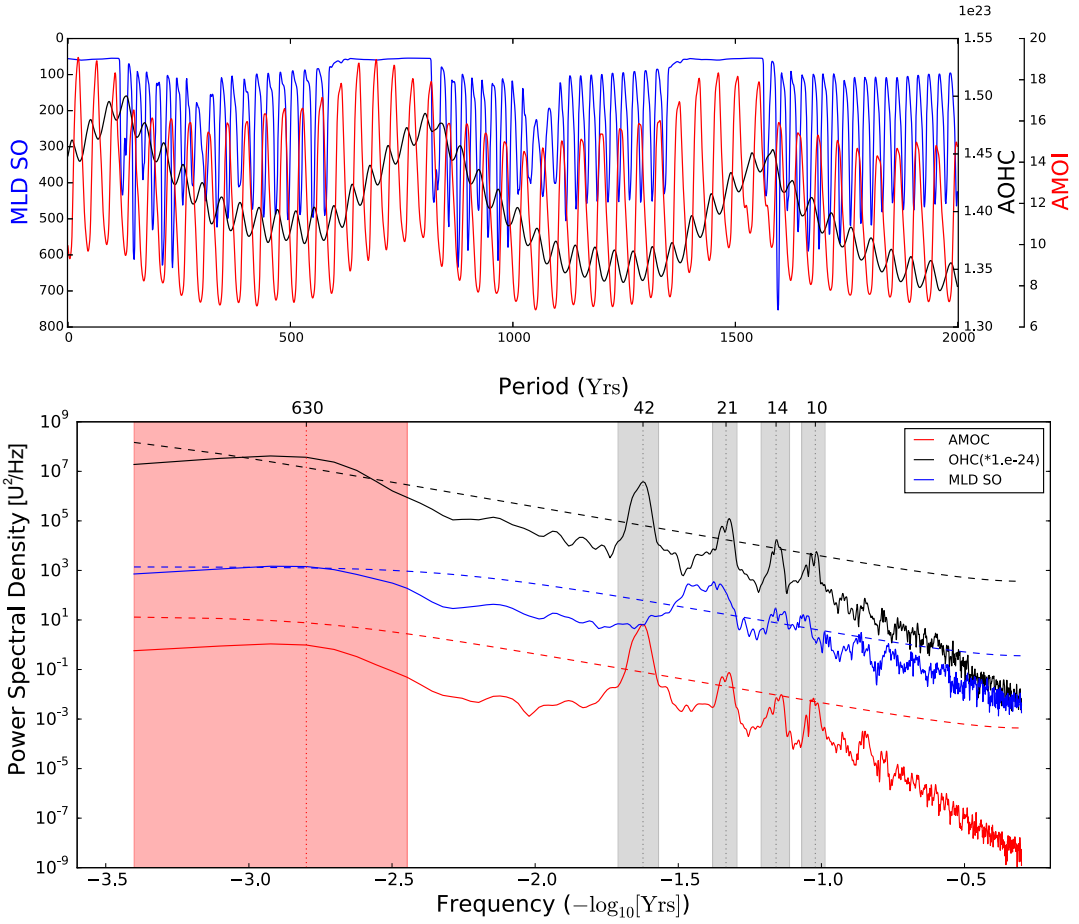

Figure 2.10: Top panel for time series of the Atlantic Ocean Heat Content (OHC) in black (AOHC), AMOC Index at 30°N at 1000 m in red and mean Mixed layer depth in the Weddell Sea in blue, and in the bottom panel the corresponding Power spectral density. The Atlantic Ocean heat content has been computed as the temperature integrated in the three dimensions (x,y,z) multiplied by the mean density (28.7 kg m^{-3}) and the specific heat capacity of the sea water (4000 J K^{-1} kg^{-1}). The spectra has been computed using the Welch's method (Welch, 1967). Dashed lines indicate the 99-% confidence values assuming a red-noise distribution of the time series. Peaks associated with the North Atlantic with periods of 42, 21, 14 and 10.5 years are shown as shaded grey bands. Additionally, a longer time scale variability with a significant peak in both heat content and MLD with a centennial time scale is shown (red shaded band). The units of the power spectral density are indicated as U^2/Hz with U the corresponding unit of each variable: Sv, W and m (from top to bottom in the legend).

To locate the mechanism involving this variability I used Empirical Orthogonal Functions (EOFs) (Preisendorfer and Mobley, 1988) of the mixed layer depth variability since both potential regions have strong connection to deep convective events. Two main sources of the mixed layer depth variability with independent periods arise only in each hemisphere in the Atlantic: the convective areas

in the North Atlantic and the Weddell Sea in the Southern Ocean. The first 4 EOFs obtained explain about 73% of the variability of the MLD in the Atlantic (Fig.2.11a). The patterns of EOF1 and EOF3 are located shows largest variability in the Weddell Sea, whereas EOF2 is located mainly in the North Atlantic and EOF4 shows variability in both regions. The time series of the Principal Components (PCs), associated with each EOF, show different evolutions of the patterns obtained. When considering separately northern and southern hemisphere MLD, Fig. 2.11b, the distinction is even more clear. Southern Ocean and North Atlantic act as period-independent oscillators of the system in the North Atlantic. The decadal to multidecadal peaks in the AMOC index are exclusively related to a North Atlantic mode of variability and the centennial oscillation to a Southern Ocean mode. The latter is associated with periods of strong deep convection in the Southern Ocean of about 500-600 years. These periods are consistent with the coupled version of the Kiel Climate Model that shares the same ocean component (Park and Latif, 2008; Martin et al., 2013) and will be the focus of Chapter 5. The Atlantic variability will be the focus of Chapter 4.

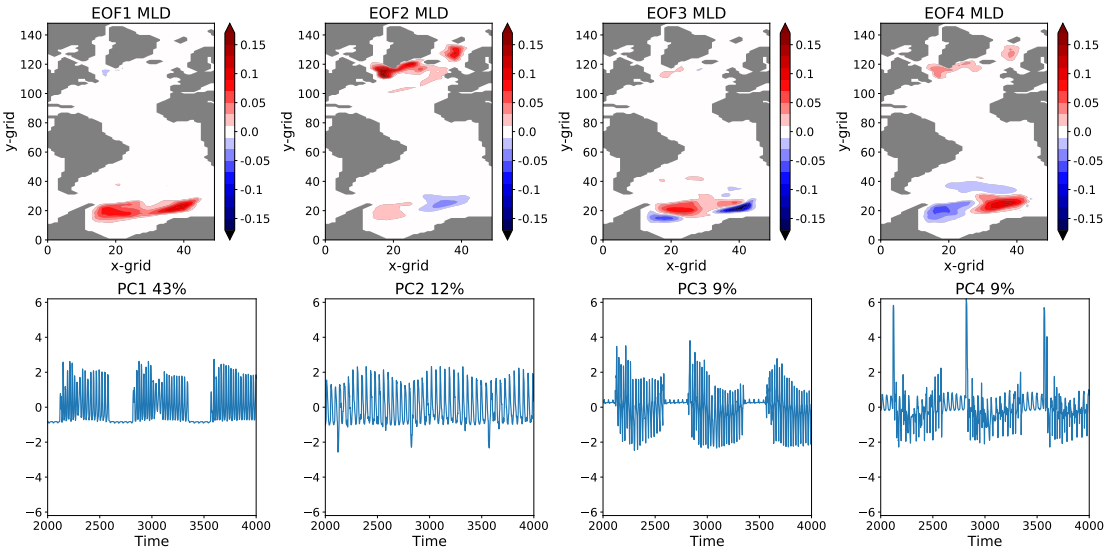

(a) EOFs and PCs in the whole Atlantic basin and Southern Ocean.

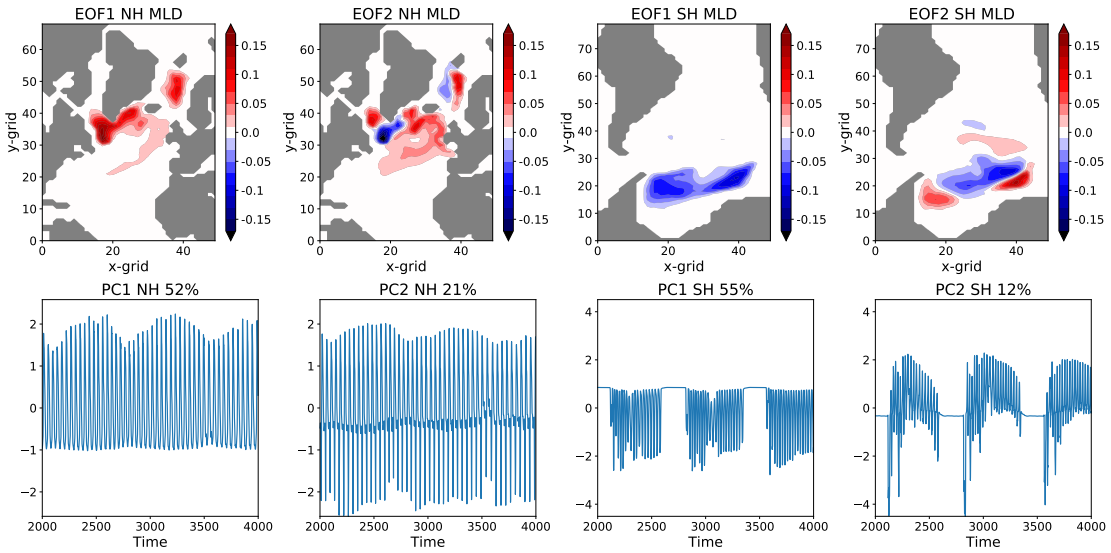

(b) First two EOFs and PCs of the Northern Hemisphere (NH) and Southern Hemisphere (SH).

Figure 2.11: EOFs of the MLD of the Atlantic and Weddell Sea with their corresponding PCs and the first two EOFs for each hemisphere.

2.4 Key points of this chapter

- The model used in this thesis is a low-resolution oceanic model used as the oceanic component of a few climate models of the Coupled Model Inter-Comparison Project 5 (CMIP5).
- I described the model evolution under different boundary conditions.
- A characteristic variability was found in the North Atlantic under MBC. The multidecadal time scale variability is further described in Chapter 4 and the centennial one in Chapter 5.

Chapter 3

Impacts of sea-surface salinity anomalies on AMOC variations

Errors in the initial conditions are an important factor to improve climate predictability. Although normally associated with shorter time predictions (Lorenz, 1975) the implications for decadal time scales are still uncertain (Hawkins and Sutton, 2009b). This chapter has a twofold aim: on the one hand to explore the impact of initial errors on decadal variability of the North Atlantic and, on the other to study the consequences of naturally occurring ocean surface salinity anomalies such as the Great Salinity Anomalies (GSAs).

3.1 Introduction

The Atlantic Meridional Overturning Circulation (AMOC) is an important metric for climate variability and global change as it transports a large amount of heat to the northern latitudes (see Section 1.1.1). Its variability affects global climate, and critically the European climate, on a wide range of timescales (Jackson et al., 2015). As a consequence, the AMOC response to global warming, its variability and impacts have received extensive attention. Even though the AMOC response to the observed long-term trends in temperature and salinity in the northern high latitudes is well established, with a weakening in the CMIP5 experiments, the

magnitude and timing of the response remain uncertain.

In the past few decades, the upper ocean in the subpolar North Atlantic has become cooler and fresher whereas the subtropics have become warmer and saltier (Wang et al., 2010; Friedman et al., 2017). In addition, the enhancement of the hydrological cycle in the last decades has increased freshening in precipitation-dominated regions and salinity at the sea surface in evaporation-dominated regions (Durack and Wijffels, 2010). The robust links between the North Atlantic and the Arctic, such as transport of freshwater, relate these changes with possible variations in the polar region (Jungclaus et al., 2005). The Arctic has undergone considerable changes in the last decades: an increase in the oceanic and atmospheric temperatures, decrease of volume and extent of the sea ice together and an increased melting of the permafrost (Proshutinsky et al., 2015). Also, changes in the surface heat fluxes and surface freshwater fluxes are of key importance for the future state of the AMOC, with a main role of heat fluxes impacting the AMOC (Gregory et al., 2005; Sévellec et al., 2017). The Coupled Model Inter-Comparison Project 5 (CMIP5) shows evidence of a decline of the AMOC by about $11 - 34\%$ by 2100 while a complete collapse of the overturning was deemed unlikely in the last IPCC report (Collins et al., 2013). However, the possibility of too stable models affects the likelihood of simulating abrupt climate changes (Valdes, 2011; Drijfhout et al., 2011; Hansen et al., 2016) and hence the accurate representation of the full AMOC sensitivity to variations in the forcing.

The development of adjoint methods (Marotzke et al., 1999) have given further insight on the sensitivity of the North Atlantic to surface perturbations. These methods provide the sensitivity of an objective function, i.e. the volume transport at 27°N, with respect to the variability of certain forcings (e.g. surface forcing). Although they do not give insights on the reasons behind this sensitivity, they may provide a set of initial conditions that contribute to the strongest change of the objective function (Sévellec and Fedorov, 2015). Czeschel et al. (2010), using the Adjoint MITgcm, showed that the AMOC, defined as the volume transport at 27°N, has an oscillatory response when forced at high latitudes by surface salinity or temperature. Heimbach et al. (2011) provided insights of the sensitivity of the

meridional volume transport and the meridional heat transport in the subtropical North Atlantic in order to design a useful observational program. These two studies showed that a mechanism based on trains of oceanic baroclinic Rossby waves could explain the high sensitivity found in the subpolar gyre region.

Concentrating on initial condition uncertainty rather than surface flux perturbations, generalized stability analysis focuses on the study of the ocean response to perturbations in a linear framework to transient growth processes (Farrell and Ioannou, 1996a,b). This approach has been developed to obtain Linear Optimal Perturbations (LOPs) in several configurations of ocean models, including planetary-geostrophic (Sévellec et al., 2009) and general circulation models (Sévellec et al., 2008). This work was further extended in Sévellec and Fedorov (2015) by taking into account the climatological seasonal cycle of the ocean. It uses linear functions such as the AMOC volume or heat transport to provide the maximal linear response of these metrics to surface salinity and temperature perturbations under several boundary conditions and perturbation constraints. The results of Sévellec and Fedorov (2015) show a maximal impact of these perturbations after 7-9 years. The anomalies give way to a decaying oscillatory response controlled by large-scale "thermal" Rossby waves of a period of 24 years that can induce a 10-20% of change of the mean overturning in the model (mean of about 14 Sv). Complementary studies by Zanna et al. (2011) used quadratic measures based on singular value decomposition to compute AMOC optimal perturbations in an idealized version of the MITgcm. All these previous results, based on linear methods, point to the northern latitudes as the most sensitive region to surface forcing and, a decadal timescale for the AMOC transient growth to initial conditions. However, this study was never performed in a fully non-linear context, which is one of the aims of this thesis.

The sensitivity of the North Atlantic is a key factor for decadal predictability of the climate. The correct initialization of the sensitive regions of the oceanic component will enhance the accuracy of decadal predictions (Dunstone et al., 2011; Germe et al., 2017). Within a linear framework, errors introduced in the initialization of Sea Surface Temperature (SST) or Sea Surface Salinity (SSS) would be

bounded by the anomalies generated by optimal initial perturbations on the corresponding metrics of the climate system. Instead, in the full nonlinear model, there are processes such as convection that are difficult to treat fully within a linear context (Sévellec and Fedorov, 2015). Sévellec et al. (2008) tested the impact of nonlinearities in the evolution of the LOPs by introducing them in the fully nonlinear model obtaining an over-estimation with respect to the linear model of about 15-30% on the AMOC response. The work presented here follows up the results of Sévellec et al. (2008) but taking a different approach: to obtain a statistically linear regime from a set of perturbation experiments in the full nonlinear model and then to quantify the impact of nonlinearities in the response. The aim is to obtain a more thorough description of the impact of surface errors in the North Atlantic within a full ocean GCM; to test whether errors in the initial conditions can be modelled by linear responses or instead, nonlinear responses must be taken into account.

In addition, to explore the impacts of initial condition errors, I investigate the response to the AMOC to extreme initial conditions, in particular to the GSAs. The GSAs are medium scale minima in salinity (and temperature) that have been observed in the North Atlantic subpolar region in the 1970s, 1980s and 1990s (Belkin et al., 1998). The salinity anomalies observed had values of about 0.2-0.4 psu in the upper 250 m in the Labrador Sea (Lazier, 1995). They were probably caused by anomalous fluxes of sea ice from the Arctic to the subpolar gyre (Walsh and Chapman, 1990) together with regional northerlies (Dickson et al., 1988) and possibly aided by the increased North American run off into the Arctic (Mysak et al., 1990; Mysak and Power, 1991). The AMOC record unfortunately doesn't date back to this period, and no direct implication of the GSAs on the AMOC have been observed. The GSAs were measured in the upper ocean, with a signal potentially perceived at the surface. By considering the GSAs only as a superficial anomalous salinity, we can provide on the one hand an estimation of the impacts of the GSAs on the global circulation, and in particular on the AMOC, as it "propagates" through the north-western subpolar gyre. On the other hand, we can give an estimate of the error generated by nudging techniques to incorrect surface salinity in historical reconstructions.

The structure of this chapter is as follows: Section 3.2 describes the experimental set up, Section 3.3 presents the impact of SSS perturbations on the AMOC. Section 3.4 describes the procedure used to define the linear regimes. It follows a characterization of the differences between the linear and nonlinear responses in Section 3.6. Finally, Section 3.7 concludes with the main results and discussion of the implications of this study.

3.2 Experimental set-up

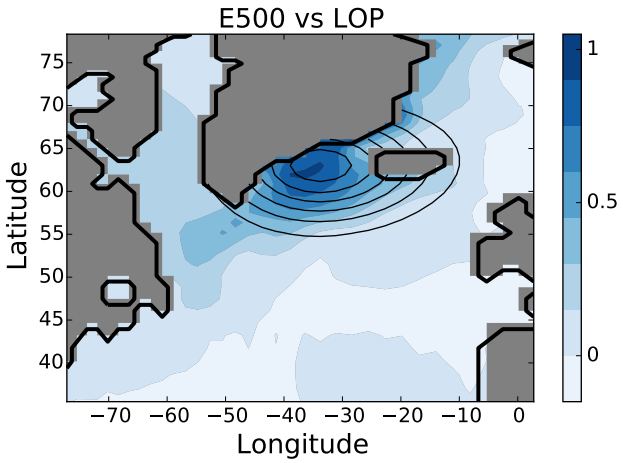

Figure 3.1: Comparison of the Gaussian perturbation of medium size (E500 in black contours) against the SSS LOP of Sévellec and Fedorov (2015). The LOP represents the SSS anomaly that most strongly affects volume transport (blue contours). Both perturbations are normalized to give a maximum value of unity.

The experiments were designed by imposing a perturbation at the beginning of the year (1st of January) on the surface layer, first 10 metres, of the salinity field in Océan PArallélisé (OPA, see Chapter 2). The perturbation, with a 2-dimensional Gaussian spatial distribution, is centred on [33.5°W, 63°N] off the East coast of Greenland. The location was motivated firstly by the position of the Linear Optimal Perturbations (LOPs), shown in Fig. 3.1. These are defined as perturbations with the largest impact on the AMOC within the linear version of the model (Sévellec and Fedorov, 2015). Secondly, sensitivity analysis by Yu et al. (2016) pinpointed the east coast of Greenland as the most sensitive to ice melting outflow.

The perturbation is defined as a two-dimensional normal distribution that depends on two variables: horizontal extension (E) and magnitude (M). The distribution of the perturbation is defined as follows,

$$\mathrm{P(E,M)} = \mathrm{M}e^{-\frac{(x-x_0)^2+(y-y_0)^2}{2\mathrm{E}^2}}, \tag{3.1}$$

with (x_0, y_0) the centre of the distribution (33.5°W, 63°N), E the horizontal extension (50 km, 100 km, etc.) and M the magnitude. The anomaly with each horizontal extension is normalized to values within the interval [0,1] and then multiplied by the magnitude M.

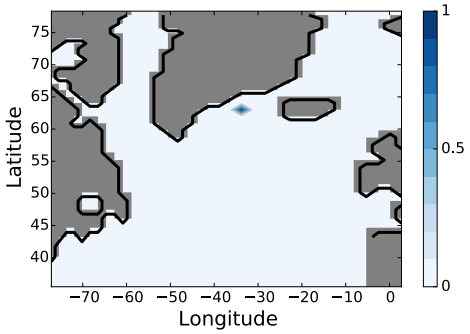

(a) E50

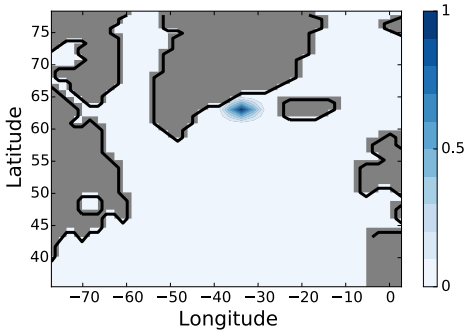

(b) E100

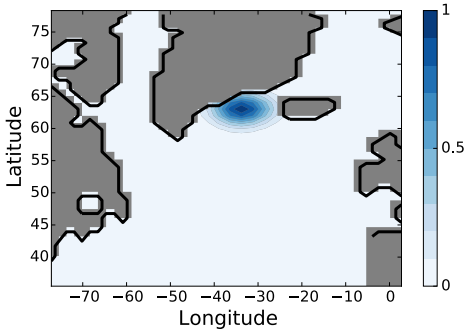

(c) E200

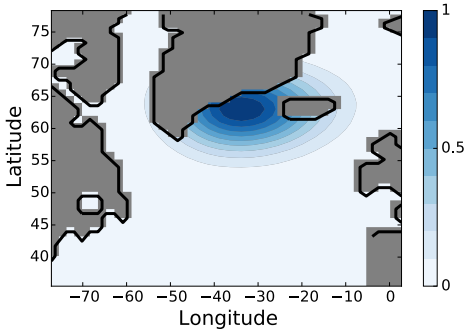

(d) E500

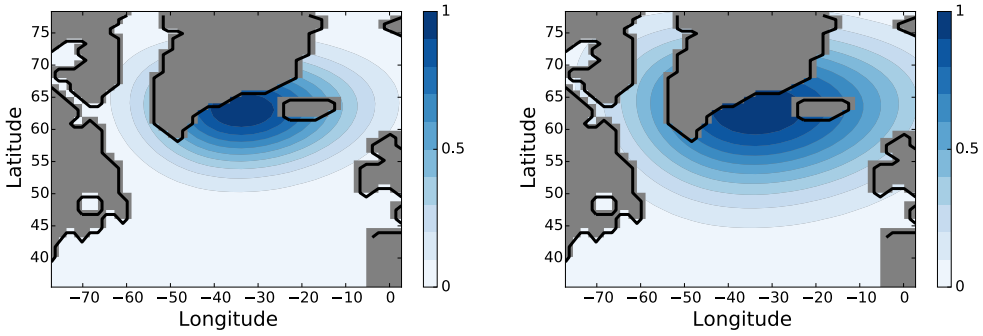

(e) E700 **(f)** E1000

Figure 3.2: Plots illustrating the different horizontal extension: E50, E100, E200, E500, E700 and E1000. The figures are plotted on the model grid, hence the contours are not perfectly circular in this projection. Latitudes and longitudes limiting the plots are nominal, they are averaged values of the section shown of the North Atlantic.

I computed a total of 6 different horizontal extensions (E) with values of 50, 100, 200, 500, 700 and 1000 km, named respectively E50, E100, E200, E500, E700 and E1000. The motivation behind this choice was to understand the impact of initial errors from an almost point-like perturbation to a large basin-scale perturbations in the initial conditions. The magnitudes of the salinity perturbations are in the range [-34, 60] psu: the lower threshold is set by the minimum value of the salinity allowed in the model, while the upper value is chosen to simulate large responses to the salinity perturbations (located only in the first 10 m of the ocean). The magnitude values selected in this range are chosen with the following criteria: an initial step up to ±0.2 psu considering 0 and ±0.1 psu perturbations; in steps of 0.5 psu from ±0.5 to ±5 psu; in steps of 3 psu from ±5 to ±26 psu; for positive values from +26 to +50 psu in steps of 3 psu and for negative values from -26 to -34 psu in steps of 1 psu. The last 3 positive magnitudes (53, 56 and 60 psu) are added without a negative magnitude.

The perturbations previously described are compared to two metrics of Greenland: an equivalent percentage of total Ice volume of Greenland and an equivalent years of Greenland discharge over the Atlantic with the 2005-2010 rate (McMillan et al., 2016). The salinity introduced in the perturbation is integrated to obtain the total salinity introduced. Then it is transformed, following Griffies et al.

(2005), to an equivalent freshwater volume as in $F_W = -F_S h/S_0$, with F_W the freshwater volume, F_S the salinity introduced, h the depth of the first layer of the model (where the perturbation is introduced) and S_0 a salinity reference of 35 psu. Once the total volume of freshwater is computed, and taking into account that the volume of water increases by 9.05%, the equivalent ice volume is computed as percentage of the total ice mass in Greenland (Fig. 3.3). McMillan et al. (2016) reported a discharge of the Greenland ice sheet between 2005-2010 with a mean of 262 km^3/year, with this quantity the equivalent years of Greenland discharge to the perturbation introduced are shown in Fig. 3.3 together with the % of total ice volume in Greenland. The total ice volume in Greenland, around 2,850,000 km^3 (Stocker et al., 2013) allows us to put in context our perturbations, which reach values less than a 3% of the total ice mass in Greenland.

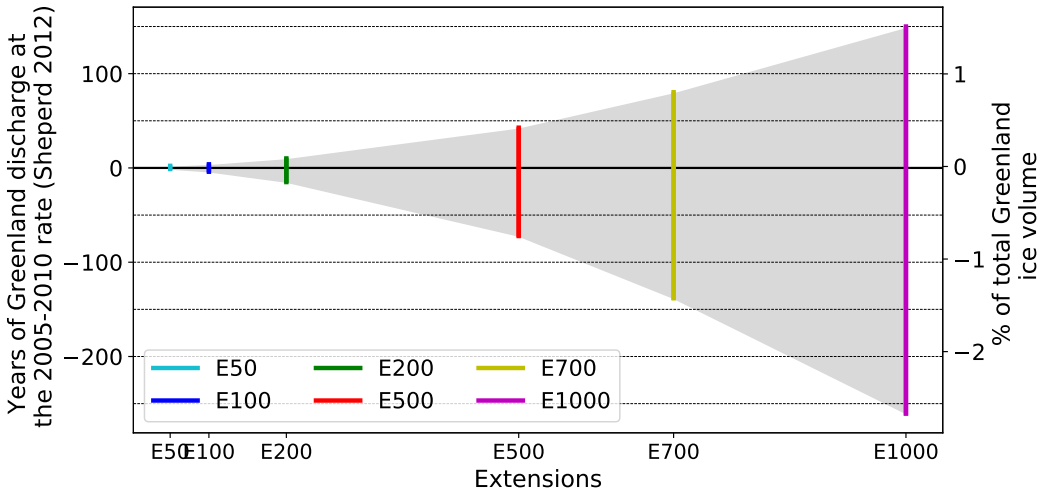

Figure 3.3: Equivalence of the perturbations here presented and two metrics of Greenland: equivalent % of the total Greenland's ice volume required to obtain the salinity anomalies of the perturbations imposed and Years of ice discharge of the Greenland ice sheet at the 2005-2010 rate of 262 km^3/year (McMillan et al., 2016). Horizontal dashed lines represent 50 years of discharge. Horizontal dashed lines represent each 0.5% of the total ice volume in Greenland and 50 years of discharge respectively.

The experiments are initialized after the spin-up under Restoring Boundary Conditions (RBC), and after a change in the boundary conditions to Fixed Boundary Conditions (FBC, with surface heat and freshwater fluxes specified) was done at the same time that the perturbation is introduced. The conditions used for fixed boundary conditions have been computed by averaging the fluxes of ten years from

the spin up run with RBC. FBC allows the perturbations to develop without direct surface restoring. It avoids unrealistic explicit salinity damping due to restoring conditions and, represents a more realistic atmospheric feedback (Huck and Vallis, 2001; Arzel et al., 2006; Sévellec et al., 2009). All the experiments are run for 40 years after introducing the perturbation and outputs of annual means are used for our analysis.

3.2.1 Evolution of the 40 years after changing boundary conditions

To understand the impact of the change of boundary conditions, I analysed the evolution of the unperturbed case. The aim is to detect and be able to differentiate the impact of the perturbations and the impact of the change in the boundary conditions. A background state in quasi-equilibrium during the first 25 years, less than a 0.1 Sv in AMOC variability (Fig. 3.4), gives confidence that the initial impacts are generated solely by the perturbations discarding the possibility of being the boundary conditions being the major role in the initial evolution of the experiments.

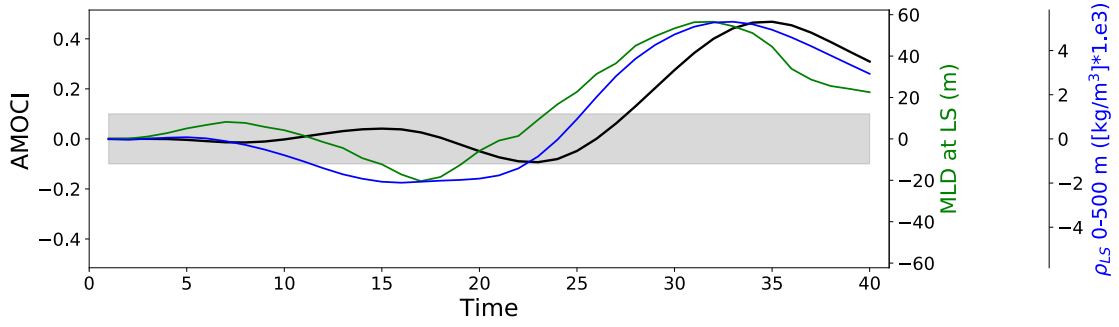

Figure 3.4: The vertical labels and corresponding colors indicate: AMOCI (black), MLD anomaly in the Labrador Sea (green) and density anomaly in the Labrador Sea averaged in the first 500 m. The grey band shows the limit of 0.1 Sv on the AMOC.

After the change of boundary conditions, a reduction of ice cover in the Arctic and Canadian archipelago, generate surface density anomalies, less than 0.12 kg/m^3, that are advected following the coast towards the Labrador. As this anom-

aly propagates South reaching the Newfoundland coast, generates an anomalous cyclonic circulation (Fig. 3.5 3c)). This contributes to generating a positive density anomaly right on its eastern margin and another positive anomaly appears as well on year 20 around 500 m depth and located in the region $[55, 50]\text{N} \times [35, 40]\text{W}$. This anomaly on the West promotes its propagation as a "thermal" Rossby wave, mechanism depicted in (Sévellec and Fedorov, 2013b) and explained in the next sections. The density anomalies generated, develop an anomalous zonal density gradient modifying firstly the meridional transport with an impact on the AMOC and secondly interacting with the Labrador Sea convection site. In fact, it is not until a positive surface density anomaly reaches the Labrador Sea by year 20, that a deepening of the MLD and a consecutive increase of the AMOCI is obtained. The anomalies of density in the upper ocean around 55°N continue propagating westwards. The negative anomaly reaches the convection site in the Labrador around year 36 in which the convection starts to decrease and the consecutive AMOCI decrease 4-5 years later.

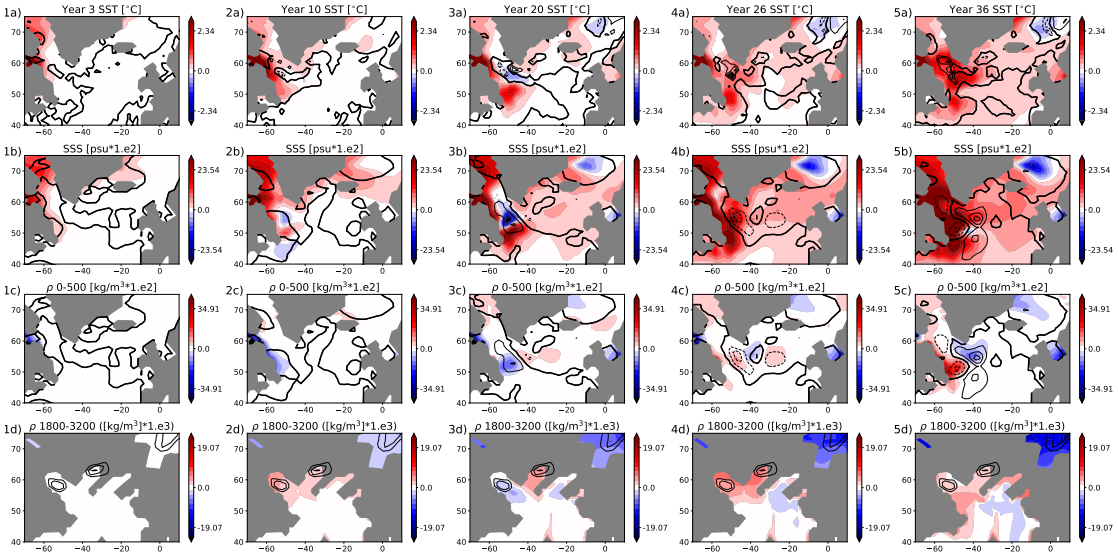

Figure 3.5: Snapshots of the evolution of the unperturbed case due to a change in the boundary conditions. The rows indicate anomalies with respect to the initial state, before changing the boundary conditions and the columns different times in the evolution, years 3, 10, 19, 26 and 36. a) SST anomalies (first row) are shown with contours of the mixed layer depth with contours every 100 m and the bold line representing the zero anomaly. b) SSS anomalies are shown with a factor of 10^2 and contours of the barotropic stream function anomaly every 0.5 Sv with the bld line indicating the zero anomaly. c) Averaged density in the first 500 metres is shown corrected by a factor of 10^2 and the same contours show the barotropic stream function as in b. d) Density anomalies averaged between 1800 and 2300 metres. Contours show the mixed layer depth with contours every 500 m.

Although there is a mechanism behind the change of boundary conditions, the anomalies generated are quite small in the first 10-15 years of the simulation, which is our main period of interest. The anomalies generate in the AMOCI are smaller than 0.1 Sv (shaded grey area in Fig. 3.4), small values compared to the impact of our perturbations with the exception of E50.

3.3 AMOC response to the perturbations

The general response of the AMOC is represented by the Atlantic Meridional Overturning Circulation Index (AMOCI) (Fig. 3.6), with positive perturbations generating a positive increase in the overturning and negatives reducing it. A first peak is obtained between years 8-10. This response time is in concordance with previous

studies based on linear perturbations (Sévellec and Fedorov, 2015) and with the AMOC response in the MITgcm to anomalous heat fluxes in the subpolar region (Czeschel et al., 2010). The times of maximal response in the first peak are shown in Fig. 3.7. We can start to spot differences in the impact of both magnitude and extension that could lead to differences between linear and nonlinear responses. For lower extensions, the response is bounded between year 9 and 10. As we increase the extension, the response is faster for larger magnitudes and shows an asymmetry in the peak time for positive and negative magnitudes.

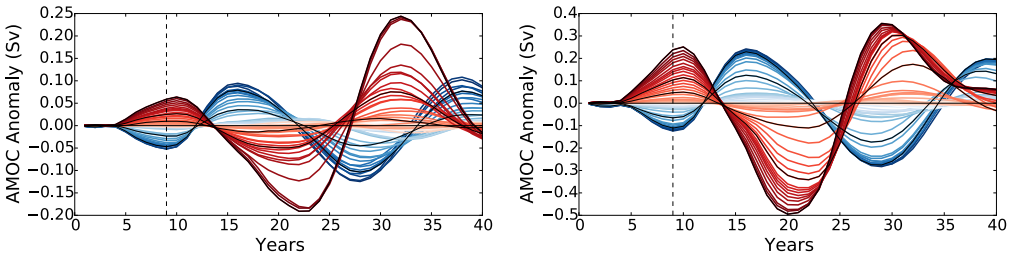

(a) E50 **(b)** E100

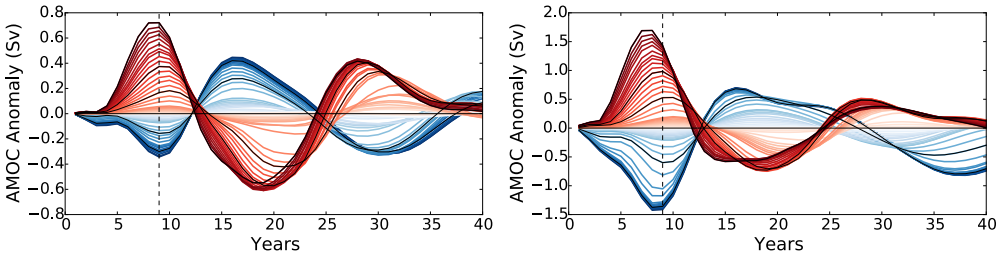

(c) E200 **(d)** E500

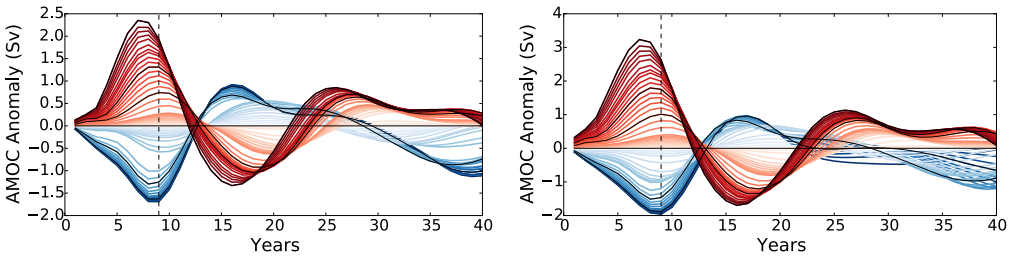

(e) E700 (f) E1000

Figure 3.6: Evolution of the AMOCI after introducing the perturbations. Positive magnitudes are represented in red and negative magnitudes in blue. The color intensity relates to the increase in absolute magnitude of the perturbation imposed. Black lines represent magnitudes of values ± 14 psu, ± 30 psu and $+60$ psu.

Both variables that define the imposed perturbation have an impact on the evolution and the intensity of the initial response. The horizontal length scale impacts firstly in the intensity of the response: the larger the horizontal response, the larger the impact on the AMOC maxima. Smaller horizontal scales show a very low initial peak around year 10 with smaller anomaly values than the following peaks. The sign of the anomaly has an impact on the response, showing an asymmetric response with larger values for the positive perturbations. These differences are about a 10% of the positive magnitude but can reach up to a 25% of the positive response.

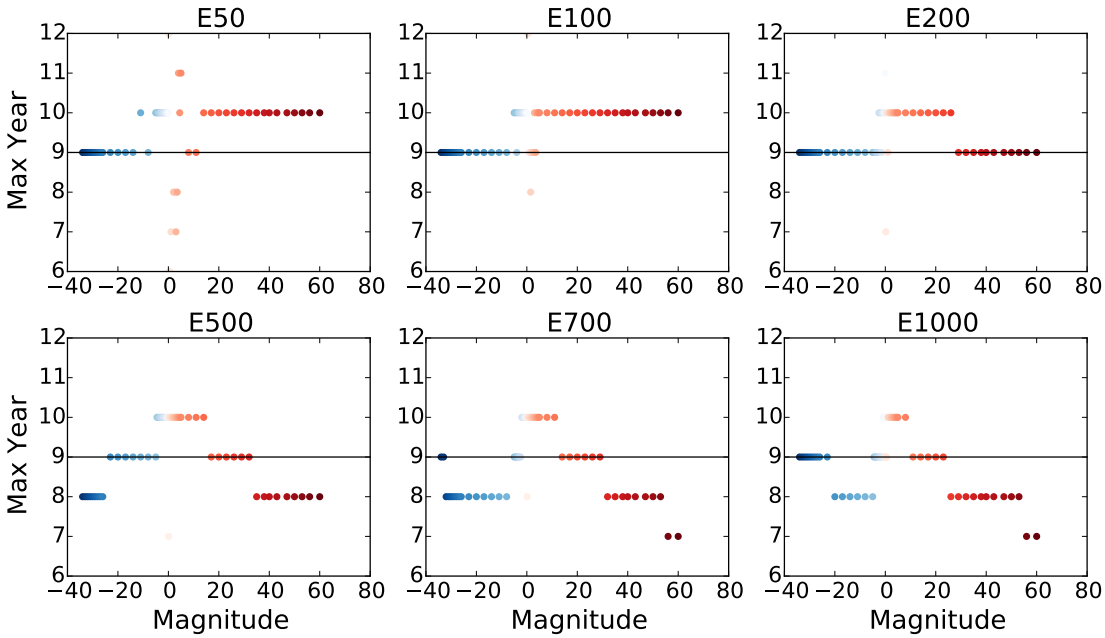

Figure 3.7: Time of the first peak for the different magnitudes considered, the increase in magnitude is shown by the strength of the dots (dark blue - bright blue - white - bright red - dark red). On average 9 years is a good approximation of the first peak (horizontal black line). For all horizontal scales, the peak at 10 years seems associated more with perturbations of small magnitude, with positive anomalies peaking more often at this time (showing an asymmetric response). For large horizontal extensions, the response is shorter when compared to smaller horizontal scales.

After the first peak, a cycle of a period of around 20 years continues regulating the evolution of the AMOCI. These cycles are the result of the propagation of "thermal" Rossby waves intrinsic in the model, later explained in the Section 3.5.2. The 20-year cycle has a larger impact on the AMOCI for lower extensions than the perturbations (bright colours in Fig. 3.6), characterized by a larger peak around year 20 and 30. On the other hand, for higher extensions the largest impact is caused by the first peak after the perturbation. The unperturbed case, zero perturbation, has a cycle peaking at about year 20 and 30 possibly due to the change in the boundary conditions. It reaches to anomalies of about 0.3 Sv in those peaks, anomalies with respect the initial state before changing the initial conditions.

3.3.1 Consistency of the AMOC response

Several features of the experiments were modified to test the robustness of the results previously presented. In this subsection I describe these variations always using the experiment E500. This is an experiment with a medium horizontal extension and with similar size to the LOPs from Sévellec and Fedorov (2015). I firstly tested the sensitivity to the chosen location and secondly to the time at which the perturbation is imposed. For the location, I chose two other positions as center for the E500 perturbation: one at the northern boundary of the Subtropical Gyre (STG) and the a second one in the Greenland Sea. The time sensitivity experiments consisted of introducing the perturbation at various times of the year, as opposed to introducing it on the 1^{st} of January, testing the impact of seasonality on our results.

Impact of location The original location of the perturbation, Location 0 (L0), was chosen to compare our results with previous studies based on LOPs (Sévellec et al., 2009; Sévellec and Fedorov, 2015). The LOP generates the largest impact on the objective function chosen, i.e. meridional volume transport, in a linear framework. To test whether this still holds in the nonlinear model, I changed the location of the perturbation to see if I obtained similar responses, mechanisms or time scales. As mentioned before, I repeated the E500 experiment, with magnitudes in the range $[-5, 5]$ psu, in other locations: one in the northern boundary of the STG, Location 1 (L1), and another one in the Greenland Sea, Location 2 (L2). The choice of the location L1 was motivated not only to get a sensitivity of our perturbations with respect to a change in location but as well to understand the potential propagation mechanisms of salinity anomalies through the SPG such as the Great Salinity Anomalies. The locations are shown on the left of Fig. 3.8 and the associated AMOC anomalies on the right.

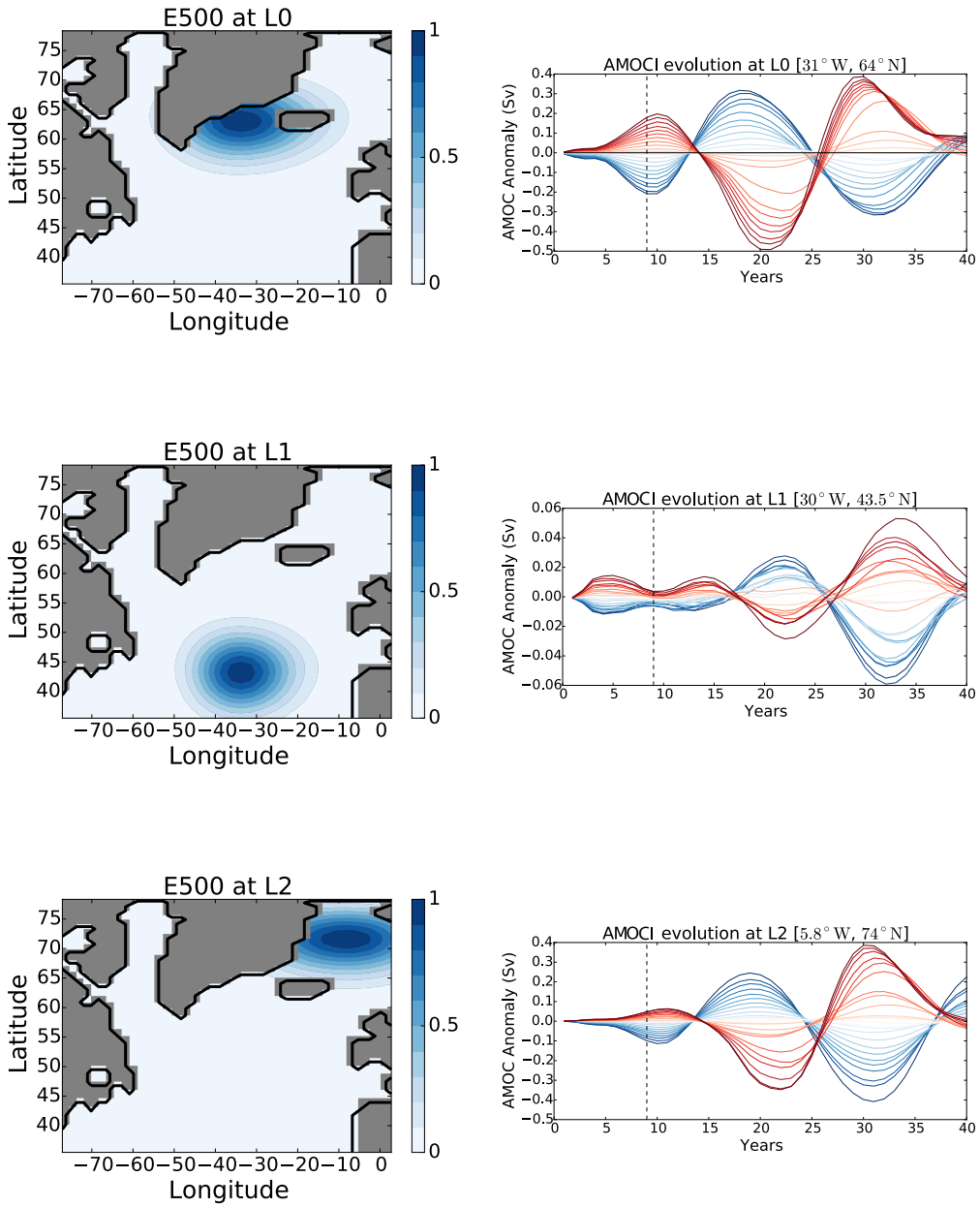

Figure 3.8: Left: the location of the three tested locations. L0 is located at the centre of the LOP at $[31°\mathrm{W}, 64°\mathrm{N}]$, L1 on the northern boundary of the SPG centered at $[30°\mathrm{W}, 43°\mathrm{N}]$ and L2 in the Greenland Sea with center at $[5.8°\mathrm{W}, 74°\mathrm{N}]$. Right: evolution of the AMOCI in the three locations used in the study, we limited this test to magnitudes within the $[-5, 5]$ psu range. Positive magnitudes are represented in red and negative magnitudes in blue. The color strength relates to the increase absolute magnitude of the perturbation imposed. Remark the different scales on the AMOC anomaly on each case.

The results show, as with the linear models that a different location from L0 gives a lower AMOCI response. L2 has a similar oscillatory response but delayed with respect to L0 and lower anomaly magnitudes. The initial anomaly interacts with

the Greenland sea convection site promoting the advection of density anomalies to the Irminger and Labrador Sea. Once it impacts the Irminger sea, the response continues on similar time scales as L0. In the case of L1 we can see that has an initial peak within the first 5 years, but with really small values of AMOCI anomalies. The evolution of this case has been described further in the Appendix A. The description of the evolution of this perturbation is out of the scope that a perturbation located at L0 was giving the strongest initial perturbation as predicted by the linear models (Sévellec et al., 2009; Sévellec and Fedorov, 2015).

Another potential location that we could have chosen would have been a direct perturbation in the Labrador Sea. It would have been interesting to understand the impact of initial conditions in this region by considering instead the use of a more recent model with better parametrization and possibly coupled would be more appropriate for a better understanding of this case, as air-sea fluxes are of key importance to this region.

Impact of perturbation time Although the choice of 1st of January as perturbation date was chosen to simplify computations, I tested as well E500 perturbations imposed at different points of the seasonal cycle. The magnitudes for these experiments were ± 1 psu for each of the starting dated. The aim of these experiments was to understand the implications of our perturbation time both. In winter, when convection is active, the perturbations may evolve differently if choosing another time to impose our perturbations such as summer.

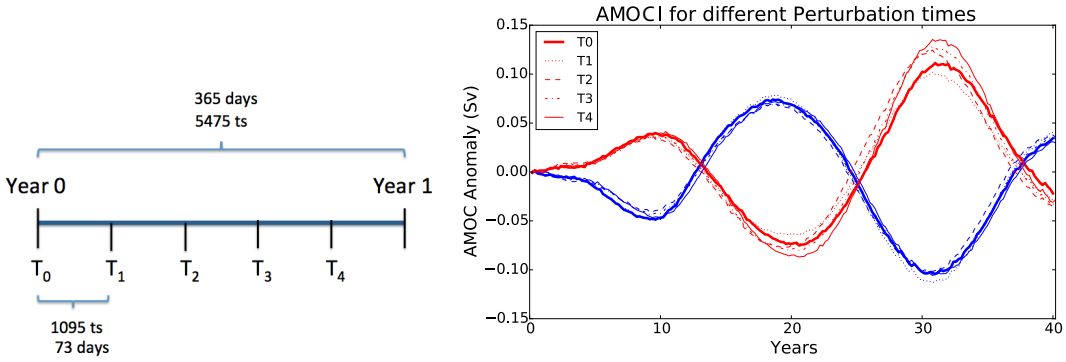

Figure 3.9: On the left, diagram to represent the times where the perturbations were introduced in this set of experiments and on the right the AMOCI anomalies for each of the experiments. T0 is the perturbation time in all the standard experiments. The other T_i with $i \in 1, .., 4$ are the new perturbation times separated by 73 days each (1095 time steps, ts). The starting points on each of the experiments are located in the figure on the right according to the diagram on left.

The main set of experiments introduce the perturbation on the 1st of January. The normal year of the model, 365 days or 5475 time steps (ts), has been divided by 5 in order to obtain an extra 4 time steps to introduce the perturbation. The separation is of 73 days (1095 ts), shown at the diagram on the left of Fig. 3.9. For these computations, instead of obtaining annual means, the model produced outputs each 73 days in order to be able to compare all the experiments.

The results show in fact that the time of the perturbation within the same year doesn't impact the timescale and magnitude of the anomaly generated. This reinforces the results here obtained, in which the errors introduced at any time of the year would have a similar impact on a decadal time scale on the AMOC.

3.4 Definition of Linear regimes

The aim of this section is to describe the method I used to define the linear regime. Here each model corresponds to a different set of magnitudes included in the linear regime and the best model is chosen by selecting that with the lowest Bayesian Information Criterion (BIC, Schwarz (1978)). This criterion, unlike for example the goodness of fit derived as the coefficient of determination R^2, accounts not only for how well the model fits the data but also for the number of points considered in

the regression and the number of model parameters. In particular, since in this case all the different models are characterized by the same number of parameters, for models fitting equally well the data, the BIC will penalize the model that includes more points (magnitudes) to avoid overfitting the data.

In the first part of this section, I will describe how I have computed the BIC and the comparison algorithm used to select the model that best fit the linear regime. Secondly, I will discuss the results obtained for the AMOCI (30°N and 1000 m depth) and I will conclude with a discussion about the consistency of the chosen linear regimes in the Atlantic basin.

3.4.1 Finding the best linear regression

In order to obtain the best linear regression amongst the combination of the magnitudes and the induced response on the AMOCI (AMOC anomaly at 30°N and 1000 m depth), we considered the Bayesian information criterion to compare between possible combinations of magnitudes.

The Bayesian Information Criterion The BIC is generally used to select the 'best' model amongst a set of models. As a model is fitted, we can add more parameters or observations increasing the likelihood function, but as well we can overfit the model to the data. Overfitting means that our model is very related to the actual data considered and does not represent the relationship predictor-predictand if other set of data is introduced, possibly leading to fail a prediction. To avoid this problem, the BIC introduces a penalty term for the number of parameters in the model and data points used.

In our problem, we want to predict the response of the AMOCI in terms of the magnitude of the perturbation introduced for each of the different extensions. Hence we assume a regression model of the form $y = x\beta + \epsilon$ where y is the AMOCI anomaly, x the set of chosen magnitudes, β and ϵ our regression parameters: linear regression coefficient and residual normally distributed, $\epsilon \sim N(0, \sigma^2)$. The model has a total of 2 regression parameters. With this notation, the BIC score is defined

as follows:

$$BIC = -2\log(\hat{L}(\beta, \sigma^2)) + k\ln(M), \tag{3.2}$$

where $L(\beta, \sigma^2)$ is the likelihood function and $\hat{L}(\beta, \sigma^2)$ its maximized value with respect to β and σ^2. The likelihood function represents the probability of the regression parameter, conditional to the given data. For our model it is

$$\hat{L}(\beta, \sigma^2) = (2\pi\sigma^2)^{-M/2}\exp(-\frac{1}{2}\frac{\mathrm{RSS}^2}{\sigma^2}). \tag{3.3}$$

Where RSS represents the residual sum of squares (i.e. the accuracy of the regression fit).

The second term, $k\ln(M)$, is the penalty introduced to avoid overfitting the model. k is the number of parameters estimated (2 in our case) and M the number of data points (chosen magnitudes)

Computation of the BIC The method works as follows. First, it computes the first score with magnitudes up to ±0.2, (i.e. ±0.1, ±0.2; blue triangle on top of Fig. 3.10a and Fig. 3.11). We increment the magnitude up to ±0.5 psu obtaining 3 scores: initial magnitudes and -0.5 psu, initial magnitude and ±0.5 psu, and initial magnitudes and +0.5 psu. These are represented in the second line of Fig.3.10a (left, center and right respectively). To illustrate further the next step of the algorithm I depicted the corresponding BIC scores when considering magnitudes up to ±1 psu in Fig. 3.10. The symbols on the second line of Fig. 3.10a identify each of the scores with the elements chosen to compute it in Fig. 3.10b. The left extreme indicates when only negative magnitudes are considered together with the initial magnitudes (magnitudes up to ±0.2). Each score to the right from the extreme left is computed adding one positive magnitude until we reach the central point, which considers all magnitudes. Continuing to the right, the lowest negative magnitudes is discarded in each score until reaching the right extreme, where only positive magnitudes are considered for the regression together with the initial magnitudes (magnitudes up to ±0.2).

The algorithm continues the next steps including one positive and one negative

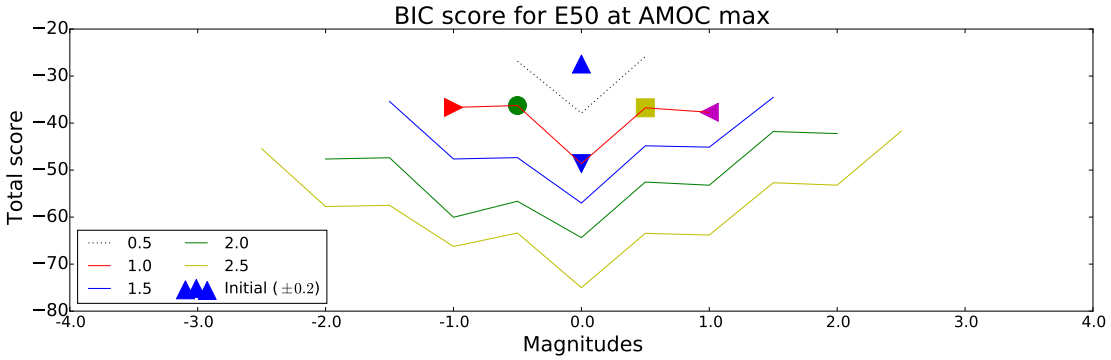

(a) BIC scores of the first steps of the algorithm. Each line represents the scores considering up to ± 0.5, ± 1.0, ± 1.5, ± 2.0, ± 2.5 from top to bottom respectively. In the third line, magnitudes up to ± 1.0, each symbol corresponds in Fig. 3.10b to the magnitudes chosen to compute the score.

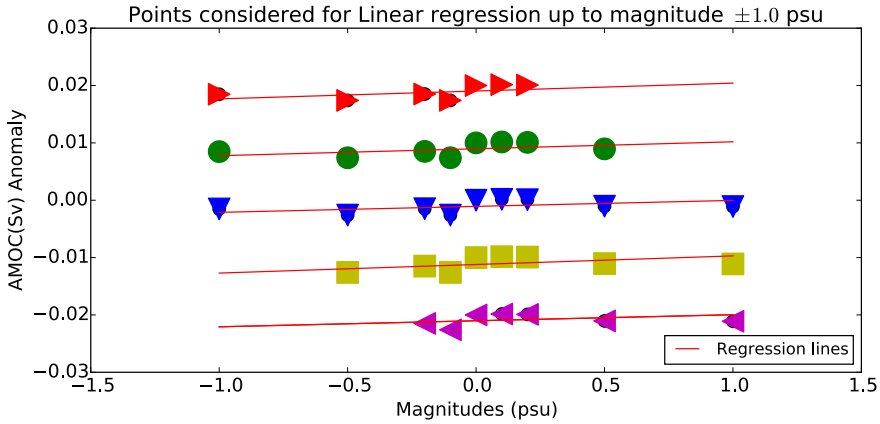

(b) Schematic of the combination of magnitudes chosen to compute each of the BIC scores in the third line in Fig.3.10a. The colors and figures indicate the chosen magnitudes for the same colour and figure in Fig.3.10a.

Figure 3.10: First steps of the algorithm for the computation of the BIC scores of the linear regressions used to define the linear regime.

value in the regression analysis at each step and computing the BIC for all the combinations within the range defined by the minimum and maximum values following the steps described before. The computation of the complete combination of evolution for each extension is depicted in Fig. 3.11. The linear regime is then defined as the combination of perturbations with the lowest BIC (represented by the green square in Fig. 3.11).

The algorithm is computed considering the AMOC response at each maximal response for each of the magnitudes. Additional tests were performed using the AMOC response at 9 years after introducing the perturbation, discussed later in section 3.4.2. These results already give some information about the stability and behaviour of the responses of the AMOCI to the perturbations. Lower horizontal resolutions have a more consistent response to what a linear regime should be. The scores have a rhomboid shape with the initial point on top as the worst score (blue triangle in Fig.3.11). As more elements are included, an improve in the score is obtained with the best representation of the linear regime given when all the magnitudes are considered.

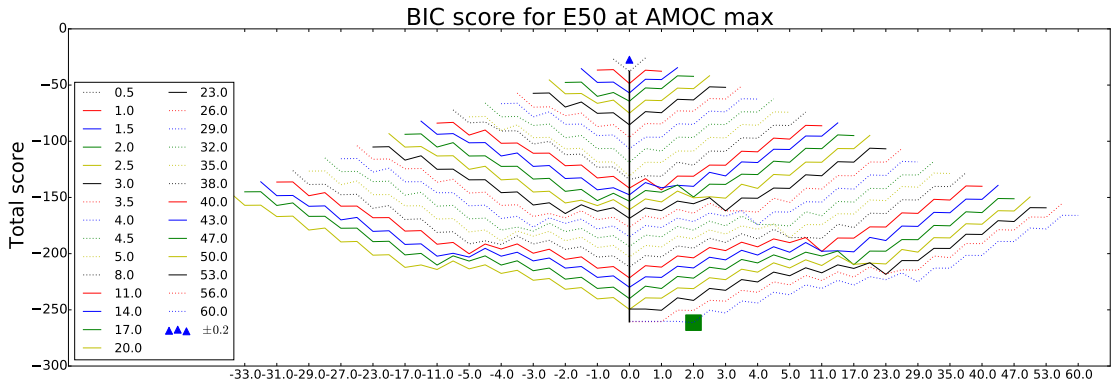

(a) BIC E50

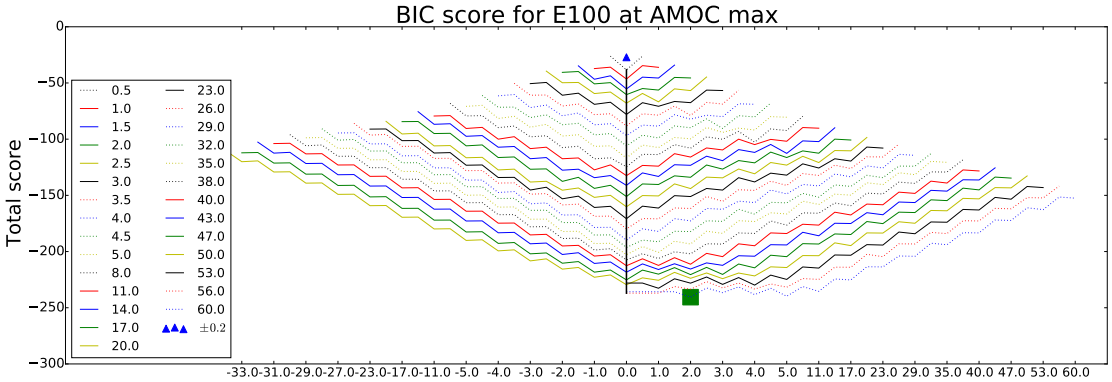

(b) BIC E100

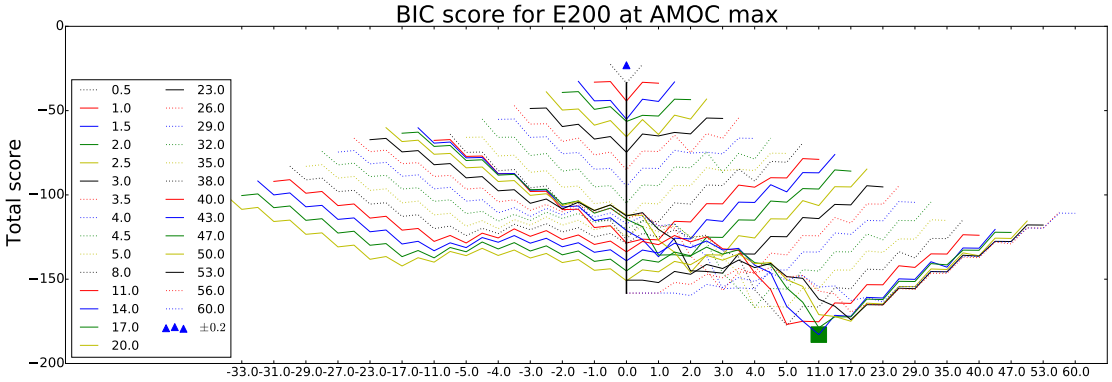

(c) BIC E200

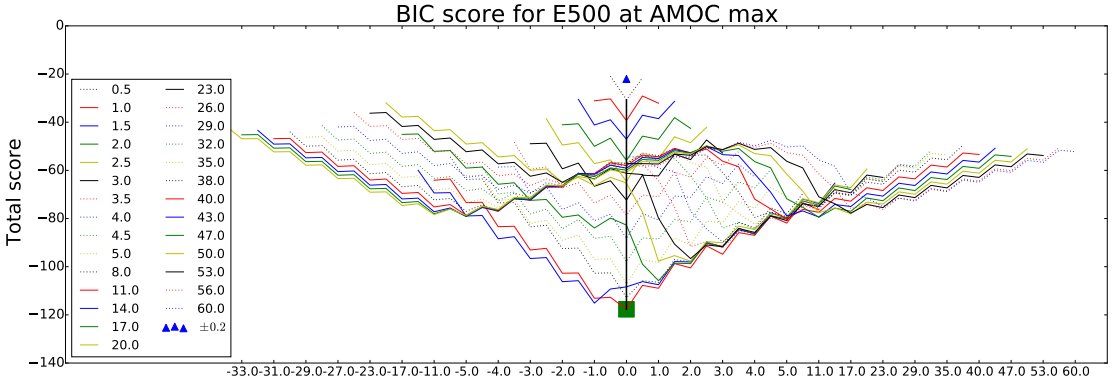

(d) BIC E500

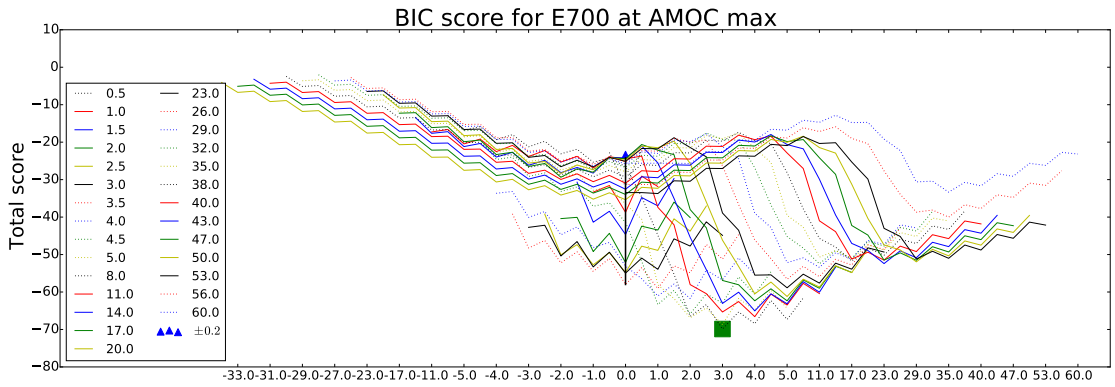

(e) BIC E700

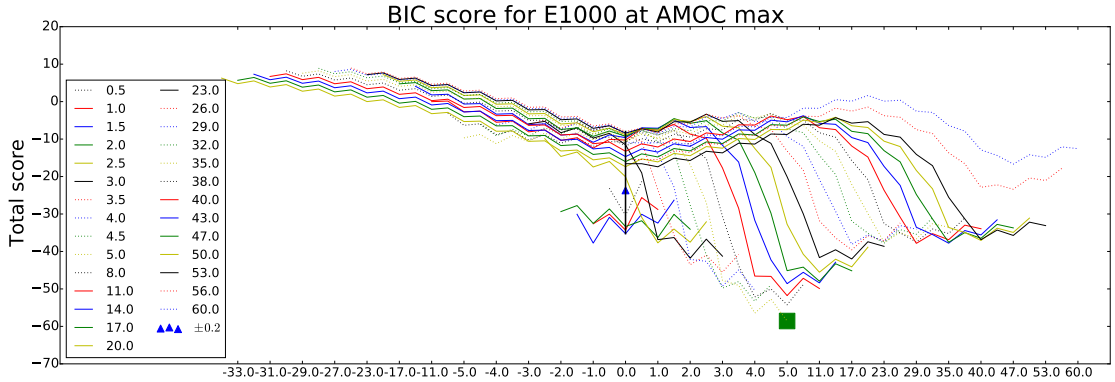

(f) BIC E1000

Figure 3.11: BIC scores for all the horizontal scale experiments. Each line of each panel corresponds to the scores with a maximum magnitude considered indicated by their extremes. The initial step is represented by a blue triangle including ±0.1 and ±0.2. The central black dots denote the score when all the magnitudes for each line are considered and far left/right with more positive/negatives magnitudes considered respectively. Green squares represent the best BIC score for each extension (minimum of BIC scores).

The rhomboid shape starts to change as we increase the horizontal extension, it collapses on itself top onto bottom. Better scores are given to the initial steps than to those in which more magnitudes are considered. This shows that the linear assumption starts to break as the linear regression can not predict well the response for all the magnitudes, obtaining a nonlinear response. Also, better scores tend to be on the right-hand side of the panels, scores with less negative magnitudes considered, and hinting towards a more linear response when positive magnitudes are considered. In fact, the best scores, green squares in 3.11, are located on

this side. P500 is the only exception in which the minima is still located in a central point. Maybe due to the resemblance of this perturbation to the LOP from Sévellec et al. (2009) in horizontal extension preserving the symmetry up to lower magnitudes or maybe due to the way the initial steps of the algorithm collapses onto the regression with higher magnitudes.

3.4.2 Analysis of the best regression

To understand further the results of the score chosen, I took a further look at the minima of the BIC scores (green squares in Fig.3.11). The regressions with a minimal BIC are all significant to a 99% when compared to a null hypothesis of zero slope using the Wald test with a t-distribution of the test statistic. In general, they are located on the right-hand side of the BIC of scores, meaning that positive magnitudes tend to be included more frequently in the linear regime. In fact, when plotting the AMOC response against the magnitudes, the anomaly departure from the linear regression line is smoother for the positive magnitudes compared to the negative ones (Fig. 3.12).

The break of linearity and symmetry is easily identified in the regressions as the horizontal extension increases. The larger the spatial extension, the less elements are considered within the linear regimes (the limit of the linear regime is shown by the vertical dashed lines in Fig. 3.12). For extensions larger than E200 the negative AMOCI anomaly generated by negative magnitudes decreases with respect to the symmetric positive magnitudes, and hence negative magnitudes start to be not considered within the linear regime. Already in E100 the departure of negative magnitudes from the linear response starts to be visible in Fig. 3.12 but it is not statistically significant to a 99% level. In the higher extensions, it is clear that negative magnitudes have an increased nonlinear response. It starts from the lower absolute values with a stronger change (strong break of linear response) and reaches a saturation point in the lowest magnitudes. The slope of this "saturation" regime, the regression coefficient for the lowest values, shows similar values with a 25% of change as the extension increases. Hence this saturation occurs in all the higher extension experiments in a similar way. For the positive magnitudes it occurs more

monotonically, the response tends to be reduced when the magnitude increases when compared to the linear predictions.

As mentioned earlier, these analyses were done with the average time of the first peak on each extension, 9 years. We repeated them at the maximal time of each magnitude for each extension and magnitudes. Differences in the magnitudes chosen within the linear regime were only found in the extensions E200, E500 and E700. 2-4 extra magnitudes are considered in the linear regime when the time considered is at year 9 for E200 and E700, with ranges between $[-11, 53]$ and $[-0.2, 11]$ when year 9 is considered against the obtained $[-8, 43]$ and $[-2.5, 8]$ when the maximal time is considered. For the E500, the analysis at 9 years instead increases the number of positive magnitudes considered, from $[-11, 11]$ in our analysis to $[-11, 17]$. These changes in the slope are about a 5% of the regression coefficient showed in Fig. 3.12 and support the idea that positive magnitudes have a more linear response than the negatives, what we find in our previous results.

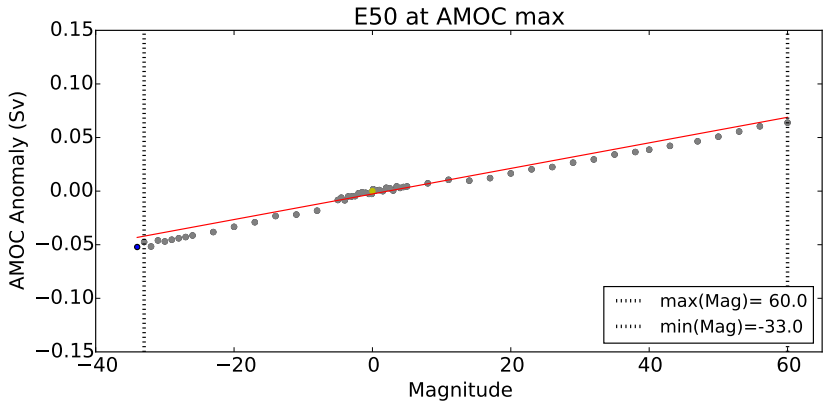

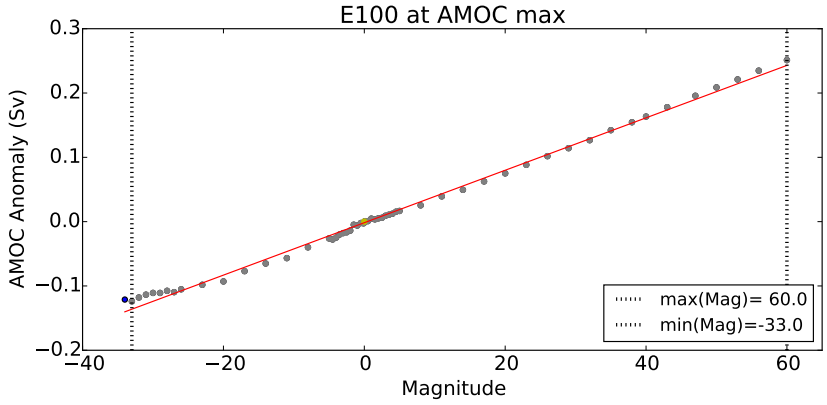

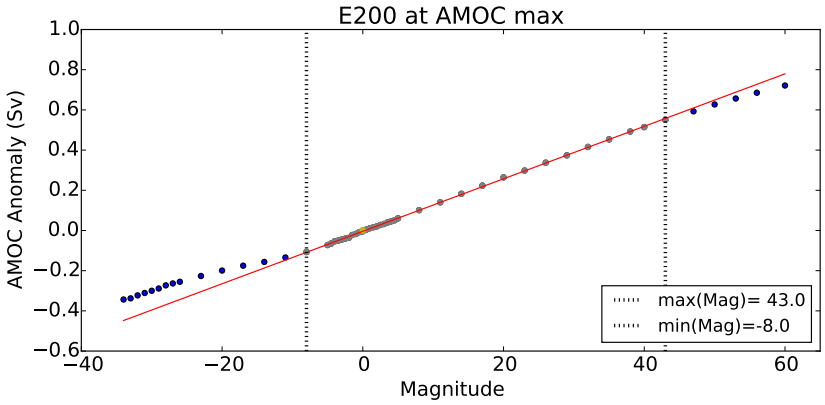
E200 at AMOC max
AMOC Anomaly (Sv)
Magnitude
max(Mag)= 43.0
min(Mag)=-8.0

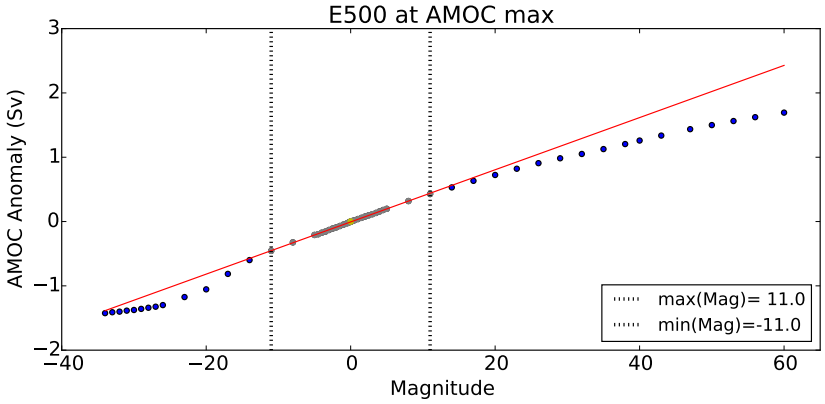
E500 at AMOC max
AMOC Anomaly (Sv)
Magnitude
max(Mag)= 11.0
min(Mag)=-11.0

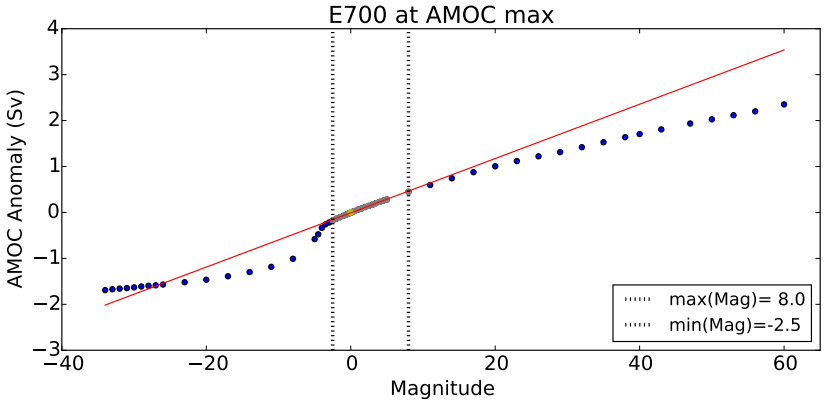
E700 at AMOC max
AMOC Anomaly (Sv)
Magnitude
max(Mag)= 8.0
min(Mag)=-2.5

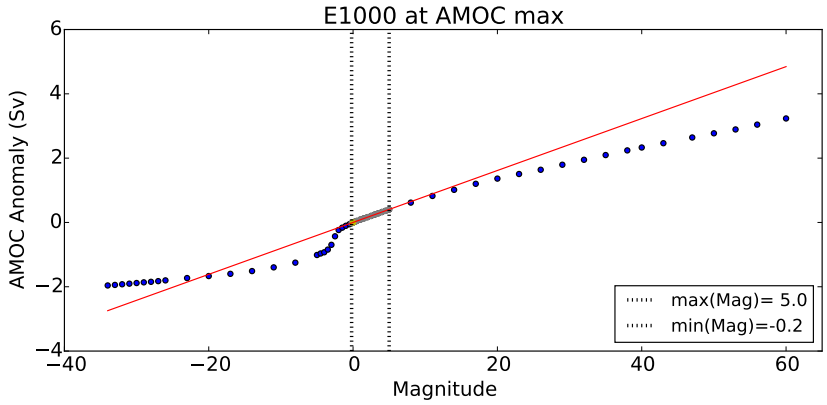

Figure 3.12: Linear regressions with minimum BIC scores for each of the horizontal extensions. Magnitudes are plotted against the AMOCI and the regression line obtained is shown in red. The vertical dotted lines shows the maxima and minima of the magnitudes considered to have a linear response, coloured in grey.

The coefficients of the linear regression, slope of the red lines in Fig. 3.12, vary between 0.001 and 0.08 Sv/psu. Sévellec et al. (2008) obtained a coefficient of 0.04 Sv/psu, value close to E500. In fact, when plotted against the extension, we find that the relationship is approximately linear (Fig. 3.13). The robustness of this relationship provides potential linear responses in the extensions with values between the ones explored in this study are used, i.e. E600.

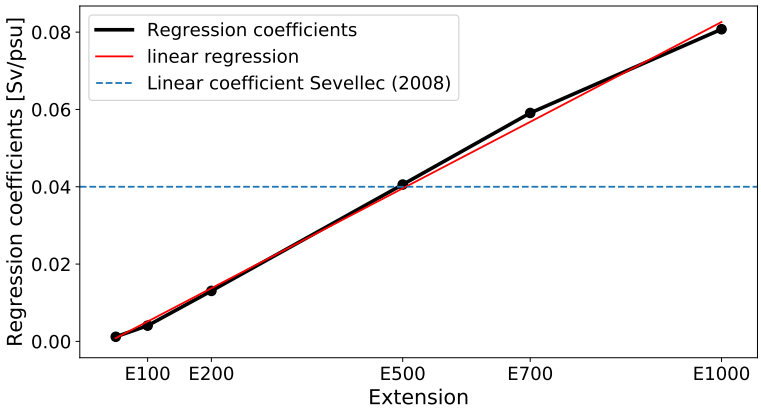

Figure 3.13: Black dots represent the coefficients of the linear regression for each of the extensions, joined by a black line. The red line shows the linear regression applied to these coefficients with an almost exact match with the black line. The horizontal dashed line indicates the linear coefficient of the AMOC response obtained by Sévellec et al. (2008)

3.4.3 Meridional coherence of the linear regression

After focusing on the linear regime defined by the algorithm in the AMOC maxima (AMOCI), I extended the previous analyses to the rest of the overturning stream function in the North Atlantic to assess the spatial dependence of the "linearity" on the response of the full stream function to the perturbations. This is shown in Fig. 3.14 with three panels: the first two representing the lower and upper boundary of the magnitudes within the linear regime for each latitude-depth gridpoint, and a third with the linear regression coefficient. The computation of the best BIC score and the associated regression parameters have been done in each grid point of the lat-depth plane. From the results, some grid point delivered a non significant regression and were discarded from the plotted data in Fig. 3.14 (grey dots above the bathymetry). The significance is considered compared to a null hypothesis of zero slope using the Wald test with a t-distribution of the test statistic over a 99%.

Lower extensions, E50 and E100, show a good coherence along the North Atlantic (Fig. 3.14 (a) and (b)). Almost all of the possible magnitudes are considered in the linear regime (indicated by dark colours), with the exception of the subpolar gyre area (brown-yellow colours). In this region, where deep convection occurs, the nonlinearities of the process reduce the number of magnitudes considered for the linear regime.

The subpolar region has the highest values of the regression coefficient and the lowest magnitudes considered in the linear regime.

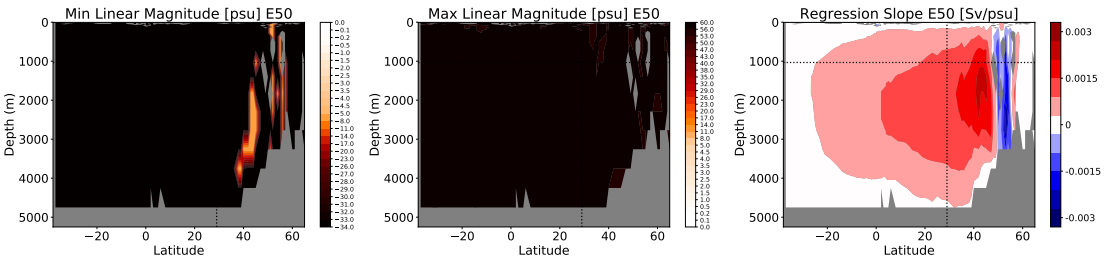

(a) E50

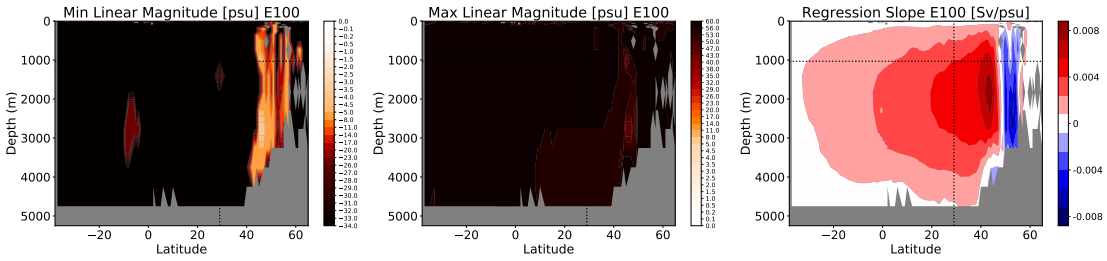

(b) E100

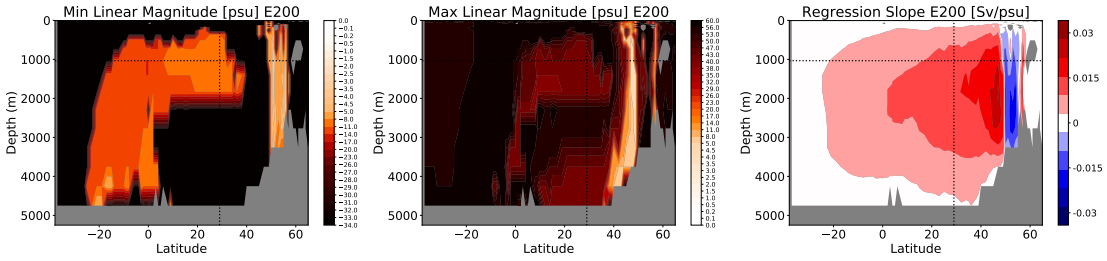

(c) E200

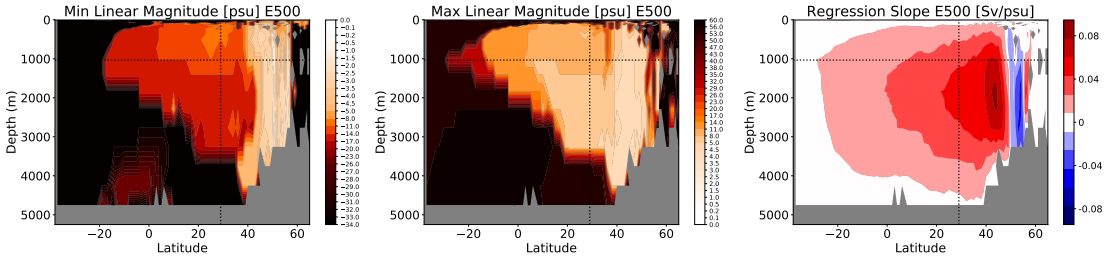

(d) E500

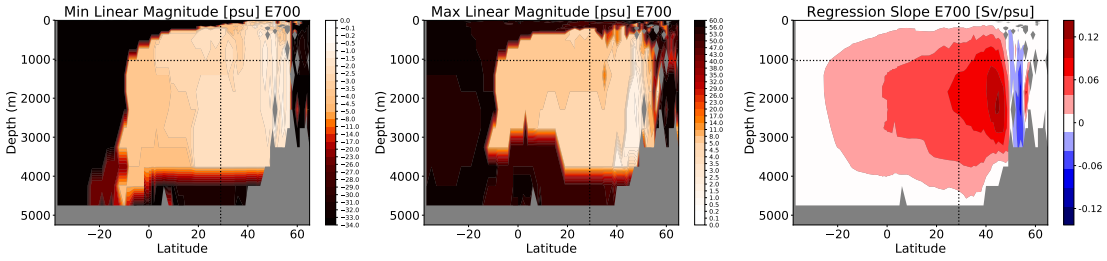

(e) E700

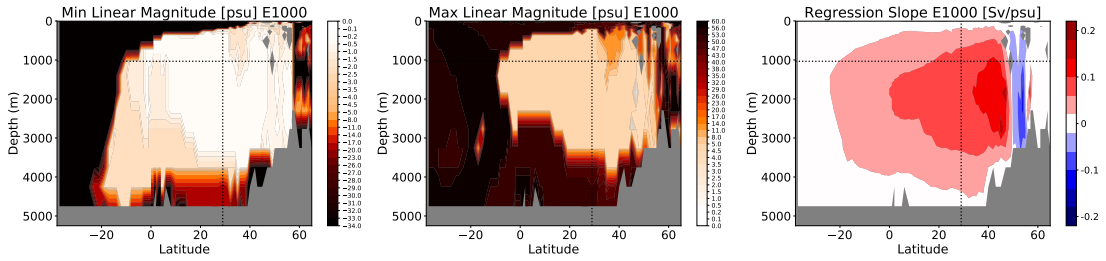

(f) E1000

Figure 3.14: Minimum Linear Magnitude, Maximum Linear Magnitude and Regression coefficient for the whole overturning at each grid point in latitude-depth space. For each panel and each extension, from left to right, it is plotted the first element considered for the linear regression, the last one and the linear regression coefficient. The maxima and minima color scales go from white for the lowest absolute value and black for the highest absolute value of the magnitude. The values have been additionally masked when the linear regression had a two-sided p-value larger than 0.05 for a hypothesis test whose null hypothesis is that the slope is zero. The location of the AMOCI is defined as the intersection between the two dashed lines.

The linear regression coefficients maintain the same structure with increasing extension. The coefficients reduce their value in concentric regions around the maximum reaching 20° N with a $40 - 50\%$ of the maximum slope value. The signal of the perturbations is still strong in the subtropical region, with highest values located in the subpolar. The defined AMOCI index is located at the 50% of maximal response in most of the experiments, meaning that the values obtained in Fig. 3.12 are of about half of the maximum value of the linear response, located in the southern SPG. The core with negative slope is always restricted to the northern part of the subpolar gyre and decreases its width as extension increases. This decrease is associated with the delay in the initial impact with increasing extension.

The spatial structure of the minimal and maximal linear magnitudes matches the structure of the regression coefficients, particularly in the larger spatial. The signal caused by the initial perturbation has maximum magnitudes that decrease as the regression coefficient increases, showing an increase in the nonlinear responses as we get closer to the subpolar gyre (yellow to white areas in Fig. 3.14). The black areas, including all magnitudes, in the magnitude plots that coincide with

almost no linear regression coefficient

3.5 Linear composites

After defining the linear regime, I computed a representation of the regime and described its physical characteristics. The use of composites is very frequent to identify the features of certain regimes such as higher/lower AMOC states (Yoshimori et al., 2010) or to identify features of well defined cycles (Martin et al., 2013). In this section I present the numerical implementation and later the description of the physics of the composite.

3.5.1 Composite computation

The definition of composite taken here is based on the idea that the AMOC composite field would have the same order of magnitude of the AMOC (Sv) normalized by the magnitude, m, used in the initial perturbation,

$$\text{COMPOSITE} \sim \frac{\text{AMOCanom}_M}{M}. \tag{3.4}$$

The composite can be mathematically represented as the operator "weighted average" applied to itself to equal the weighted average of the AMOC anomalies of the perturbations considered to be within the linear regime. The equation used to define it is:

$$\frac{COMPOSITE}{(\#\text{LM})} \sum_{m \in L} \frac{1}{|m|} = \frac{1}{(\#\text{LM})} \sum_{m \in \text{LM}} \frac{\text{AMOC anom}_m}{m}. \tag{3.5}$$

where COMPOSITE is our defined composite, in this case for the AMOC, LM is the set of chosen magnitudes to be considered in the linear regime and AMOC anom_m is the anomaly for each of the magnitudes considered in LM. By simplifying the equation we can define our composite as

$$\text{COMPOSITE} = \Big(\sum_{m \in \text{LM}} \frac{1}{|m|} \Big)^{-1} \sum_{m \in \text{LM}} \frac{\text{AMOC anom}_m}{m}. \tag{3.6}$$

The composites obtained for the AMOCI are shown in Fig. 3.15. All the composites show an oscillatory behaviour with positive peaks at years 10 and 30 and a negative one around 20. The first peak is the lowest in magnitude of the three, especially in the C_{E1000}. Most of the chosen experiments for the composite have lower magnitudes, these experiments have generally a lower response on the first peak generated by the initial perturbation than the following cycle.

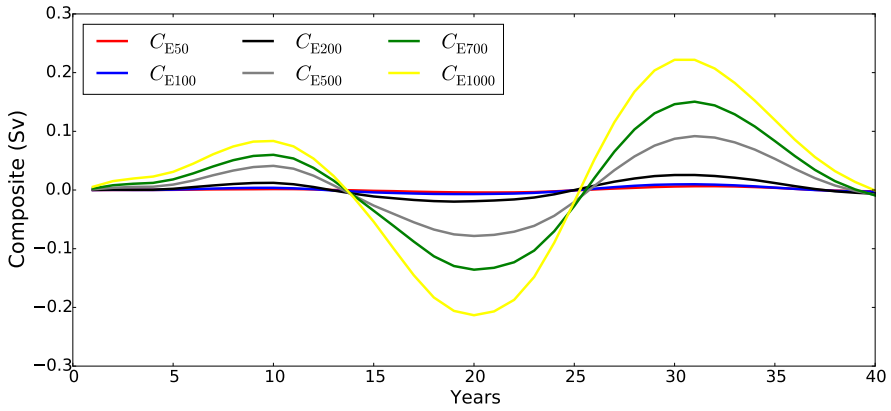

Figure 3.15: Panel showing the composite of the AMOCI obtained for each of the experiments normalized by the factor $\frac{1}{\#\text{LM}} \sum_{m \in \text{LM}} \frac{1}{|m|}$. These values should be comparable to the values for the AMOCI divided by the magnitude of each of the experiments, m.

Once the composite is defined, I compared it to the evolution of the AMOCI anomalies of the magnitudes considered within the linear regime (Fig. 3.16) The composite (red line), when weighted through the corresponding factor, is located in the cloud of anomalies of the magnitudes within the linear regime (grey lines). Some outliers, associated with very low magnitudes (0.01, 0.02 psu), are distinctively out of the conglomerate of anomalies due to the normalization factor imposed (m^{-1}) which for $m < 1$, it amplifies its value. This gives these lower magnitudes a higher weight in the composite giving more weight to the second and third peak.

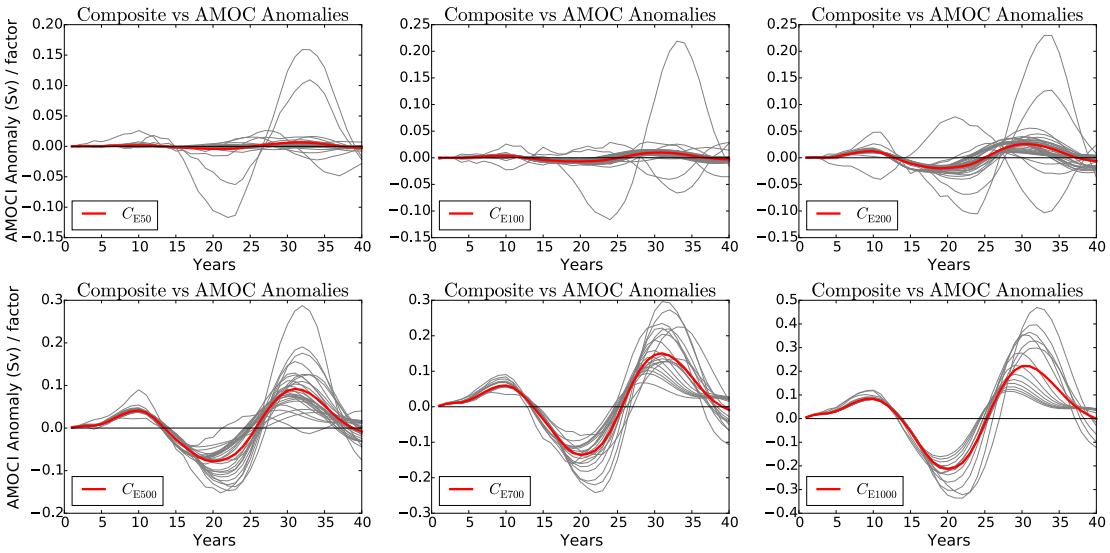

Figure 3.16: Cycle of the AMOC anomalies considered in the linear regime normalized by the multiplicative factor for each experiment (m) compared to the composite computed in red for each experiment normalized with the averaged multiplicative factor $\frac{1}{\#\mathrm{LM}} \sum_{m \in \mathrm{LM}} \frac{1}{|m|}$.

Other fields Using the same approach to compute the composite of the AMOCI index, I computed composites of the other fields (S, T, etc.). Firstly, to understand the physics behind the composite and then to be able to project the expected "linear regime" fields of temperature, salinity, etc. onto the magnitudes not defined as linear and, secondly to be able to analyze their differences.

For example, for the temperature anomalies we will define the composite of the temperature field as

$$\mathrm{T}_{\mathrm{COMPOSITE}} = \Big(\sum_{m \in \mathrm{LM}} \frac{1}{|m|} \Big)^{-1} \sum_{m \in \mathrm{LM}} \frac{\mathrm{T\ anom}_m}{m}. \tag{3.7}$$

where T is temperature, LM the set of experiments defined within the "linear regime".

3.5.2 Mechanism of the response of the linear composite

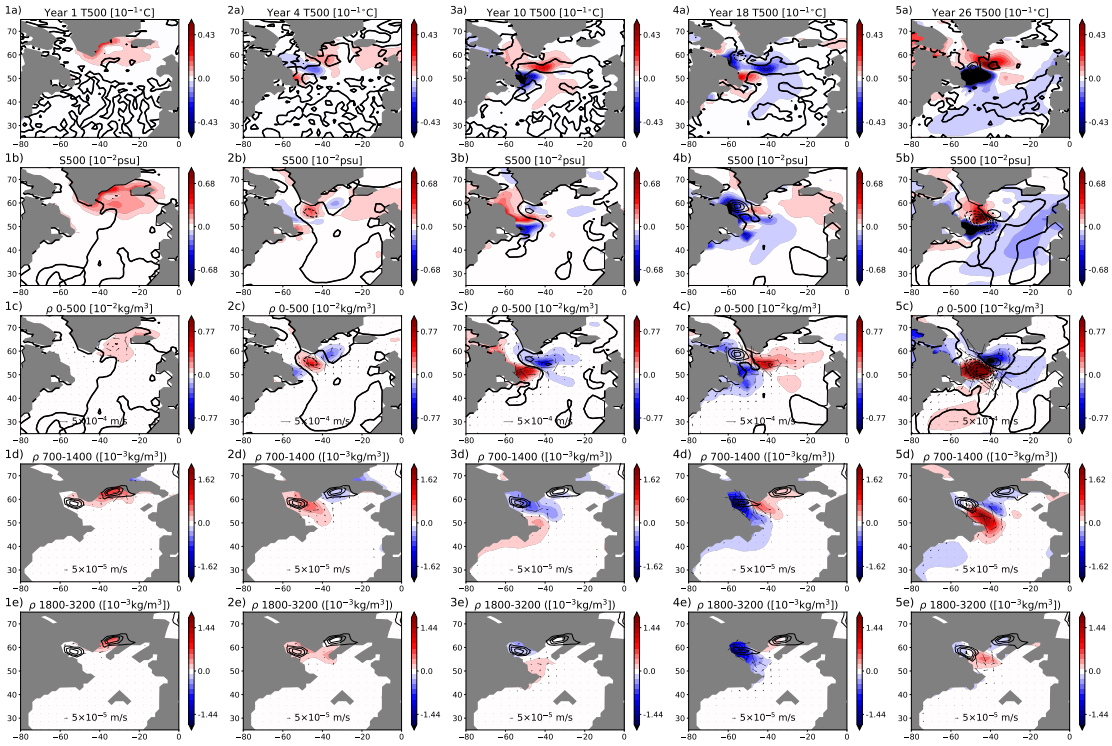

Figure 3.17: Snapshots of the North Atlantic after 1, 4, 9, 18 and 26 years for the composite of E500, C_{500}. a) upper 500 m temperature anomalies are shown with contours of the mixed layer depth with contours every 100 m and the bold line representing the zero anomaly. b) upper 500 m salinity anomalies are shown with a factor of 10^2 and contours of the barotropic stream function anomaly every 0.5 Sv with the bold line indicating the zero anomaly. c) Averaged density in the first 500 metres is shown by a factor of 10^2 and the same contours as the S500. As well anomalous velocities averaged in the 500 m are shown with arrows with a unit length of an arrow 5×10^{-4}m/s . e) Density anomalies averaged between 700 and 1400 metres. Anomalous velocities averaged in the 500 m are shown with arrows with a unit length of an arrow 5×10^{-5}m/s. Contours of the total mixed layer depth is shown with contours every 500 m. d) Density anomalies averaged between 1800 and 2300 metres, showing as before velocity at this depth and total mixed layer depth contours.

The mechanism of propagation is depicted in Fig. 3.17 with snapshots at year 1, 4, 9, 18 and 26. Once the perturbation is introduced, the positive salinity perturbation generates a positive density anomaly that reaches the deep ocean within the first year (1d) and 1e) in Fig. 3.17). The density anomaly, with the main core located in the Irminger Sea promotes deep-water formation at the convection site. If the extension of the perturbation is higher (for E> $E500$), the Labrador Sea convection site is additionally affected.

The local density anomaly, embedded in a mean meridional density gradient, triggers the geostrophic advection mechanism that propagates the anomaly (Fig. 3.17 1c). A cyclonic response for positive anomalies, brings denser water to their western flank and lighter waters to their eastern flank contributing to their western propagation. Similarly, a negative anomaly, associated to an anticyclonic circulation, will bring denser water to its eastern flank and lighter water to its western flank, contributing to a western propagation. In Fig. 3.17 c, the anomaly (red anomaly) has generated a negative anomaly on the eastern flank. This mechanism acts in simultaneously with the β-effect. As the anomaly is advected, changes in latitude contribute to variations in the coriolis parameter reinforcing the westward propagation of the anomaly. The density anomalies are tilted towards the north-west with the surface/subsurface leading the propagation, Fig. 3.18. This tilt is a sign of the propagation of unstable baroclinic Rossby waves since it promotes downgradient eddy heat fluxes and releases potential energy (Colin de Verdière and Huck, 1999).

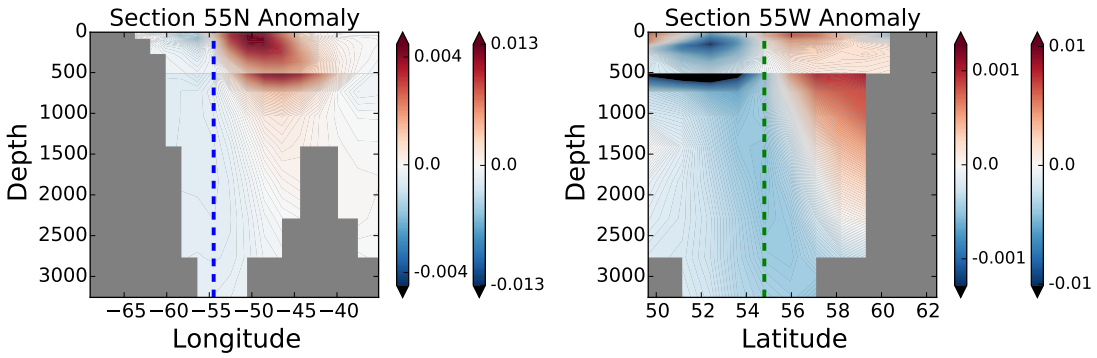

Figure 3.18: Figures showing a zonal section of the temperature anomaly at 55°N and a meridional section of temperature anomaly at 55°W at year 7 in the Labrador Sea region of the E500 composite, C_{500}. In each figure, colour scales of the anomalies on the first 500 m are represented with the colour-bars on the right and from the 500 m to the deep ocean with the left colour-bar. In both sections the surface of the wave propagates ahead of the subsurface and bottom of the wave. As the wave propagates south-west, the surface leads the wave with a tilt, signature of unstable baroclinic Rossby waves (Sévellec and Fedorov, 2013b).

The anomalies modify mainly the convection area in the Labrador Sea as they propagate. The first peak in the upper ocean density in the Labrador sea (orange dotted line in Fig. 3.19) is contributed equally by temperature and salinity,

this anomalous density modifies the stratification decreasing the difference density between the upper and lower ocean and decrease the convection in the region (green line in Fig. 3.19).In the deep ocean, the anomaly propagates on delay with respect the upper ocean, i.e. differences between Fig.3.17 2d and 2e.

After the initial peak, year 10, the positive anomaly fades away in the coast of Newfoundland. At the same time, in the deep ocean the positive density anomalies propagates through the deep western boundary (Fig. 3.17 3c). The strongest signal observed is from the anomaly of the opposite sign (blue respectively in Fig. 3.17 3c). The incoming anomaly, negative, leads the change in the upper ocean in the Labrador Sea decreasing convection in the region and the subsequent decrease in the AMOC few years after (Fig.3.19).

By year 25 the upper 500 m density is in the opposite phase as in Year 18, showing that the propagation of the waves continues. These waves modify the density in the western SPG modifying convection and the AMOC accordingly to the sign of the density anomaly. The anomalies are propagated between 700-1400m 4d-5d.

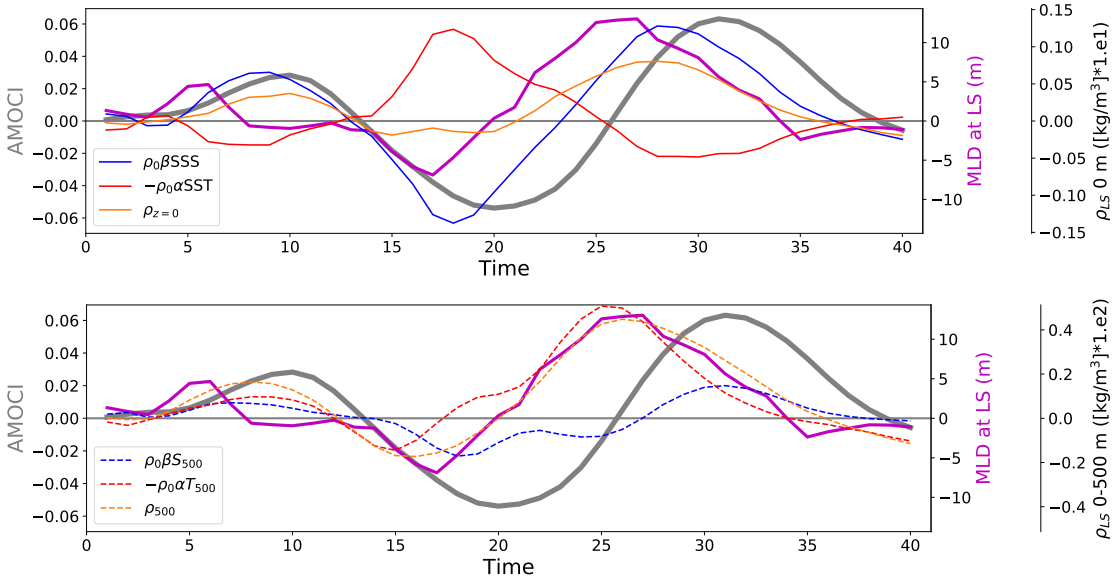

Figure 3.19: Evolution of different indices of the composite of E500, C_{500}. Showing the AMOCI (grey), the overturning at 30°N and 1000 m depth. Mixed layer depth in the Labrador Sea (magenta) and averaged values in the Labrador Sea area. Contribution of salinity (SSS) and temperature (SST) to density and surface density on top figure (solid blue, red and orange respectively). Density and salinity/temperature contribution averaged on the first 500 metres on bottom figure (dotted orange and red/blue respectively). Factors of 10 and 10^2 are applied for surface and upper ocean density values.

3.6 Differences with the nonlinear regimes

The final step of this study is to understand the factors and elements that characterize the linear and nonlinear regimes defined through the AMOCI response. As mentioned earlier, the impact of nonlinearities increase with the magnitude and extension. The early departure from linearity in the negative magnitudes was already mentioned in Fig. 3.12. From extension E500 to larger extensions, the negative magnitudes experience a saturation of the response. This saturation is evident when we look at the impact of the perturbation in the mixed layer depth.

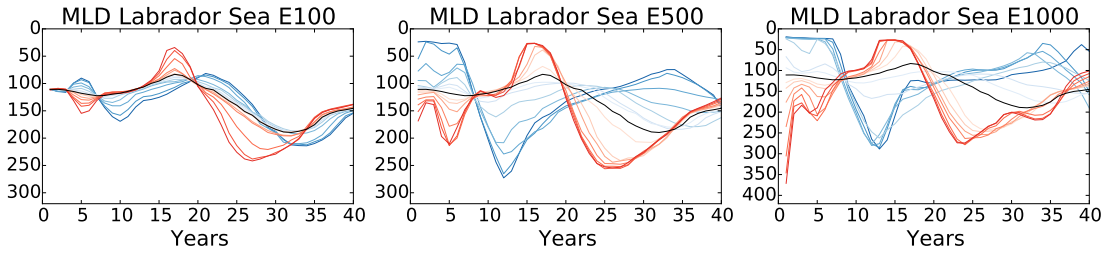

Figure 3.20: Evolution of the yearly averaged mixed layer depth in the Labrador Sea for three perturbation length scales: E100, E500 and E1000. Black denotes the unperturbed case, red positive salinity perturbations and blue negative magnitudes. The increase in the color intensity relates to the increase of the magnitude imposed. Magnitude imposed were $\pm 1, 2, 4, 8, 14, 20, 29$.

The Mixed Layer Depth (MLD) is defined in the model based on a density criterion: potential density exceeding the 10-m value by 0.03 kg m^{-3}. The model has three locations of deep convection in the North Atlantic: Greenland Sea (South of Svalbard), Irminger Sea and Labrador Sea. The impact of the perturbations is mainly focused on the Labrador Sea, but have an effect on the other deep convection sites as the extension increases. The evolution of the MLD in Fig. 3.20 shows in blue the saturation of the impact of freshwater perturbations as the perturbation increase its intensity. With positive magnitudes, the impact on the MLD increases proportionally to the magnitude of the imposed perturbation. Whereas for negative perturbations the MLD is quickly reduced to zero, or very low annual mean values, after the perturbation generating a limit in the possible impact on the AMOC.

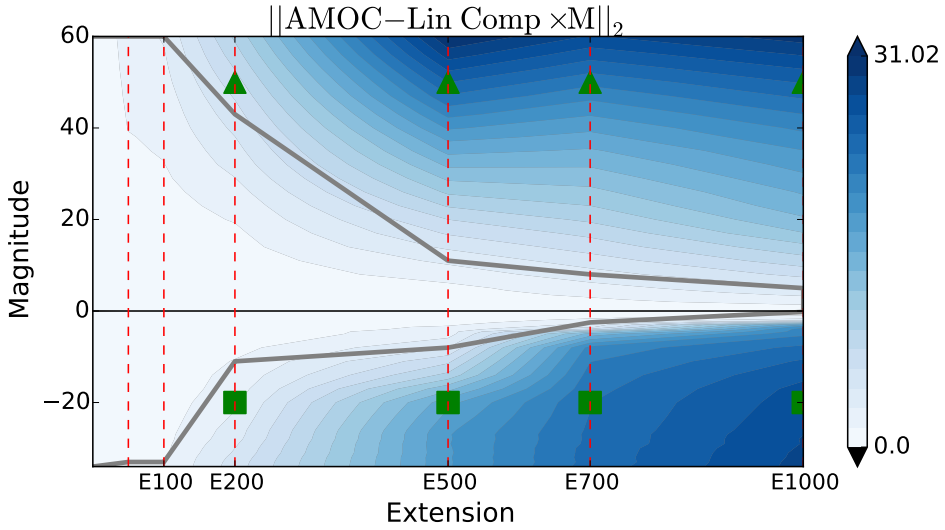

Figure 3.21: Quadratic norms of the error for the projected linear composite measured for each extension and magnitude. The dashed vertical lines indicate the different extensions considered for this study (from E50 to E1000), the grey line indicates the limit between the defined linear regime (associated with lower magnitudes) and the nonlinear regime. Green squares and green triangles denote the examples chosen to illustrate the structure of the errors shown in Fig. 3.22

The definition of a linear regime allows us to compute the differences between the AMOC evolution and the projected linear composite of the AMOC. If we focus on the differences in the first peak, the linear composite predicts larger anomalies compared to the actual nonlinear response (Fig. 3.12). In order to quantify the error produced, a quadratic score of this error at the first peak is shown in Fig. 3.21 for all the magnitudes and extensions. The error increase seems to have a different nature for positive and negative magnitudes. For positive magnitudes the increase is related more predominantly with an increase in the magnitude value, whereas for negative magnitudes it is more related to the increase in extension. The response of positive magnitudes is on average between 60 to 150 % larger with respect to the symmetric negative magnitude. These higher values of error in the symmetric magnitudes represents the missing information of the linear regime to describe the negative magnitudes, as the antisymmetric response of the system to salinity and freshwater errors.

In order to locate the processes or main differences between the linear regime and the individual experiments I performed an Empirical Orthogonal Function

(EOF) analysis on the differences between each experiment and the linear composite projected onto each experiment by multiplying it by the magnitude. I chose experiments of E500, E700 and E1000 with positive magnitudes of 50 psu and −20 psu (green triangle and square in Fig. 3.21). The first EOF, EOF1, shows a large-scale pattern of increase/decrease in the whole Atlantic basin. In general, in all the experiments it accounts for $70-80$ % of the total variability of the error. The Linear composite overestimates the response in the nonlinear magnitudes mainly in a large-scale pattern that increases proportionally to the extension.

The second EOF, EOF2, accounts for a 10-20% of the variability in all of the experiments. This EOF and the remainder of the EOFs generate the responses located mainly in the SPG. EOF2 corresponds to an anomaly affecting the SPG with the corresponding deep-water formation and the previous anomaly of the opposite sign still affecting the STG. Finally, the rest of the EOFs from the 3$^{\text{rd}}$ until the 20$^{\text{th}}$ (last row in Fig. 3.22) show the main errors located in the SPG. The EOF decomposition shown is very consistent in all the ranges of extensions and magnitudes confirming the homogeneity of the nonlinear impact of the perturbations.

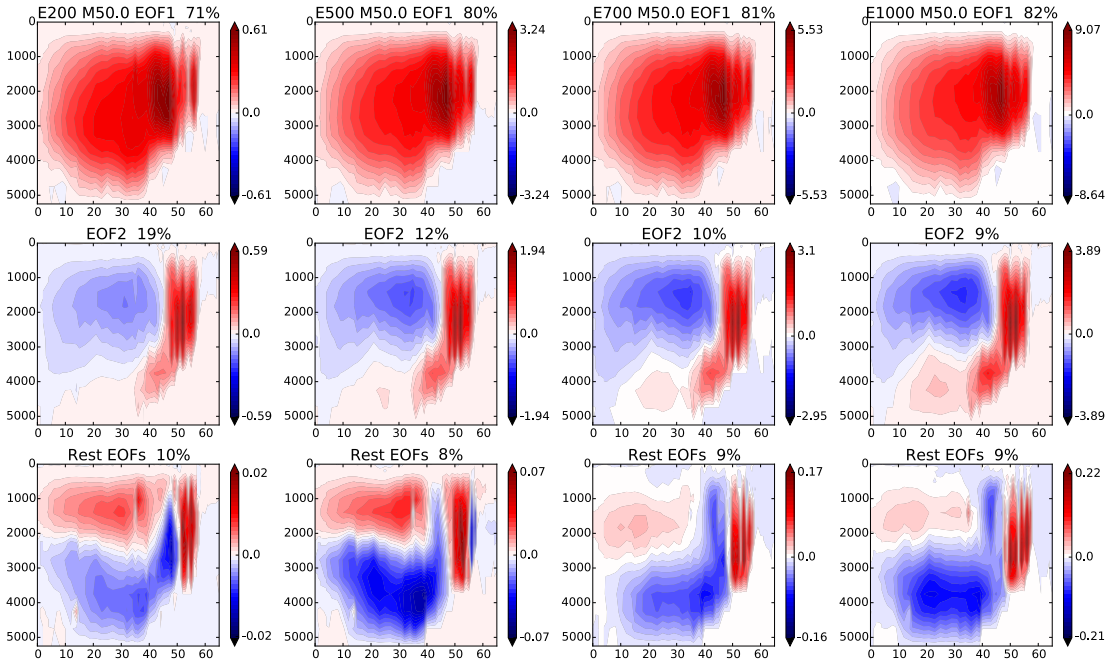

(a) Positive magnitude 50

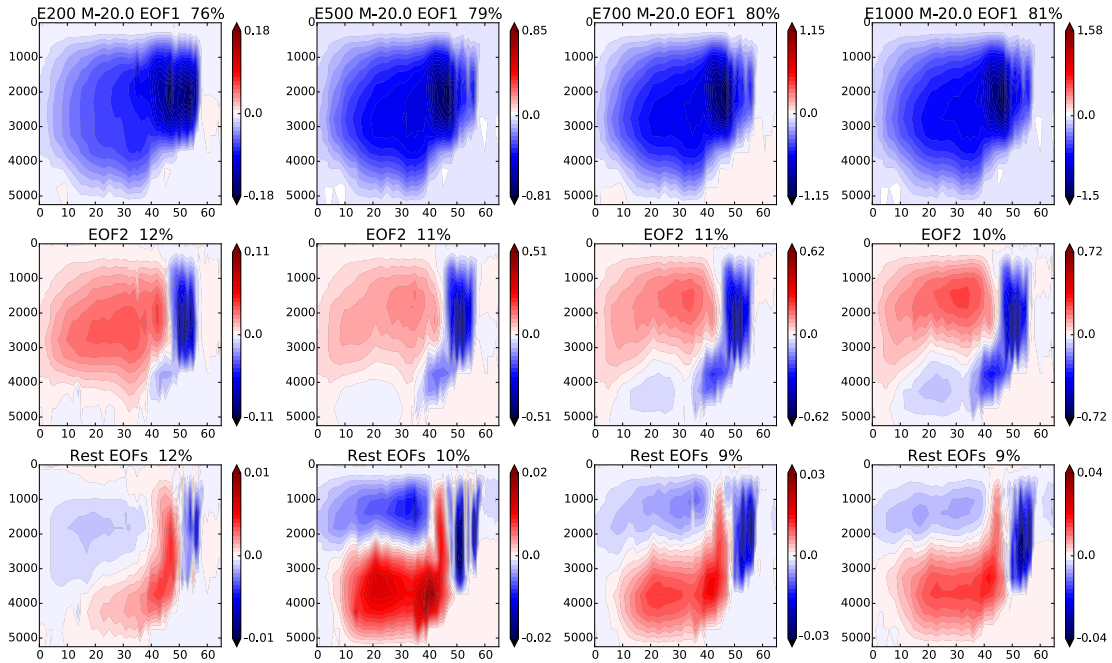

(b) Negative magnitude -20

Figure 3.22: EOF decomposition of the difference between nonlinear responses with magnitude 50 (a) and -20 (b) and the linear predictions. For each figure, the first two rows represent the two first EOFs for the different extensions on each column. The percentage of each EOF is shown as well. The third row represent a mean of the rest of the EOFs and the percentage of the variability explained jointly by the residual EOFs

3.7 Discussion

The decadal predictability problem can be both described as an initial and boundary value problem (Hawkins and Sutton, 2009b). Hence obtaining skilful decadal predictions remains a challenging task requiring both improvements in the initial climate state and in the processes resolved by climate models. In general, the relative importance of the initial conditions in climate predictions decreases as the forecast time increases. The impact of initial conditions can vary with respect to the system observed, local versus global climate or even with respect to the metric under study i.e. AMOC, OHC, etc. This chapter focuses on the impacts of surface salinity anomalies in the initial conditions for the North Atlantic predictability, particularly in the AMOC.

I perturbed the initial salinity field with a 2-dimensional Gaussian perturbation located in the Irminger Sea that generates a peak of the AMOC anomaly around 8-10 years, with variations on the extension and magnitude. Both variables used to define the perturbations, horizontal extension and magnitude, have an impact on the anomaly obtained. As early modelling studies suggested, the surface freshening increases the buoyancy, stabilizing the upper ocean layers and weakening the rate of deep convection which would slow-down the AMOC (Stommel, 1961; Rahmstorf, 1996). Although the sign of the AMOC response agrees, the spread of the AMOC sensitivity to freshwater forcing varies (Yu et al., 2016). Here the variations of the horizontal extension give in fact large differences in the anomalies on the first peak, i.e. for positive anomaly perturbations from ± 0.05 Sv up to 3 and -2 Sv for different sign anomalies. Not only were obtained differences in the value of the anomaly for each magnitude sign but the time scales associated with the peak are shorter for freshwater perturbations than for positive salinity perturbations. To test the consistency of these results, different configurations of the experimental set-up confirm firstly the choice of this location as the most sensitive for the AMOC, consistent with the location of the LOPs computed in Sévellec and Fedorov (2015). Secondly, the results show that changing the perturbation times to other seasons would not impact the perturbation impact.

To put our results in the context of previous linear approaches, I defined statistically a linear regime. For each horizontal extension, the regimes have been considered linear if the anomaly of the AMOC index is proportional to the magnitude considered. The increase in the horizontal extension induces a change in the linear response, intensifying from a factor of 0.001 to 0.08 Sv psu^{-1}. The regression coefficients follow an almost linear relationship, with a positive factor of 8.60×10^{-05} Sv (psu km)$^{-1}$ relating them. This linear evolution of the regression coefficients can be used to estimate the linear responses for the intermediate extensions not considered in this study. The response obtained in Sévellec et al. (2008) is close to the linear response of E500. The linear regime predicts larger values for both negative and positive magnitudes compared to the nonlinear response. Also, an asymmetric response between positive and negative magnitudes is obtained. Negative magnitudes differ from the linear prediction in with lower

ranges of magnitudes, being more susceptible to nonlinear responses.

The response to the initial perturbations consistently impacts the whole Atlantic basin preserving to a good extent the "linear" definition by using the AMOCI. With the exception of the subpolar gyre which has a higher nonlinear response possibly due to convection occurring in the region. The cyclic response of the anomalies generated by the perturbations is similar to that obtained in Czeschel et al. (2010) by perturbing the heat fluxes in the subpolar gyre. Although these perturbations are salinity anomalies, the variations in density are mainly driven by temperature, as $|\alpha T'| > |\beta S'|$, hence obtaining a similar response.

A linear composite for each extension gives understanding on the impacts of nonlinearities. The differences between the projected composite onto the nonlinear response was measured firstly by a quadratic metric at year 9. This norm of the error differentiates positive and negative magnitudes: for positive magnitudes is more related to the increase of the magnitude value whereas for negative magnitude is linked to the increase in extension. A spatial study of these differences, through EOF decomposition, has shown consistency amongst the different magnitudes and extensions supporting the results obtained here.

These experiments were performed under fixed boundary conditions, in which we imposed a fixed heat freshwater fluxes computed as averaged fluxes under restoring boundary conditions to a climatology. With this configuration, we allow surface anomalies to evolve independently from any interaction with the atmosphere. In Fig.3.19 we can see that there is a surface temperature signal associated with the perturbation. In a more realistic set-up, i.e. coupled with the atmosphere, this temperature signal would be evolved differently from the experiments here presented. For example, in the case of imposing a positive salinity perturbation, such as in our composite, the associated positive temperature anomaly would be damped. The surface cooling would increase the density in the surface, and, through the mixed layer depth, of the anomaly at depth. Repeating a set of this experiments in a coupled model would probably test the differences and similarities of our response to a more realistic one.

One of the aims of this work is to relate the perturbations with possible impacts

of salinity anomalies in the Northern Atlantic such as the GSAs. Although the generation and propagation of the anomalies have been studied in depth (Dickson et al., 1988; Belkin et al., 1998), the implications or possible mechanisms by which they may have impacted the AMOC has not been fully explored previously. Considering our perturbations similar to a GSA, we conclude that the impact of the anomalies in the surface salinity in this model affects not only the surface but also the deep ocean. Hence, GSA-like anomalies in this model would not remain as upper ocean salinity anomalies advected around the SPG but could be potentially part of an active mechanism of North Atlantic variability. GSA observations attributed about a -0.5 psu over the first 250 m for the GSA in the Labrador Sea (Belkin et al., 1998), by taking the salinity anomaly observed into the assumption of a 10-meter salinity anomaly it would give a -12.5 psu anomaly. Computing the total salinity introduced by such perturbation homogenized by the Gaussian distribution we can attribute the impact of the GSA to AMOC changes (Fig. 3.23), obtaining a change of around 1-2 Sv for the largest perturbations (E500, E700 and E1000).

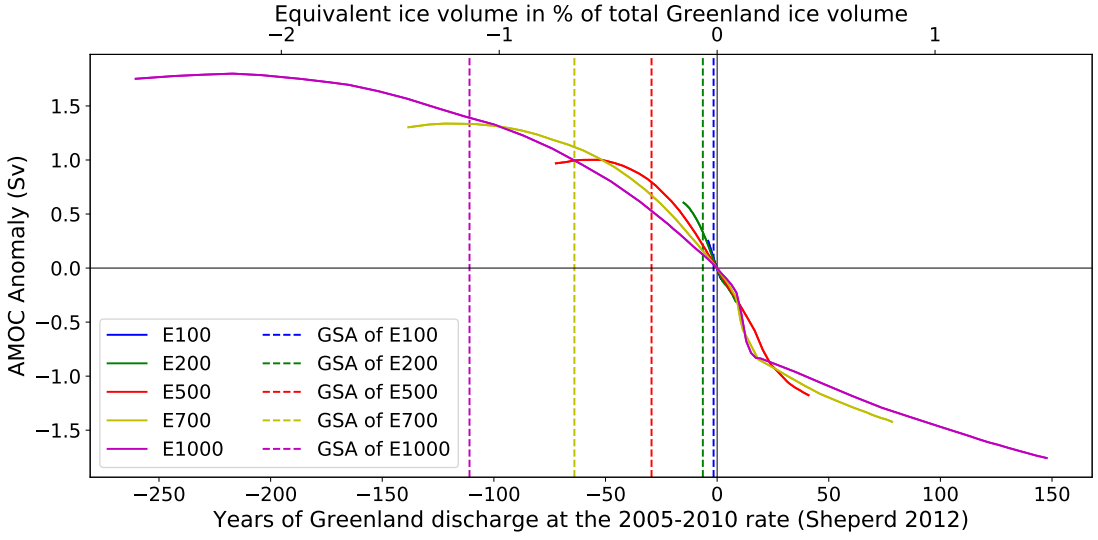

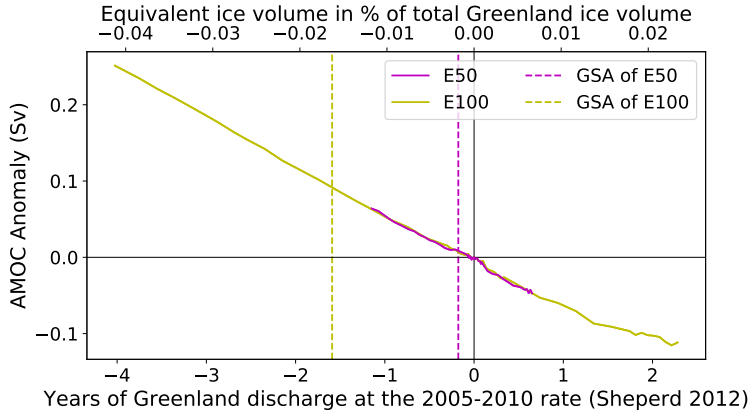

Figure 3.23: Top: Plot showing the relationship between the potential impact on the AMOC against the equivalent years of Greenland discharge to the salinity anomaly of the perturbations introduced and against equivalent ice volume of the salinity anomaly of the perturbations introduced measured as % of the total Greenland ice volume. Continuous lines shows the number of years for each of the perturbations/% of total ice volume for each of the perturbations. Vertical dashed lines represent the hypothetical years of discharge for the GSAs with the extensions considered in this study. This has been computed by considering the salinity anomaly observed, -0.5 psu over the first 250 m in the Labrador Sea (Belkin et al., 1998), to have the extension of each experiment and to be located only in the first 10 m. We obtained a -12.5 psu anomaly, computing the equivalent impact of such anomaly. Bottom: same as top but zoomed for the lower extensions.

Initializations based on estimates of the observed climate state have demonstrated an improvement in the prediction skills (Meehl et al., 2009; Germe et al., 2017). The results presented here show potential impacts of the incorrect initialization of the salinity field in decadal predictability studies. Although LOPs provide an upper boundary for perturbations in the linear framework, in this work I showed that nonlinearities play an important role as the extension or the sign of the perturbation changes. Nonlinear Optimal perturbations are not fully developed in state-of-the-art ocean models. The best approximations to-date are the Conditional Nonlinear Optimal perturbations (Mu et al., 2004) which restrict the amplitude of the perturbation imposed. This limitation can be a key factor in a non linear framework as the impact of the magnitude is relevant to distinguish linear and nonlinear response for certain extensions and perturbation sign.

Finally, this study gives insights on the possible impacts of the SSS uncertainties in data used in reanalyses and historical reconstructions. The Atlantic has been

historically better sampled than other basins but not on a large-scale pattern, until recently (Friedman et al., 2017). The results here presented could be used to reduce the divergence between models and observations in reanalyses and reconstructions. Performing surface perturbations, within the limits of the observational record, in data assimilation approaches could represent a possible method to approximate the model evolution towards the observed state.

3.8 Key Results of this chapter

- The maximal initial impact of sea surface salinity perturbations, which is located in the Irminger sea, occurs about 8-10 years depending on magnitude and extension of the perturbation.
- The response is asymmetric with respect to the sign of the perturbation, with a larger impact of the negative magnitudes.
- The differences between the linear and nonlinear responses have a similar spatial description but the key factor contributing for these differences are the increase in extension for negative perturbations and the increase in magnitude for positive perturbations.
- Depending the extension of the GSA, the impact on the AMOC would be either almost none (less than 0.3 Sv) or between 1-2 psu.

Chapter 4

AMO and AMOC variability influenced by "Thermal" Rossby waves

After exploring the impacts of initialization errors in the North Atlantic, the following chapters focus on mechanisms of variability in the Atlantic. The uncertainty of the boundary conditions of the climate system, the second kind of predictability problem, makes it necessary to understand possible mechanisms that could arise under different forcings. GCMs provide a valuable tool to improve the understanding of the different mechanisms behind variability of the climate system from decadal to centennial time scales. Simplifications and parametrizations have to be taken to achieve feasible computational times. Assuming a perfect model framework, the evolution of the attractor of the system would reproduce the behaviour of the climate attractor. But unfortunately, the uncertainty and errors result in a system that resembles reality but may evolve through a different trajectory.

This chapter concentrates on the variability simulated by Océan PArallélisé (OPA) in the North Atlantic. In particular, the aim of this chapter is to describe a mechanism of variability that contributes to the understanding of the multidecadal variability associated with the Atlantic Multidecadal Oscillation (AMO)-Atlantic Meridional Overturning Circulation (AMOC) and their relationship.

4.1 Introduction

The AMO, estimated from the Sea Surface Temperature (SST) records, is computed as the detrended multidecadal SST anomaly averaged over the entire North Atlantic (Trenberth and Shea, 2006). In the observational record, over the past 150 year approx., this index has fluctuated between positive and negative phases with a period of 30-35 years. The pattern obtained when the SST is regressed to such index has a typical shape of a horseshoe, with warm anomalies in the western SPG and from the west coast of Africa to the eastern coast of the equatorial America (pattern shown in Fig 1.5 in Chapter 1). Numerous impacts have been associated with North Atlantic SST variability, to name a few: Indian-Sahel rainfall (Zhang and Delworth, 2006), hurricanes in the Atlantic (Zhang and Delworth, 2006; Wang et al., 2012) and seasonal climate over Europe and North America (Sutton and Hodson, 2005b; Sutton and Dong, 2012; Chylek et al., 2014).

Several studies have linked changes in the AMO to changes in ocean circulation. Not directly, but with the use of dynamical variables such as the difference between gyre circulations (McCarthy et al., 2015) and Labrador Sea density (Robson et al., 2014), a link to oceanic physical variables have been observed to lead changes in the AMV phase since 1950. Changes in the AMO are not only driven by oceanic variability since the atmospheric variability, in particular the NAO, has been observed to have persisting phases leading AMO changes (McCarthy et al., 2015; Gastineau and Frankignoul, 2015). These links have also been obtained in several configurations of GCMs (Zhang and Delworth, 2006; Knight et al., 2006; Gastineau and Frankignoul, 2012; Ruprich-Robert et al., 2017).

In general variability of the AMO is associated with the combined influence of the NAO and oceanic response. A persistent NAO positive phase in winter favours a maximum heat loss in the Labrador Sea. The regulation of deep-water formation through the NAO forcing induces a response in the both thermohaline and wind-driven circulation. This mechanism gives as well a feedback to the atmosphere via an increase in northward heat transport. This plausible mechanism has the potential to link both ocean and atmosphere as drivers of changes in the SST.

Recent studies have questioned the previous mechanism and the role of ocean dynamics in the variability of Atlantic SST (Clement et al., 2015; Srivastava and DelSole, 2017). The impact of both, ocean dynamics and atmosphere, is still an ongoing debate.

This chapter focuses, on the role of ocean dynamics contributing to variability of the surface temperatures. In particular with a focus on the relationship to the AMOC. Variability of the AMOC is a key driver of the North Atlantic climate system. Different time scales and mechanisms have been invoked to contribute to AMOC variability. From shorter time scales such as the decrease of around 30% of the AMOC in the winter of 2009 (Bryden et al., 2014) to millennial variability (Sévellec and Fedorov, 2014). In the review of Buckley and Marshall (2016), the authors group low-frequency variability in two groups: those relating to deep convection changes and those relating to baroclinic Rossby waves.

Although the AMO is thought to be a representative of AMOC variations (Knight et al., 2005; Zhang, 2008), the large diversity of AMOC variability mechanisms in models make difficult to define a direct link in different models. In Greenland ice cores, SST proxies show a dominant period of about 20 years together with a longer timescale component of 45-65 years (Chylek et al., 2012). These time scales have been supported by observations and model studies on Sea Level Height (SLH) (Frankcombe and Dijkstra, 2009). Understanding the mechanisms of AMOC variability lead to a better understanding of how to observe and predict current and future states of the AMOC and its relationship with the AMO.

Further work based on theoretical approaches and simulations using General Circulation Models (GCMs) have supported the idea of westward density anomaly propagation as one of the potential mechanisms contributing to AMOC variability (Huck et al., 1999; Colin de Verdière and Huck, 1999; te Raa and Dijkstra, 2002; Sévellec and Fedorov, 2013b; Sévellec and Huck, 2015). The mode has been associated with large-scale Rossby waves that propagate westward in the presence of a meridional temperature gradient. Density variance budget analysis has provided further support for the role of baroclinic instabilities in the propagation of these anomalies (te Raa and Dijkstra, 2002; Arzel et al., 2006).

The association of variations in the AMOC and the AMO have been rigorously demonstrated in Sévellec and Fedorov (2013b) and extended further by Sévellec and Huck (2015). Based on linear stability analysis, the authors obtained a weakly damped oscillatory mode of the system based on the propagation of large-scale Rossby waves propagating in a mean zonal flow and meridional temperature gradient. The sequence of propagation links the AMOC evolution and surface warming in the North Atlantic (AMO). The mechanism consists of oscillations of AMOC and AMO, with the AMOC oscillations leading by a quarter of the oscillation period. Buckley et al. (2012) also obtained an oscillatory response generated by westward propagation of density anomalies in a coupled model with idealized geometry. Instead of proposing a tight link between the AMOC and the density propagation, the authors suggest the passive response of the AMOC to the Rossby wave propagation through the thermal wind relation. They also suggest that the Rossby waves have no role in modifying the SST and upper ocean heat content in the northern regions.

More recent work by Muir and Fedorov (2017) looked at the presence of the mode described by Sévellec and Huck (2015) in the models involved in the Coupled Model Inter-Comparison Project 5 (CMIP5). Over the 25 models, more than half showed indications of: significant spectral peaks in the bands between 15 and 35 years, westward propagation of density anomalies in the subpolar region, with the same phases of oscillation as described in Sévellec and Fedorov (2013b) and the lead role of temperature in the anomaly propagation. The recurrence of the mechanism in the different models endorse the westward propagation of density anomalies as a likely candidate to link the AMOC and the AMO/AMV. The importance of understanding this relationship on decadal timescales rests on being able to associate a well evaluated component of the climate system, the SST, with a less measured component of the North Atlantic, the AMOC.

4.2 Simulated AMOC variability

This configuration has been already explained in detail in subsection 2.3.1. The spin-up took the model 2000 years to run under Mixed Boundary Conditions

(MBC). The evolution after the spin-up, Fig. 4.1, is characterized by an oscillation with a mean period of 42 years. We consider a period of 2000 years for the analysis using annual means of the output fields.

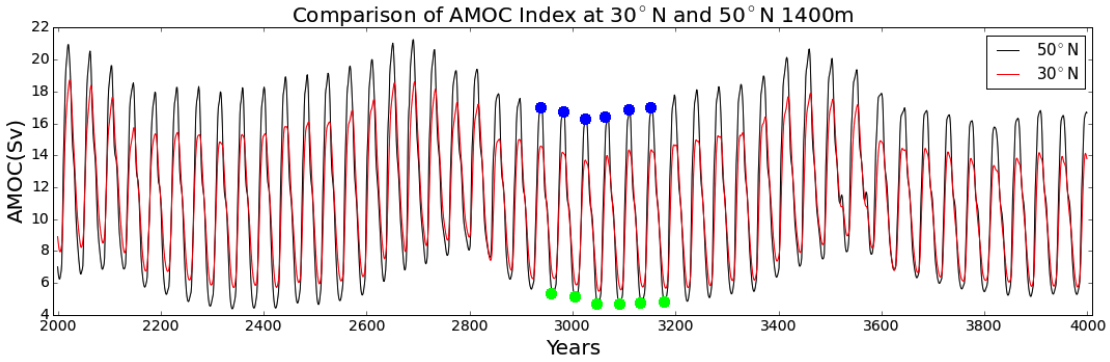

Figure 4.1: Evolution of the AMOC stream function at 30°N in red and 50°N in black, both indices are taken at 1000m depth, where the maximum of the stream function occurs the most. The spin-up period consists of the first 2000 years after the change of boundary conditions at year 0. In the stable period (shown) we can characterize two modes of variability: one with a 42-year period with variations of 10 and 15 Sv for 30°N and 50°N respectively. The longer modulation of the cycle has a period of around 700 years and variations of around 3 Sv. Blue and green dots indicate the peaks chosen to compute the composite of the maximum and minimum of the oscillation in Fig. 4.2

4.3 Detection of driving mechanisms and time scales

I characterized the structure of the high AMOC state, a low state, and their difference in Fig. 4.1. I obtained the two composites with an average of 6 high peaks and 6 low peaks (blue and green dots respectively). The high AMOC peaks, top panel of Fig. 4.2, have higher overturning values in the North Atlantic reaching below 3000 metres in the northern hemisphere. The Antarctic Bottom Water (AABW) cell is reduced very drastically when compared to the mean state of the model in Fig.2.7 in Chapter 2. Lower peaks show a shallower overturning in the North Atlantic, above 2500 m depth in the whole basin, allowing AABW to enter the North Atlantic at a shallower depth (middle panel). Also, the surface signature in the subpolar region suggests a weaker northward mass transport over the upper 500 meters. The differences with the lower peaks are located mainly in the subpolar

region, where deep convection occurs in the North Atlantic (40°N-60°N, bottom panel).

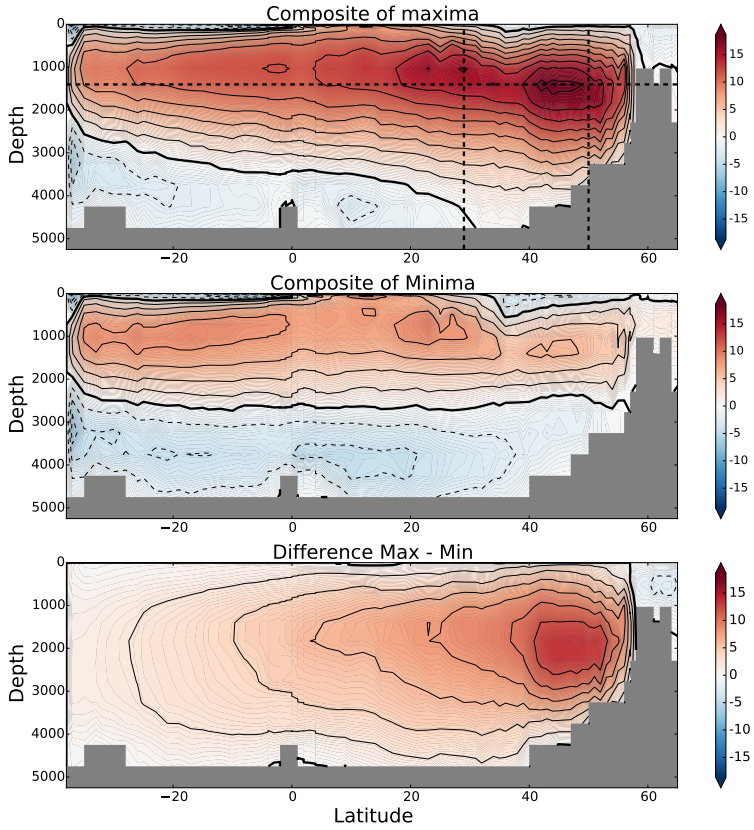

Figure 4.2: Schematic of the composite of the stream function of the maximum peaks (top), minimum peaks (middle) and difference (bottom). In the top figure, intersection of the dashed lines denotes the point where the indices of Fig. 4.1. The figures show contours each 2 Sv. Solid, bold and dashed lines indicate respectively positive, zero and negative values of the stream function. Main differences located in the subpolar gyre depicted by an intensified positive stream function over the whole basis for a maximum peaks.

The first goal of the analysis is to understand the time scales involved in these oscillations. I examined at the spectrum of several metrics of the North Atlantic obtaining the same peaks for different metrics (AMOC, AMO and North Atlantic heat content) on timescales centred at periods of 42, 21, 14 and 10.5 years. The similarity in the periods of the different metrics suggests a tight relationship between them. The three indices show the same significant peaks. Significance is measured with respect to the 99-confidence value when compared to a red noise distribution.

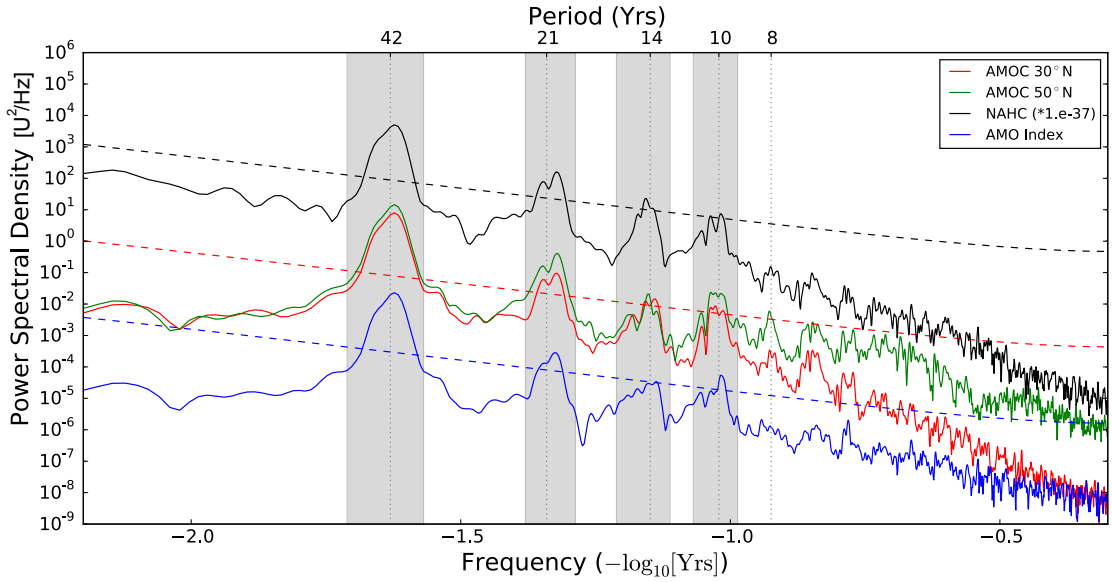

Figure 4.3: Power spectral density of the Atlantic heat content (NAHC full depth 20-70°N, black), AMOC Index at 30°N at 1000 m (red), 50°N at 1000 m (green) and AMO (blue). The spectra have been computed using the Welch's method (Welch, 1967). In dashed lines are shown the 99-confidence values assuming a red-noise distribution of the time series. Grey bands indicate the frequencies chosen for the band pass filters for each peak around periods of 42, 21, 14 and 10.5 years.The units of the power spectral density is indicated as U^2/Hz with U the corresponding unit of each variable: Sv, Sv and W (from top to bottom in the legend and without considering a unit for the AMO Index).

Band pass filters are used to isolate the main frequencies with the largest impact on the variability (grey shaded bands in Fig. 4.3). The main peak of the spectrum has a period of about 42 years (BP42, band pass filter between years $37-51.4$). For lower frequencies, we have peaks at 21 years (BP21, band pass filter between years $19.3-24.0$), around 14 years (BP14, filter between years $12.9-16.2$) and 10.5 years (BP10, filter between years $9.7-11.7$). The same bandpass filters were applied to the different outputs of the model to characterize the evolution of each frequency. The percentage of variance for the AMOC, and Atlantic 3-D temperature, salinity and density are summarised in Table 4.1. BP42 remains as the main contributor to variability in the four metrics shown on the table, whereas the other BPs never exceed jointly the 15% of the reconstructed variability. Looking at the AMOC index at 30°N, about 83% of the total variance comes from the BP42 oscillation. BP42 is then considered as the principal frequency of the variability. The rest of the frequencies are associated higher harmonics of this frequency: 1/2, 1/3 and

1/4 of the period of the main frequency mode. The corresponding amplitudes are equivalent to 3.7% for BP21 and less than 2% for the sum of BP14 and BP10.

In the next sections I will describe firstly the general characteristics of the 42-year mode. Secondly, I will focus briefly on the structure and differences of the associated higher harmonics.

	Reconstructed ($\sum \mathrm{BP}i$)	BP42	BP21	BP14 + BP10
AMOC index	88.87	83.47	3.7	1.7
Temperature	85.05	69.9	9.7	5.2
Salinity	72.9	63.8	5.7	3.3
Density	71.8	61.7	6.3	3.5

Table 4.1: Table showing percentage of the total variance of the model of the different Band Pass filters applied for the AMOC index north of 20°, Temperature, Salinity and Density in the North Atlantic.

4.4 Main frequency of the oscillation

The cycles obtained in Fig. 4.1 for the Atlantic Meridional Overturning Circulation Index (AMOCI) are not exactly 42 years, they vary between 41 up to 47 years (first shaded grey band of Fig.4.3). I considered in this case the AMOC index (AMOCI) relevant to be at 50°N (black line in Fig. 4.1), since most of the variability occurs in the subpolar region. I obtained the variability by filtering the outputs with BP42. From the filtered data, I chose 10 cycles between year 2000 and 2500 to compute the composite of BP42. The composite was computed by averaging the main variables over the 10 cycles, e.g. salinity, temperature, etc. The composite of the main frequency, BP42, is described based on the overturning index differentiating four stages: Increase, Peak, Decrease and Trough. The main indices of the evolution are shown in Fig. 4.4a and, later a separation between variables in the subpolar and subtropical regions are shown in Fig.4.4b (top and bottom respectively).

As for the AMOC, for variables such as temperature or salinity (and density) BP42 is symmetric in time with opposite sign for the second half of the cycle, hence half cycle is enough to describe the evolution of these variables. This does not occur with other variables such as the mixed layer depth or the gyre intensity.

Looking at the main metrics considered in Fig. 4.4a, the AMO evolves roughly on the same time scales of the AMOC at 50°N. They both peak with a lag of 1-2 years, led by the AMOC, but the minimum is reached first by the AMO index. The AMOC seems to transition faster during the increase phase. Also, the increase in the AMOC is associated with an increase in convection (deepening of the mixed layer depths in the Irminger Sea and later in the Labrador Sea). Note that the variables used in this analysis are annual means. Hence, although in some periods the annual mean convection is reduced, winter convection is still active.

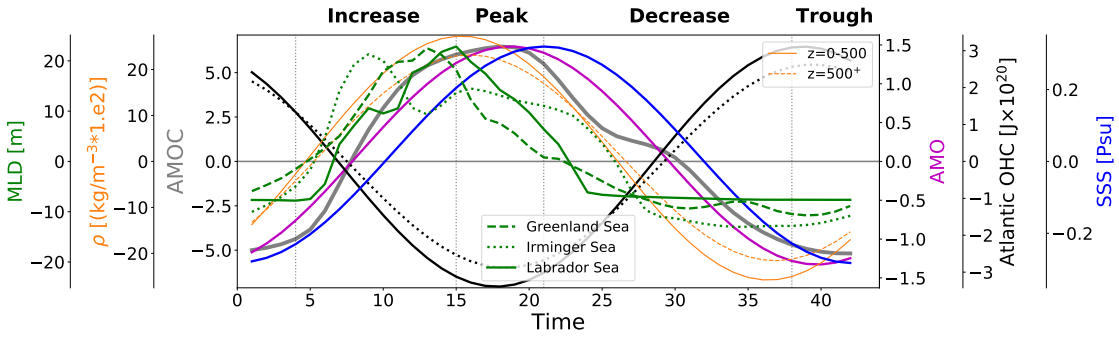

(a) Main indices of the Atlantic named from left to right. Area averaged mixed layer depth on each convection site: Greenland Sea (dashed green), Irminger sea (dotted green) and Labrador Sea (solid green). Density in the western SPNA, paticularly in the box $[-60°, -40°]$W$\times[50°, 60°]$N in the Labrador Sea region depth averaged in the first 500 metres (solid orange) and in between 1000 and deeper ocean (dashed orange), applying to the deeper average a correction factor of 10. AMOC index at $50°$N and 1000 m depth (bold grey). AMO Index computed as in Trenberth and Shea (2006) (magenta). Atlantic Ocean Heat content considering the SPG basin between $50° - 60°$N and up to 2000m depth (black), also the western part of the SPG considering only west of -40W (dotted black). SSS area averaged in the SPG regions between $50° - 60°$N.

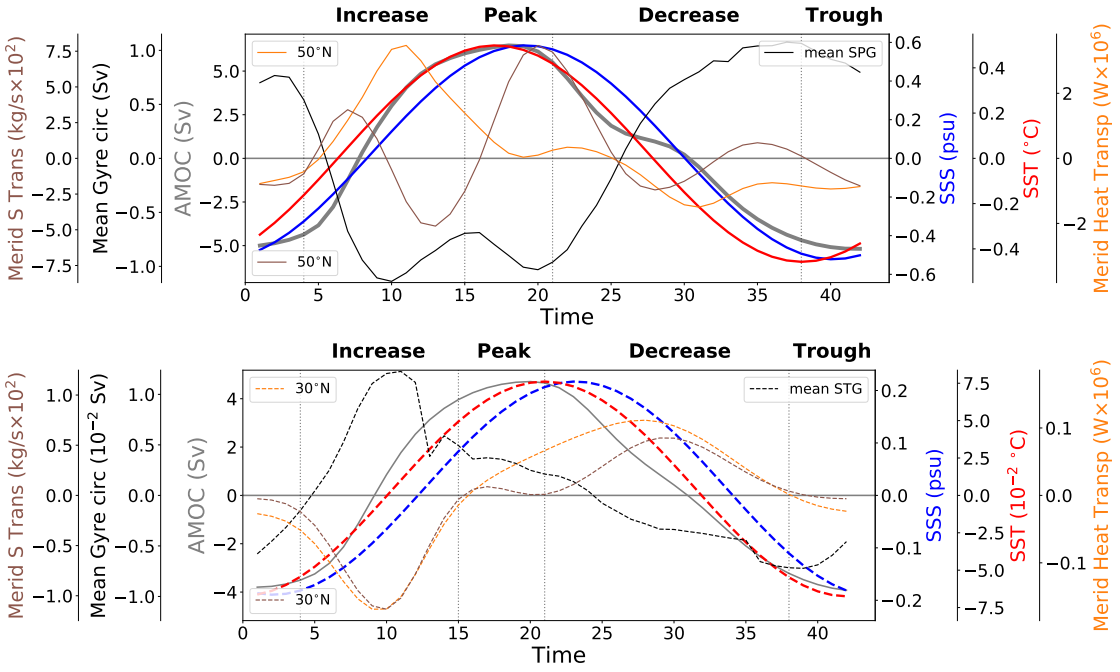

(b) Main indices of the subpolar Atlantic (top panel) and subtropical Atlantic (bottom panel) named from left to right. Meridional Salinity transport (brown) at $30°$N and $50°$N (dashed and solid respectively). Area averaged of the barotropic stream function indicating the gyre circulation in the subpolar Gyre $[50°, 60°]$N and subtropicalgyre $[20°, 50°]$N (solid and dashed black line). AMOC index at $30°$N and 1000 m depth (thin grey) and at $50°$N and 1000 m depth (bold grey). Area averaged SSS in the subpolar region $[50°, 60°]$N (solid blue) and subtropical region $[20°, 50°]$N (dashed blue). Area averaged SST in the subpolar region $[50°, 60°]$N (solid red) and subtropical region $[20°, 50°]$N (dashed red). Meridional heat transport (orange) at $30°$N and $50°$N (dashed and solid respectively).

Figure 4.4: Indices of the main variables in the regular cycle

The increased convection is associated with both a stronger circulation in the North Atlantic SubPolar Gyre (NASPG), and an increase in density west of the SPG in the Labrador Sea region. The density in the upper 500 m leads the increase in density below 1000 m. Changes in the Atlantic Ocean heat content (heat content in the band $[40°, 60°]$N and up to 2000 m depth) are in phase with the AMOC but in opposite sign. An increase of the AMOC is associated with a decrease in ocean heat content and vice versa. As the AMOC increases the northward transport of heat and salt in the surface increases (AMO - SSS). Instead, the heat content in the ocean interior decreases due to an increased convection releasing heat from the ocean interior and forming denser water masses in depth.

In the subtropical region, bottom panel of Fig. 4.4b, the AMOC at 30°N (thin grey line) seems to reach to maximal point delayed by a couple of years with respect to 50°N. The evolution of the surface variables seems to be in delay with respect to the AMOC and therefore to the variables in the subpolar region.

4.4.1 Description of the main frequency

As mentioned earlier, the evolution of the composite (Fig. 4.4a) we differentiated four stages: Increase, Peak, Decrease and Trough. I describe next each of these phases using mainly Fig.4.5 showing density, salinity and temperature is averaged in the upper 500 m, a section at 55°N and the state of the SPG convection and circulation. I also mention in the description the evolution of the SST, shown in Fig. 4.7 and related with the AMO. A more global picture of the North Atlantic is shown in this figure.

Increase (Year 5-13) - This phase is shown in the first column of Fig.4.5. In the upper 500 metres a bi-polar anomaly characterizes temperature and density in the SPG in this period (1a-1c). This strong zonal density gradient (positive on the west and negative on the east) is associated with the increase of the overturning anomaly. Also, in the upper 500 m density (1c) we can see a strong northward transporting the limits between the positive and negative density anomaly (arrows in the panel).

As the overturning increases, there is as well an increased meridional heat transport towards the northern latitudes and a strengthening of the mean of the Subpolar Gyre. The AMO, calculated as in Trenberth and Shea (2006) evolves in this phase as the AMOC (AMOC at 50°N and 1000 m depth), as we increase the upper ocean transport to the north both salinity and temperature increase its surface values. SSS seems to have a delayed increase and evolution with respect to the temperature, pointing towards this evolution as a passive variation.

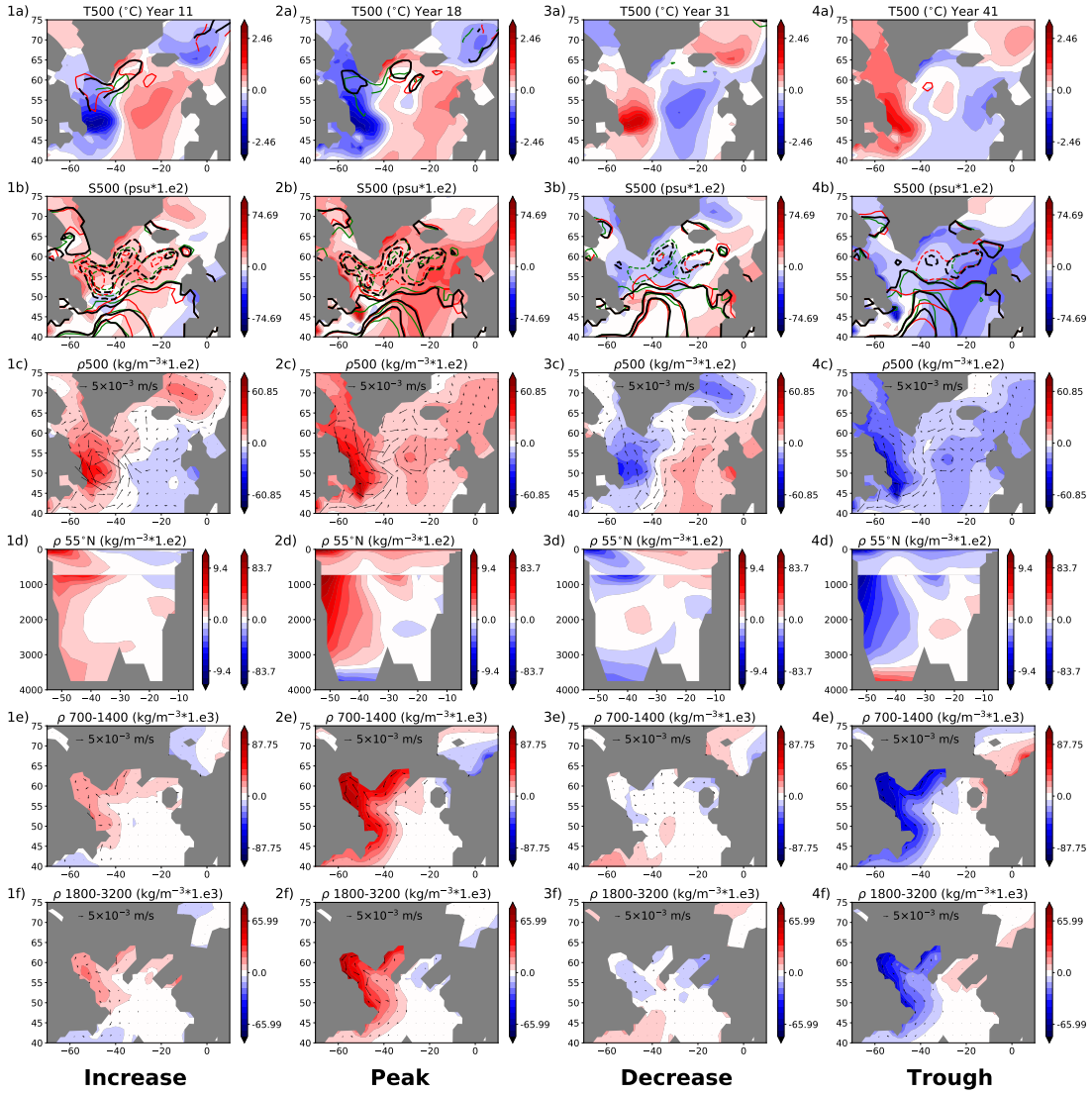

Figure 4.5: Evolution of the SPNA during the different phases: Increase, Peak, Decrease and Trough (each column). a) depth averaged temperature in the first 500 metres with contours of the Mixed layer depth every 500 metres for 4 years before (green), year stated (black) and after 4 years (red). b) depth averaged salinity in the first 500 metres (factor of 10^2) with contours of the barotropic stream function every 5 Sv for 4 years before (green), year stated (black) and after 4 years (red). c) depth averaged density in the first 500 metres (factor of 10^2). The arrows indicate the directions of the averaged velocities in the upper 500 metres with a unit of 5×10^{-3} m/s. d) Section at $55°$N of density scaled by a factor of 10^2. Different colorbars are used in the section: for the upper 700 m (right) and below 700 m (left). e) and f) show the depth averages of density between 700-1400 m and 1800-3200 m, arrows indicate directions of velocity anomalies in the corresponding depths with a unit arrow 5×10^{-3} m/s .

This phase is characterized by a strong convection at Labrador Sea and Irminger Sea (contours in 1a indicate annual averages of mixed layer depth of multiples of

500 m). The strong convection increases the heat release from the ocean to the atmosphere decreasing the SPG ocean heat content (Fig. 4.4a). The evolution of the MLD is shown in Fig. 4.5 1a, illustrating its time evolution by the contours: green year 7, black year 11 and red year 15. A strong period of convection occurs during this phase in both Irminger Sea and Labrador Sea, with the Irminger sea convection site leading the one in the Labrador Sea (Fig. 4.4a). The convection area propagates towards the inner Labrador, locating closer to the coast of Greenland. Convection is maximal at year 9 (black contours). It then reduces its extension as it divides in two (red contours). Along with the increased convection, the strength of the SPG reaches its maximum at about year 10, then decreases slowly during this phase (SPG index in Fig. 4.4b)

In the section at 55°N in Fig.4.5 1d a negative density anomaly is confined in the first 1000 metres on the eastern margin of the SPG (East of 40°W). The front of the anomaly is tilted towards the east with respect to the deeper part. This tilt is a necessary condition for baroclinic instabilities that sustain the propagation of this anomaly (Pedlosky, 1990). A more detailed description of the tilt is given in Fig. 4.6 and described next. Also, positive density anomaly is located west of the subpolar region, west of 40°W. It extends from the surface to the deep ocean.

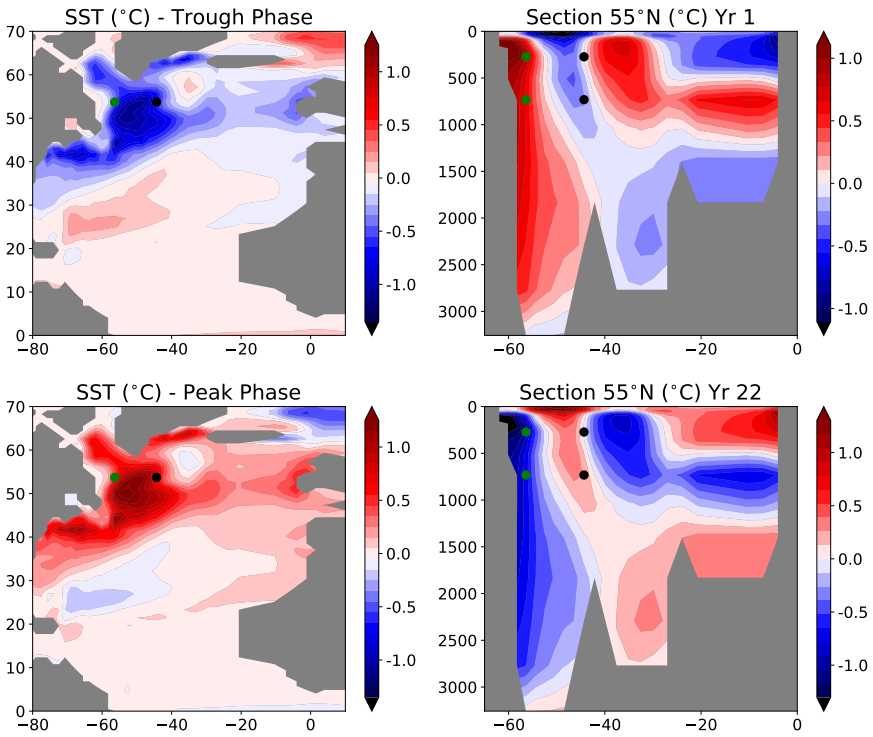

Figure 4.6: SST (left) and section of temperature at 55°N (right) at year 1 (Trough Phase, top) and 22 (Peak Phase, bottom). It is shown the location of the two points chosen to compute vertical structure of the wave. The two depths considered are 250 m and 750 m.

Peak (Year 14-22) - This phase is represented in the second column of Fig.4.5. The maximum peak in the AMOC at 50°N is obtained during this stage at year 18. The change from an increasing trend to a decreasing is associated with the appearance of two negative temperature anomalies modifying the zonal density gradient in the SPG. One anomaly located in the upper 500 m at $[40°, 30°]$ W-$[50°, 55°]$N and a second one east of $-30°$W at 700 m depth. The two foci can be seen in the bottom right panel of Fig.4.6 by the end of this phase with the two anomalies already developed.. The differences in density between the eastern boundary and western are very low, as it can be seen in the section at 55°N in 2d.

The negative temperature anomaly at $[40°, 30°]$ W reaches the surface, with a positive SST anomaly, by the end of this phase, bottom left panel of Fig. 4.6. This negative anomaly in the surface, and its western propagation, contribute to a decreasing trend on the AMO index. As with the AMO, the SPG peaks during this phase starting to reduce its strength.

The maximum of the AMOC occurs 2 years after the convection area in the west divides in two sites: Irminger and Labrador Sea (black contours in 2a). The reduced convection is associated with the arrival of a positive temperature anomaly propagating westward which reduces the vertical density difference in the upper 500 m in the convective regions, blocking firstly the Irminger Sea convection and later the Labrador Sea (2a).

Meanwhile, in the deep ocean the increased deep convection during the previous phase continues to propagate through the DWBC reaching the subtropics below 700 m depth (2e-2f).

The two negative temperature anomalies in the east develop independently, and sometimes at different rates, obtaining slight differences in the propagation times. This can be seen in the two Hovmöller plots in Fig. 4.9 with different anomaly propagation patterns between the anomaly in the $[40°, 30°]$W region and the one west of 30°W. This will be discussed further later.

Decrease (Year 23-38) - This stage has the same evolution as the increase phase in terms of density and temperature but with opposite signs. Comparing the first and third column of Fig.4.5, a and c, the first three rows are identical, but with opposite signs. The strong zonal density gradient with a bipolar density anomaly, negative on the west and positive in the east, contributes to the reduction of the overturning rate. A transition to a negative AMO phase occurs in this phase, with the positive density anomaly located on the west fading as the negative anomaly grows at the surface (Fig. 4.4b 3a).

The main differences with respect the increase phase are the strength of the SPG and the reduction of deep convection intensity. The SPG has an anomalous strength weaker than -5 Sv (there is no dashed contours of that intensity in 3b). This lack of SPG strength allows the boundary of the inter-gyre region to move north when compared to the increase phase (1b versus 3b), particularly in the western SPG. Convection is reduced, shown by annual means of the MLD not exceeding 500 m by year 31 (there are no contours in 3a). The Labrador Sea convection site is the first one to decrease followed by the Irminger Sea and South of Iceland.

Trough (Year 39-4) - As with the decrease phase, this stage is similar in density and temperature space as the peak but with opposite signs in the anomalies. The weaker zonal density gradient does continue with the negative trend of the AMOC. The positive temperature anomalies (negative density) generated in the eastern SPG contributes to change the zonal gradient as the negative temperature anomaly (positive density) propagates to the west. The AMO follows the same trend of the AMOC, as it starts to increase with the propagation of the positive temperature anomaly.

It is in this phase that the propagation of the negative temperature anomaly to the west restarts the cycle activating convection (red contour in 4a) and strengths the SPG (red dashed contours in 4b).

Although I focused on the evolution of the SPG, the anomalies also propagate in the Subtropical Gyre (STG), the phases are described in Fig. 4.7 with a section at 30°N (row d). In the increase phase in the SPG the anomaly in the western margin propagates below 500 m along the western boundary current. Associated with this anomaly, there is a negative temperature anomaly propagating between 500 m and 1000 m at 30°N (1d). This anomaly corresponds to the one in the western boundary current in the SPG that has been propagating south crossing the STG. As the AMOC is intensifying, the STG index (maximum of the barotropic stream function between 10-40°N) has the highest values of the cycle (dash black line in Fig. 4.4b). During the peak phase, second column of Fig. 4.7, we have still the negative anomaly in the 30°N section in the subsurface, but a positive anomaly is advected in the surface by the increase in the gyre intensity (2d in Fig. 4.7) and at depth, a positive density appears by the return flow propagating from the SPG. The positive anomaly is keeps propagating south during the decreasing phase (3e in Fig. 4.7). The process continues the oscillation with similar temperature evolution but with opposite signs, second and third column are the opposite of first and second.

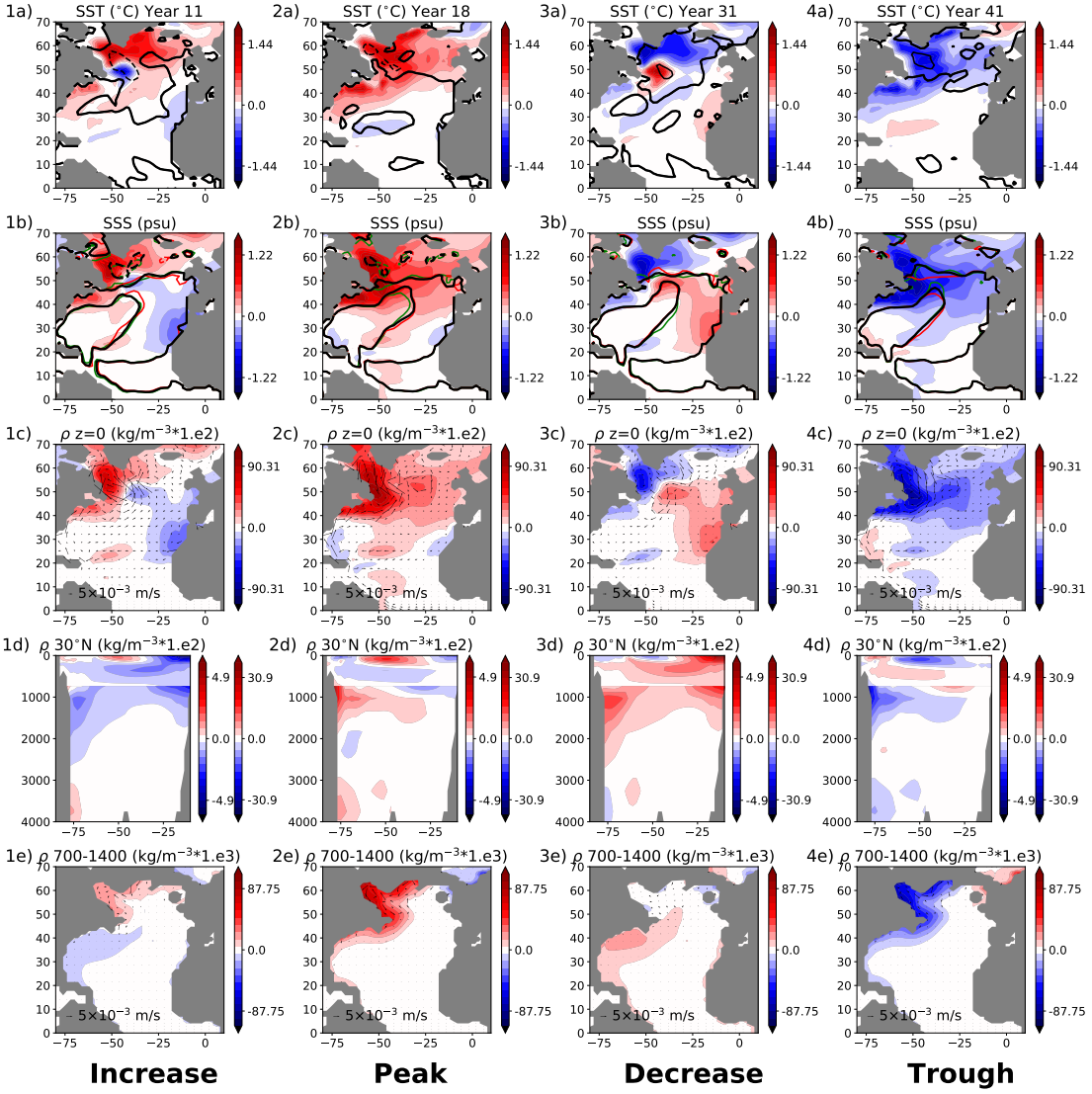

Figure 4.7: Evolution of the STNA during the different phases: Increase, Peak, Decrease and Trough (each column). a) SST of the Atlantic region, contours of the anomalous (with respect to the mean) barotropic stream function are shown. Solid line indicates 0 anomaly and the thin contours show 5 Sv anomalies. b) SSS with contours of the barotropic stream function every 10 Sv for 4 years before (green), year stated (black) and after 4 years (red). c) Density in the surface with a factor of 10^2. Arrows indicate the directions of the surface ocean anomalous velocities with a unit of 5×10^{-3} m/s. d) Section of density at $30°$N scaled by a factor of 10^2, different colorbars are used in the section: for the upper 700 m (right) and below 700 m (left). e) show the depth averages of density between 100-2000 m, arrows indicate directions of velocity anomalies in the corresponding depths with a unit of 5×10^{-3} m/s.

The band pass filter used to obtain BP42, and in general the other BPs, contains more than a single frequency. For example, BP42 consists on frequencies between 37 and 50 years. This allows to encounter some time variability in the anomaly

propagation. The two factors identified that contribute to the temporal variability observed in the propagation of the waves are the fact that the anomaly in the eastern SPG is formed by the junction of two foci and the phenomenon known as beating. Variability in the formation of the two anomalous foci ($[40°, 30°]$W region and the one west of 30°W) is observed in the Hovmöller plots in Fig. 4.9. The two regions develop both anomalies independently and, some delay contributes to the time variability in the region between $[40°, 30°]$W develops in concordance with the eastern part or slightly delayed. The other temporal variability relies on the beating phenomenon, which occurs when frequencies with similar values and amplitudes interact changing temporally the amplitude of the propagating wave. This phenomenon can be represented as a single wave whose amplitude varies with time. This time dependency is expressed in the following equation:

$$\cos(\omega_1 t) + \cos(\omega_2 t) = 2\cos(\frac{1}{2}(\omega_1 + \omega_2)t)\sin(\frac{1}{2}(\omega_1 - \omega_2)t) = 2\cos(\Omega t)A(t). \quad (4.1)$$

The combination of the two frequencies ω_1 and ω_2 through trigonometric properties provide a temporal variability in the amplitude $A(t)$ represented by $\sin(\frac{1}{2}(\omega_1 - \omega_2)t)$.

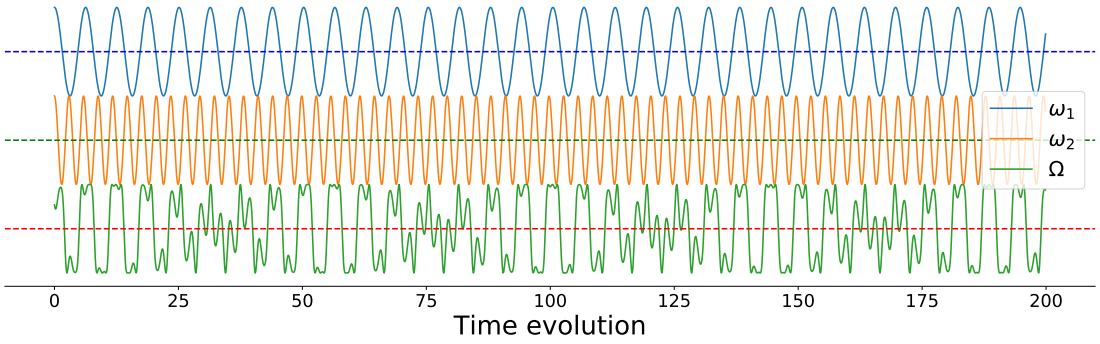

Figure 4.8: Illustration of the Beating phenomenon. The two individual frequencies, ω_1 and ω_2 (following the notation on Eq. 4.1), show a temporal variability in amplitude when they are combined (Ω bottom).

The phenomenon is shown in the Hovmöller plots of the anomalies on the meridionally averaged subpolar gyre ($50 - 60$°N) at 1000 m depth. We can observe

that the propagation of the waves changes with respect to time, especially in the central area around the $35° - 30°$ West. This is the region in which one of the foci is created and propagates westwards interacting with the western boundary current. The propagation not only varies in the subpolar region but also in the subtropics. Two snapshots on the right of the figure show different patterns in the propagation of the waves through the SPG and STG.

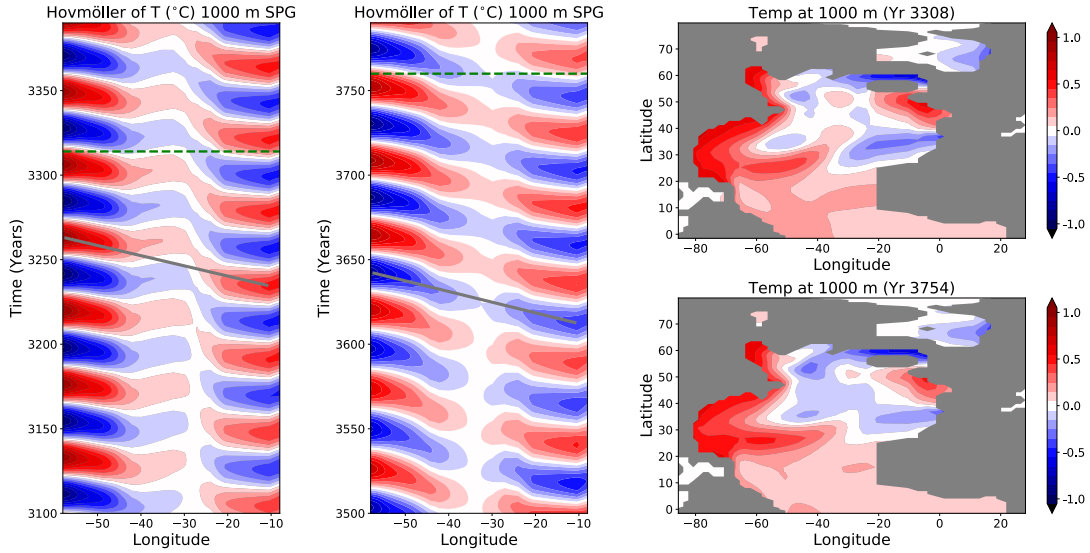

Figure 4.9: The Hovmöller plot shows the evolution of the average of the band $50 - 60°$N at 1000 m depth in different times of the main cycle: years 3100-3400 and 3500-3800. Dashed lines indicate the years of the snapshots showed on the right, snapshots at 1000 m depth of the North Atlantic. These snapshots are taken 6 years after the minimum on the maximum on the AMOC index. Anomalies propagate with different intensity and amplitude, generating different propagation patterns especially in the Subtropical Gyre due to beating of the analyzed frequencies. Grey lines indicate the slope used to compute the propagation velocity of the wave.

The temporal variability would potentially occur in the propagation of these waves in a realistic ocean. This would complicate the detection of the propagating wave. The different frequencies do not propagate in isolation, but instead they interact as they propagate obtaining the patterns shown in Fig. 4.9.

4.4.2 Mechanism of the main frequency

The mechanism previously described is depicted in Fig.4.10. The figure shows the background state of the SPG (a) with a meridional temperature gradient, standard circulation of the SPG (violet arrow) and deep convection (brown shaded area). The other two states, denoted as Active phase (b) and Neutral phase (c), correspond to a state during the Increase Phase and at the end of the Peak phase respectively. These names are chosen to highlight the impact of the propagating wave on the SPG state.

The evolution of the mechanism from a low AMOC (about year 38, similar to column 4 in Fig. 4.5) is associated to a new positive temperature anomaly (negative density) at $[40°, 30°]$W and $[50°, 55°]$N in the upper 500 m and east of $-30°$W at 700 m depth. Another anomaly of the opposite sign has preceded the positive anomaly, located about $-40°$W, and it is propagating west (similar to Fig. 4.6 top panels).

As the positive anomaly increases, reaching the surface around year 43 the strong temperature gradient, and density gradient, generates an anomalous horizontal velocity around the anomaly. The anomalous geostrophic flow (anticyclonic for a positive anomaly) brings warm waters from the south into the western flank of the anomaly, contributing to its propagation together with the β-effect. This meridional transport contributes, in the Active phase, to the increase of the western SPG strength. The surface SST anomaly propagates faster with the stronger SPG reaching the west of the SPG. The propagation of the positive anomaly in the upper ocean initiates convection in the Irminger and later Labrador Sea, initiating the period of active convection about year 5.

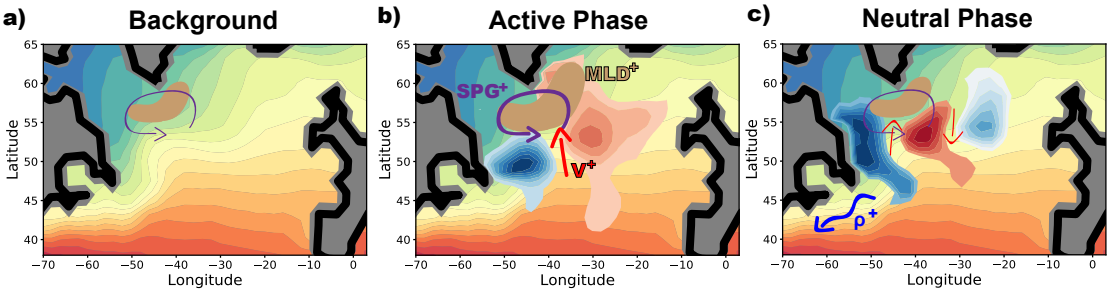

Figure 4.10: Schematic of the propagation of Thermal Rossby waves. Background state of the subpolar Gyre (left), state of the SPG during the increase phase (Active phase) and state by the end of the peak phase (Neutral phase). **a** the averaged surface temperature is indicated by the colours in the background, the strength of the SPG (violet arrow) associated by the thickness (thick-strong SPG and thin-weak SPG). The convective region is shown in the shaded region (brown). **b** Associated to the increase phase. The two anomalies of the averaged upper 500 m are shown over the zonal temperature in the background gradient (and density) generating anomalous meridional transports (red arrow). The increased SPG and convection (MLD) is indicated by a thicker violet arrow and larger brown area. **c** The end of the peak phase is indicated by the appearance of a new negative anomaly reducing convection and anomalous meridional transports through thermal wind balance. The propagation of the anomalies along the western boundary current is indicated by the blue arrow.

During the Active Phase, in the increase phase (year 4-15), there is a strong zonal temperature gradient in the Atlantic (also density gradient, not shown in the figure). With the negative temperature anomaly on the west and positive temperature anomaly on the east (opposite signs for density), the density difference between the eastern and western boundary promotes the increase of the AMOC coinciding with the propagation of the SST in the SPG. In this phase we also have an increased convection contributing to the formation of dense water in the deep ocean and release of heat reducing the SPG heat content.

The positive anomaly (in temperature) keeps propagating to the west as other anomaly during the peak phase appears around year 21, which leads to the Neutral Phase. In this phase the propagation of the anomalies generates opposite meridional flows that do not have a large impact on the subpolar region. The cycle shown in the previous section, 4.4.1, continues from this Neutral Phase in the Peak to an Active phase as in Fig.4.10b but with the temperature anomalies in the opposite sign. The new propagating anomaly on the east induces southward anomalous

meridional velocities on its western flank reducing the SPG intensity. The propagation of the positive temperature anomaly to the western SPG reduces convection in this phase obtaining the characteristics described in the decreasing phase. The cycle continues during the Trough phase as we reach another Neutral phase of the mechanism with opposite values as the ones shown in Fig.4.10c which restart the cycle.

The anomalies intensify as they propagate: this can be seen in the figure by comparing shades of red between Fig.4.10b and Fig.4.10c, the temperature anomaly has increased. And also, comparing both negative anomalies in Fig.4.10c, the eastern anomaly has lower anomalous temperature values than the anomaly on the west. The intensification of the wave plays a key role in the SPG heat content. In Fig.4.4a the two black lines represent the SPG heat content up to 2000 m: solid line for the whole 50°-60°N band and the dashed line restricted to west of 40°W. The heat content in the west has almost the same magnitude as the heat content on the whole SPG, supporting this idea of western intensification.

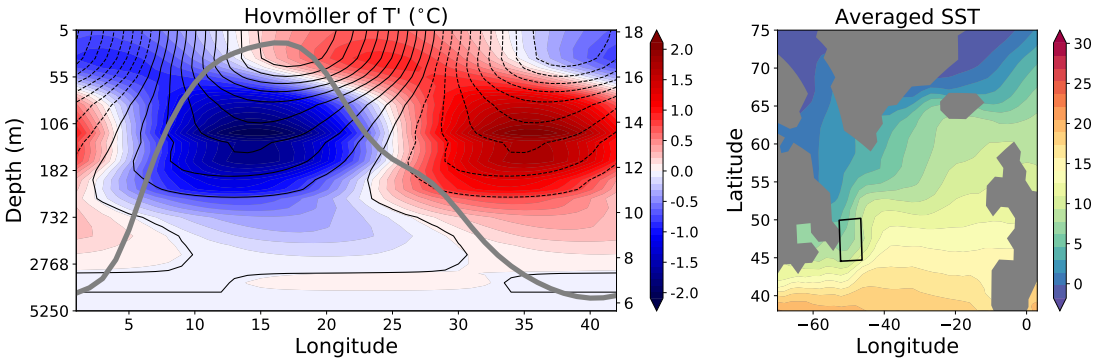

Figure 4.11: Left: Hovmöller of the averaged region in the coast of Newfloundland. Coloured contours indicate temperature anomalies and black contours indicate density anomalies. It is shown as well the evolution of the AMOC at 50° and 1000 m depth. The y-axis is the model axis, the depths are the depths of each of the model cell. Right: chosen region for the average.

The anomalies impact the deep ocean and the STG with their propagation through the DWBC. For example, the negative anomaly in temperature (left in 4.10c), associated with a lack of deep convection, propagates through the deep western boundary current. This propagation is delayed with respect to the peaks of the AMOC. Fig.4.11 shows a Hovmöller plot of the averaged region in the coast

of Newfoundland of the cycle for temperature (colors) and density (black contours). The negative anomaly is still propagating at depth during the decrease phase. The temperature leads the evolution of the wave at the surface, and later follows the rest of the water column. For density that is not the case, contours of density in the figure on the left leads at 250-500 m depth. The differences between the propagation of density and temperature can be related through the contribution of both temperature and salinity to density. Fig. 4.12 left shows that on the western SPG the contribution of temperature to density is the largest below 250 m, being temperature the main factor changing density at depth. Whereas in the surface, despite having positive anomalies leading the wave, that does not reflect on density as salinity is the main contributor.

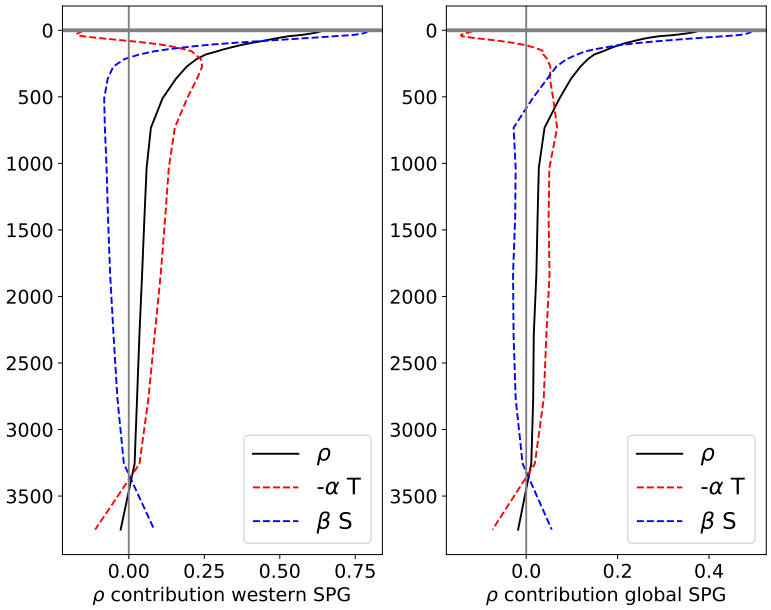

Figure 4.12: Salinity and temperature contribution to density with respect to depth. For the whole 50°-60°N band (right) and western SPG, west of 40°W (left)

The vertical structure of the wave, hinted in Fig. 4.6, has been quantified by looking at the time differences between the two points used to compute the velocity at two depths: 250 m and 750 m, shown in the right the figure. At the point located about 40°W, right in blue, the time difference between a peak in the top and bottom points is of 16 years. This indicates that the propagation is indeed tilted. As classified by Sévellec and Huck (2015), depending on the stratification of the ocean, either the top part of the ocean leads, is delayed, in phase or out of

phase with respect of the mid-depth ocean. This time difference would indicate that the wave is actually an unstable Thermal Rossby wave, the top leads the westward propagation introducing a less dense fluid that will readjust releasing potential energy form the mean temperature gradient (Pedlosky, 1990). Instead at the other point, the propagation is almost instantaneous, the difference is only one year. The closeness to the boundary current may be the reason for not to observe the delay between the two depths at 55°W, as the wave approaches the boundary this difference between upper and deeper ocean is no longer present due to the anomalies coming from the Deep Western Boundary Current (DWBC). I looked as well at the propagation speed estimated from the grey lines in Fig. 4.9. The approximated propagation velocity of about 0.3 cm s^{-1} for this frequency (phase velocity v_p), and considering 42 years the period would give a wave length of about 397 km ($v_p = \lambda/T$, with T period and λ wave length).

The features previously described have numerous similarities with the growing mode obtained by Sévellec and Huck (2015). In their work, the authors demonstrated the existence of an oceanic multidecadal mode of variability associated with the westward propagation of large-scale baroclinic Rossby waves. These waves contribute to the frequency variability observed in the North Atlantic as they propagate to the west (see subsection 1.1.3).

Firstly, the four phases presented previously coincide with the ones described by the authors: a North Atlantic basin-scale warming (AMO positive phase), reduction of the poleward transport (AMOC decrease), cooling of the Atlantic basin (negative AMO), and to complete the cycle an AMOC intensification. The pattern of the AMO obtained is shown in Fig. 4.13 with the SST regressed to the AMO index computed as Trenberth and Shea (2006). The pattern has some similarities with the SST regressed to the AMO index of the observational record (Fig 1.5 in chapter 1). The traditional horseshoe pattern is similar to the pattern here obtained in the subpolar region but is missing the subtropical positive anomaly. Even in the common region, subpolar, there are some differences that we can spot: the higher regression values in the Labrador Sea and a small negative signal in the Greenland Sea. The first one possibly related to the stronger impact of Lab-

rador Sea convection in this mechanism. The regression pattern does not show any positive regression in the subtropical region. This can be related to the lack of atmospheric feedbacks, wind-evaporative and cloud feedbacks have been detected as key processes to extend the warming into the tropical Atlantic (Brown et al., 2016; Yuan et al., 2016; Bellomo et al., 2018). The pattern in Fig. 4.13 also resembles the subpolar component of the internal multidecadal pattern for the SST computed by Yang (2013). This pattern in the GFDL model can be predicted up to 4 years in advance with a 95% significance level and 10 years for a 90% significance. If an accurate link can be done between the pattern and the propagation of Thermal Rossby waves, we could have a link between the surface and ocean interior predictable up to a decade in advance and its relationship with other components of the North Atlantic.

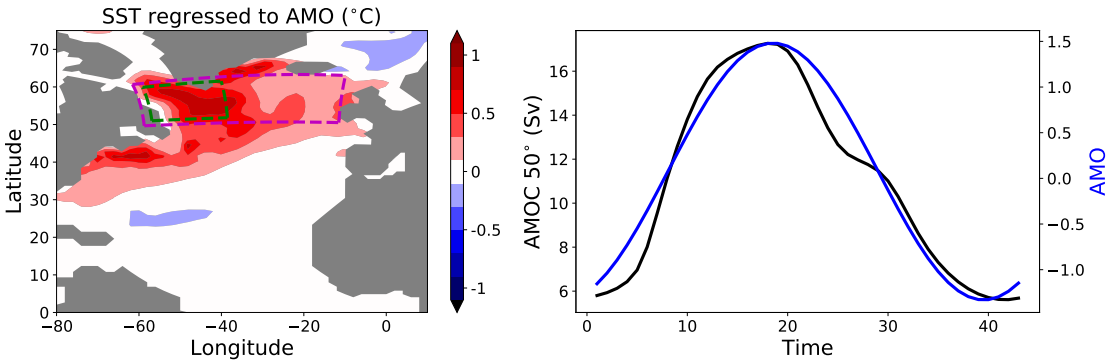

Figure 4.13: Left: SST regressed to the AMO index. Blue and black boxes indicate the regions used for averaging to compute the contributions of salinity and temperature to density in 4.12. Right: AMOC index (overturning at 30°N and 1000 m depth) and the normalized AMO index (computed as Trenberth and Shea (2006))

Another characteristic similar to Sévellec and Huck (2015) is the tilt in the propagating wave. This wave is generated by the junction of two temperature anomalies, one between $[40°, 30°]$ west, $[50°, 55°]$ north and, first 700 m depth and other in the eastern boundary at around 1000 m depth. These anomalies join generating the tilt and the necessary downgradient eddy heat fluxes necessary for the growth and propagation of the baroclinic waves (Colin de Verdière and Huck, 1999). The mechanism, known as geostrophic self-advection, competes with the β effect (standard Rossby wave propagation mechanism) and the mean advection. It propagates the density anomalies in the same way as the generalized Rossby waves

but instead of induced by changes in the coriolis parameter, by temperature (density) gradients inducing anomalous meridional transports. The propagation of the waves contributes to additional meridional transport anomalies through thermal wind balance promoting or decreasing the overturning.

The authors also pointed that the propagation of this waves is not driven by convection, which is the case here presented, claiming that changes in the AMOC can occur without changes in the MLD and convection (Sévellec and Fedorov, 2013b). In our case that is somehow true: the propagation of the waves is not driven by convection but they contribute to variations in convection. A strong period of convection is associated to the propagation of negative temperature anomaly on the west and a positive in the east. The increased convection contributes strengthening the anomalous western deep density that returns through the western boundary current contributing to the AMOC.

4.5 Higher harmonics variability

The higher harmonics of the main frequency correspond to filtered data around 21 years (filtered between years $19.3 - 24.0$, BP21), around 14 years (filtered between years $12.9 - 16.2$, BP14) and around 10.5 years (filtered between years $9.7 - 11.7$, BP10). As with the BP42 cycle, these BP filters include several frequencies and, beating allows for time variations in the amplitude of the filtered data. The contribution to the temperature variance of each of the band pass filters correspond to a 10%, 4% and 3% of the variance of the total temperature variability. In the other metrics, the contribution of the higher harmonics never exceeds the contribution to temperature variability.

The main activity of these higher harmonics is localized in the SPG with largest contribution from BP21. I will first describe the BP21 case and then look for differences between this harmonic and at the sum of the remaining harmonics (BP21 + BP14 + BP10). As previously, the starting point of the description is the increase of the AMOC rate associated with each of these modes followed by the peak. The other two phases of the cycles are symmetric with respect to the sign of

the temperature anomalies, so there is no need to repeat these phases.

BP21 The cycle is represented in the fourth column of Fig. 4.14, with the temperature evolution at 1000 m depth. The cycle, starts with the minimum of the overturning in this harmonic, with a strong negative zonal temperature gradient in the SPG above the first 2000 m. Following that, in the increase phase a tripole is observed at 1000 m depth (second row Fig. 4.14): a positive anomaly developing in the eastern basin, a negative anomaly propagating to the west with the upper 500 m leading the propagation and tilted on depth towards the east (not shown), and a positive anomaly located on the western Labrador Sea. The propagation velocity for this mode is about 0.6 cm s^{-1} and the delay between 250 m and 750 m is only of one year, hence the wave behaves as unstable baroclinic Rossby wave.

In the STG, we observe a propagation of anomalies along the 1000 m depth across the subtropical basin. The magnitudes of these anomalies are very small compared to the ones in the SPG, which are already a low contribution to the total variability. In the section at 30°N anomalies propagate from east of the Subpolar Gyre (SPG) below 1000 m, coming from the SPG, to west. Negative anomalies reaching the western margin are associated with a decrease phase and positive in the increase phase of the AMOC anomaly filtered for BP21.

Lower frequencies (BP14, BP10) BP21 is about a 65% of the signal of BP21, BP14 and BP10 combined, the impact of lower periods is almost insignificant for the complete unfiltered cycle. Despite being of lower impact, the mechanisms behind their propagation is similar. As if the different wave numbers propagate along the subpolar gyre and subtropics. The low values of the filtered data show a higher temporal variability than in the case of BP42 or BP21. The main difference between the residual of BP42 and BP21 is the interference of other lower frequencies disturbing the BP21 signal.

The mechanism comprises the propagation of anomalies from $[40°, 30°]$W and $[50°, 55°]$N to the west. The propagation mechanism of BP21 resembles the propagation of these higher frequencies. The tilted wave is a common signature of the

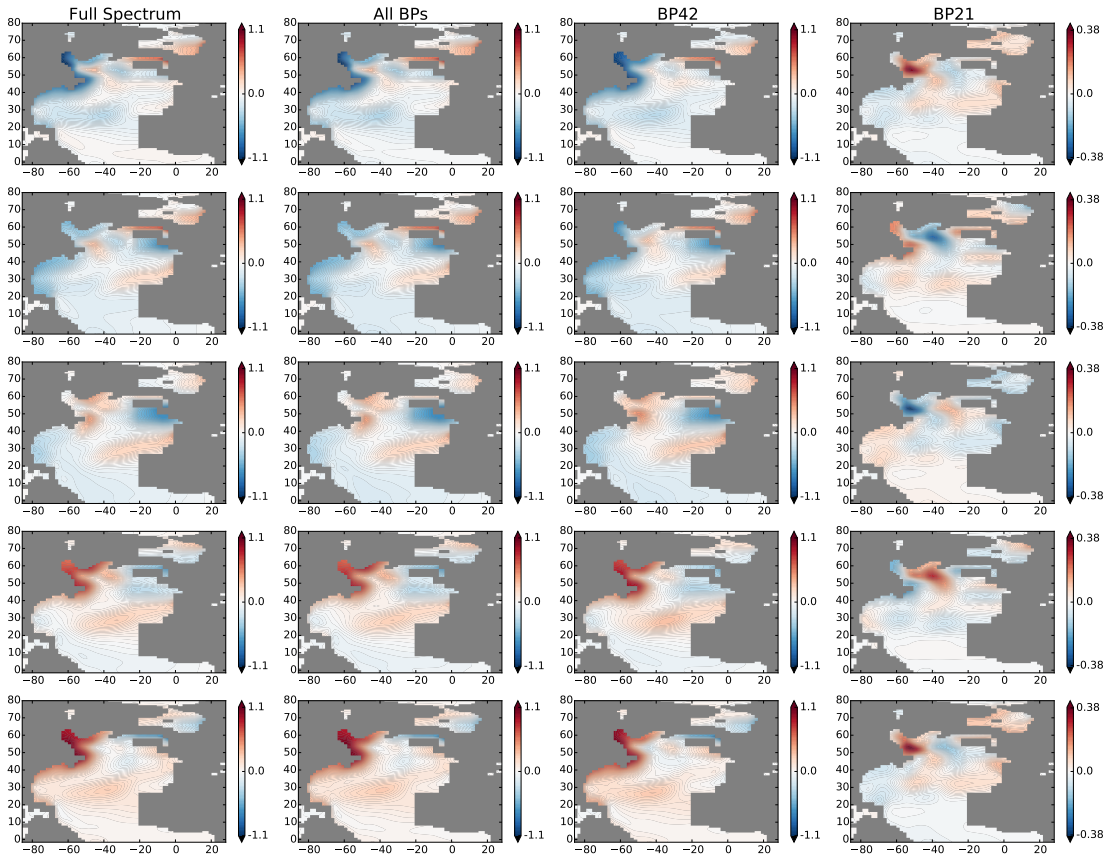

Figure 4.14: Evolution at 1000 m depth of quarter cycle of the composite of the temperature field starting from the AMOC maximum peak (filtered for BP21 and BP42). From left to right columns are the composites of the general cycle (Full Spectrum), second column the sum of all filtered data (BP10, BP14, BP21 and BP42), BP42 on the third column and last column BP21. We choose 1000 m as a representative of the evolution of the composites due to the correspondence to the anomalies' evolution. Denote that the quarter cycle depends on the data considered, for the first columns correspond to 11 years (year 0,3,6,9,11) and the last one of 5 years (years 0,1,3,4,5).

different frequencies. Compared to BP21 or BP42, the anomalies only propagate along the SPG with no signal in the STG. Whereas for BP42 in the SPG there is a bipolar structure in the SPG, for the increase phase the western part of the SPG has a negative density anomaly whereas the east has a negative anomaly (Fig. 4.5 1b). In the high frequency cases, the structure is similar to BP21 with a tripole propagating westwards.

The vertical structure and velocity propagation of the main frequency of BP14 and BP10 is slightly different from the ones of BP21 and BP42. In the case of BP14, I obtained that the wave actually a faster wave, when compared to the other ones, 1.7 cm s^{-1} and it is in fact 1 year delayed the upper 250 m with respect to 750 m

at 40°W whereas that for 50°W the propagation is delayed at 750 m of about 2 years.

4.6 Discussion

The North Atlantic, as one of the key components of the Climate system, has attracted much attention not only due to its own physical importance but due to the potential impacts to the society and economy. Understanding its variability and the potential mechanisms driving it is one of of the focuses of the climate community. In the Atlantic climate, components such as NAO, dense water formation in the Labrador Sea, AMOC and SST represented by the AMO are individually understood. But it still has to be understood the general mechanisms by which they interact.

Several mechanisms are candidates to contribute to the multidecadal variability in the North Atlantic: from purely oceanic modes (Sévellec and Huck, 2015), coupled modes (Menary et al., 2015; Ortega et al., 2015; Zhang et al., 2016a) or purely atmospheric (Clement et al., 2015). Amongst some of the coupled and purely oceanic, there is a strong support in the tight relation between the AMV and ocean dynamics including AMOC variability (McCarthy et al., 2015; Zhang et al., 2016a), which in junction with the impact of the atmosphere (particularly the NAO) provide the variability obtained in ocean models. In the oceanic component, a plausible candidate contributing to changes in the AMO/AMV is the propagation of baroclinic Rossby waves in the subpolar gyre (Huck et al., 1999; Colin de Verdière and Huck, 1999; te Raa and Dijkstra, 2002; Sévellec and Fedorov, 2013b; Sévellec and Huck, 2015).

In this work I focus on a purely oceanic mode obtained with OPA 8.1 corresponding to the propagation of baroclinic Rossby waves. The mode is characterized by a period of about 42 years (BP42) and corresponds to the following evolution: AMO positive phase (North Atlantic warming), a decrease in the poleward transport (with the corresponding overturning decrease), AMO negative phase (Atlantic basin cooling) and a poleward transport intensification. As the anomalies, generated by baroclinic instability due to a feedback between the tilt in the upper pycnocline and in the deeper pycnocline, propagate westwards contributing to changes in the meridional velocities increasing or decreasing the overturning. The propaga-

tion mechanism, geostrophic self-advection, resembles the regular propagation of Rossby waves but instead of changes of the β parameter modifying the meridional transport, density gradients contribute to the density propagation (mainly contributed by temperature, hence known as "thermal" Rossby waves).

The main period of the driving the mechanisms, 42 years, is limited by the instability, which is induced by a feedback in the upper pycnocline and the deeper pycnocline (Sévellec and Huck, 2015). By being an unstable wave, led by the surface, the baroclinic instability acts as pacemaker for the propagation of the waves. A different stratification would provide a different propagation speed as obtained in various CMIP5 models (Muir and Fedorov, 2017). Together with the 42-year variability, higher frequencies surpassed the 99% confidence in the spectrum of the AMOCI with periods of 21, 14 and 10.5 years (1/2, 1/3 and 1/4 of the main period). These periods were filtered in the different fields to obtain the evolution of these lower period cycles. Despite a lower impact on the total variability (about a 6-15% of the total variance of the variability), high frequencies show a steady propagation with respect to the strongest mode of variability. These time scales have been obtained previously as periods of North Atlantic variability (Escudier et al., 2013; Kwon and Frankignoul, 2014).

The propagation of the temperature (and density) anomalies have a large impact on the subpolar region. As a positive temperature anomaly propagates from east to west, the anomalous meridional velocity on its west flank contributes to reinforce the SPG, which contributes to the propagation of the positive SST anomaly in the surface and leading to a positive AMO phase. The opposite occurs with the propagation of a negative temperature anomaly. The anomalies also interact with the convection regions in the western SPG (Irminger and Labrador). The propagation of a positive anomaly, first by the surface and later with the subsurface, reduces convection intensifying the propagating anomaly by not releasing heat through convection. The opposite holds when a negative temperature anomaly propagates, contributing to the intensification of the anomaly in the western margin and increasing the density difference between the eastern and western boundary modifying the AMOC. Then by the mechanism here presented the AMOC acts

passively to the propagation of the density anomalies, coinciding with the passive role of the AMOC proposed by Buckley et al. (2012). The interaction of the density anomalies with the convection confirms, as Sévellec and Huck (2015), that the propagation is not driven by convection. The authors suggested that changes in the AMOC can occur without changes in the MLD and convection. This is not true in our case, since the propagation of the density anomalies have an impact on the vertical density distribution in the convective regions promoting or blocking convection. This contributes further to the western intensification of the anomalies and increasing the impact on the AMOC.

Although this mechanism is very robust in our model under the model setup chosen, it is still a "low" resolution ocean only model. The possible limitations of the mechanism due to the low resolution of the model, 2°, were previously addressed by Huck et al. (2015). The authors confirmed the presence of these modes of variability under eddy resolving model in an idealized bathymetry. Also, the lack of atmosphere can be a drawback to our mechanism, in particular related to the AMO. We used mixed boundary conditions to try to have an effect similar to the atmosphere: we would restore the temperature to certain values (in our case a climatological atmospheric state) but would leave the salinity free to evolve without a strong interaction with the atmosphere. The lack of direct interaction with the atmosphere would probably damp the strong surface signal obtained during the increase and peak phase.

Recent work of Wills et al. (2018) suggested, through low-frequency component analysis in historical simulations of CMIP5, that the AMO temperature anomalies in couple models are driven by ocean heat transport convergence in the subpolar North Atlantic associated with AMOC anomalies. Also, in his work the second low frequency pattern (the first one is associated with global warming) is very similar to the pattern obtained here in this work located exclusively in the North Atlantic. The authors computed these patterns combining the traditional EOFs with an optimization algorithm maximizing the ratio of interdecadal to intradecadal variance to obtain the patterns associated with multidecadal variability. Although the leading role of the atmosphere in AMO variability has been discussed extensively

(Zhang et al., 2016a; Delworth and Zeng, 2016), Wills et al. (2018) rules out the atmosphere to be a dominant mechanism in the North Atlantic at multidecadal time scales, supporting the possibility of this mechanism as a contributor to variability in the North Atlantic.

Muir and Fedorov (2017) used 25 simulations of the CMIP5 to test the mechanism presented in Sévellec and Huck (2015) and also in this chapter obtaining variability consistent with this mode in more than half models investigated: statistically significant spectral peaks in the band between 15 and 35 years, westward propagation of density anomalies in the band 40°-60°N, the same phases described in this work and the predominant effect of temperature on density anomalies. Future work should be directed toward the new generation of models being prepared for the CMIP6, coming in the next few months, in which the improved parametrizations and processes could lead to a better understanding of these modes in a more realistic setting. The work of Muir and Fedorov (2017) could be repeated looking for the features presented in Sévellec and Huck (2015) and observed here: AMO-AMOC cycle, common peaks in the spectrum, features of propagating baroclinic Rossby waves. Besides, in order to confirm this mechanism, we could look for indicators of the relationship between the SPG intensity or convection in the model with the propagation of the Rossby waves in the models. Also, we would need to compare the characteristics of each model with respect to the appearance of these features to understand the possibility of any model dependency. For example, some models use NEMO as ocean component, raising the question to explore about the possible common features associated with the characteristics of the oceanic model considered.

4.7 Key Results of this chapter

- Thermal Rossby waves are supported as a candidate promoting AMOC variability in decadal-to-multidecadal time scales in OPA, precursor of NEMO.
- The waves obtained propagate on different frequencies, 42-21-14-10.5 coinciding with variability obtained in the observational records.
- The main mode of variability has four phases: an AMO positive phase (North Atlanic warming), a decrease in the poleward transport (with the corresponding overturning decrease), a AMO negative phase (Atlantic basin cooling) and a poleward transport intensification.
- The propagation of the Thermal Rossby Waves interact with the evolution of the SPG modifying convection in the western SPG, intensity of the SPG and the zonal density gradient contributing to changes in the AMOC.

Chapter 5

Weddell Sea contributing to Atlantic heat variability

In this Chapter, I describe a mode of variability obtained under Mixed Boundary Conditions (MBC), same boundary conditions as in the previous chapter. The mode is characterized by changes in open ocean winter convection in the Weddell Sea, which has a large impact in the Atlantic Ocean heat content.

The Southern Ocean and North Atlantic are the main deep-water formation sites in the ocean, becoming key components of the climate system. The relation at different time scales between these two regions still has to be fully described. This chapter identifies a mechanism by which the Weddell Sea impacts the Atlantic heat content on long timescales. Both multi-decadal and centennial time scales require the use of models to interpret possible observations of the climate in these time scales.

5.1 Introduction

The Southern Ocean (SO) connects all of the oceanic basins through the Antartic Circumpolar Current (ACC) redistributing heat, freshwater and nutrients (Rintoul and Naveira Garabato, 2013). It plays an important role as one of the main loc-

ations where deep dense waters are formed, accounting for about 43% ± 3% of anthropogenic CO_2 in the Coupled Model Inter-Comparison Project 5 (CMIP5) models (Frölicher et al., 2015; Roemmich et al., 2015). It is also known to be one of the main locations for heat uptake in the ocean, estimated by models to be about a 75% ± 22% over the historical period (Frölicher et al., 2015; Roemmich et al., 2015).

The circulation in the Southern Ocean is connected to the North Atlantic through the southwards deep flow of the North Atlantic Deep Water (NADW). At high latitudes NADW upwells and transforms. On the one hand into a surface water mass that moves northward towards the Atlantic and later sinking as Antarctic Intermediate Water (AAIW), NADW-AAIW cell. On the other hand some NADW is transformed into Antarctic Bottom Water (AABW) as an abyssal northward flow back to the Atlantic, the NADW-AABW cell (Talley, 2013; Orsi et al., 1999). AABW forms the lower limb of an overturning that flows northwards in the deep ocean and joins with NADW originating from the North Atlantic, thus closing the overturning cell. The main process of deep-water formation in the Southern Ocean is through brine rejection as sea ice forms on the continental shelves (Rintoul and Naveira Garabato, 2013). There is also a less observed mode of deep-water formation, deep convection in the open ocean, only observed as a Polynya during the winters of 1974-76 (Gordon, 1991).

The interactions between the North Atlantic and the Southern Ocean have been studied since Weyl (1968) proposed that reduction of NADW would expand ice cover through salinity-temperature feedbacks affecting convection. This was later known as the Bipolar Oceanic Seesaw mechanism, associated with centennial-to-millennial time scales, suggesting that changes in the northward heat transport in the Atlantic modulate the ocean heat content in both hemispheres (Broecker, 1998). This mechanism has been suggested to explain the last deglaciation (ca. 19 to 11 thousand years before present) in which opposite climate trends were observed between mid and high latitudes in both hemispheres (Sowers et al., 1995; Blunier et al., 1998; Kaplan et al., 2013). Most of the proposed mechanisms rely on ocean dynamics, in particular on the thermohaline circulation, to explain the relationship

between the North Atlantic and Southern Ocean. However, some details and the timing of this relationship is still unclear.

Several studies have explored the implications between Atlantic and Southern Ocean by perturbing for example the freshwater input in northern/southern high latitudes and the impact on the southern/northern high latitudes, obtaining a mixture of results. Johnson and Marshall (2002) extended the work of Kawase (1987) based on the buffering effect of the equator on the propagation of Kelvin waves through the Western boundary current due to variations in the thermohaline circulation. This buffering limits the size of the responses in the Southern Atlantic to high frequency thermohaline variability coinciding with previous descriptions of the cross equatorial flow by Marotzke and Klinger (2000). Stouffer et al. (2007) suggested a low impact of North Atlantic freshwater input on AABW formation. From the other perspective, studies have been conducted on the impacts of freshwater variations in the Southern hemisphere. Seidov et al. (2001) performed numerical experiments perturbing the Southern Ocean obtained the result that a decrease in AABW formation did not increased the NADW formation, contradicting the theory of the bipolar oceanic seesaw. Instead the authors obtained a decrease in the the AMOC after 100 years. (Swingedouw et al., 2009) later confirmed that the increase or decrease of North Atlantic deep-water formation was at expenses of the deep-water formation in the Southern Ocean. The authors were able to note three processes with an impact in the NADW formation: deep-water formation adjustment, salinity anomalies spreading from the SO and increase in the Southern hemisphere wind stress. The first and last process contribute to enhance the NADW formation, whereas the second it reduces it. Finally, to add to this pool of theories and mechanisms, Latif et al. (2013) and Martin et al. (2013) found that in the Kiel model convection in the Southern Ocean and SST have an independent centennial internal variability.

Whether the AMOC influences the AABW is still unclear. Long term observational data, especially in the Southern Ocean, limited temporally and spatially, is restricted mostly to the surface as most of the data comes from satellite measurements. This contributes to the lack of understanding of internal and natural

variability on decadal time scales and beyond. For example, open ocean convection is a potential driver for variability on those time scales (as will be shown later), but has been observed only in the winters of 1974-1976 in the Weddell Sea region (Weddell Sea Polynya in Fig. 5.2c). The surface of the polynya was estimated to be about 250,000 km^2 through satellite measurements (Zwally and Gloersen, 1977; Carsey, 1980). The polynya intensified surface cooling with an estimated 100-200 W m^{-2} oceanic heat loss and contributed to the formation of about 2-3 Sv of deep-water (Gordon, 1982). Coles et al. (1996) observed with data collected during the 1980s a cooling and a freshening of AABW in the Southern Atlantic basin, potentially associated with the open deep convection. Nevertheless, another polynya has not been observed since then (Gordon, 2014). In addition, de Lavergne et al. (2014) suggest that global warming will increase stratification preventing the occurrence of polynyas in the 21st century.

Despite the lack of observations, CMIP5 simulations suggest open ocean convection may be a potential mechanism for ocean variability on decadal to multidecadal timescales. There is a strong model-dependency in the location and intensity (de Lavergne et al., 2014), mainly due to representation of the sea ice cover (Turner et al., 2013), SST (Wang et al., 2014) or incorrect model parametrizations (Heuzé et al., 2015). Although this is the main process creating AABW in these models, it is not exactly the process observed, brine rejection. According to Kjellsson et al. (2015) two factors limit models to accurately represent processes in the Southern Ocean: model resolution and vertical mixing. Model resolution plays a very important role in the coastal formation of AABW and insufficient vertical mixing limits the ability to reproduce Southern Ocean hydrography, circulation and sea ice in a model. Despite these limitations, the ensemble behaviour of the CMIP5 gives us confidence in projected trends and insights into potential variability mechanisms.

In this chapter, I focus on the interactions between the Weddell Sea and North Atlantic. Multidecadal-to-centennial variability is obtained under MBC in which periods of active deep convection and non convective periods are obtained in the Weddell Sea. These changes impact the North Atlantic overturning and the ocean

heat content in both hemispheres. First I describe the general characteristics of the variability obtained. This variability has been obtained after 2000 years of spin-up, the same time frame as in the previous chapter. Secondly, I will describe the impacts of this variability in the Atlantic and the two regimes obtained in the Weddell Sea. The values represented in the plots and analysis are annual means of the fields.

5.2 Description of the Weddell Sea Variability

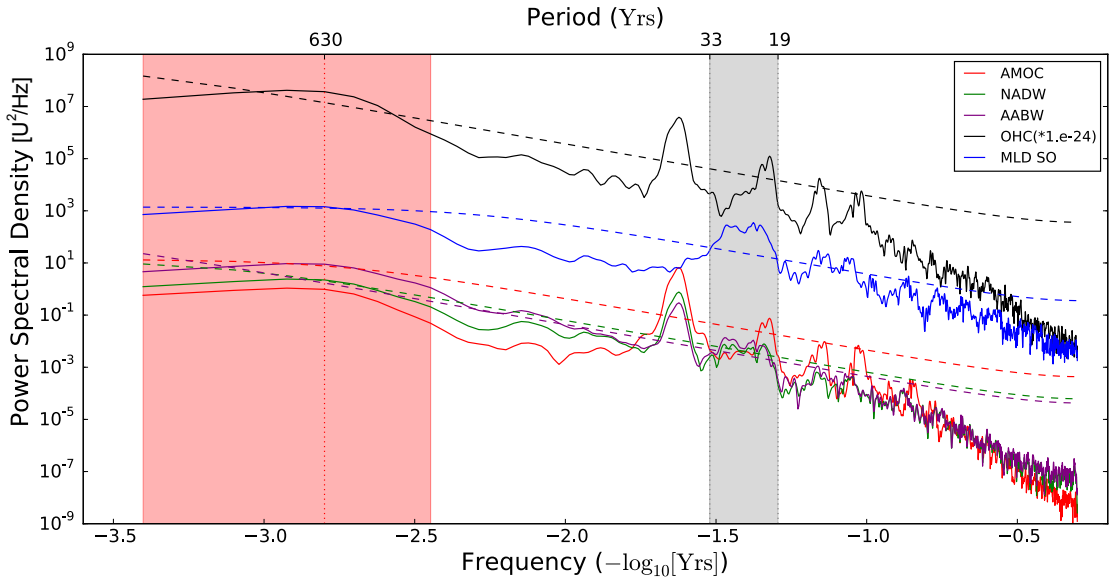

Figure 5.1: Power spectral density of the Atlantic OHC (black), AMOC Index at 30°N at 1000 m (red), 30°S 1000 m depth (green) for NADW, 37°S 3700 m depth (purple) for AABW and mean Mixed layer depth in the Weddell Sea (blue). The spectra has been computed using the Welch's method (Welch, 1967). In dashed lines are shown the 99-% confidence values assuming a red-noise distribution of the time series. Peaks associated with the Weddell Sea vary between a period of 19 and 33 years (shaded grey band). Additionally, as in the heat content, a longer time scale variability shows a significant peak in a multicentennial time scale (red shade). The units of the power spectral density are indicated as U^2/Hz with U the corresponding unit of each variable: Sv, Sv, Sv, W, m (from top to bottom in the legend).

The results presented here were already hinted in Chapter 2, subsection 2.3.1. Whilst in the North Atlantic, the AMOC showed a periodic oscillation of around 42 years with an impact on the North Atlantic Heat content having the same

oscillation period, there was a centennial time scale associated with a Southern Ocean variability mode. In fact, the spectral density of the averaged Mixed Layer Depth (MLD) of the Weddell Sea shows the same peak at centennial time scales (shaded red area in Fig. 5.1). In addition to this centennial time scale, the MLD in the Weddell Sea has a broad peak ranging between 19 to 33 years (shaded in grey), almost invisible in the North Atlantic metrics due to the independence of the frequencies at a multidecadal time scales.

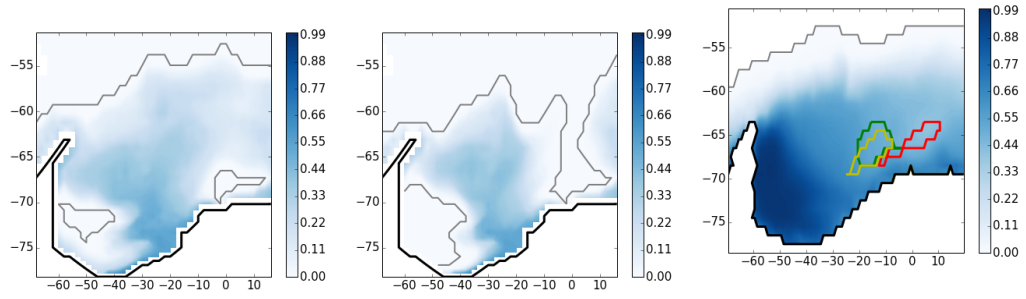

(a) Non-convective Ice cover **(b)** Convective Ice cover **(c)** HadISST mean ice cover and polylnya location

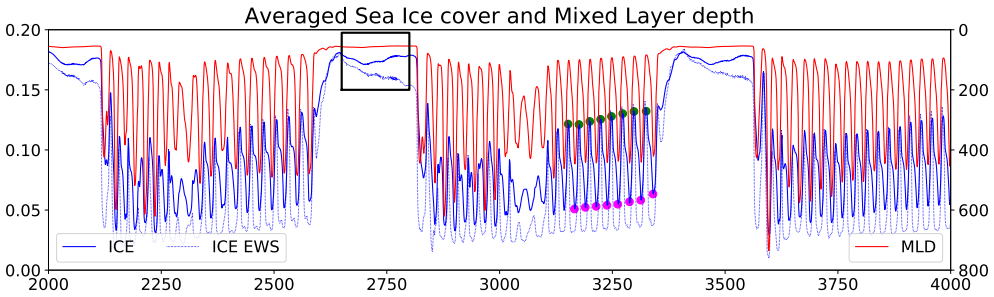

(d) Averaged Ice cover and MLD of the Weddell Sea region.

Figure 5.2: (a): averaged ice cover of non-convective period within the black square in (d). (b): ice cover 3 years after the maximum of ice cover in the convective cycle showing the first regions where the ice is reduced. (c): averaged ice cover in 1970-1990 of HadISST with contours of the observed polynya in 74 (red), 75 (green) and 77 (yellow). (d): Evolution of Sea ice cover and mixed layer depth averaged in the area west of [-60°,10°] and south of [62°,75°] in the 2000 years considered for this study. Also shown is an average of the region west of [-10°,10°] and (5.1 in page 129)[62°,70°] for the ice cover (thin blue)..

The two-time scales in the Southern Ocean are easy to identify in the evolution of the mixed layer depth and ice cover of the Weddell Sea (red and blue lines in

Fig. 5.2d). On the one hand, we observe a multidecadal cycle with variability between 19-33 years and, on the other hand, periods of about 200-300 years of reduced convection and hence a shallow MLD. Together, both modes of variability generate a cycle of about 600-700 years in the Atlantic heat content, leading to a peak in the spectrum in Fig. 5.1. The convective activity represented by the annual average of the MLD in the region is used to name the modes: convective and non-convective.

In the 2000 years that we included in the model analyses, we obtained two full periods of non-convection (years 2577-2822 and 3340-3569) and three periods of active convection (years 2123-2577, 2822-3340 and 3569-4000). These periods have means of 255 years and 486 years respectively. The first and second column of Fig.5.3 show a representative of both periods, non-convective (first) and convective (second) by averaging through one of the periods mentioned before. Firstly, in the surface the convective period has a warmer SST and higher salinity in the western part of the region. A deeper averaged mixed layer depth in the convective region is associated with a lower ice cover in the convective period. Also, a lower circulation in the gyre in the non convective period is obtained modifying the distribution of the upper 500 m temperature, salinity and density distributions.

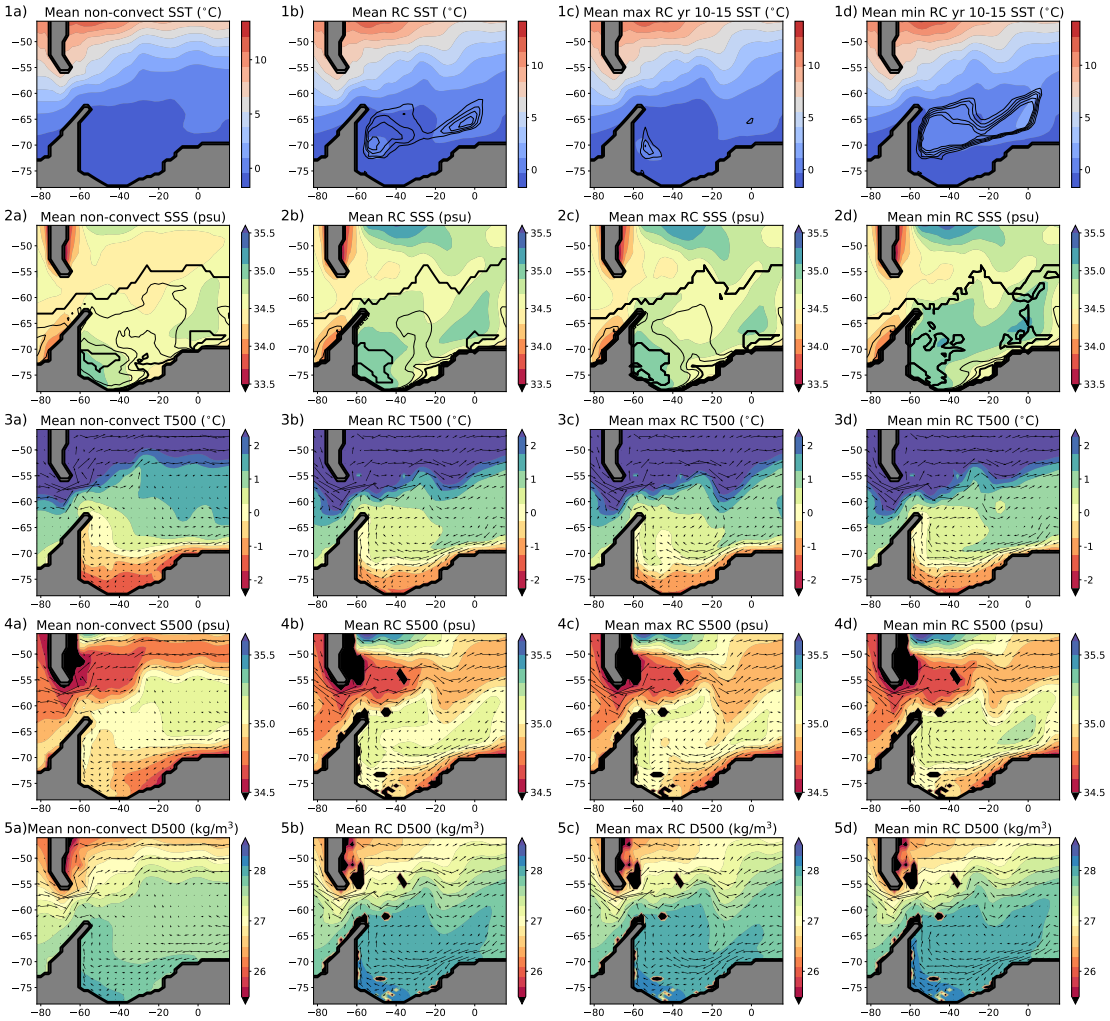

Figure 5.3: Mean state of the Weddell Sea region during non-convective and convective periods. **a** mean of the convective period, **b** mean of the non convective period, **c** high convection in the convective period and **d** low convection in the convective period. **1**: mean SST with contours of MLD from 500 m each 250 m. **2**: SSS and contours of the ice cover with thick lines representing the 0 and 0.5 values and thin values 0.2. **3**: Averages of upper 500 metres temperature with arrows indicating the averaged circulation in the upper 500 m. **4** Averages of upper 500 metres salinity. **4**: Averages of upper 500 density.

5.2.1 Convective Periods

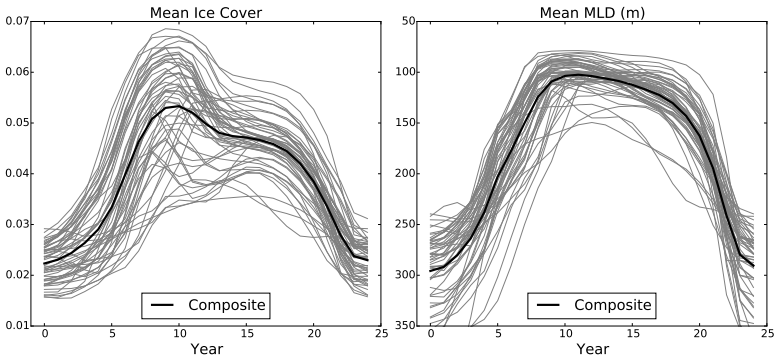

Figure 5.4: Comparison between composite of the ice cover (left) and mixed layer depth (MLD, right) in black and the values of each individual convective period in grey.

About 54 cycles occur between year 2000 and 4000 of the integrations. I defined each cycle as the period between two maxima of the averaged mixed layer depth in the region. The length of the cycles varies between 20 and 29 years with a mean length of 24 years (19 of the 54 cycles have this length). To understand the main characteristics of the cycle, a composite of the 54 cycles was obtained by adjusting the length of each of the cycle to the average cycle duration (24 years). Fig. 5.4 shows composites of spatially averaged MLD and the ice cover, on top of the individual cycles adjusted to the 24-year time scale.

Fig. 5.5 shows the main variables involving the evolution of the Regular Cycle averaged over the whole region west of [-60°,10°] and south of [62°,75°]. The cycle has an asymmetric evolution with respect to time, the strong convective period is shorter (10 years) than the non-convective one (15 years). The mean state of these periods and the overall mean state of the regular cycle is shown in Fig.5.3, column c and d. The main changes between the two periods involve differences east of the Weddell gyre, in the region [-10°,10°] west and [62°,70°] south.

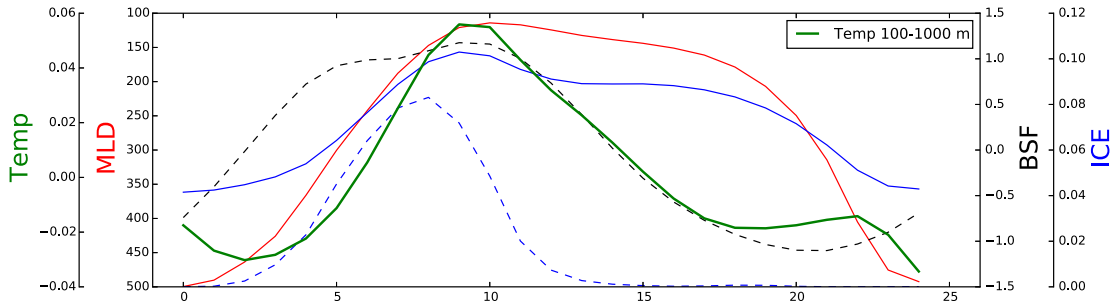

Figure 5.5: Evolution of the composite variables of the cycle averaged over the Weddell Sea area of our study. Shown is the evolution of the temperature averaged between 100-1000 m (solid green line), averaged MLD (red line), ice cover extension (solid blue line) and anomaly of the barotropic stream function (black). The ice cover of the eastern region of the region, where the convection is initiated (dotted blue line). As convection decreases (lowering MLD), ice cover increases and the gyre intensifies, reaching a plateau until the ice cover starts to decrease and convection restarts.

The evolution of the composite starts with the maximum averaged convection in the Weddell Sea . The intense convection is generalized in the Weddell Sea and lower ice cover in the region.It takes about 10 years to reach to the peak of minimum convection in the cycle. During this period, the ice cover east of the Weddell Sea, blue dashed line in Fig. 5.5, increases and as the Gyre intensifies advection contributes to an increase in the upper 500 metres density in this region. The formation of ice doesn't last, initiating convection in the region east of the Weddell Sea around year 14. This region is associated with observations in the 1970s Polynya.

The period of low convection is characterized by increased ice cover in the whole region, a stronger Weddel gyre and an increased upper 500 m salinity (and density), potentially advected by the stronger gyre. Salinity in the surface, as main contributor to the density (Fig. 5.9), contributes to the restart of convection in the region. Convection starts on the eastern and western sides of the Weddell Sea (two foci of the MLD in Fig. 5.3 1b). The area of deep convection expands joining the two initial foci into a single convection region in the maximum convection period.

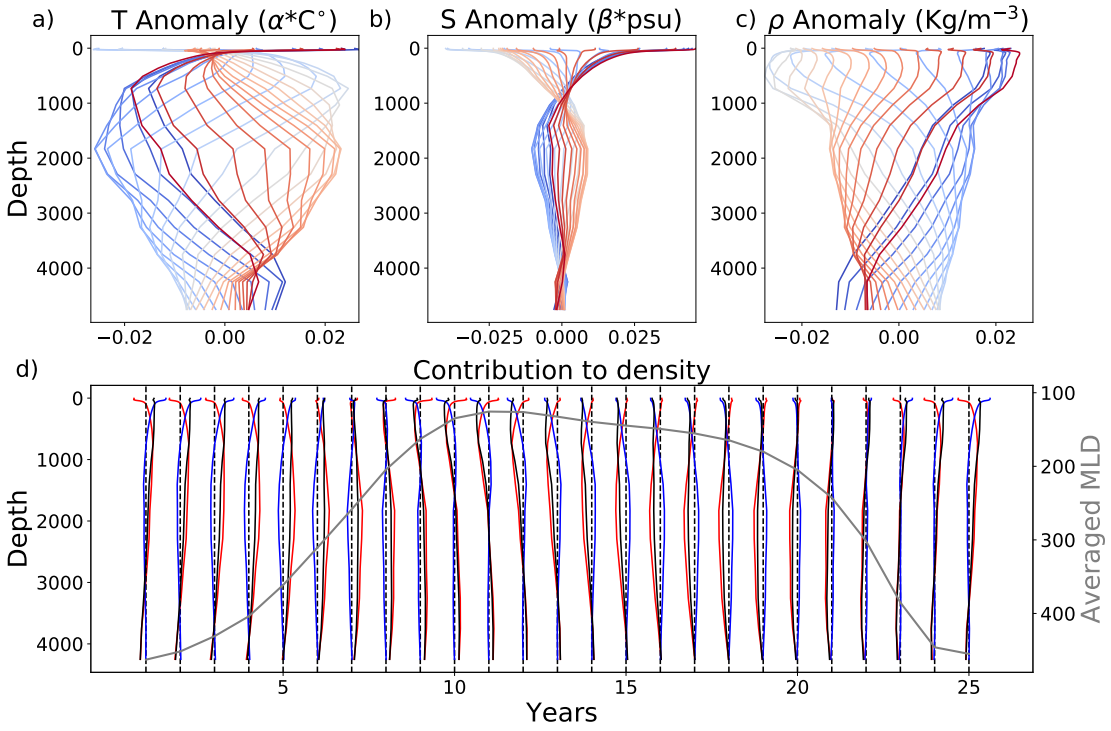

Figure 5.6: Evolution of temperature (**a**), salinity (**b**) and density (**c**) in the regular cycle with respect to depth in the Weddell Sea. Temperature (a) and salinity (b) have been adjusted by α and β respectively. Colorscale indicate the time evolution from year 1 (dark blue) to year 25 (dark red). **d**: Contribution to density in each time step: salinity (blue), temperature (red) and salinity in black. Vertical dashed lines indicate the zero anomaly in each time step. The averaged Mixed layer depth is shown in the Weddell Sea regions (bold grey).

5.2.2 Convection Shutdown

During convective cycles an ice increase/decrease is associated directly with the open convection process. Each cycle cools the ocean surface progressively, contributing to an increasing trend in ice concentration in the final regular cycles before the convection shutdown (green dots in Fig. 5.2d). A complete cycle of a convective and non-convective period is shown in Fig. 5.7. Red-to-blue colors between black and green dots represent the non-convective period and blue-yellow-red the convective period until reaching the convection shut down (black dot). When the convective cycles are stable (red colour), a large amount of heat is released through the surface cooling during active convection. In each cycle the ice cover increases and the upper temperature decreases (blue to yellow to red in Fig. 5.7). It is not

until we reach a threshold of about 0.5°C and 0.14 in the ice concentration that the jump to the non-convective period occurs.

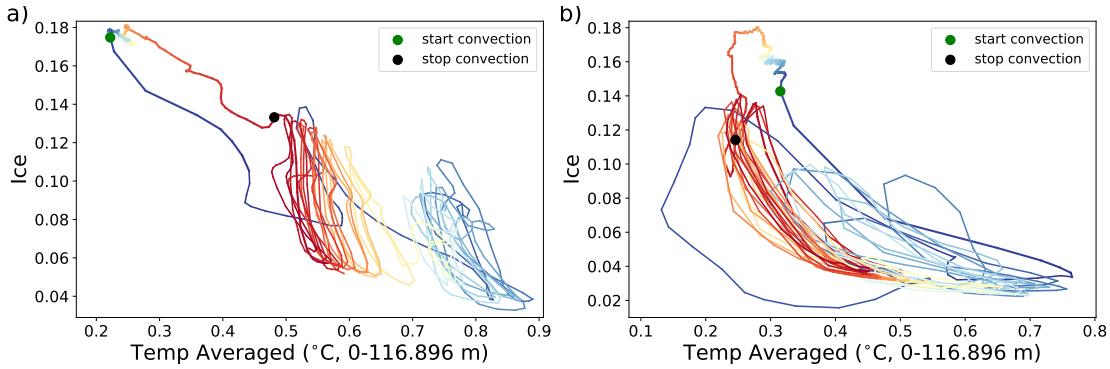

Figure 5.7: Plot of the evolution on a whole centennial cycle of averaged temperatures against ice concentration of the region east of the Weddell Sea, [-10°,10°] west and [62°,70°] south. On the y-axis the ice concentration in the Weddell Sea and, x-axis the temperature averaged over the first 116 m (a) and the average between 100 and 1000 m representing the subsurface (b). The colors indicate the time evolution. It starts in blue as the convection starts (green dot) transitioning from blue to yellow and red during the convective cycles. The black dot represents the stop of convection and, the evolution of the non-convective period is shown as the transition from red to grey and blue.

Spatially, the increase of ice cover is particularly focused on the east of the Weddell Sea. The main differences in the ice cover distribution between the mean of the regular cycle and the non-convective period in Fig. 5.2 are in this region, where the Weddell Sea polynyas were observed. Although our ice parametrization is not perfect and a fair comparison with a polynya can't be done, this suggests that the region is of key importance in the model to control the initiation or cease of deep convection.

5.2.3 Non-convective period and Convection restart

The evolution of the averaged ice concentration against the upper 100 metres, Fig. 5.7a, shows an increase of ice concentration as the temperature decreases during the non-convection period (between black and green dots). As the surface in the whole region cools on average, the subsurface of the ocean warms right before jumping onto a new convective event. The variations in temperature during this period are shown in Fig. 5.8 with a depth integrated, zonal and meridional sections showing

the distribution of the difference in temperatures between the beginning and end of the non-convective period. Also, variability of the water column during the period in temperature, salinity and density are shown in Fig. 5.9.

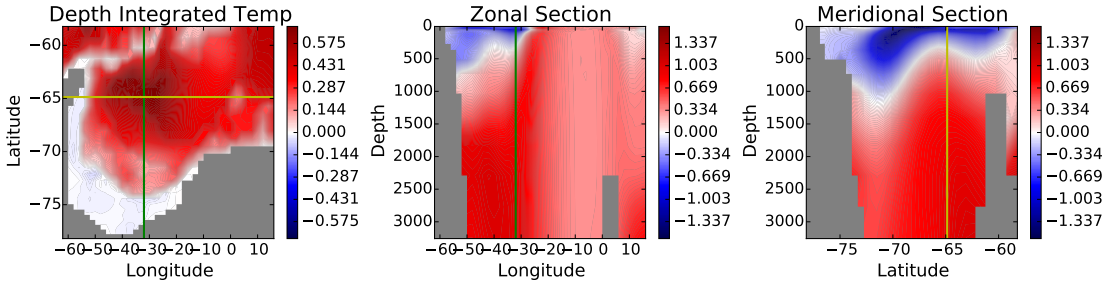

Figure 5.8: Differences between the beginning and the end of the non-convective period. The first panel shows the accumulated temperature (in depth) difference between the initial and final state of the period showing a general warming of the whole region. The following panels show a zonal and meridional section of the temperature differences between the starting point and the final time of the non-convective period.

The main reason behind the restart of convection is related with the ice cover of the region east of the Weddell Sea, west of [-10°,10°] and south of [62°,70°]. After the generalized increase in ice cover, this region is not able to maintain the levels of ice cover, thin blue line in Fig. 5.2d, decreasing with time. This does not occur on the average of the wider region, west of [-60°,10°] and south of [62°,75°], thick blue line in Fig. 5.2d. By looking locally at the evolution of the region in Fig. 5.7b, the evolution of the non convective period in the region and upper 100 m shows an increase of the ice cover and a later decrease as the temperature increases.

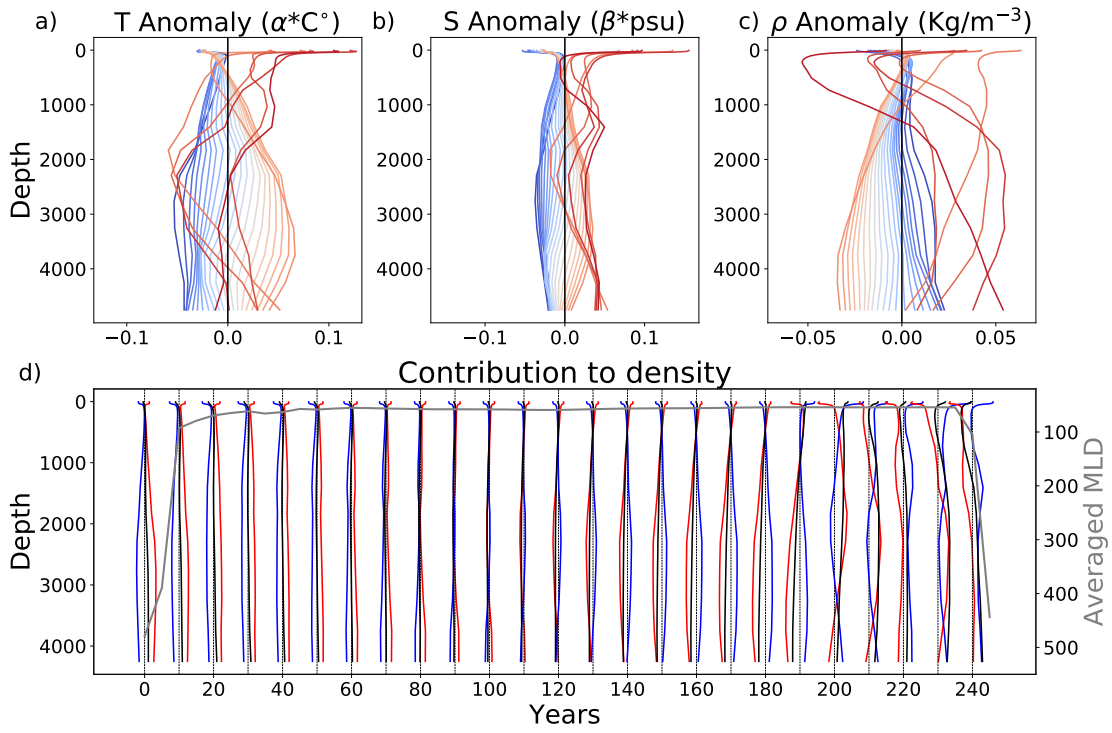

Figure 5.9: Evolution of temperature (**a**), salinity (**b**) and density (**c**) in the non convective period with respect to depth. The nonconvective period shown is between years 2577 and 2822, 245 years in total. Temperature and salinity (**b**) have been adjusted by α and β respectively. Colorscale indicates the time evolution from year 1 (dark blue) to year 240 (dark red). **d**: Contribution to density in each time step: salinity (blue), temperature (red) and salinity in black. Vertical dashed lines indicate the zero anomaly in each time step. The averaged MLD is shown in the Weddell Sea regions (bold grey).

5.3 Impacts of the variability in the Atlantic

The variability observed in the Southern Ocean does not impact exclusively this region, it also impacts the whole Atlantic.In Fig. 5.10a the evolution of heat content in the Atlantic (north of 30°S) and in the northern hemisphere show a synchronized response to changes in the Southern Ocean convection. The ocean heat content has been computed integrating in 3-dimensions the temperature field in the appropriate volume (Atlantic, northern hemisphere or Southern Ocean) multiplied by an averaged density 28.7 kg m^{-3} and the specific heat of seawater (4×10^{-3} J/C/g). Variations averaged over the entire Atlantic Ocean are about 1.5×10^{22}J between high and lower peak of the oscillations, about a 10% of its total value. For the Southern Ocean and northern hemisphere this is reduced to 0.6×10^{22}J and

0.9×10^{22}J respectively. These values show the large contribution of the Southern Ocean variability to the heat content in the Atlantic.

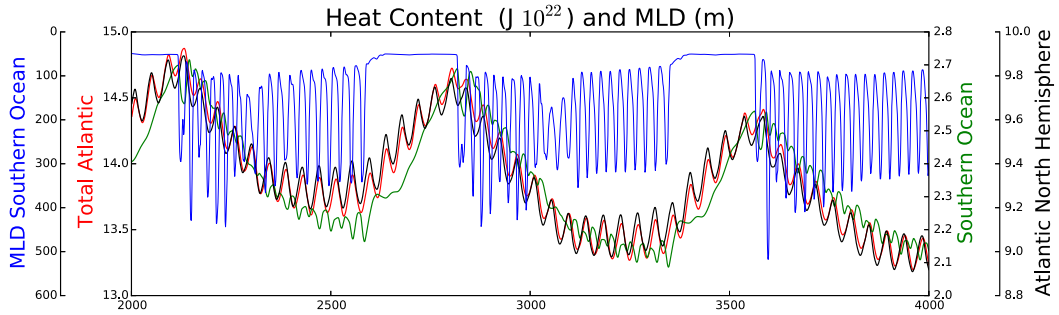

(a) Variability of the Atlantic heat content, SO heat content and MLD in the SO

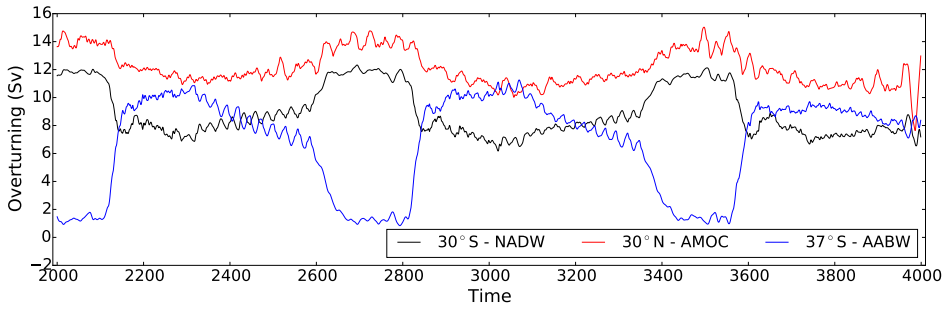

(b) Filtered circulation in the Atlantic

Figure 5.10: In the top panel, the evolution of the heat content in the Atlantic (above 30°S, black), Southern Ocean (Below 60°S, green) and Atlantic northern hemisphere (red), global Atlantic (black) and MLD of the Weddell Sea (blue). In the bottom panel, filtered time series of the circulation in the peaks of the North Atlantic (periods between 37-51.4 years, 19.3-24 years, 12.9-16.2 years and 9.7-11.7 years). A representative of NADW is considered by the overturning rate at 30°S and 1000 m depth, circulation of AABW is represented by the circulation at 37°S and 3700 m depth. As before, the AMOC is measured by the overturning at 30°N and 1000 m depth. Here the AABW values are multiplied by -1 for convenience.

As observed in the variability of the heat content, both modes impact strongly the total Atlantic heat content: increasing during non-convective periods and decreasing during convective periods in the Weddell Sea (black line in 5.10a). This highlights the importance of the Southern Ocean regulating the ocean heat content.

Changes in deep convection in the Weddell Sea also affects the AMOC, measured with the AMOCI (30°N and 1000 m depth). I took a representative of the two main

water masses in the Atlantic: NADW (at 30°S and 1000 m depth) and AABW (at 37°S and 3000 m depth). Their evolution along the 2000 years is shown in Fig. 5.10b with a band pass filter filtering out the periods between 37-51.4 years, 19.3-24 years, 12.9-16.2 years and 9.7-11.7 years. The band pass filter has been applied to remove off the variability generated in the North Atlantic already explained in the previous chapter. Under these considerations, changes in AABW are about 10 Sv between periods of active convection and non-convection. The variability in the other two values, NADW and AMOC, are lower and, on an average of 5 Sv and 3 Sv respectively. The shutdown of active convection in the Weddell Sea modifies mainly the lower cell (AABW cell), reducing from the -10 Sv to about -1 Sv on average between both periods. Note that in Fig. 5.10b this quantity is multiplied by -1 for convenience. The meridional average of the non-convective period shows a very weak lower cell, with the North Atlantic overturning reaching 3000 m depth at 40°S (not shown).

The relationship presented here, supports the idea of a bipolar oceanic see-saw: an increase/decrease of AABW production is associated with a decrease/increase of NADW and vice versa. Swingedouw et al. (2009) explained this phenomenon with reduced AABW production by a downward shift of the isopycnals in the South Atlantic, which causes an anomalous density gradient allowing the NADW to reach unusually high southern latitudes in the deep ocean.

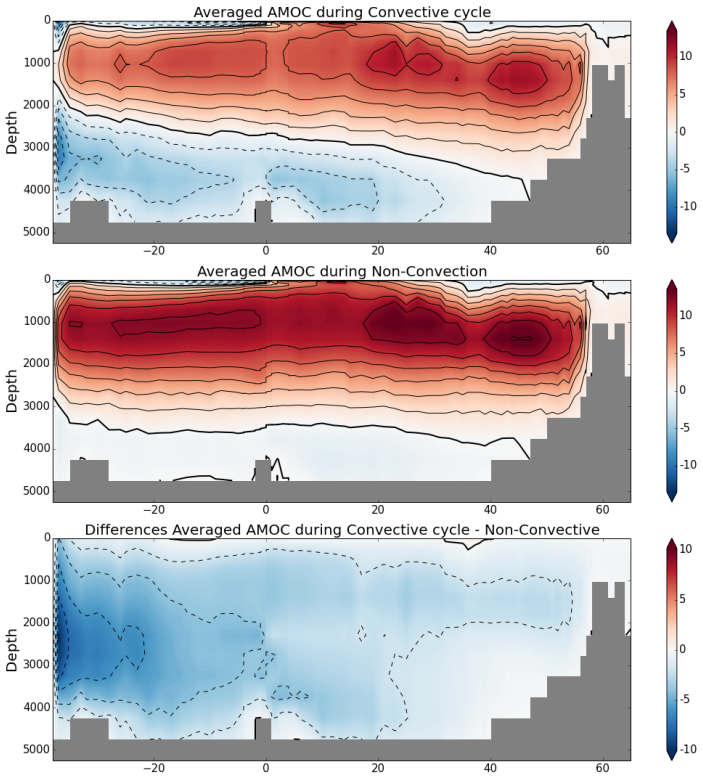

Figure 5.11: Comparison between composite of the ice cover (left) and mixed layer depth (MLD, right) in black and the values of each individual convective period in grey.

In the work here presented, the see-saw mechanisms is slightly more complicated and several timescales are involved. Changes in the North Atlantic have a strong impact reaching the Southern Ocean, in Fig. 5.1 all the representatives of the main water masses show a significant peak in the power spectral density around 42 years, making the variability in the North Atlantic the main driver of the water masses in this configuration in multidecadal time scales. On the other hand, the Southern Ocean controls the long time scales increasing the formation/rate of NADW when AABW ceases due to a lack of deep convection in the Weddell Sea region. The changes in the values of AABW are about the double of the changes in NADW. Once the 42-year period and higher harmonics are filtered, Fig. 5.11 shows that once the convective cycles become regular (about half way between two non-convective periods) there is a see-saw-like interaction between NADW and AABW, showing that this competition between NADW and AABW occurs on different time scales.

5.4 Conclusions

The mechanism described in this chapter, consists on a centennial variability in which the combination of convective and non-convective periods in the Southern Ocean contribute to changes in the heat content in the Atlantic. This mechanism was observed previously by Martin et al. (2013), remarking the central role of the ice formation parametrization to limit the length of these non-convective periods. Their work has been reproduced here in a more simplistic set-up highlighting the importance of the ocean-ice interactions for this mode to occur. Additionally, I related the mode in the Southern Ocean to the variability obtained in Chapter 4, showing the bidirectional relationship between the two multidecadal mechanisms, although the North Atlantic is the lead mechanism in both hemispheres impacting both deep-water masses.

The variability in the Weddell Sea shows on the one hand a period of active deep convection with a cycle of a mean duration of 24 years. This multidecadal cycle initiates enhanced open ocean convection as ice decreases in a sensitive region in which previous polynyas have been observed. After the period of deep convection, the reduced convection promotes heat storage at mid-depth de-stabilizing the stratified water column and enhancing deep-water formation. On the other hand, longer periods of about 255 years of complete non-convection in the Weddell Sea promote the increase of ocean heat content with the cessation of AABW formation.

The transition between the convective period to non-convective is promoted by both the cooling effect of the convection in the whole water column on each cycle and the increase of ice formed after each cycle reducing the formation of AABW. In particular it occurs as the eastern region of the Weddell Sea gyre has an increased ice concentration blocking the beginning of convection in the following cycle. After the non-convective period, the shift back onto a regular convective cycle occurs both by a decrease in the ice cover east of the Weddell Sea (where convection is initiated in the regular cycle, and an accumulation of heat at mid-depth which preconditions the water column to initiate the active convection again.

Open ocean deep convection, although not currently observed in the Antarctic

region, is a mechanisms dominant in most of the models considered for CMIP5 as the principal formation process of AABW. Instead, in the Antarctic basin the main observed process for deep-water formation is through brine rejection. It is argued by Gordon (2014) that open ocean deep convection was more common in the past and dominated the formation of deep-waters in the Southern Ocean as the ice sheets advanced over the continental shelf (Golledge et al., 2013). Hence the mechanisms presented here may have played a role in past climate.

The interaction between the formation of AABW and NADW is known as the bi-polar ocean seesaw (Broecker, 1998). The mechanism presented here shows this interaction very clearly, an increase in AABW is associated with a decrease in NADW and vice versa. The tight relation between both water masses can be related to the modes of variability found in this configuration. The North Atlantic variability depicted in Chapter 4 and that in the Southern Ocean presented here, describe further our understanding between these two components of the climate. The 42-year variability of the North Atlantic affects all the water masses in the Atlantic, showing a peak in the spectrum including the AABW. The Weddell Sea mechanism has an impact mainly on the NADW and more weakly on the AMOC. In this case, the signal seems to propagate on shorter time scales when compared to the work of Martin et al. (2013) using the Kiel Climate Model, in which the reaction of NADW to the reduction of AABW formation in the Weddell Sea had a time lag of about 100 years. The model was coupled with the atmosphere and an ice model, these changes may contribute to the difference in the time scales.

The work here presented is obtained in an ocean only model under MBC, with their corresponding limitations and characteristics previously explained (Chapter 2). Also, by being an only ocean model, we are missing interactions of the modes here presented with the atmosphere. In fact, previous work has shown that the atmosphere is a key component connecting changes in the AMOC with the Southern Ocean (Zhang et al., 2016b). Future work can be directed to find possible similarities in the long control runs of the new CMIP6 experiments. Also, further analysis can be performed for future publication of this chapter exploring the role of mechanisms such as the equatorial buffer (Kawase, 1987) in which we can consider the

buffering of strong changes in the North Atlantic transferred through Kelvin waves by Rossby waves radiated in the east coast by the Kelvin wave crossing the equator from west to east and then splitting to the north and south. Marshall et al. (2001) showed that the periods of the North Atlantic variability was of key importance for the buffering limiting the size of the response. With the various periods here presented we could look at this mechanisms and interactions between the north and south hemisphere relationship further. We could also potentially investigate evidence of multidecadal to centennial variability in the paleo-records.

5.5 Key Results of this Chapter

- A centennial mode of variability that depends on the ice cover and heat storage in the Weddell Sea causes large changes in the Atlantic heat content.
- This mode supports up the opposite evolution of AABW and NADW (Atlantic see-saw) on different time scales (multi decadal lead by the North Atlantic and centennial lead by the Weddell Sea).
- Weddell sea variability shows high signature in regions where previous polynyas have been observed.

Chapter 6

Discussion

6.1 Overview of the Results

The general approach presented in this thesis is based on dynamical systems theory. This means that I am not only interested in the climate system itself, represented by climate models as best approximation, but also on the sensitivity and interactions between the different components. With a focus on the ocean, I centred my work on potential mechanisms of Atlantic variability and the impact of initial condition errors in the Sea Surface Salinity (SSS) on the Atlantic Meridional Overturning Circulation (AMOC). In order to remind the aims of this thesis, the research objectives are shown below:

Research objectives

1. To assess the impact of errors in the initialization of the surface salinity and predictability on decadal time scales and its impacts on the AMOC.

2. To investigate under what surface forcing conditions does the ocean spontaneously generate (Atlantic) variability on decadal and longer timescales and to elucidate the mechanisms of such variability

In Chapter 3, I presented a set of experiments testing the sensitivity of the AMOC to errors in the SSS. An SSS anomaly, shaped as a Gaussian distribution,

was defined by two parameters: horizontal extension and intensity (factor multiplying the maxima of the distribution). I tested 6 different horizontal extensions ranging from an almost a punctual perturbation to a large scale perturbation. Intensity varied between -33 psu up to 60 psu. Note that the perturbation was only applied in the first 10 m of the model and large values were moderated when considering their impact on the whole water column.

The results show an initial impact about 8-10 years after the perturbation, which is consistent in all the experiments. The AMOC response to these initial errors range between 0.001 to 0.08 Sv psu^{-1} for lower and higher extensions respectively. I defined statistically a linear regime as a tool to relate this work to previous linear approaches and to understand the limits of non-linearities in the AMOC response. The different sign of the initial perturbation is a key factor enhancing or limiting the non-linear response. Negative perturbations generate a larger AMOC anomaly compared to the linear prediction which depends strongly on the extension of the perturbation. Instead the response of positive perturbations is better predicted by linear approximations, with errors mainly associated to the magnitude of the perturbation. Finally, I related this work to the precursors of AMOC variability such as the Great Salinity Anomalies (GSAs). Assuming that the geometry of our perturbations could be considered as the GSAs, I computed the possible impact of errors in historical reconstructions which do not force their model with similar anomalies to observed ones. The impact on the AMOC vary between less than 0.3 Sv for the smallest extensions, almost punctual perturbations, up to 1-2 psu for the largest ones.

Both Chapter 4 and Chapter 5 are focused on different modes of variability obtained in Océan PArallélisé (OPA) under Mixed Boundary Conditions (MBC). Firstly, I described in Chapter 4 the variability in the North Atlantic induced by the propagation of Thermal Rossby waves. The main frequency of variability, with a period of 42 years, was described as a cycle with the following characteristics:

- The cycle has four phases: a AMO positive phase (North Atlantic warming), a decrease in the poleward transport (with the corresponding overturning decrease), a AMO negative phase (Atlantic basin cooling) and a poleward

transport intensification.

- The propagation of the waves are tilted, the subsurface leads with respect to the lower depths of the wave. This indicates that the mechanism of self-advection proposed by Sévellec and Fedorov (2013b) contributes to the instability of the wave reducing the propagation speed of the wave.

- The propagation of the Thermal Rossby Waves interact with the evolution of the SPG modifying convection in the western SPG, intensity of the SPG and the zonal density gradient contributing to changes in the AMOC.

As well higher harmonics of this variability were obtained with periods of 21, 14 and 10.5 years. However, the impact of these high frequencies contributed to less than 15% of the variability in the main indexes of the North Atlantic (AMOCI, T, S, ρ).

After looking at the North Atlantic, Chapter 5 explores the variability obtained in the Weddell Sea, which is responsible for a peak in the North Atlantic spectrum on a centennial time scale. A combination of convective and non-convective periods creates changes in the heat content of the whole Atlantic, affecting as well the circulation. An increased overturning in the North Atlantic is obtained as the convection in the Weddell Sea is shutdown. The sensitivity of the Weddell Sea to ice cover and subsurface heat storage are key players leading the variability obtained. In the case of the ice cover, a similar signature of ice variability was obtained in regions where previous polynyas have been observed.

6.2 Implications of the results

The chapters of this thesis contribute to the knowledge on model variability of the North Atlantic on different time scales. The implications of this thesis are important for better understanding of the mechanisms of North Atlantic variability, for predictability and data assimilation.

Implications for the mechanisms of North Atlantic variability In this work I showed a close interaction between the AMO and AMOC. I presented a mechanism previously obtained as weakly damped mode of variability in the North Atlantic that corresponds to a westward propagation of density anomalies (Sévellec and Huck, 2015). The mode is characterized by a period of about 42 years evolving as follows: AMO positive phase (North Atlantic warming), a decrease in the poleward transport (with the corresponding overturning decrease), AMO negative phase (Atlantic basin cooling) and a poleward transport intensification. Muir and Fedorov (2017) investigated the existence of this mode in the simulations of the Coupled Model Inter-Comparison Project 5 (CMIP5) models obtaining that more than half of the models exhibit variability similar to the mechanism proposed in Sévellec and Huck (2015). Here I obtained the same mechanism in an ocean only model, OPA, under MBC. Some of the models in the CMIP5 models have Nucleus for European Modelling of the Ocean (NEMO) (advanced version of OPA) as their ocean component, which would explain why some of them show this mode in their variability.

Decadal-to-multidecadal variability have been observed in a state-of-the-art global-ocean reanalysis product, GloSea5. Jackson et al. (2016) concluded that in the recent decrease in the AMOC of the past decade, decadal variability have played a key role. In their work they remarked the crucial role of the Labrador Sea propagating density anomalies through the deep western current. A further look on these reanalysis products such as GloSea5 or EN4 could be pursued in order to verify the existence of modes such as the ones presented in this thesis. Or even in the new CMIP6 models soon to be ready to be analyzed. Firstly, it could be interesting to understand decadal-to-multidecadal peaks in the spectrum of each model in the pre-industrial control runs on the AMOC, what are the differences between the models, peak in the frequencies, etc. Secondly, it could be also worth identifying common patterns of temperature propagation in the models in the subpolar gyre using a tool recently developed named Lower frequency component analysis (Wills et al., 2017), which differ from the standard empirical orthogonal functions since the resultant EOF maximize the ratio of low-frequency (signal) to high-frequency (noise) variance. This method was proved to describe better processes which sev-

eral time scales are involved. For the case of a mode such as that here presented with different frequencies, this method could be used potentially to untangle the different modes of variability. Finally, we could look for indicators of the mechanism presented on chapter 4 of the mechanism, relating the propagation of the waves to the SPG intensity or convection in the western SPG with the propagation of the anomalies in the models showing propagation of density anomalies.

Implications for predictability This thesis contributed to understand the predictability limits obtained by errors in the initial conditions for decadal predictions. Currently, the impact of initial conditions in predictions is not completely understood and advances are contributing to their understanding (Germe et al., 2017; Volpi et al., 2016). In particular with the oceanic component, unknown uncertainties in historical datasets increase with depth, with non of the studies focused on the surface and subsurface. The importance of the deep ocean on decadal time scales has been demonstrated by Sévellec and Fedorov (2013a). The authors showed that the reduction of model biases developed when models are forced with surface data can be achieved by imposing deep ocean perturbations (in particular in the southern Ocean).

Hawkins et al. (2016) differentiated in the context of near-term predictions two approaches to the impact of initial conditions, macro initial conditions and micro initial conditions. The first one refers to the impact of large scale initial conditions, e.g. different ocean states, to understand the response of the model to changing forcing conditions. In a way this would correspond to study the impacts of large scale anomalies on surface fields such as the large extension perturbations in Chapter 3. The results of the chapter showed that the response of the AMOC to these anomalies is non-linear with respect to the intensity of the perturbation introduced, mainly for perturbations of negative salinity. Testing the impact of these large scales anomalies in different oceanic states could provide information on the sensitivity of the system. For example, focusing on the AMOC, we could test the impact of these initial perturbations in the system from a high AMOC peak or a low peak. Experiments could be designed to test this kind of sensitivity in all the models of the CMIP5/CMIP6 models choosing from pre-industrial runs

and coordinate the initialization of historical runs on these states.

In contrast to the macro initial conditions, in the smallest scales exists an irreducible uncertainty in the initial conditions in single grid points e.g. small changes of SST at a grid point. The initial conditions would provide a probability distribution function given a model and a macro initial state for different prediction times. These micro initial conditions relate to the smaller extensions in Chapter 3. As an almost punctual perturbations the errors in the initial conditions have a linear impact on the AMOC.

In order to fully understand the behaviour and impacts of initial conditions in the models, with a focus on decadal time scales, a good approach would be to coordinate experiments in the CMIP models to test individual impacts of the micro-scale on several macro-states. This approach would test the sensitivity in a multi-model approach giving confidence intervals and predictability measures of the different metrics of the climate system.

Implications for data assimilation Modelling groups have been exploring various techniques for reconstruct the climate including observations in the different models (Meehl et al., 2014). The data considered vary from including only surface data to 3-dimensional fields (salinity, temprature, winds, etc.). The techniques range from a simple Newtonian relaxation, or nudging, to a more complex assimilation such as optimal interpolation (Mogensen et al., 2012).

In particular, nudging techniques are computationally cheap techniques to include data information minimizing drift of the model towards the state of the data. By including anomalies of the data we only "push gently" the model with the information without forcing it onto a different state. In general, models have their own trajectory in phase space different from the realistic climate (observations). Introducing the raw observations generates a response in the model directing itself towards the observed state and back again towards the model state after the impact of the nudging fades away. This would show an artificial variability that would make more difficult to detect real model variability.

Subsurface nudging is probably the most efficient method to constrain the density gradients influencing the ocean circulation through geostrophic balance (Sévellec and Fedorov, 2013b). Nevertheless, accuracy and good temporal-spatial sampling in the subsurface data is limited to the last 17 years thanks to the ARGO era. Before that, the sparse observations would introduce uncertainty affecting the reliability of assimilation in regions of key importance for some components of the climate. For example, uncertainty in the information on the Gulf Stream or Labrador Sea would decrease the reliability on the AMOC state (Turpin et al., 2016). In fact, ocean reanalyses tend to disagree in certain features of the climate such as the subpolar gyre (Born et al., 2015), the AMOC (Karspeck et al., 2015) or the temperature evolution below 500 m (Ray et al., 2015). This might suggest that surface nudging is a good approach. Also, while the gaps in the subsurface record are a key barrier to constrain subsurface temperature, the SST at the largest scales record is well understood (Kent et al., 2017).

Nudging have only been applied in a perfect model framework (Servonnat et al., 2014; Ortega et al., 2017). From a long control run a period considered as target and another as control are chosen. The information from the target (SST, SSS, winds, etc.) is then used to nudge the control run approximating it as much as possible the state of the run to the target. The results of Servonnat et al. (2014) indicate that in order to obtain a good 3-dimensional oceanic reconstruction, it is necessary to include both SST and SSS. Further work of Ortega et al. (2017) showed that in order to represent the AMOC extreme events both wind and a factor controlling the strength of the nudging had to vary proportionally to the mixed layer depth.

The next step is to use these techniques in the historical context, but the need to include SSS in the reconstruction rise questions about the accuracy of salinity records and how the uncertainty on those will play a role in the reconstruction. The work in these thesis provided a sensitivity analysis that could serve as guidance for the impact of the uncertainty involved in the historical surface salinity record. Friedman et al. (2017) have published a data set of Atlantic surface salinity from from 1896 to 2013 with potential to be used in this context. The work here presen-

ted with the perturbations (Chapter 3) can be considered as a previous step to this kind of applications. It helps to understand the possible impacts of uncertainties introduced in the system as the records have quite large spatial (the Atlantic is divided in 32 boxes of scales between 100-1000 km) and temporal uncertainty (the record shows no data for example during the two World War periods, 1914-21 and 1941-49). The perturbation experiments have shown, in the case of the AMOC, the impact of uncertainty in the SSS. The largest impact obtained was about 2-3 Sv for very large amplitude and extension, but mostly important was the difference in the response depending on the sign of the perturbation introduced.

Appendix A

Evolution of Perturbation in L1

I included this description in the appendix to avoid describing the evolution of the perturbations located on L1 before actually describing the evolution of the perturbations at L0.

In the case of L1, the initial anomaly imposed between 40-50°N in the center of the Atlantic generates in the first year an anomalous deepening of the mixed layer depth and a reduction of the Gulf Stream. The density anomaly quickly propagates north-east with the north Atlantic current. Part of the anomaly is as well advected through the subpolar gyre reaching south of the Labrador Sea (Fig. A.1 1c)). This anomaly propagates westward as Thermal Rossby wave, generating changes in the meridional velocities impacting the AMOC. The propagation process is exactly the same as with L0 but delayed by the time the initial anomaly takes to arrive through the SPG to the Labrador Sea.

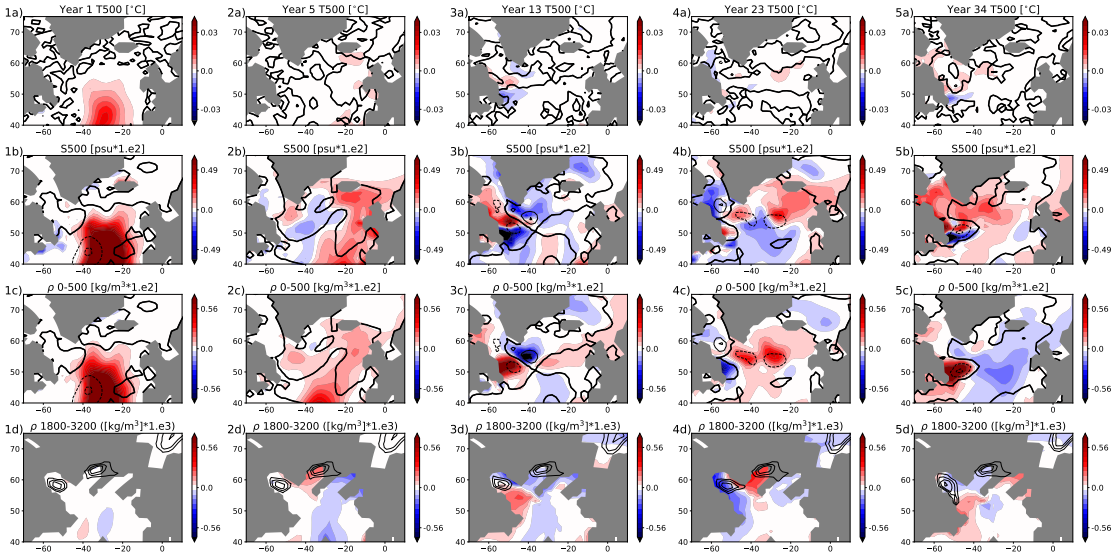

Figure A.1: Snapshots of the evolution of the L1. The rows indicate anomalies with respect to the initial state, before changing the boundary conditions and the columns different times in the evolution, years 1, 5, 13, 23, 34. a) SST anomalies (first row) are shown with contours of the mixed layer depth with contours every 100 m and the bold line representing the zero anomaly. b) SSS anomalies are shown with a correction factor of 10^2 and contours of the barotropic stream function anomaly every 0.5 Sv with the bld line indicating the zero anomaly. Averaged density in the first 500 metres is shown corrected by a factor of 10^2 and the same contours as the SSS. d) Density anomalies averaged between 1800 and 2300 metres. Contours show the mixed layer depth with contours every 500 m .

Bibliography

Arzel, O., T. Huck, and A. Colin de Verdière, 2006: The Different Nature of the Interdecadal Variability of the Thermohaline Circulation under Mixed and Flux Boundary Conditions. *Journal of Physical Oceanography*, **36 (9)**, 1703–1718, doi:10.1175/JPO2938.1.

Balmaseda, M. A., K. Mogensen, and A. T. Weaver, 2013: Evaluation of the ECMWF ocean reanalysis system ORAS4. *Quarterly Journal of the Royal Meteorological Society*, **139 (674)**, 1132–1161, doi:10.1002/qj.2063.

Belkin, I. M., S. Levitus, J. Antonov, and S. A. Malmberg, 1998: 'Great Salinity Anomalies' in the North Atlantic. *Progress in Oceanography*, **41 (1)**, 1–68, doi:10.1016/S0079-6611(98)00015-9.

Bellomo, K., L. N. Murphy, M. A. Cane, A. C. Clement, and L. M. Polvani, 2018: Historical forcings as main drivers of the Atlantic multidecadal variability in the CESM large ensemble. *Climate Dynamics*, doi:10.1007/s00382-017-3834-3.

Ben Jelloul, M., and T. Huck, 2003: Basin-Mode Interactions and Selection by the Mean Flow in a Reduced-Gravity Quasigeostrophic Model. *Journal of Physical Oceanography*, **33 (11)**, 2320–2332, doi:10.1175/1520-0485(2003)033⟨2320:BIASBT⟩2.0.CO;2.

Ben Jelloul, M., and T. Huck, 2005: Low-frequency basin modes in a two-layer quasigeostrophic model in the presence of a mean gyre flow. *Journal of Physical Oceanography*, **35 (11)**, 2167–2186, doi:10.1175/JPO2797.1.

Bigg, G. R., T. D. Jickells, P. S. Liss, and T. J. Osborn, 2003: The role of the

oceans in climate. *International Journal of Climatology*, **23 (10)**, 1127–1159, doi:10.1002/joc.926, arXiv:1011.1669v3.

Bindoff, N., and Coauthors, 2013: Detection and Attribution of Climate Change: from Global to Regional. *Climate Change 2013 - The Physical Science Basis*, Intergovernmental Panel on Climate Change, Ed., Cambridge University Press, Cambridge, 867–952, doi:10.1017/CBO9781107415324.022.

Biondi, F., A. Gershunov, and D. R. Cayan, 2001: North Pacific Decadal Climate Variability since 1661. *Journal of Climate*, **14 (1)**, 5–10, doi:10.1175/1520-0442(2001)014⟨0005:NPDCVS⟩2.0.CO;2.

Blanke, B., and P. Delecluse, 1993: Variability of the Tropical Atlantic Ocean Simulated by a General Circulation Model with Two Different Mixed-Layer Physics. *J. Phys. Oceanogr.*, **23 (7)**, 1363–1388, doi:10.1175/1520-0485(1993)023\%3C1363:VOTTAO\%3E2.0.CO;2.

Blunier, T., and Coauthors, 1998: Asynchrony of Antarctic and Greenland climate change during the last glacial period. *Nature*, **394**, 739–743, doi:10.1038/29447.

Born, A., J. Mignot, and T. F. Stocker, 2015: Multiple equilibria as a possible mechanism for decadal variability in the North Atlantic Ocean. *Journal of Climate*, **28 (22)**, 8907–8922, doi:10.1175/JCLI-D-14-00813.1.

Branstator, G., and H. Teng, 2010: Two limits of initial-value decadal predictability in a CGCM. *Journal of Climate*, **23 (23)**, 6292–6311, doi:10.1175/2010JCLI3678.1.

Branstator, G., and H. Teng, 2012: Potential impact of initialization on decadal predictions as assessed for CMIP5 models. *Geophysical Research Letters*, **39 (12)**, 1–5, doi:10.1029/2012GL051974.

Branstator, G., H. Teng, G. A. Meehl, M. Kimoto, J. R. Knight, M. Latif, and A. Rosati, 2012: Systematic estimates of initial-value decadal predictability for six AOGCMs. *Journal of Climate*, **25 (6)**, 1827–1846, doi:10.1175/JCLI-D-11-00227.1.

Broecker, S., 1998: Paleocean circulation during the Last Deglaciation: A bipolar seesaw? **13 (2)**, 119–121.

Brown, P. T., M. S. Lozier, R. Zhang, and W. Li, 2016: The necessity of cloud feedback for a basin-scale Atlantic Multidecadal Oscillation. *Geophysical Research Letters*, doi:10.1002/2016GL068303.

Bryan, K., 1969: A numerical method for the study of the circulation of the world ocean. *Journal of Computational Physics*, **4 (3)**, 347–376, doi:10.1016/0021-9991(69)90004-7.

Bryden, H. L., B. A. King, G. D. McCarthy, and E. L. McDonagh, 2014: Impact of a 30% reduction in Atlantic meridional overturning during 2009-2010. *Ocean Science*, **10 (4)**, 683–691, doi:10.5194/os-10-683-2014.

Buckley, M. W., D. Ferreira, J.-M. Campin, J. Marshall, and R. Tulloch, 2012: On the Relationship between Decadal Buoyancy Anomalies and Variability of the Atlantic Meridional Overturning Circulation. *Journal of Climate*, **25 (23)**, 8009–8030, doi:10.1175/JCLI-D-11-00505.1.

Buckley, M. W., and J. Marshall, 2016: Observations, inferences, and mechanisms of the Atlantic Meridional Overturning Circulation: A review. *Reviews of Geophysics*, **54 (1)**, 5–63, doi:10.1002/2015RG000493.

Carsey, F., 1980: Microwave observation of the weddell polynya. *Monthly Weather Review*, **108 (12)**, 2032–2044.

Cessi, P., and F. Paparella, 2001: Excitation of basin modes by ocean-atmosphere coupling. *Geophysical Research Letters*, **28 (12)**, 2437–2440, doi:2000GL012660, 2000GL012660.

Chylek, P., C. Folland, L. Frankcombe, H. Dijkstra, G. Lesins, and M. Dubey, 2012: Greenland ice core evidence for spatial and temporal variability of the Atlantic Multidecadal Oscillation. *Geophysical Research Letters*, **39 (9)**, 1–6, doi:10.1029/2012GL051241.

Chylek, P., J. D. Klett, G. Lesins, M. K. Dubey, and N. Hengartner, 2014: The Atlantic Multidecadal Oscillation as a dominant factor of oceanic in-

fluence on climate. *Geophysical Research Letters*, doi:10.1002/2014GL059274, 2014WR016527.

Clement, A., K. Bellomo, L. N. Murphy, M. A. Cane, T. Mauritsen, G. Rädel, and B. Stevens, 2015: The Atlantic Multidecadal Oscillation without a role for ocean circulation. *Science*, doi:10.1126/science.aab3980, arXiv:1408.1149.

Coles, V. J., M. S. McCartney, D. B. Olson, and W. M. Smethie, 1996: Changes in antarctic bottom water properties in the western south atlantic in the late 1980s. *Journal of Geophysical Research: Oceans*, **101 (C4)**, 8957–8970.

Colin de Verdière, A., and T. Huck, 1999: Baroclinic Instability: An Oceanic Wavemaker for Interdecadal Variability. *Journal of Physical Oceanography*, **29 (5)**, 893–910, doi:10.1175/1520-0485(1999)029⟨0893:BIAOWF⟩2.0.CO;2.

Collins, M., and B. Sinha, 2003: Predictability of decadal variations in the thermohaline circulation and climate. *Geophysical Research Letters*, **30 (6)**, 1306, doi:10.1029/2002GL016504.

Collins, M., and Coauthors, 2006: Interannual to decadal climate predictability in the North Atlantic: A multimodel-ensemble study. *Journal of Climate*, **19 (7)**, 1195–1203, doi:10.1175/JCLI3654.1.

Collins, M., and Coauthors, 2013: *Long-term climate change: projections, commitments and irreversibility*. Cambridge University Press, Cambridge, United Kingdom and New York, NY, USA, in: Stocker TF, Qin D, Plattner G-K, Tignor M, Allen SK, Boschung J, Nauels A, Xia Y, Bex V, Midgley PM (eds) Climate change 2013: the Physical science basis. Contribution of working group I to the fifth assessment report of the intergovernmental panel on climate change.

Cunningham, S. a., and Coauthors, 2007: Temporal Variability of the Atlantic Meridional Overturning Circulation at 26.5 N. *Science*, **317 (5840)**, 935–938, doi:10.1126/science.1141304.

Curry, R. G., M. S. McCartney, and T. M. Joyce, 1998: Oceanic transport of subpolar climate signals to mid-depth subtropical waters. *Nature*, **391 (6667)**, 575–577, doi:Doi10.1038/35356.

Czeschel, L., D. P. Marshall, and H. L. Johnson, 2010: Oscillatory sensitivity of Atlantic overturning to highlatitude forcing. *Geophysical Research Letters*, **37 (L10601)**, doi:10.1029/2010GL043177, 10/2010GL043177.

Davey, M., 1998: Decadal climate variability: Dynamics and predictability. edited by david l. t. anderson and jurgen willebrand. springer, heidelberg. nato asi series 1, vol. 44. 1996. 493 pp. price 139.50 (hardback). isbn 3 540 61459 1. *Quarterly Journal of the Royal Meteorological Society*, **124 (552)**, 2867–2868, doi:10.1002/qj.49712455216.

de Lavergne, C., J. B. Palter, E. D. Galbraith, R. Bernardello, and I. Marinov, 2014: Cessation of deep convection in the open Southern Ocean under anthropogenic climate change. *Nature Climate Change*, **4 (4)**, 278–282, doi:10.1038/nclimate2132.

DelSole, T., 2004: Predictability and Information Theory. Part I: Measures of Predictability. *Journal of the Atmospheric Sciences*, **61 (20)**, 2425–2440, doi:10.1175/1520-0469(2004)061⟨2425:PAITPI⟩2.0.CO;2.

Delworth, T., S. Manabe, and R. J. Stouffer, 1993: Interdecadal Variations of the Thermohaline Circulation in a Coupled Ocean-Atmosphere Model. *Journal of Climate*, **6 (11)**, 1993–2011, doi:10.1175/1520-0442(1993)006⟨1993:IVOTTC⟩2.0.CO;2.

Delworth, T. L., and M. E. Mann, 2000: Observed and simulated multidecadal variability in the Northern Hemisphere. *Climate Dynamics*, doi:10.1007/s003820000075.

Delworth, T. L., and F. Zeng, 2016: The impact of the North Atlantic Oscillation on climate through its influence on the Atlantic meridional overturning circulation. *Journal of Climate*, **29 (3)**, 941–962, doi:10.1175/JCLI-D-15-0396.1.

Delworth, T. L., F. Zeng, L. Zhang, R. Zhang, G. A. Vecchi, and X. Yang, 2017: The Central Role of Ocean Dynamics in Connecting the North Atlantic Oscillation to the Extratropical Component of the Atlantic Multidecadal Oscillation. *Journal of Climate*, **30 (10)**, 3789–3805, doi:10.1175/JCLI-D-16-0358.1.

Dickson, R. R., J. Meincke, S. A. Malmberg, and A. J. Lee, 1988: The "great salinity anomaly" in the Northern North Atlantic 1968-1982. *Progress in Oceanography*, **20 (2)**, 103–151, doi:10.1016/0079-6611(88)90049-3.

Dijkstra, H. A., L. Te Raa, M. Schmeits, and J. Gerrits, 2006: On the physics of the Atlantic Multidecadal Oscillation. *Ocean Dynamics*, **56 (1)**, 36–50, doi:10.1007/s10236-005-0043-0.

Dong, B., and R. T. Sutton, 2005: Mechanism of interdecadal thermohaline circulation variability in a coupled ocean-atmosphere GCM. *Journal of Climate*, **18 (8)**, 1117–1135, doi:10.1175/JCLI3328.1.

Donner, R., S. Barbosa, J. Kurths, and N. Marwan, 2009: Understanding the Earth as a Complex System - Recent advances in data analysis and modelling in Earth sciences. *European Physical Journal: Special Topics*, **174 (1)**, 1–9, doi:10.1140/epjst/e2009-01086-6.

Drijfhout, S. S., S. L. Weber, and E. van der Swaluw, 2011: The stability of the MOC as diagnosed from model projections for pre-industrial, present and future climates. *Climate Dynamics*, **37 (7-8)**, 1575–1586, doi:10.1007/s00382-010-0930-z.

Du, H., F. J. Doblas-Reyes, J. García-Serrano, V. Guemas, Y. Soufflet, and B. Wouters, 2012: Sensitivity of decadal predictions to the initial atmospheric and oceanic perturbations. *Climate Dynamics*, **39 (7-8)**, 2013–2023, doi:10.1007/s00382-011-1285-9.

Dunstone, N. J., D. M. Smith, and R. Eade, 2011: Multi-year predictability of the tropical Atlantic atmosphere driven by the high latitude North Atlantic Ocean. *Geophysical Research Letters*, **38 (14)**, 1–6, doi:10.1029/2011GL047949.

Durack, P. J., and S. E. Wijffels, 2010: Fifty-Year trends in global ocean salinities and their relationship to broad-scale warming. *Journal of Climate*, **23 (16)**, 4342–4362, doi:10.1175/2010JCLI3377.1.

Eden, C., and J. Willebrand, 2001: Mechanism of interannual to decadal vari-

ability of the North Atlantic circulation. *Journal of Climate*, doi:10.1175/1520-0442(2001)014⟨2266:MOITDV⟩2.0.CO;2.

Escudier, R., J. Mignot, and D. Swingedouw, 2013: A 20-year coupled ocean-sea ice-atmosphere variability mode in the North Atlantic in an AOGCM. *Climate Dynamics*, **40 (3-4)**, 619–636, doi:10.1007/s00382-012-1402-4.

Farrell, B., and P. Ioannou, 1996a: Generalized Stability Theory. Part I: Autonomous Operators. *Journal of the atmospheric sciences*, **53 (14)**, 2025–2040.

Farrell, B., and P. Ioannou, 1996b: Generalized Stability theory. Part II: Nonautonomous Operators. *Journal of the atmospheric sciences*, **53 (14)**, 2041–2053.

Feng, Q. Y., and H. Dijkstra, 2014: Are North Atlantic multidecadal SST anomalies westward propagating? *Geophysical Research Letters*, **41 (2)**, 541–546, doi:10.1002/2013GL058687.

Frankcombe, L. M., and H. A. Dijkstra, 2009: Coherent multidecadal variability in North Atlantic sea level. *Geophysical Research Letters*, **36 (15)**, n/a–n/a, doi:10.1029/2009GL039455.

Frankcombe, L. M., H. A. Dijkstra, and A. von Der Heydt, 2008: Sub-surface signatures of the Atlantic Multidecadal Oscillation. *Geophysical Research Letters*, **35 (19)**, doi:10.1029/2008GL034989.

Frankcombe, L. M., H. A. Dijkstra, and A. von der Heydt, 2009: Noise-Induced Multidecadal Variability in the North Atlantic: Excitation of Normal Modes. *Journal of Physical Oceanography*, **39 (1)**, 220–233, doi:10.1175/2008JPO3951.1, URL http://journals.ametsoc.org/doi/abs/10.1175/2008JPO3951.1.

Frankcombe, L. M., A. von der Heydt, and H. A. Dijkstra, 2010: North atlantic multidecadal climate variability: An investigation of dominant time scales and processes. *Journal of Climate*, **23 (13)**, 3626–3638, doi:10.1175/2010JCLI3471.1.

Friedman, A. R., G. Reverdin, M. Khodri, and G. Gastineau, 2017: A new record of Atlantic sea surface salinity from 1896-2013 reveals the signatures of

climate variability and long-term trends. *Geophysical Research Letters*, 1–11, doi:10.1002/2017GL072582.

Frölicher, T. L., J. L. Sarmiento, D. J. Paynter, J. P. Dunne, J. P. Krasting, and M. Winton, 2015: Dominance of the Southern Ocean in anthropogenic carbon and heat uptake in CMIP5 models. *Journal of Climate*, **28 (2)**, 862–886, doi: 10.1175/JCLI-D-14-00117.1.

Ganachaud, A., and C. Wunsch, 2000: Improved estimates of global ocean circulation, heat transport and mixing from hydrographic data. *Nature*, **408 (6811)**, 453–457, doi:10.1038/35044048.

García-Serrano, J., and F. J. Doblas-Reyes, 2012: On the assessment of near-surface global temperature and North Atlantic multi-decadal variability in the ENSEMBLES decadal hindcast. *Climate Dynamics*, **39 (7-8)**, 2025–2040, doi: 10.1007/s00382-012-1413-1.

Gastineau, G., and C. Frankignoul, 2012: Cold-season atmospheric response to the natural variability of the Atlantic meridional overturning circulation. *Climate Dynamics*, doi:10.1007/s00382-011-1109-y.

Gastineau, G., and C. Frankignoul, 2015: Influence of the North Atlantic SST variability on the atmospheric circulation during the twentieth century. *Journal of Climate*, doi:10.1175/JCLI-D-14-00424.1.

Gent, P. R., and J. C. McWilliams, 1990: Isopycnal mixing in ocean circulation models. *J. Phys. Oceanogr.*, **20**, 150–155.

Germe, A., F. Sévellec, J. Mignot, D. Swingedouw, and S. Nguyen, 2017: On the robustness of near term climate predictability regarding initial state uncertainties. *Climate Dynamics*, **48 (1-2)**, 353–366, doi:10.1007/s00382-016-3078-7.

Ghil, M., 2002: Natural Climate Variability. *Encyclopedia of Global Environmental Change*, **1**, 544–549.

Golledge, N. R., and Coauthors, 2013: Glaciology and geological signature of the Last Glacial Maximum Antarctic ice sheet. *Quaternary Science Reviews*, **78**, 225–247, doi:10.1016/j.quascirev.2013.08.011.

Gordon, A. L., 1982: Weddell deep water variability. *J. Mar. Res*, **40 (suppl)**, 199–217.

Gordon, A. L., 1991: Two stable modes of southern ocean winter stratification. *Elsevier Oceanography Series*, **57**, 17–35.

Gordon, A. L., 2014: Oceanography: Southern Ocean polynya. *Nature Climate Change*, **4 (4)**, 249–250, doi:10.1038/nclimate2179.

Gregory, J. M., and Coauthors, 2005: A model intercomparison of changes in the Atlantic thermohaline circulation in response to increasing atmospheric CO2 concentration. *Geophysical Research Letters*, **32 (12)**, 1–5, doi:10.1029/2005GL023209.

Griffies, S. M., and Coauthors, 2005: Formulation of an ocean model for global climate simulations. doi:10.5194/os-1-45-2005.

Hall, M. M., and H. L. Bryden, 1982: Direct estimates and mechanisms of ocean heat transport. *Deep Sea Research Part A, Oceanographic Research Papers*, **29 (3)**, 339–359, doi:10.1016/0198-0149(82)90099-1.

Ham, Y. G., M. M. Rienecker, M. J. Suarez, Y. Vikhliaev, B. Zhao, J. Marshak, G. Vernieres, and S. D. Schubert, 2014: Decadal prediction skill in the GEOS-5 forecast system. *Climate Dynamics*, **42 (1-2)**, 1–20, doi:10.1007/s00382-013-1858-x.

Hansen, J., and Coauthors, 2016: Ice melt, sea level rise and superstorms: Evidence from paleoclimate data, climate modeling, and modern observations that 2 ??c global warming could be dangerous. *Atmospheric Chemistry and Physics*, **16 (6)**, 3761–3812, doi:10.5194/acp-16-3761-2016, arXiv:1011.1669v3.

Hawkins, E., R. S. Smith, J. M. Gregory, and D. A. Stainforth, 2016: Irreducible uncertainty in near-term climate projections. *Climate Dynamics*, **46 (11-12)**, 3807–3819, doi:10.1007/s00382-015-2806-8.

Hawkins, E., and R. Sutton, 2009a: Decadal Predictability of the Atlantic Ocean in a Coupled GCM: Forecast Skill and Optimal Perturbations Using Linear Inverse Modeling. *Journal of Climate*, **22 (14)**, 3960–3978, doi:10.1175/2009JCLI2720.1.

Hawkins, E., and R. Sutton, 2009b: The Potential to Narrow Uncertainty in Regional Climate Predictions. *Bulletin of the American Meteorological Society*, **90 (8)**, 1095–1107, doi:10.1175/2009BAMS2607.1.

Heimbach, P., C. Wunsch, R. M. Ponte, G. Forget, C. Hill, and J. Utke, 2011: Timescales and regions of the sensitivity of Atlantic meridional volume and heat transport: Toward observing system design. *Deep-Sea Research Part II: Topical Studies in Oceanography*, **58 (17-18)**, 1858–1879, doi:10.1016/j.dsr2.2010.10.065.

Heuzé, C., J. K. Ridley, D. Calvert, D. P. Stevens, and K. J. Heywood, 2015: Increasing vertical mixing to reduce Southern Ocean deep convection in NEMO3.4. *Geoscientific Model Development*, **8 (10)**, 3119–3130, doi:10.5194/gmd-8-3119-2015.

Hirschi, J., J. Baehr, J. Marotzke, J. Stark, S. Cunningham, and J. O. Beismann, 2003: A monitoring design for the Atlantic meridional overturning circulation. *Geophysical Research Letters*, doi:10.1029/2002GL016776.

Ho, C. K., E. Hawkins, L. Shaffrey, and F. M. Underwood, 2013: Statistical decadal predictions for sea surface temperatures: A benchmark for dynamical GCM predictions. *Climate Dynamics*, **41 (3-4)**, 917–935, doi:10.1007/s00382-012-1531-9.

Holland, M. M., D. A. Bailey, and S. Vavrus, 2011: Inherent sea ice predictability in the rapidly changing Arctic environment of the Community Climate System Model, version 3. *Climate Dynamics*, **36 (7)**, 1239–1253, doi:10.1007/s00382-010-0792-4.

Huck, T., O. Arzel, and F. Sévellec, 2015: Multidecadal Variability of the Overturning Circulation in Presence of Eddy Turbulence. *Journal of Physical Oceanography*, **45 (1)**, 157–173, doi:10.1175/JPO-D-14-0114.1.

Huck, T., A. Colin de Verdière, A. J. Weaver, A. Colin de Verdi?re, and A. J. Weaver, 1999: Interdecadal Variability of the Thermohaline Circulation in Box-Ocean Models Forced by Fixed Surface Fluxes. *Journal of Physical Oceanography*, **29 (5)**, 865–892, doi:10.1175/1520-0485(1999)029⟨0865:IVOTTC⟩2.0.CO;2.

Huck, T., and G. Vallis, 2001: Linear stability analysis of the three-dimensional thermally-driven ocean circulation: application to interdecadal oscillations. *Tellus A*, **53 A**, 526–545.

Hurrell, J., and Coauthors, 2010: Decadal climate prediction: Opportunities and challenges. *... and Information for ...*, **2 (1)**.

Hurrell, J. W., Y. Kushnir, G. Ottersen, and M. Visbeck, 2003: An overview of the north atlantic oscillation. *Geophysical Monograph Series*, doi:10.1029/134GM01.

Jackson, L. C., R. Kahana, T. Graham, M. A. Ringer, T. Woollings, J. V. Mecking, and R. A. Wood, 2015: Global and European climate impacts of a slowdown of the AMOC in a high resolution GCM. *Climate Dynamics*, **45 (11-12)**, 3299–3316, doi:10.1007/s00382-015-2540-2.

Jackson, L. C., K. A. Peterson, C. D. Roberts, and R. A. Wood, 2016: Recent slowing of Atlantic overturning circulation as a recovery from earlier strengthening. *Nature Geoscience*, **9 (May)**, doi:10.1038/ngeo2715.

Johns, W. E., and Coauthors, 2011: Continuous, array-based estimates of atlantic ocean heat transport at 26.5N. *Journal of Climate*, **24 (10)**, 2429–2449, doi:10.1175/2010JCLI3997.1.

Johnson, H. L., and D. P. Marshall, 2002: A Theory for the Surface Atlantic Response to Thermohaline Variability. *Journal of Physical Oceanography*, **32 (4)**, 1121–1132, doi:10.1175/1520-0485(2002)032⟨1121:ATFTSA⟩2.0.CO;2.

Jungclaus, J. H., H. Haak, M. Latif, and U. Mikolajewicz, 2005: Arctic-North Atlantic interactions and multidecadal variability of the meridional overturning circulation. *Journal of Climate*, **18 (19)**, 4013–4031, doi:10.1175/JCLI3462.1.

Kaplan, M. R., and Coauthors, 2013: The anatomy of long-term warming since 15 ka in new zealand based on net glacier snowline rise. *Geology*, **41 (8)**, 887–890.

Karl, T. R., and K. E. Trenberth, 2003: Modern global climate change. *Science (New York, N.Y.)*, **302 (5651)**, 1719–23, doi:10.1126/science.1090228, arXiv:1011.1669v3.

Karspeck, A. R., S. Yeager, G. Danabasoglu, T. Hoar, N. Collins, K. Raeder, J. Anderson, and J. Tribbia, 2013: An Ensemble Adjustment Kalman Filter for the CCSM4 Ocean Component. *Journal of Climate*, **26 (19)**, 7392–7413, doi:10.1175/JCLI-D-12-00402.1.

Karspeck, a. R., and Coauthors, 2015: Comparison of the Atlantic meridional overturning circulation between 1960 and 2007 in six ocean reanalysis products. *Climate Dynamics*, doi:10.1007/s00382-015-2787-7.

Kawase, M., 1987: Establishment of Deep Ocean Circulation Driven by Deep-Water Production. *Journal of Physical Oceanography*, doi:10.1175/1520-0485(1987)017⟨2294:EODOCD⟩2.0.CO;2.

Kent, E. C., and Coauthors, 2017: A call for new approaches to quantifying biases in observations of sea surface temperature. *Bulletin of the American Meteorological Society*, **98 (8)**, 1601–1616, doi:10.1175/BAMS-D-15-00251.1.

Kerr, R. A., 2000: A North Atlantic Climate Pacemaker for the Centuries. *Science*, **288 (5473)**, 1984–1985, doi:10.1126/science.288.5473.1984, URL http://www.sciencemag.org/cgi/doi/10.1126/science.288.5473.1984.

Kiehl, J. T., and K. E. Trenberth, 1997: Earth's Annual Global Mean Energy Budget. *Bulletin of the American Meteorological Society*, **78 (2)**, 197–208, doi:10.1175/1520-0477(1997)078⟨0197:EAGMEB⟩2.0.CO;2.

Kjellsson, J., and Coauthors, 2015: Model sensitivity of the Weddell and Ross seas, Antarctica, to vertical mixing and freshwater forcing. *Ocean Modelling*, **94**, 141–152, doi:10.1016/j.ocemod.2015.08.003.

Knight, J. R., R. J. Allan, C. K. Folland, M. Vellinga, and M. E. Mann, 2005: A signature of persistent natural thermohaline circulation cycles in observed climate. *Geophysical Research Letters*, **32 (20)**, 1–4, doi:10.1029/2005GL024233.

Knight, J. R., C. K. Folland, and A. A. Scaife, 2006: Climate impacts of the Atlantic multidecadal oscillation. *Geophysical Research Letters*, doi:10.1029/2006GL026242.

Kuhlbrodt, T., A. Griesel, M. Montoya, A. Levermann, M. Hofmann, and S. Rahmstorf, 2007: On the driving processes of the Atlantic meridional overturning circulation. *Atlantic*, **45 (2004)**, RG2001, doi:10.1029/2004RG000166.1. INTRODUCTION.

Kushnir, Y., 1994: Interdecadal Variations in North Atlantic Sea Surface Temperature and Associated Atmospheric Conditions. *Journal of Climate*, **7 (1)**, 141–157, doi:10.1175/1520-0442(1994)007⟨0141:IVINAS⟩2.0.CO;2.

Kwon, Y.-o., and C. Frankignoul, 2014: Mechanisms of Multidecadal Atlantic Meridional Overturning Circulation Variability Diagnosed in Depth versus Density Space. *Journal of Climate*, **27 (24)**, 9359–9377, doi:10.1175/JCLI-D-14-00228.1.

Latif, M., M. Collins, H. Pohlman, and N. Keenlyside, 2006: A review of predictability studies of Atlantic sector climate on decadal time scales. *Journal of Climate - Special Section*, **19**, 5971–5987.

Latif, M., T. Martin, and W. Park, 2013: Southern ocean sector centennial climate variability and recent decadal trends. *Journal of Climate*, **26 (19)**, 7767–7782, doi:10.1175/JCLI-D-12-00281.1.

Lazier, J., 1995: The salinity decrease in the labrador sea over the past thirty years. *Natural Climate Variability on Decade-to-Century Time Scales*, **331**, 296–302.

Levitus, S., 1989: Interpentadal variability of temperature and salinity at intermediate depths of the north atlantic ocean, 19701974 versus 19551959. *Journal of Geophysical Research: Oceans*, **94 (C5)**, 6091–6131, doi:10.1029/JC094iC05p06091.

Lorenz, E. N., 1963: Deterministic Nonperiodic Flow. *Journal of the Atmospheric Sciences*, **20 (2)**, 130–141, doi:10.1175/1520-0469(1963)020⟨0130:DNF⟩2.0.CO;2.

Lorenz, E. N. E., 1975: Climate Predictability. *The physical basis of climate and climate modelling*, **16**, 132–136.

Madec, G., 2008: *NEMO ocean engine*. Note du Pôle de modélisation, Institut Pierre-Simon Laplace (IPSL), France, No 27, ISSN No 1288-1619.

Madec, G., P. Delecluse, M. Imbard, and C. Levy, 1998: OPA 8.1 Ocean General Circulation Model reference manual. *Institut Pierre-Simon Laplace (IPSL), France*, **No. 11**, 91 pp.

Maier-Reimer, E., U. Mikolajewicz, and K. Hasselmann, 1993: Mean Circulation of the Hamburg LSG OGCM and Its Sensitivity to the Thermohaline Surface Forcing. *Journal of Physical Oceanography*, doi:10.1175/1520-0485(1993)023⟨0731:MCOTHL⟩2.0.CO;2.

Manabe, S., and R. J. Stouffer, 1988: Two Stable Equilibria of a Coupled Ocean-Atmosphere Model. 841–866 pp., doi:10.1175/1520-0442(1993)006⟨0175:COSEOA⟩2.0.CO;2.

Marotzke, J., R. Giering, K. Q. Zhang, D. Stammer, C. Hill, and T. Lee, 1999: Construction of the adjoint mit ocean general circulation model and application to atlantic heat transport sensitivity. *Journal of Geophysical Research: Oceans*, **104 (C12)**, 29 529–29 547, doi:10.1029/1999JC900236, URL http://dx.doi.org/10.1029/1999JC900236.

Marotzke, J., and B. A. B. Klinger, 2000: The dynamics of equatorially asymmetric thermohaline circulations. *Journal of Physical Oceanography*, doi:10.1175/1520-0485(2000)030⟨0955:TDOEAT⟩2.0.CO;2.

Marotzke, J., and J. Willebrand, 1991: Multiple Equilibria of the Global Thermohaline Circulation. 1372–1385 pp., doi:10.1175/1520-0485(1991)021⟨1372:MEOTGT⟩2.0.CO;2.

Marshall, J., and Coauthors, 2001: North Atlantic climate variability: phenomena, impacts and mechanisms. *International Journal of Climatology*, **21 (15)**, 1863–1898, doi:10.1002/joc.693, URL http://doi.wiley.com/10.1002/joc.693.

Martin, T., W. Park, and M. Latif, 2013: Multi-centennial variability controlled by Southern Ocean convection in the Kiel Climate Model. *Climate Dynamics*, **40 (7-8)**, 2005–2022, doi:10.1007/s00382-012-1586-7.

McCarthy, G. D., and Coauthors, 2015: Measuring the Atlantic Meridional Over-

turning Circulation at 26??N. *Progress in Oceanography*, **130**, 91–111, doi:10.1016/j.pocean.2014.10.006.

McMillan, M., and Coauthors, 2016: A high-resolution record of Greenland mass balance. *Geophysical Research Letters*, doi:10.1002/2016GL069666.

Meehl, G. a., and Coauthors, 2009: Decadal Prediction. *Bulletin of the American Meteorological Society*, **90 (10)**, 1467–1485, doi:10.1175/2009BAMS2778.1.

Meehl, G. a., and Coauthors, 2014: Decadal climate prediction an update from the trenches. *Bulletin of the American Meteorological Society*, **95 (February)**, 243–267, doi:10.1175/BAMS-D-12-00241.1.

Menary, M. B., D. L. R. Hodson, J. I. Robson, R. T. Sutton, and R. A. Wood, 2015: A mechanism of internal decadal Atlantic Ocean variability in a high-resolution coupled climate model. *Journal of Climate*, **28 (19)**, 7764–7785, doi:10.1175/JCLI-D-15-0106.1.

Mikolajewicz, U., and E. Maier-Reimer, 1994: Mixed boundary conditions in ocean general circulation models and their influence on the stability of the model's conveyor belt. *Journal of Geophysical Research*, doi:10.1029/94JC01989.

Mitchell, J., 1976: An overview of climatic variability and its causal mechanisms. *Quaternary Research*, **6 (4)**, 481–493, doi:10.1016/0033-5894(76)90021-1.

Mogensen, K., M. Alonso Balmaseda, and A. Weaver, 2012: The NEMOVAR ocean data assimilation system as implemented in the ECMWF ocean analysis for System 4. *Technical Memorandum*, **668 (February)**, 1–59.

Msadek, R., and C. Frankignoul, 2009: Atlantic multidecadal oceanic variability and its influence on the atmosphere in a climate model. *Climate Dynamics*, **33 (1)**, 45–62, doi:10.1007/s00382-008-0452-0.

Mu, M., L. Sun, and H. a. Dijkstra, 2004: The Sensitivity and Stability of the Ocean ' s Thermohaline Circulation to Finite- Amplitude Perturbations. *Journal of Physical Oceanography*, **34**, 2305–2315.

Muir, L. C., and A. V. Fedorov, 2017: Evidence of the AMOC interdecadal mode related to westward propagation of temperature anomalies in CMIP5 models. *Climate Dynamics*, doi:10.1007/s00382-016-3157-9.

Mysak, L. A., D. K. Manak, and R. F. Marsden, 1990: Sea-ice anomalies observed in the Greenland and Labrador seas during 1901-1984 and their relation to an interdecadal Arctic climate cycle. *Climate Dynamics*, **5 (2)**, 111–133, doi:10.1007/BF00207426.

Mysak, L. A., and S. B. Power, 1991: Greenland Sea Ice and Salinity anomalies and interdecadal climate variability. *Climat. Bull.*, **25 (514)**, 81–91.

Orsi, A. H., G. C. Johnson, and J. L. Bullister, 1999: Circulation,mixing and production of {A}ntarctic {B}ottom {W}ater. *Progr.\ Oceanogr.*, **43**, 55–109.

Ortega, P., E. Guilyardi, D. Swingedouw, J. Mignot, and S. Nguyen, 2017: Reconstructing extreme AMOC events through nudging of the ocean surface: a perfect model approach. *Climate Dynamics*, **0 (0)**, 1–17, doi:10.1007/s00382-017-3521-4.

Ortega, P., J. Mignot, D. Swingedouw, F. Sévellec, and E. Guilyardi, 2015: Reconciling two alternative mechanisms behind bi-decadal variability in the North Atlantic. *Progress in Oceanography*, **137**, 237–249, doi:10.1016/j.pocean.2015.06.009.

Ortega, P., J. Robson, R. T. Sutton, and M. B. Andrews, 2016: Mechanisms of decadal variability in the Labrador Sea and the wider North Atlantic in a high-resolution climate model. *Climate Dynamics*, **0 (0)**, 0, doi:10.1007/s00382-016-3467-y.

Park, W., and M. Latif, 2008: Multidecadal and multicentennial variability of the meridional overturning circulation. *Geophysical Research Letters*, **35 (22)**, L22 703, doi:10.1029/2008GL035779.

Pedlosky, J., 1990: *Geophysical Fluid Dynamics*. 2nd ed., Springer-Verlag, New York, NY, USA, 710 pp.

Pérez-Hernández, M. D., G. D. McCarthy, P. Vélez-Belchí, D. A. Smeed, E. Fraile-Nuez, and A. Hernández-Guerra, 2015: The Canary Basin contribution to the seasonal cycle of the Atlantic Meridional Overturning Circulation at 26N. *Journal of Geophysical Research: Oceans*, doi:10.1002/2015JC010969.

Pohlmann, H., M. Botzet, M. Latif, A. Roesch, M. Wild, and P. Tschuck, 2004: Estimating the decadal predictability of a coupled AOGCM. *Journal of Climate*, **17 (22)**, 4463–4472, doi:10.1175/3209.1.

Poincaré, H., and R. Magini, 1899: Les méthodes nouvelles de la mécanique céleste. *Il Nuovo Cimento*, **10 (1)**, 128–130, doi:10.1007/BF02742713.

Preisendorfer, R., and C. Mobley, 1988: *Principal component analysis in meteorology and oceanography*. doi:10.1029/JD093iD09p10815.

Proshutinsky, A., D. Dukhovskoy, M.-l. Timmermans, R. Krishfield, and J. L. Bamber, 2015: Arctic circulation regimes Subject Areas. *Arctic circulation regimes. Phil.Trans.R. Soc.*

Rahmstorf, S., 1996: On the freshwater forcing and transport of the Atlantic thermohaline circulation. *Climate Dynamics*, **12 (12)**, 799–811, doi:10.1007/s003820050144.

Rahmstorf, S., 2002: Ocean circulation and climate during the past 120,000 years. *Nature*, **419 (6903)**, 207–214, doi:10.1038/nature01090.

Ray, S., D. Swingedouw, J. Mignot, and E. Guilyardi, 2015: Effect of surface restoring on subsurface variability in a climate model during 19492005. *Climate Dynamics*, **44 (9-10)**, 2333–2349, doi:10.1007/s00382-014-2358-3.

Redi, M. H., 1982: Oceanic isopycnal mixing by coordinate rotation. *Journal of Physical Oceanography*, **12 (10)**, 1154–1158, doi:10.1175/1520-0485(1982)012⟨1154:OIMBCR⟩2.0.CO;2.

Reintges, A., T. Martin, M. Latif, and N. S. Keenlyside, 2016: Uncertainty in twenty-first century projections of the Atlantic Meridional Overturning Circulation in CMIP3 and CMIP5 models. *Climate Dynamics*, 1–17, doi:10.1007/s00382-016-3180-x.

Reynolds, R. W., and T. M. Smith, 1994: Improved global sea surface temperature analyses using optimum interpolation. *Journal of Climate*, **7 (6)**, 929–948, doi: 10.1175/1520-0442(1994)007⟨0929:IGSSTA⟩2.0.CO;2.

Rintoul, S., and A. Naveira Garabato, 2013: *Dynamics of the Southern Ocean circulation*. 103, Academic Press, 471–492 pp.

Robson, J., R. Sutton, and D. Smith, 2014: Decadal predictions of the cooling and freshening of the North Atlantic in the 1960s and the role of ocean circulation. *Climate Dynamics*, **42 (9-10)**, 2353–2365, doi:10.1007/s00382-014-2115-7, URL http://link.springer.com/10.1007/s00382-014-2115-7.

Roemmich, D., J. Church, J. Gilson, D. Monselesan, P. Sutton, and S. Wijffels, 2015: Unabated planetary warming and its ocean structure since 2006. *Nature Climate Change*, **5 (February)**, 2–7, doi:10.1038/nclimate2513.

Ruelle, D., and F. Takens, 1971: On the nature of turbulence. *Communications in Mathematical Physics*, **20 (3)**, 167–192, doi:10.1007/BF01646553, 0507254.

Ruprich-Robert, Y., R. Msadek, F. Castruccio, S. Yeager, T. Delworth, and G. Danabasoglu, 2017: Assessing the climate impacts of the observed atlantic multidecadal variability using the GFDL CM2.1 and NCAR CESM1 global coupled models. *Journal of Climate*, **30 (8)**, 2785–2810, doi:10.1175/JCLI-D-16-0127.1.

Saltzman, B., and B. Saltzman, 1962: Finite Amplitude Free Convection as an Initial Value ProblemI. *Journal of the Atmospheric Sciences*, **19 (4)**, 329–341, doi:10.1175/1520-0469(1962)019⟨0329:FAFCAA⟩2.0.CO;2.

Schwarz, G., 1978: Estimating the dimension of a model. *Annals of Statistics*, **6**, 461–464.

Seidov, D., E. Barron, and B. J. Haupt, 2001: Meltwater and the global ocean conveyor: Northern versus southern connections. *Global and Planetary Change*, doi:10.1016/S0921-8181(00)00087-4.

Servonnat, J., J. Mignot, E. Guilyardi, D. Swingedouw, R. Séférian, and S. Labetoulle, 2014: Reconstructing the subsurface ocean decadal variability using

surface nudging in a perfect model framework. *Climate Dynamics*, **44 (1-2)**, 315–338, doi:10.1007/s00382-014-2184-7.

Sévellec, F., and A. A. V. Fedorov, 2014: Millennial variability in an idealized ocean model: predicting the AMOC regime shifts. *Journal of Climate*, **(July)**, doi:10.1175/JCLI-D-13-00450.1.

Sévellec, F., and A. V. Fedorov, 2013a: Model bias reduction and the limits of oceanic decadal predictability: Importance of the deep ocean. *Journal of Climate*, **26 (11)**, 3688–3707, doi:10.1175/JCLI-D-12-00199.1.

Sévellec, F., and A. V. Fedorov, 2013b: The leading, interdecadal eigenmode of the atlantic meridional overturning circulation in a realistic ocean model. *Journal of Climate*, **26 (7)**, 2160–2183, doi:10.1175/JCLI-D-11-00023.1.

Sévellec, F., and A. V. Fedorov, 2015: Optimal excitation of AMOC decadal variability: Links to the subpolar ocean. *Progress in Oceanography*, **132**, 287–304, doi:10.1016/j.pocean.2014.02.006.

Sévellec, F., A. V. Fedorov, and W. Liu, 2017: Arctic sea-ice decline weakens the Atlantic Meridional Overturning Circulation. *Nature Climate Change*, **7 (8)**, 604–610, doi:10.1038/nclimate3353.

Sévellec, F., and T. Huck, 2015: Theoretical Investigation of the Atlantic Multidecadal Oscillation. *Journal of Physical Oceanography*, **45 (9)**, 2189–2208, doi:10.1175/JPO-D-14-0094.1.

Sévellec, F., T. Huck, M. Ben Jelloul, N. Grima, J. Vialard, and A. Weaver, 2008: Optimal Surface Salinity Perturbations of the Meridional Overturning and Heat Transport in a Global Ocean General Circulation Model. *Journal of Physical Oceanography*, **38 (12)**, 2739–2754, doi:10.1175/2008JPO3875.1.

Sévellec, F., T. Huck, M. Ben Jelloul, and J. Vialard, 2009: Nonnormal Multidecadal Response of the Thermohaline Circulation Induced by Optimal Surface Salinity Perturbations. *Journal of Physical Oceanography*, **39 (4)**, 852–872, doi:10.1175/2008JPO3998.1.

Siedler, G., S. M. Griffies, J. Gould, and J. A. Church, 2011: Ocean Circulation and Climate: A 21st Century Perspective. *Ocean Circulation and Climate: A 21st Century Perspective*, 1–893.

Sirkes, Z., and E. Tziperman, 2001: Identifying a damped oscillatory thermohaline mode in a general circulation model using an adjoint model. *Journal of physical oceanography*, doi:10.1175/1520-0485(2001)031⟨2297:IADOTM⟩2.0.CO;2.

Smith, D. M., R. Eade, N. J. Dunstone, D. Fereday, J. M. Murphy, H. Pohlmann, and A. A. Scaife, 2010: Skilful multi-year predictions of Atlantic hurricane frequency. *Nature Geoscience*, **3 (12)**, 846–849, doi:10.1038/ngeo1004.

Smith, D. M., R. Eade, and H. Pohlmann, 2013: A comparison of full-field and anomaly initialization for seasonal to decadal climate prediction. *Climate Dynamics*, **41 (11-12)**, 3325–3338, doi:10.1007/s00382-013-1683-2.

Smith, T. M., R. W. Reynolds, T. C. Peterson, and J. Lawrimore, 2008: Improvements to NOAA's historical merged land-ocean surface temperature analysis (1880-2006). *Journal of Climate*, doi:10.1175/2007JCLI2100.1.

Sowers, T., M. Bender, and Coauthors, 1995: Climate records covering the last deglaciation. *SCIENCE-NEW YORK THEN WASHINGTON-*, 210–210.

Spall, M. A., 2008: Buoyancy-Forced Downwelling in Boundary Currents. *Journal of Physical Oceanography*, **38 (12)**, 2704–2721, doi:10.1175/2008JPO3993.1.

Srivastava, A., and T. DelSole, 2017: Decadal predictability without ocean dynamics. *Proceedings of the National Academy of Sciences*, **114 (9)**, 201614085, doi:10.1073/pnas.1614085114, URL http://www.pnas.org/lookup/doi/10.1073/pnas.1614085114.

Srokosz, M. a., and H. L. Bryden, 2015: Observing the Atlantic Meridional Overturning Circulation yields a decade of inevitable surprises. *Science*, **348 (6241)**, 1255575–1255575, doi:10.1126/science.1255575, URL http://www.sciencemag.org.libezproxy.open.ac.uk/content/348/6241/1255575.full{%}5Cnhttps://twitter.com/icey{_}mark/status/611787119204433920.

Stammer, D., and Coauthors, 1999: The Consortium for Estimating the Circulation and Climate of the Ocean (ECCO). *Report*, **(1)**.

Stocker, T., and Coauthors, 2013: *Climate Change 2013: The Physical Science Basis. Contribution of Working Group I to the Fifth Assessment Report of the Intergovernmental Panel on Climate Change*. Cambridge University Press, doi: 10.1017/CBO9781107415324.

Stommel, H., 1961: Thermohaline Convection with Two Stable Regimes of Flow. *Tellus A*, **11**, doi:10.3402/tellusa.v13i2.9491.

Stouffer, R. J., B. Seidov, and B. J. Haupt, 2007: Climate Response to External Sources of Freshwater: North Atlantic versus the Southern Ocean. *Journal of Climate*, **20**, 436–448.

Strogatz, S., 2001: Nonlinear dynamics and chaos: with applications to physics, biology, chemistry and engineering. *Cambridge, MA: Westview Press.*

Sutton, R. T., and B. Dong, 2012: Atlantic Ocean influence on a shift in European climate in the 1990s. *Nature Geoscience*, doi:10.1038/ngeo1595.

Sutton, R. T., and D. L. R. Hodson, 2005a: Atlantic Ocean forcing of North American and European summer climate. *Science (New York, N.Y.)*, **309 (5731)**, 115–8, doi:10.1126/science.1109496.

Sutton, R. T., and D. L. R. Hodson, 2005b: Atlantic Ocean forcing of North American and European summer climate. *Science (New York, N.Y.)*, **309 (5731)**, 115–118, doi:10.1126/science.1109496.

Swingedouw, D., T. Fichefet, H. Goosse, and M. F. Loutre, 2009: Impact of transient freshwater releases in the Southern Ocean on the AMOC and climate. *Climate Dynamics*, **33 (2-3)**, 365–381, doi:10.1007/s00382-008-0496-1.

Swingedouw, D., and Coauthors, 2013: Decadal fingerprints of freshwater discharge around Greenland in a multi-model ensemble. *Climate Dynamics*, **41 (3-4)**, 695–720, doi:10.1007/s00382-012-1479-9.

Talley, L. D., 2013: Closure of the global overturning circulation through the Indian, Pacific and Southern Oceans: schematics and transports. *Journal of Chemical Information and Modeling*, **53 (9)**, 1689–1699, doi:10.1017/CBO9781107415324.004, arXiv:1011.1669v3.

Taylor, K. E., R. J. Stouffer, and G. A. Meehl, 2012: An overview of CMIP5 and the experiment design. *Bulletin of the American Meteorological Society*, **93 (4)**, 485–498, doi:10.1175/BAMS-D-11-00094.1, arXiv:1011.1669v3.

te Raa, L., J. Gerrits, and H. a. Dijkstra, 2004: Identification of the Mechanism of Interdecadal Variability in the North Atlantic Ocean. *Journal of Physical Oceanography*, **34 (12)**, 2792–2807, doi:10.1175/JPO2655.1.

te Raa, L. a., and H. a. Dijkstra, 2002: Instability of the Thermohaline Ocean Circulation on Interdecadal Timescales. *Journal of Physical Oceanography*, **32 (1)**, 138–160, doi:10.1175/1520-0485(2002)032⟨0138:IOTTOC⟩2.0.CO;2.

Teng, H., G. Branstator, and G. A. Meehl, 2011: Predictability of the Atlantic overturning circulation and associated surface patterns in two CCSM3 climate change ensemble experiments. *Journal of Climate*, **24 (23)**, 6054–6076, doi:10.1175/2011JCLI4207.1.

Toyoda, T., and Coauthors, 2011: Impact of the Assimilation of Sea Ice Concentration Data on an Atmosphere-Ocean-Sea Ice Coupled Simulation of the Arctic Ocean Climate. *Sola*, **7 (1989)**, 37–40, doi:10.2151/sola.2011-010.

Trenberth, K. E., and D. J. Shea, 2006: Atlantic hurricanes and natural variability in 2005. *Geophysical Research Letters*, **33 (12)**, 1–4, doi:10.1029/2006GL026894.

Tulloch, R., and J. Marshall, 2012: Exploring mechanisms of variability and predictability of Atlantic meridional overturning circulation in two coupled climate models. *Journal of Climate*, **25 (12)**, 4067–4080, doi:10.1175/JCLI-D-11-00460.1.

Tulloch, R., J. Marshall, and K. S. Smith, 2009: Interpretation of the propagation of surface altimetric observations in terms of planetary waves and geostrophic

turbulence. *Journal of Geophysical Research: Oceans*, **114 (2)**, 1–11, doi:10.1029/2008JC005055.

Turner, J., T. J. Bracegirdle, T. Phillips, G. J. Marshall, and J. Scott Hosking, 2013: An initial assessment of antarctic sea ice extent in the CMIP5 models. *Journal of Climate*, **26 (5)**, 1473–1484, doi:10.1175/JCLI-D-12-00068.1.

Turpin, V., E. Remy, and P. Y. Le Traon, 2016: How essential are argo observations to constrain a global ocean data assimilation system? *Ocean Science*, **12 (1)**, 257–274, doi:10.5194/os-12-257-2016.

Valdes, P., 2011: Built for stability. *Nature Geoscience*, **4 (7)**, 414–416, doi:10.1038/ngeo1200, URL http://dx.doi.org/10.1038/ngeo1200.

Vellinga, M., and P. Wu, 2004: Low-latitude freshwater influence on centennial variability of the Atlantic thermohaline circulation. *Journal of Climate*, **17**, 4498–4511, doi:10.1175/3219.1.

Vianna, M. L., and V. V. Menezes, 2013: Bidecadal sea level modes in the North and South Atlantic Oceans. *Geophysical Research Letters*, **40 (22)**, 5926–5931, doi:10.1002/2013GL058162.

Volpi, D., V. Guemas, F. J. Doblas-Reyes, E. Hawkins, and N. K. Nichols, 2016: Decadal climate prediction with a refined anomaly initialisation approach. *Climate Dynamics*, 1–13, doi:10.1007/s00382-016-3176-6.

Walsh, J. E., and W. L. Chapman, 1990: Arctic Contribution to Upper-Ocean Variability in the North Atlantic. 1462–1473 pp.

Wang, C., S. Dong, A. T. Evan, G. R. Foltz, and S. K. Lee, 2012: Multidecadal covariability of north atlantic sea surface temperature, African dust, Sahel Rainfall, and Atlantic hurricanes. *Journal of Climate*, doi:10.1175/JCLI-D-11-00413.1.

Wang, C., S. Dong, and E. Munoz, 2010: Seawater density variations in the North Atlantic and the Atlantic meridional overturning circulation. *Climate Dynamics*, **34 (7)**, 953–968, doi:10.1007/s00382-009-0560-5.

Wang, C., L. Zhang, S.-K. Lee, L. Wu, and C. R. Mechoso, 2014: A global perspective on CMIP5 climate model biases. *Nature Climate Change*, **4 (3)**, 201–205, doi:10.1038/nclimate2118.

Weaver, A. J., and E. S. Sarachik, 1991: The Role of Mixed Boundary Conditions in Numerical Models of the Ocean's Climate. 1470–1493 pp., doi:10.1175/1520-0485(1991)021⟨1470:TROMBC⟩2.0.CO;2.

Welch, P. D., 1967: The Use of Fast Fourier Transform for the Estimation of Power Spectra: A Method Based on Time Averaging Over Short, Modified Periodograms. *IEEE Transactions on Audio and Electroacoustics*, **15**, 70–73.

Weyl, P. K., 1968: The role of the oceans in climatic change: A theory of the ice ages. 37–62.

Wills, R. C., D. S. Battisti, D. L. Hartmann, and T. Schneider, 2017: Extracting modes of variability and change from climate model ensembles. 7$^{\text{th}}$ *International Workshop on Climate Informatics*, 25–28.

Wills, R. C. J., K. C. Armour, D. S. Battisti, and D. L. Hartmann, 2018: Ocean-Atmosphere Dynamical Coupling Fundamental to the Atlantic Multidecadal Oscillation. *Journal of Climate*, JCLI–D–18–0269.1, doi:10.1175/JCLI-D-18-0269.1, URL http://journals.ametsoc.org/doi/10.1175/JCLI-D-18-0269.1.

Wunsch, C., 2002: OCEANOGRAPHY: What Is the Thermohaline Circulation? *Science*, **298 (5596)**, 1179–1181, doi:10.1126/science.1079329.

Yang, L., 2013: Conditional Nonlinear Optimal Perturbation of a Coupled Lorenz Model. *Mathematical Problems in Engineering*, **2013**, URL http://www.hindawi.com/journals/mpe/2013/846973/abs/.

Yeager, S., A. Karspeck, G. Danabasoglu, J. Tribbia, and H. Teng, 2012: A decadal prediction case study: Late twentieth-century north Atlantic Ocean heat content. *Journal of Climate*, **25 (15)**, 5173–5189, doi:10.1175/JCLI-D-11-00595.1.

Yoshimori, M., C. C. Raible, T. F. Stocker, and M. Renold, 2010: Simulated decadal oscillations of the Atlantic meridional overturning circulation

in a cold climate state. *Climate Dynamics*, **34 (1)**, 101–121, doi:10.1007/s00382-009-0540-9.

Yu, L., Y. Gao, and O. H. Otterå, 2016: The sensitivity of the Atlantic meridional overturning circulation to enhanced freshwater discharge along the entire, eastern and western coast of Greenland. *Climate Dynamics*, **46 (5-6)**, 1351–1369, doi:10.1007/s00382-015-2651-9.

Yuan, T., L. Oreopoulos, M. Zelinka, H. Yu, J. R. Norris, M. Chin, S. Platnick, and K. Meyer, 2016: Positive low cloud and dust feedbacks amplify tropical North Atlantic Multidecadal Oscillation. *Geophysical Research Letters*, doi:10.1002/2016GL067679.

Zanna, L., P. Heimbach, A. M. Moore, and E. Tziperman, 2010: The Role of Ocean Dynamics in the Optimal Growth of Tropical SST Anomalies. *Journal of Physical Oceanography*, **40 (5)**, 983–1003, doi:10.1175/2009JPO4196.1.

Zanna, L., P. Heimbach, A. M. Moore, and E. Tziperman, 2011: Optimal Excitation of Interannual Atlantic Meridional Overturning Circulation Variability. *Journal of Climate*, **24 (2)**, 413–427, doi:10.1175/2010JCLI3610.1.

Zanna, L., P. Heimbach, A. M. Moore, and E. Tziperman, 2012: Upper-ocean singular vectors of the North Atlantic climate with implications for linear predictability and variability. *Quarterly Journal of the Royal Meteorological Society*, **138 (January)**, 500–513, doi:10.1002/qj.937.

Zhang, C., 2005: Madden-Julian Oscillation. *Reviews of Geophysics*, **43 (2)**, RG2003, doi:10.1029/2004RG000158, arXiv:1011.1669v3.

Zhang, R., 2008: Coherent surface-subsurface fingerprint of the Atlantic meridional overturning circulation. *Geophysical Research Letters*, **35 (20)**, 1–6, doi:10.1029/2008GL035463.

Zhang, R., and T. L. Delworth, 2006: Impact of Atlantic multidecadal oscillations on India/Sahel rainfall and Atlantic hurricanes. *Geophysical Research Letters*, **33 (17)**, doi:10.1029/2006GL026267.

Zhang, R., R. Sutton, G. Danabasoglu, T. L. Delworth, W. M. Kim, J. Robson, and S. G. Yeager, 2016a: Comment on "The Atlantic Multidecadal Oscillation without a role for ocean circulation". *Science*, **352 (6293)**, 1527–1527, doi:10.1126/science.aaf1660.

Zhang, R., R. Sutton, G. Danabasoglu, T. L. Delworth, W. M. Kim, J. Robson, and S. G. Yeager, 2016b: Comment on "the Atlantic Multidecadal Oscillation without a role for ocean circulation". doi:10.1126/science.aaf1660.

Zwally, H. J., and P. Gloersen, 1977: Passive microwave images of the polar regions and research applications. *Polar Record*, **18 (116)**, 431–450.

List of changes